NASA Contractor Report 189614

$P.~222$

VISCOUS-SHOCK-LAYER ANALYSIS OF HYPERSONIC
FLOWS OVER LONG SLENDER VEHICLES

Kam-Pui Lee and Roop N. Gupta

OLD DOMINION UNIVERSITY
Norfolk, Virginia

NASA

National Aeronautics and
Space Administration

Langley Research Center
Hampton, Virginia 23665-5225

ABSTRACT

A method for solving the viscous shock-layer equations for hypersonic flows over long slender bodies is presented. The governing equations are solved by employing a spatial-marching implicit finite-difference technique. The two first-order equations, continuity and normal momentum, are solved simultaneously as a coupled set. This method yields a simple and computationally efficient technique.

Flows past hyperboloids and sphere cones with body half angles of five to 35 degrees are considered. The flow conditions included are from high Reynolds numbers at low altitudes to low Reynolds numbers at high altitudes. Detailed comparisons have been made with other predictions and experimental data for slender body flows.

The results show that the coupling between the continuity and normal momentum equations is essential and adequate to obtain stable and accurate solutions past long slender bodies. Both the Cebeci-Smith and Baldwin-Lomax turbulence models are found to be adequate for application to long slender bodies. Using the corrected slip models, the viscous shock-layer predictions compare quite favorably with experimental data. Under chemical nonequilibrium conditions, the surface catalytic effects can significantly influence the surface heat transfer.

i

Acknowledgement

TABLE OF CONTENTS

LIST OF TABLES

LIST OF FIGURES

LIST OF FIGURES - CONCLUDED

LIST OF SYMBOLS

A^* local cross-section area

A^+ damping factor in Cebeci-Smith model

$\tilde{A}^+$ damping factor in Baldwin-Lomax model

C_{cp} constant in Baldwin-Lomax model

C_D total drag coefficient based on the local cross-section area, $2\,\text{Drag}/(\rho_\infty^* U_\infty^{*2} A^*)$

C_f skin friction coefficient, $2\,\tau_W^*/(\rho_\infty^* U_\infty^{*2})$

C_i mass fraction of species i, ρ_i/ρ

C_H heat transfer coefficient, $2\,Q_W^*/(\rho_\infty^* U_\infty^{*3})$

C_{Kleb} constant in Baldwin-Lomax model

C_p^* specific heat at constant pressure

C_p pressure coefficient, $2p^*/(\rho_\infty^* U_\infty^{*2})$

g stretching function

H $= h + u^2/2$

H_t total enthalpy, $H + v^2/2$

h static enthalpy, h^*/U_∞^{*2}

h_i enthalpy of species i, h_i^*/U_∞^{*2}

J_i diffusion mass flux of species i, $J_i^* R_N^* / \mu_{ref}^*$

K_1 von Karman constant

$K_{b,r}^*$ backward rate constant

$K_{f,r}^*$ forward rate constant

Kn freestream Knudsen number, λ_∞^* / R_N^*

k_W^* catalytic recombination rate

ℓ mixing length

M_∞ freestream Mach number

M_i^* molecular weight of species i

$\bar{M}^*$ molecular weight of mixture

n coordinate measured normal to the body, n^* / R_N^*

n^+ normal coordinate in turbulent model

n_{sh} shock stand-off distance

Pr Prandtl number, $C_p^* \mu^* / \kappa^*$

Pr,t turbulent Prandtl number

P^+ pressure-gradient parameter in turbulent model

p pressure, $p^* / (\rho_\infty^* U_\infty^{*2})$

Q_W^* heat transfer rate

q heat transfer rate, $Q_W^* / (\rho_\infty^* U_\infty^{*3})$

R^* universal gas constant

R_N^* body nose radius

r   radius measured from axis of symmetry to a point on the body surface, r^*/R_N^*

$Re,_\infty$ freestream Reynolds number, $\rho_\infty^* U_\infty^* R_N^*/\mu_\infty^*$

St   Stanton number, $-q/(H_\infty - H_w)$

S_∞ speed ratio, $U_\infty^* \sqrt{M^*/2R^*T_\infty^*}$

s   coordinate measured along the body surface, s^*/R_N^*

T   temperature, T^*/T_{ref}^*

$T_{o\infty}^*$ freestream adiabatic stagnation temperature

T_{ref}^* reference temperature, $U_\infty^{*2}/C_{p,\infty}^*$

U_∞^* freestream velocity

u   velocity component tangent to body surface, u^*/U_∞^*

u_e velocity component tangent to body surface at boundary layer edge

u_τ friction velocity

v   velocity component normal to body surface, v^*/U_∞^*

$\dot{w}_i$ mass rate of formation of species i, $\dot{w}_i^* R_N^*/\rho_\infty^* u_\infty^*$

X_i^* concentration of species i, mole/volume

x   axial distance

x_i mole fraction of species i

α shock angle defined in Fig. 2.1

$\bar{\alpha}$ mesh refinement parameter

$\alpha_1, \alpha_2, \alpha_3, \alpha_4$ coefficients in Eq. 2.25

$\alpha_{i,r}$ stoichiometric coefficients for reactants

β angle defined in Fig. 2.1

$\bar{\beta}$ mesh refinement parameter

$\beta_{i,r}$ stoichiometric coefficients for products

γ ratio of specific heats

γ_i catalytic recombination coefficient

$\gamma_{i,\bar{\eta}}$ normal intermittency factor

$\gamma_{i,\xi}$ streamwise transition intermittency factor

δ boundary layer thickness

δ_k incompressible displacement thickness

ε Reynolds number parameter, $[\mu^*_{ref}/\rho^*_\infty U^*_\infty R^*_N]^{1/2}$

ε^+ normalized eddy viscosity , μ_T/μ

ε^+_i eddy viscosity from inner law

ε^+_o eddy viscosity from outer law

η transformed $\bar{\eta}$ coordinate, $g(\bar{\eta})$

$\bar{\eta}$ transformed n coordinate, n/n_{sh}

θ body angle defined in Fig. 2.1

$\bar{\theta}$ accommodation coefficient

κ body curvature, $\kappa^* R^*_N$

κ thermal conductivity, $\kappa^*/\mu_{ref} C^*_{p,\infty}$

κ_T eddy thermal conductivity, $\kappa_T^*/\mu_{ref}^* C_{p,\infty}^*$

λ_∞^* freestream mean-free path

μ viscosity, μ^*/μ_{ref}^*

μ_{ref}^* reference viscosity, $\mu^*(T_{ref}^*)$

μ_T eddy viscosity

ξ coordinated measured along the body surface, $\xi = s$

ρ density, ρ^*/ρ_∞^*

τ shear stress, $\tau^*/(\rho_\infty^* U_\infty^{*2})$

ω vorticity

Subscripts

aw   adiabatic wall

e   boundary-layer edge

i   ith species

s   value at edge of Knudsen layer

sh   shock value

w   wall value

∞ freestream value

Superscripts

j   zero for plane flow and one for axisymmetric flow

~   shock oriented velocity components

'   total differential

*   dimensional quantity

Abbreviations

BL   Baldwin-Lomax

CS	Cebeci-Smith
NS	Navier-Stokes
PNS	Parabolized Navier-Stokes
VSL	Viscous shock-layer
VSL2D	Two-dimensional viscous shock-layer
VSL3D	Three-dimensional viscous shock-layer

Chapter 1

INTRODUCTION

1.1 Physical Features of the High Mach Number Flow

A renewed interest in hypersonic aerothermodynamics has been motivated by new vehicle concepts such as the national aero-space plane (NASP) [1]*, and the transatmospheric vehicle (TAV) [2]. The term "hypersonic" implies that the flight velocity is much greater than the ambient speed of sound. An approximate classification of this flow regime is where the freestream Mach number is greater than five. These vehicles will encounter a variety of flow conditions which include atmospheric flight and the transitional flow regimes. For example [3], the TAV will take off from the Earth's surface, and enter a low Earth orbit. The vehicle will carry out a global mission either inside or outside the atmosphere, and eventually land back on Earth under its own power. The range of flow conditions includes low altitude, high density flow, to high altitude, low density flow. These conditions include the continuum flow regime where the no-slip assumption is made. In addition the transitional flow regime, where slip effects are important, must be considered.

---

*The numbers in brackets indicate references.

There are two main effects associated with hypersonic flows [4,5]: (1) the fluid dynamic effects arising from the high velocity gas, and (2) the real gas effects due to the high temperature gas. For hypersonic speeds, the shock layer, which is defined as the distance between the shock and body, is small. The boundary layer thickness grows more rapidly because kinetic energy dissipation within the boundary layer, which yields a high gas temperature, results in an increase in gas viscosity and a decrease in density. Along with the thin shock layer, the thick boundary layer creates an important disturbance in the outer flow that gives rise to the viscous interaction phenomenon which controls the surface pressure distribution over the body. Moreover, for a blunt body, the shock wave is curved, leading to large entropy gradients in the shock layer.

Compression of the gas forward of the vehicle and heat generation due to viscous dissipation lead to elevate gas temperatures in the shock layer. Additionally, the gas will promote chemical reaction in both the boundary layer and the shock layer. As a result, the specific heat per unit mass is increased considerably, and the specific heat ratios will no longer be constant. The gas will not behave as a calorically perfect gas. Moreover, if the shock layer temperature is sufficiently elevated, radiation effects will become important, giving rise to a radiative flux to the surface. The resulting heat transfer to the surface of a hypersonic vehicle will dominate the design criteria of the vehicle.

For hypersonic speeds, Blottner [6] showed that the shock layer flow is in chemical equilibrium and has a definite boundary layer region for low altitude conditions. Also, the flow can become turbulent at these conditions [7]. However, the gas may not reach the equilibrium

state for higher altitude conditions. Moreover, the boundary layer
cannot be identified because it merges with the shock wave.

1.2 Numerical Methods for Hypersonic Flow

In general, there are two methods to analyse hypersonic flow --
experimental and theoretical . Flows in chemical equilibrium can be
simulated with small-scale laboratory experiments with corrections for
"real gas" effects. However, the chemical nonequilibrium flow around a
hypersonic vehicle operating in the upper atmosphere cannot be simulated
because it requires simultaneous reproduction of air density, flight
velocity and vehicle scale. In absence of a full-scale flight
experiment in which the thermodynamic environment is fully duplicated,
an adequate design capability for hypersonic vehicles relies on
theoretical predictions.

The great entropy gradients and the thick boundary layer in a
hypersonic flow make the classical isentropic irrotational approach and
the conventional first-order boundary layer equations inadequate to
predict the flowfield. Second-order boundary layer effects and
vorticity interaction should be considered in the flow. Three current
numerical approaches have been adopted for analysing these problems.
They are the solution of either the second-order boundary layer
equations, the full Navier-Stokes equations, or the viscous shock-layer
equations.

The simplest of these approaches is to employ the second-order
boundary layer equations [8], with matching of the first- and second-
order boundary layer and inviscid solutions at the boundary layer edge.
Although this approach has been found quite attractive for short slender

bodies [9], several computational difficulties become obvious for long slender bodies. First, the computing time required is excessive because one must compute the inviscid flow, the first-order boundary layer flow, the flow due to displacement thickness, and then the second order boundary layer flow. A second difficulty arises from strong vorticity interaction which may occur far downstream due to the entropy layer on blunt long slender bodies. This entropy layer causes difficulty in the matchup procedure between the viscous and inviscid regions because there is a question as to what the proper edge conditions should be for the boundary layer. This approach does not properly take into account the swallowing of the strong entropy layer by the boundary layer [5]. The design geometries of hypersonic vehicles are slender long bodies with blunt noses in order to reduce heat transfer rate at the stagnation region and reduce drag force on the body. The second-order boundary layer equations are not desirable for this problem.

The second approach employs the steady Navier-Stokes equations [10] and their time-dependent forms [11]. This approach successfully provides the solution for the stagnation region of short bodies. However, the complexity of the solution procedure due to the elliptic nature of the equations requires excessive computing time and computer storage, which currently limits their applications to short bodies.

Because of the difficulties encountered by the above two approaches, attention has turned toward the third approach, the viscous shock-layer equations. This set of equations which was developed by Davis [12] is obtained from the full Navier-Stokes equations by keeping terms up to second-order in the inverse square root of the Reynolds number in both viscous and inviscid regions. It is uniformly valid to

second-order throughout the entire shock layer, hence, the viscous-inviscid interactions and strong vorticity interactions are accounted for in a straight-forward manner. Moreover, this set of equations is of a hyperbolic-parabolic nature and, therefore, can be solved by using a marching procedure similar to methods employed in boundary layer theory. As a consequence, they can be solved for a hypersonic flow on a slender long body without excessive computer time and storage requirements. Moreover, this set of equations can be used to compute the viscous flow in the subsonic blunt nose region. This is desirable for long bodies, especially for analysing problems with chemical reactions.

The full viscous shock layer solution of Davis [12] was obtained through an iterative relaxation process from the thin shock layer solution. This approach encountered difficulties for the flow far downstream, especially for the slender body. Werle et al. [13] developed an Alternating Direction Implicit (ADI) Technique with an artificial time coordinate to relax the shock shape from an initial guess. Even with large relaxation factors, the instabilities were still encountered whenever the inviscid region encompasses a significant portion of the total shock layer thickness. The relaxations of the shock shape in Davis [12] and Werle et al. [13] are essential due to the slightly elliptic nature of the equations in the streamwise direction. These instabilities do not come from the shock shape relaxing technique.

From the hypersonic small disturbance theory [14], it is shown that the continuity, normal momentum, and energy equations become uncoupled from the tangential momentum equation in the inviscid region. In other words, the solution of the continuity, normal momentum and energy equations will not depend strongly on the solution of the

tangential momentum equation. The numerical methods of Davis [12] and Werle et al. [13] solved the governing equations separately which are known as the cascading method. In this method, the solution of the tangential momentum equation drives the solution of the continuity and normal momentum equations. This method becomes improper for the flow far downstream, especially for a slender body on which the shock layer thickness is very thick and the inviscid region encompasses a large portion of the shock layer. An alternative method of solution was suggested by Werle et al. [13]. The more adequate method is to solve the equations simultaneously.

A fully coupled system of all the equations is a desirable scheme. Hosny et al. [15] solved the four governing equations, namely, the continuity, tangential momentum, normal momentum and energy equations, simultaneously as a coupled set and local iterations were made to solve for the shock stand-off distance. Gorden and Davis [16] added an equation for the shock stand-off distance into the coupled set to eliminate the need for local iterations. This technique is quite appealing for perfect gas applications. But, it requires inversion of large matrices and hence the storage and computing requirements are quite large. Also, the system of equations will become very complicated if chemical reactions are included. Therefore, this approach is not desirable for long bodies.

The two second-order equations, tangential momentum and energy, are parabolic, and there are few problems in finding the solutions to these equations. The greatest difficulty exists in solving the two first-order equations, continuity and normal momentum [13]. Moreover, from the hypersonic small disturbance theory, the solution of the

tangential momentum equation becomes uncoupled with the other equations far downstream for a slender body. A more desirable approach is to solve the two first-order equations simultaneously as a coupled set rather than solve all four equations as a fully coupled set. This approach is quite attractive for slender body problems, especially with real gas effects. The instabilities will be eliminated, and the storage requirements and computing time may not increase excessively. Waskiewicz and Lewis [17] coupled the two first-order equations and reported good improvement in the solution obtained for slender (7 degree and 10 degree) but short bodies with solutions up to 20 nose radii or less. The effects of this technique on the flow field over a slender long body far downstream should be investigated.

Most of the work with viscous shock-layer equations in the past has considered either short slender or wide angle bodies. However, most of the future vehicles will be long slender blunt bodies. The calculation of hypersonic viscous flows past long slender axisymmetric blunt bodies is of prime interest to the designer of such aerospace vehicles.

A variety of flow conditions are encountered during the transatmospheric flight of these vehicles. The range is from low Reynolds numbers at high altitudes to high Reynolds numbers at low altitudes. At low altitude, the hypersonic flow over a slender body usually becomes turbulence. Direct numerical solution of turbulent flow cannot be obtained at the present. The prediction of turbulent effects depends on modeling the fluctuation terms. The algebraic eddy viscosity models are more appealing than the other models because less computer storage and computer time are required. The general algebraic

turbulence model which is implemented with the viscous shock layer method is the Cebeci-Smith model [18,19]. Due to the difficulty of determining the boundary layer edge in a hypersonic flow over a long slender body, an alternative model, the Baldwin-Lomax model [20], is more likely to be used. This model has been implemented in the Navier-Stokes equations and the parabolic Navier-Stokes equations [21,22], but not in the viscous shock-layer equations.

At high altitude, the "low density effects" become important where they can significantly influence the lift, drag, moments and aerodynamic heating of a hypersonic vehicle. However, not much attention has been given to the problems encountered with low-density aerothermodynamics. At highly rarefied gas flow conditions, the continuum approach is no longer valid. But at slightly rarefied gas flow conditions, the continuum approach can be extended to this flow regime if slip effects are properly accounted for [12,23].

At high temperature, the perfect gas assumption becomes invalid. The gases in the flow become chemically reacting, especially, at high altitude. While flows with chemical equilibrium in the shock layer have been studied intensively [24,25], there are only a limited number of analyses on flows with chemical nonequilibrium [6,26]. The effects of finite-rate chemical reactions are not fully understood yet.

The main objective of this study, therefore, is to investigate the solution for long slender blunt body; i.e., the continuity and normal momentum equations are solved simultaneously as a coupled set. The basic theoretical formulations used in this study are provided in Chap. 2. The suitability of the Cebeci-Smith and Baldwin-Lomax models for the hypersonic flow past long slender bodies at low altitudes is examined.

examined. It is presented in Chap. 3. The low-density effects using a perfect gas model are presented in Chap. 4. The investigation of a chemical nonequilibrium flow is presented in Chap. 5.

Chapter 2

BASIC THEORETICAL FORMULATION

The viscous shock-layer equations for a perfect gas [12] and for a multicomponent gas mixture [24] are presented in this chapter. The physical model and coordinate system for a body are shown in Fig. 2.1. The flow in the shock layer is assumed to be axisymmetic, steady, viscous and compressible. The shock-layer gas is assumed in local thermodynamic equilibrium.

2.1 Governing Equations For a Perfect Gas

The viscous shock-layer equations are obtained from compressible Navier-Stokes equations which are written in the body-oriented coordinate system shown in Fig. 2.1. These equations are nondimensionalized with variables which are of order one in the region near the body surface (boundary layer) for large Reynolds number. The same set of equations are then written in variables which are of order one in the essentially inviscid region outside the boundary layer. Terms in each set of equations up to second-order in the inverse square root of a Reynolds number are kept. A comparison of the two sets of equations is then made and one set of equations is obtained which is valid to second order in both the outer and inner regions. A solution to this set of equations is thus uniformly valid to second-order in the entire shock layer for arbitrary Y. Anderson and Moss [19] used the
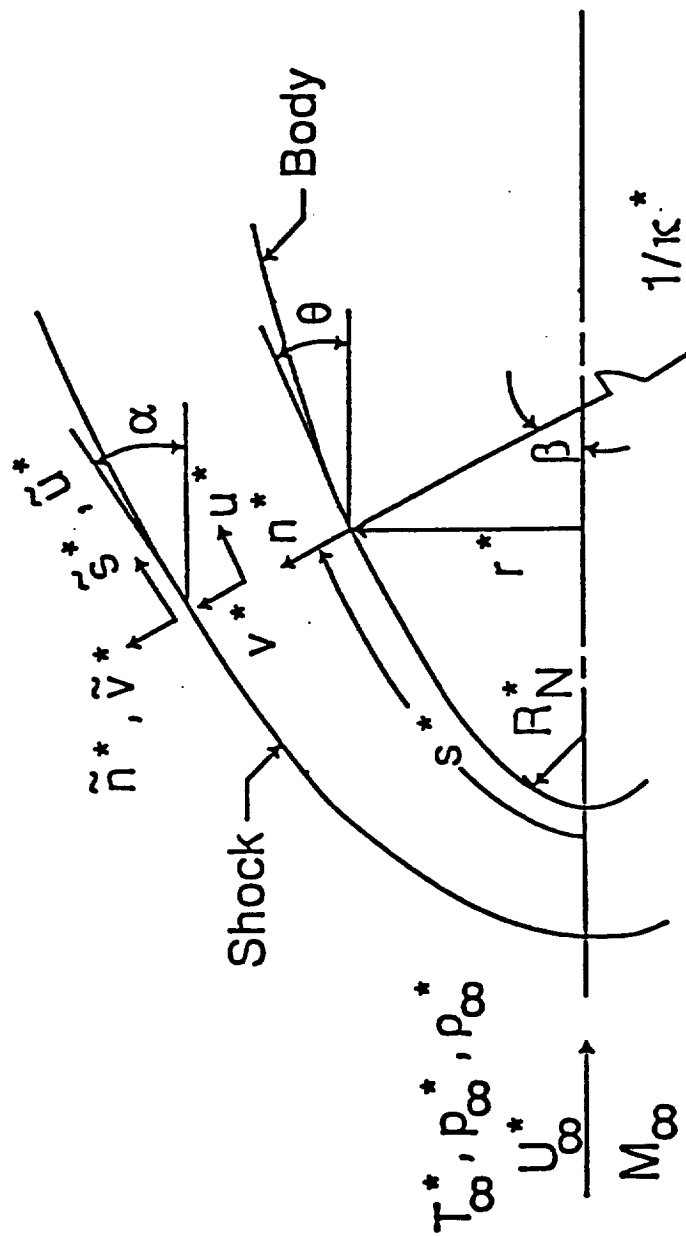
Fig. 2.1   Coordinate system.

eddy viscosity approximation to replace the Reynolds stresses and turbulent heat flux to find the solution of the turbulent flow. The viscous shock-layer equations for a perfect gas with turbulent flow are [19]

Continuity:

$$\frac{\partial}{\partial s}[(r+n\cos\theta)^j \rho u] + \frac{\partial}{\partial n}[(1+n\kappa)(r+n\cos\theta)^j \rho v] = 0 \qquad (2.1)$$

s-momentum:

$$\rho(\frac{u}{1+n\kappa}\frac{\partial u}{\partial s} + v\frac{\partial u}{\partial n} + \frac{uv\kappa}{1+n\kappa}) + \frac{1}{1+n\kappa}\frac{\partial p}{\partial s} = \epsilon^2\{\frac{\partial}{\partial n}[\mu(1+\epsilon^+)\frac{\partial u}{\partial n}$$

$$- \frac{\mu u\kappa}{1+n\kappa}] + (\frac{2\kappa}{1+n\kappa} + \frac{j\cos\theta}{r+n\cos\theta})[(1+\epsilon^+)\frac{\partial u}{\partial n} - \frac{\mu u\kappa}{1+n\kappa}]\} \qquad (2.2)$$

n-momentum:

$$\rho(\frac{u}{1+n\kappa}\frac{\partial v}{\partial s} + v\frac{\partial v}{\partial n} - \frac{u^2\kappa}{1+n\kappa}) + \frac{\partial p}{\partial n} = 0 \qquad (2.3)$$

Energy:

$$\rho(\frac{u}{1+n\kappa}\frac{\partial H}{\partial s} + v\frac{\partial H}{\partial n}) - v\frac{\partial p}{\partial n} + \frac{\rho u^2 v\kappa}{1+n\kappa} =$$

$$\epsilon^2\{\frac{\partial}{\partial n}[\frac{\mu}{Pr}(1+\epsilon^+\frac{Pr}{Pr,t})\frac{\partial H}{\partial n} + \phi] + (\frac{\kappa}{1+n\kappa} + \frac{j\cos\theta}{r+n\cos\theta})$$

$$x \ [\frac{\mu}{Pr}(1+\epsilon^+\frac{Pr}{Pr,t})\frac{\partial H}{\partial n} + \phi]\} \qquad (2.4)$$

State:

$$p = \frac{(\gamma-1)}{\gamma}\rho T \qquad (2.5)$$

where

$$\phi = \frac{\mu}{Pr}[Pr - 1 + \varepsilon^+ \frac{Pr}{Pr,t}(Pr,t - 1) \ u \ \frac{\partial u}{\partial n}] - \frac{\mu u^2 \kappa}{1+n\kappa} \qquad (2.6)$$

The molecular viscosity is given by the Sutherland's law as

$$\mu = [(1+C)/(T+C)] \ T^{3/2} \qquad (2.7)$$

where

$$C = C^*/(\gamma-1) \ M_\infty^2 \ T_\infty^* \qquad (2.8)$$

and C^* is 110.33 K for air.

The preceding equations are written in nondimensional forms where the nondimensional variables are defined as

$$s = s^*/R_N^* \qquad u = u^*/U_\infty^* \qquad p = p^*/\rho_\infty^* U_\infty^{*2}$$

$$n = n^*/R_N^* \qquad v = v^*/U_\infty^* \qquad T = T^*/T_{ref}^*$$

$$r = r^*/R_N^* \qquad \rho = \rho^*/\rho_\infty^* \qquad \mu = \mu^*/\mu^*(T_{ref}^*)$$

$$\kappa = \kappa^* R_N^* \qquad h = h^*/h_\infty^* \qquad C_p = C_p^*/C_{p,\infty}^* \qquad (2.9)$$

Also, the dimensionless parameters that appear in Eqs. (2.1) to (2.6) are defined as

$$Pr = \mu^* C_p^*/\kappa^* \qquad (2.10)$$

$$Pr,t = \mu_T^* C_p^*/\kappa_T^* \qquad (2.11)$$

$$\varepsilon = [\frac{\mu^*(T_{ref}^*)}{\rho_\infty^* U_\infty^* R_N^*}]^{1/2} \qquad (2.12)$$

and

$$\varepsilon^+ = \mu_T^*/\mu^* \qquad (2.13)$$

To simplify the numerical computations, a coordinate transformation is applied to the viscous shock-layer equations. This transformation is accomplished by normalizing the normal coordinate with respect to the local shock standoff distance. Consequently, a constant number of finite-difference grid points between the body and shock are used. Also, the need for interpolation to determine shock shape and the addition of grid points in the normal direction is eliminated as the computation moves downstream.

The transformed variables are

$$s = \xi \tag{2.14}$$

$$\bar{\eta} = n/n_{sh} \tag{2.15}$$

The transformations relating the differential quantities are

$$\frac{\partial}{\partial s} = \frac{\partial}{\partial \xi} - \frac{n'_{sh}}{n_{sh}} \bar{\eta} \frac{\partial}{\partial \bar{\eta}} \tag{2.16}$$

$$\frac{\partial}{\partial n} = \frac{1}{n_{sh}} \frac{\partial}{\partial \bar{\eta}} \tag{2.17}$$

and

$$\frac{\partial}{\partial n^2} = \frac{1}{n^2_{sh}} \frac{\partial}{\partial \bar{\eta}^2} \tag{2.18}$$

where

$$n'_{sh} = \frac{dn_{sh}}{d\xi} \tag{2.19}$$

In general, a variable grid spacing is used in the $\bar{\eta}$-direction so that the grid spacing can be made small in the region of large gradients. Since the spacing is not uniform in the $\bar{\eta}$ direction, it is convenient to apply a transformation to the $\bar{\eta}$ coordinate so that the

governing equations can be solved on a uniformly spaced grid in the computational plane. This transformation is achieved by [26]

$$\eta = g(\frac{n}{n_{sh}}) = g(\overline{\eta}) \tag{2.20}$$

The stretching function $g(\overline{\eta})$ is given by

$$g(\overline{\eta}) = 1 - [\overline{\alpha} + \frac{(1-\overline{\alpha})}{\ln(\frac{\overline{\beta}+1}{\overline{\beta}-1})} \ln \{\frac{\overline{\beta}-\overline{\eta}(2\overline{\alpha}+1)+1}{\overline{\beta}+\overline{\eta}(2\overline{\alpha}+1)-1}\}] \tag{2.21}$$

The first and second derivatives of Eq. (2.21) are expressed as

$$\frac{dg}{d\overline{\eta}} = \frac{(1-\overline{\alpha})(2\overline{\alpha}+1)}{\ln(\frac{\overline{\beta}+1}{\overline{\beta}-1})} \{\frac{1}{[\overline{\beta}-\overline{\eta}(2\overline{\alpha}+1)+1]} - \frac{1}{[\overline{\beta}+\overline{\eta}(2\overline{\alpha}+1)-1]}\} \tag{2.22}$$

$$\frac{d^2g}{d\overline{\eta}^2} = \frac{(1-\overline{\alpha})(2\overline{\alpha}+1)^2}{\ln(\frac{\overline{\beta}+1}{\overline{\beta}-1})} \{\frac{1}{[\overline{\beta}-\overline{\eta}(2\overline{\alpha}+1)+1]^2} - \frac{1}{[\overline{\beta}+\overline{\eta}(2\overline{\alpha}+1)-1]^2}\} \tag{2.23}$$

Equation (2.21) permits the mesh to be refined either near the body only ($\overline{\alpha} = 0$) or equally near both the body and bow shock ($\overline{\alpha} = 1/2$). The parameter $\overline{\beta}$ controls the amount of stretching. The coordinate $\overline{\eta}$ can be obtained from inverting Eq. (2.21) and is expressed as

$$\overline{\eta} = \frac{1}{(2\overline{\alpha}+1)} [1 - \overline{\beta} \{\frac{(\frac{\overline{\beta}+1}{\overline{\beta}-1})^{\frac{1-\eta-\overline{\alpha}}{1-\overline{\alpha}}} - 1}{(\frac{\overline{\beta}+1}{\overline{\beta}-1})^{\frac{1-\eta-\overline{\alpha}}{1-\overline{\alpha}}} + 1}\}] \tag{2.24}$$

This transformation keeps the body at $\eta = 0$ and the shock at $\eta = 1$ with uniform mesh in the computational coordinate η.

After the governing equations, Eqs. (2.1) to (2.6), are written in the transformed ξ, η coordinates, the second-order partial differential equations are expressed as [19]

$$\frac{\partial^2 W}{\partial \eta^2} + \frac{d^2 g/d\bar{\eta}^2 + \alpha_1 (dg/d\bar{\eta})}{(dg/d\bar{\eta})^2} \frac{\partial W}{\partial \eta} + \frac{\alpha_2}{(dg/d\bar{\eta})^2} W$$

$$+ \frac{\alpha_3}{(dg/d\bar{\eta})^2} + \frac{\alpha_4}{(dg/d\bar{\eta})^2} \frac{\partial W}{\partial \xi} = 0 \qquad (2.25)$$

The quantity W represents u for the s-momentum equation and H for the energy equation. The coefficients α_1 to α_4 are written as:

s-momentum, W = u:

$$\alpha_1 = \frac{1}{\mu(1+\epsilon^+)} \frac{\partial \mu(1+\epsilon^+)}{\partial \eta} \frac{dg}{d\bar{\eta}} + \frac{n_{sh}\kappa(1+2\epsilon^+)}{(1+\bar{\eta}n_{sh}\kappa)(1+\epsilon^+)} + \frac{jn_{sh}\cos\theta}{r + \bar{\eta}n_{sh}\cos\theta}$$

$$+ \frac{n'_{sh} n_{sh} \bar{\eta}\rho u}{\epsilon^2 \mu(1+\epsilon^+)(1+\bar{\eta}n_{sh}\kappa)} - \frac{n_{sh}\rho v}{\epsilon^2 \mu(1+\epsilon^+)} \qquad (2.26)$$

$$\alpha_2 = -\frac{n_{sh}\kappa}{\mu(1+\epsilon^+)(1+\bar{\eta}n_{sh}\kappa)} \frac{\partial \mu(1+\epsilon^+)}{\partial \eta} \frac{dg}{d\bar{\eta}} - \frac{n_{sh}^2\kappa}{(1+\epsilon^+)(1+\bar{\eta}n_{sh}\kappa)} \times$$

$$\left[\frac{\kappa}{1+\bar{\eta}n_{sh}\kappa} + \frac{j\cos\theta}{r+\bar{\eta}n_{sh}\cos\theta}\right] - \frac{n_{sh}^2\kappa\rho v}{\epsilon^2(1+\bar{\eta}n_{sh}\kappa)\mu(1+\epsilon^+)} \qquad (2.27)$$

$$\alpha_3 = -\frac{n_{sh}^2}{\epsilon^2(1+\bar{\eta}n_{sh}\kappa)\mu(1+\epsilon^+)} \left[\frac{\partial p}{\partial \xi} - \frac{n'_{sh}\bar{\eta}}{n_{sh}} \frac{dg}{d\bar{\eta}} \frac{\partial p}{\partial \eta}\right] \qquad (2.28)$$

$$\alpha_4 = - \frac{n_{sh}^2 \rho u}{\varepsilon^2 (1 + \bar{\eta} n_{sh} \kappa) \mu (1 + \varepsilon^+)} \tag{2.29}$$

Energy, W = H:

$$\alpha_1 = \frac{1}{\frac{\mu}{Pr}(1 + \varepsilon^+ \frac{Pr}{Pr,t})} \frac{dg}{d\bar{\eta}} \frac{\partial}{\partial \eta} \left[\frac{\mu}{Pr}(1 + \varepsilon^+ \frac{Pr}{Pr,t}) \right] + \frac{\kappa n_{sh}}{1 + \bar{\eta} n_{sh} \kappa}$$

$$+ \frac{j n_{sh} \cos\theta}{r + \bar{\eta} n_{sh} \cos\theta} + \frac{n_{sh}' n_{sh} \bar{\eta} \rho u}{\varepsilon^2 \frac{\mu}{Pr}(1 + \varepsilon^+ \frac{Pr}{Pr,t})(1 + \bar{\eta} n_{sh} \kappa)}$$

$$- \frac{n_{sh} \rho v}{\varepsilon^2 \frac{\mu}{Pr}(1 + \varepsilon^+ \frac{Pr}{Pr,t})} \tag{2.30}$$

$$\alpha_2 = 0 \tag{2.31}$$

$$\alpha_3 = \frac{n_{sh}}{\frac{\mu}{Pr}(1 + \varepsilon^+ \frac{Pr}{Pr,t})} \left[\frac{dg}{d\bar{\eta}} \frac{\partial\phi}{\partial\eta} + n_{sh}\left(\frac{\kappa}{1 + \bar{\eta} n_{sh} \kappa} + \frac{j \cos\theta}{r + \bar{\eta} n_{sh} \cos} \right) \phi \right.$$

$$\left. + \frac{v}{\varepsilon^2} \frac{dg}{d\bar{\eta}} \frac{\partial p}{\partial \eta} - \frac{n_{sh} \kappa v \rho u^2}{\varepsilon^2 (1 + \bar{\eta} n_{sh} \kappa)} \right] \tag{2.32}$$

$$\alpha_4 = - \frac{n_{sh}^2 \rho u}{\varepsilon^2 \frac{\mu}{Pr}(1 + \varepsilon^+ \frac{Pr}{Pr,t})(1 + \bar{\eta} n_{sh} \kappa)} \tag{2.33}$$

where

$$\phi = \frac{\mu}{Pr} \left[Pr - 1 + \epsilon^+ \frac{Pr}{Pr,t}(Pr,t - 1) \right] \frac{u}{n_{sh}} \frac{dg}{d\bar{\eta}} \frac{\partial u}{\partial \eta} - \frac{\mu u^2 \kappa}{1+\bar{\eta}n_{sh}\kappa} \qquad (2.34)$$

The remaining first-order equations are written as

Global Continuity:

$$\frac{\partial}{\partial\xi}[n_{sh}(r+\bar{\eta}n_{sh}\cos\theta)^j\rho u] + \frac{dg}{d\bar{\eta}} \frac{\partial}{\partial\eta}\{(r+\bar{\eta}n_{sh}\cos\theta)$$

$$x \ [(1+\bar{\eta}n_{sh}\kappa)\rho v - n'_{sh}\bar{\eta}\rho u]\} = 0 \qquad (2.35)$$

n-momentum:

$$\frac{\rho u}{(1+\bar{\eta}n_{sh}\kappa)} \frac{\partial v}{\partial\xi} - \frac{n'_{sh}\bar{\eta}\rho u}{n_{sh}(1+\bar{\eta}n_{sh}\kappa)} \frac{\partial v}{\partial\eta} \frac{dg}{d\bar{\eta}} + \frac{\rho v}{n_{sh}} \frac{\partial v}{\partial\eta} \frac{dg}{d\bar{\eta}}$$

$$- \frac{\rho u^2 \kappa}{(1+\bar{\eta}n_{sh}\kappa)} + \frac{1}{n_{sh}} \frac{\partial p}{\partial\eta} \frac{dg}{d\bar{\eta}} = 0 \qquad (2.36)$$

State:

$$p = \rho T \ (\gamma-1)/\gamma \qquad (2.37)$$

2.2 Governing Equations for a Multicomponent Mixture

The conservation equations that describe a reacting multicomponent gas mixture can be found in the literature [27,28]. The viscous shock-layer equations for a nonequilibrium multicomponent gas mixture are obtained from the conservation equations employing the same procedure as for the perfect gas [24]. The nondimensional forms of global

continuity, s-momentum, and n-momentum are written in the same form as

Eqs. (2.1) to (2.3) except the eddy viscosity, ϵ^+, is set to zero.

For a chemical nonequilibrium flow, the energy equation is formulated in terms of the temperature instead of total enthalpy. In addition to these conservation equations, the species continuity equation and equation of state are needed to complete the set of equations. The nondimensional forms of these equations are expressed as [24]

Energy:

$$\rho C_p \left(\frac{u}{1+n\kappa} \frac{\partial T}{\partial s} + v \frac{\partial T}{\partial n} \right) - \left(\frac{u}{1+n\kappa} \frac{\partial p}{\partial s} + v \frac{\partial p}{\partial n} \right) =$$

$$\epsilon^2 \left[\frac{\partial}{\partial n} \left(\kappa \frac{\partial T}{\partial n} \right) + \left(\frac{\kappa}{1+n\kappa} + \frac{j\cos\theta}{r+n\cos\theta} \right) \kappa \frac{\partial T}{\partial n} - \sum_{i=1}^{N_s} J_i C_{p,i} \frac{\partial T}{\partial n} + \right.$$

$$\left. \mu \left(\frac{\partial u}{\partial n} - \frac{\kappa u}{1+n\kappa} \right)^2 \right] - \sum_{i=1}^{N_s} h_i \dot{w}_i \tag{2.38}$$

Species continuity:

$$\rho \left(\frac{u}{1+n\kappa} \frac{\partial C_i}{\partial s} + v \frac{\partial C_i}{\partial n} \right) = \dot{w}_i - \frac{\epsilon^2}{(1+n\kappa)(r+n\cos\theta)^j}$$

$$\times \left\{ \frac{\partial}{\partial n} \left[(1+n\kappa)(r+n\cos\theta)^j J_i \right] \right\} \tag{2.39}$$

State:

$$p = \rho T \left(\frac{R^*}{\bar{M}^* C_{p,\infty}^*} \right) \tag{2.40}$$

The nondimensional variables are as defined by Eq. (2.9) and

$$\kappa = \kappa^*/\mu_{ref}^* C_{p,\infty}^*$$

$$\dot{w}_i = \dot{w}_i^* R_N^*/\rho_\infty^* U_\infty^*$$

$$J_i = J_i^* R_N^*/\mu_{ref}^*$$

(2.41)

Using the same coordinate transformations as given for a perfect gas, Eqs. (2.38) and (2.39) are written in the form of Eq. (2.25). The W in this equation represents T for the energy equation and C_i for the species continuity equation. The coefficients α_1 to α_4, in this case, are given by

Energy, W = T :

$$\alpha_1 = \frac{1}{\kappa}\frac{\partial\kappa}{\partial\eta}\frac{dg}{d\bar{\eta}} + \frac{n_{sh}\kappa}{1+\bar{\eta}n_{sh}\kappa} + \frac{jn_{sh}\cos\theta}{r+\bar{\eta}n_{sh}\cos\theta} - \frac{n_{sh}}{\kappa}\sum_{i=1}^{N_s}J_i C_{p,i}$$

$$+ \frac{n_{sh}n'_{sh}\rho C_p u\bar{\eta}}{\epsilon^2\kappa(1+\bar{\eta}n_{sh}\kappa)} - \frac{n_{sh}\rho C_p v}{\epsilon^2\kappa}$$

(2.42)

$$\alpha_2 = 0$$

(2.43)

$$\alpha_3 = \frac{n_{sh}^2\mu}{\kappa}\left(\frac{1}{n_{sh}}\frac{\partial u}{\partial\eta}\frac{dg}{d\bar{\eta}} - \frac{\kappa u}{1+\bar{\eta}n_{sh}\kappa}\right)^2 - \frac{n_{sh}^2\bar{\eta}}{\epsilon^2\kappa}\sum_{i=1}^{N_s}h_i\dot{w}_i$$

$$+ \frac{un_{sh}^2}{\epsilon^2\kappa(1+\bar{\eta}n_{sh}\kappa)}\frac{\partial p}{\partial\xi} - \frac{n_{sh}^2}{\epsilon^2\kappa}\left(\frac{u}{1+\bar{\eta}n_{sh}\kappa}\frac{n'_{sh}\bar{\eta}}{n_{sh}} - \frac{v}{n_{sh}}\right)\frac{dg}{d\bar{\eta}}\frac{\partial p}{\partial\eta}$$

(2.44)

$$\alpha_4 = -\frac{n_{sh}^2 \rho C_p u}{\epsilon^2 \kappa (1+\bar{\eta}n_{sh}\kappa)} \tag{2.45}$$

Species continuity, $W = C_i$:

$$\alpha_1 = \frac{1}{PL_i}\frac{\partial PL_i}{\partial \eta}\frac{dg}{d\bar{\eta}} + \left(\frac{n_{sh}\kappa}{1+\bar{\eta}n_{sh}\kappa} + \frac{n_{sh}\cos\theta}{r+\bar{\eta}n_{sh}\cos\theta}\right)$$

$$+ \frac{n_{sh}n_{sh}'\bar{\eta}\rho u}{\epsilon^2 PL_i(1+\bar{\eta}n_{sh}\kappa)} - \frac{n_{sh}\rho v}{\epsilon^2 PL_i} \tag{2.46}$$

$$\alpha_2 = 0 \tag{2.47}$$

$$\alpha_3 = \frac{1}{PL_i}\frac{\partial PM_i}{\partial \eta}\frac{dg}{d\bar{\eta}} + \frac{PM_i}{PL_i}\left(\frac{n_{sh}\kappa}{1+\bar{\eta}n_{sh}\kappa} + \frac{n_{sh}\cos\theta}{r+\bar{\eta}n_{sh}\cos\theta}\right) + \frac{\dot{w}_i n_{sh}^2}{\epsilon^2 PL_i} \tag{2.48}$$

$$\alpha_4 = -\frac{n_{sh}^2 \rho u}{\epsilon^2 PL_i(1+\bar{\eta}n_{sh}\kappa)} \tag{2.49}$$

where

$$PL_i = \frac{\mu}{Pr}\Delta b_{ii} \tag{2.50}$$

$$PM_i = \frac{\mu}{Pr}\sum_{\substack{k=1 \\ k \neq i}}^{N_s} \Delta b_{ik}\frac{\partial C_k}{\partial \eta}\frac{dg}{d\bar{\eta}} \tag{2.51}$$

$$
\Delta b_{ik} = \begin{cases} Le,_i & i=k \\ \\ Le,_i - \left[\dfrac{M_i^*}{\overline{M}^*} Le,_{ik} + \left(1 - \dfrac{M_i^*}{\overline{M}_k^*}\right) \displaystyle\sum_{\substack{j=1 \\ j\neq i}}^{N_s} Le,_{ij}C_j \right] & i\neq k \end{cases}
\tag{2.52}
$$

In Eq. (2.52), $Le,_{ik}$ are the multicomponent Lewis numbers and $\overline{M}^*$ is molecular weight which is given by

$$
\overline{M}^* = \frac{1}{\displaystyle\sum_{i=1}^{N_s} \frac{C_i}{\overline{M}_i^*}}
\tag{2.53}
$$

The mass flux, J_i, due to concentration gradients can be written as [29]

$$
J_i = \frac{\mu}{n_{sh}Pr} \sum_{k=1}^{N_s} \Delta b_{ik} \frac{\partial C_k}{\partial \eta} \frac{dg}{d\overline{\eta}}
\tag{2.54}
$$

The equation of state is given by

$$
p = \rho T\, R^* / \overline{M}^* C_{p,\infty}^*
\tag{2.55}
$$

2.3 Boundary Conditions

At low altitudes, slip effects are not important. No-slip and no-temperature-jump boundary conditions are used on the body surface. The wall temperature and enthalpy are specified as constant. The boundary

conditions at the shock are calculated by using the Rankine-Hugoniot relations [12,24].

At high altitudes, the continuum flow assumption breaks down in the region next to the wall. The no-slip and no-temperature jump boundary conditions are no longer valid. As such, the slip and temperature jump boundary conditions should be used.

2.3.1 Boundary Conditions on the Wall

Shidlovsky [30] has shown that at the body surface the velocity slip and temperature jump conditions are of the same order as the Knudsen number. The Knudsen number is defined as the ratio of the molecular mean free path in the gas to a characteristic dimension of the flowfield. The no-slip boundary conditions (which correspond to continuum conditions) are obtained when Kn → 0. However, when the flow density decreases, the mean free path becomes long compared to the characteristic length in a region next to the wall. This region is called the Knudsen layer. Under this condition, the slip conditions should be used.

The slip conditions are assumed to exist across the Knudsen layer. The net fluxes of momentum and energy at the outer edge of the Knudsen layer are equated to the difference between the incident and reflected fluxes at the wall. These fluxes are assumed to be constant across the Knudsen layer and are obtained from the moments of the distribution functions. The slip conditions are then obtained from the balance equations of these fluxes and are given by [31]

Velocity slip:

$$u_s = \sqrt{\frac{\pi}{2}} \frac{2-\bar{\theta}}{\bar{\theta}} \epsilon^2 \frac{\mu_s}{\sqrt{p_s \rho_s}} \left(\frac{\partial u}{\partial n} - \frac{\kappa u}{1+n\kappa}\right)_s \qquad (2.56)$$

Pressure slip:

$$p_s = p_w + \frac{4}{5\sqrt{2\pi}} \left(\frac{\gamma}{\gamma-1}\right) \frac{2-\bar{\theta}}{\bar{\theta}} \frac{\epsilon^2}{Pr} \frac{\mu_s}{T_s} \sqrt{\frac{p_s}{\rho_s}} \left(\frac{\partial T}{\partial n}\right)_s \tag{2.57}$$

Temperature slip:

$$T_s = T_w + \frac{1}{2}\sqrt{\frac{\pi}{2}} \left(\frac{\gamma}{\gamma-1}\right)\left(\frac{2-\theta}{\theta}\right)\frac{\epsilon^2}{Pr} \frac{\mu_s}{\sqrt{p_s \rho_s}}\left(\frac{\partial T}{\partial n}\right)_s \tag{2.58}$$

In the derivation of the relation for the temperature slip, it is assumed that the internal energy is frozen during the reflection from the wall. The parameter $\bar{\theta}$ is the accommodation coefficient and its value is taken to be unity in this study.

In the computational plane, Eqs. (2.56) to (2.58) are expressed as [62]

Velocity slip:

$$u_s = \sqrt{\frac{\pi}{2}} \left(\frac{2-\bar{\theta}}{\bar{\theta}}\right) \frac{\epsilon^2 \mu_s}{\sqrt{p_s \rho_s}} \left[\frac{1}{n_{sh}} \frac{dg}{d\bar{\eta}} \frac{\partial u}{\partial \eta} - \frac{\kappa u}{(1+\bar{\eta} n_{sh}\kappa)}\right]_s \tag{2.59}$$

Pressure slip:

$$p_s = p_w + \frac{4}{5\sqrt{2\pi}}\left(\frac{\gamma}{\gamma-1}\right)\left(\frac{2-\bar{\theta}}{\bar{\theta}}\right)\frac{\epsilon^2}{Pr} \frac{\mu_s}{T_s} \sqrt{\frac{p_s}{\rho_s}} \left(\frac{1}{n_{sh}} \frac{dg}{d\bar{\eta}} \frac{\partial T}{\partial n}\right)_s \tag{2.60}$$

Temperature slip:

$$T_s = T_w + \frac{1}{2}\sqrt{\frac{\pi}{2}} \left(\frac{\gamma}{\gamma-1}\right)\left(\frac{2-\bar{\theta}}{\bar{\theta}}\right) \frac{\epsilon^2}{Pr} \frac{\mu_s}{\sqrt{p_s \rho_s}} \left(\frac{1}{n_{sh}} \frac{dg}{d\bar{\eta}} \frac{\partial T}{\partial n}\right)_s \tag{2.61}$$

2.3.2 Boundary Conditions at the Shock

The boundary conditions at the shock are the modified Rankine-Hugoniot relations developed by Cheng [32]. The shock equations are obtained from one-dimensional Navier-Stokes equations which are written

in the shock-oriented coordinate system. The tangential derivatives are neglected as compared to the normal derivatives. Then, the shock equations in dimensional forms are expressed as

Continuity:

$$\frac{\partial}{\partial \hat{n}^*}(\rho^* \hat{v}^*) = 0 \tag{2.62}$$

Tangential-momentum:

$$\rho^* \hat{v}^* \frac{\partial \hat{u}^*}{\partial \hat{n}^*} = \frac{\partial}{\partial \hat{n}^*}(\mu^* \frac{\partial \hat{u}^*}{\partial \hat{n}^*}) \tag{2.63}$$

Normal-momentum:

$$\rho^* \hat{v}^* \frac{\partial \hat{v}^*}{\partial \hat{n}^*} + \frac{\partial p^*}{\partial \hat{n}^*} = \frac{\partial}{\partial \hat{n}^*}[(2\mu^* + \lambda^*) \frac{\partial \hat{v}^*}{\partial \hat{n}^*}] \tag{2.64}$$

Energy:

$$\rho^* C_p^* \hat{v}^* \frac{\partial T^*}{\partial \hat{n}^*} - \hat{v}^* \frac{\partial p^*}{\partial \hat{n}^*} = \frac{\partial}{\partial \hat{n}^*} (\kappa^* \frac{\partial T^*}{\partial \hat{n}^*}) +$$

$$(2\mu^* + \lambda^*)(\frac{\partial \hat{v}^*}{\partial \hat{n}^*})^2 + \mu^* (\frac{\partial \hat{u}^*}{\partial \hat{n}^*})^2 \tag{2.65}$$

Integrating Eqs. (2.62) to (2.65) from just behind the shock wave to freestream, the shock conditions are obtained. The nondimensional forms are given by

Continuity:

$$\rho_{sh} \hat{v}_{sh} = -\sin\alpha \tag{2.66}$$

Tangential-momentum:

$$\varepsilon^2 \mu_{sh} (\frac{\partial \hat{u}}{\partial \hat{n}})_{sh} + \hat{u}_{sh}\sin\alpha = \sin\alpha\cos\alpha \tag{2.67}$$

Normal-momentum:

$$p_{sh} = p_\infty + \sin\alpha(\sin\alpha + \hat{v}_{sh}) \tag{2.68}$$

Energy:

$$\varepsilon^2 \left(\frac{\mu}{Pr} \frac{\partial T}{\partial \bar{n}}\right)_{sh} + T_{sh} \sin\alpha - \frac{\sin\alpha}{2} (\bar{u}_{sh} - \cos\alpha)^2$$

$$= \frac{\sin\alpha}{2} \left\{ \frac{4\gamma}{(\gamma+1)^2} \sin^2\alpha + \left[\left(\frac{2}{\gamma-1}\right) - \frac{4(\gamma-1)}{(\gamma+1)^2}\right] \frac{1}{M_\infty^2} \right.$$

$$\left. - \frac{4}{(\gamma+1)^2 M_\infty^4 \sin^2\alpha} \right\} \tag{2.69}$$

Since velocity components tangent and normal to the shock are not the same as those tangent and normal to the body surface, transformations are needed to relate these quantities. The transformations are given by

$$\bar{u}_{sh} = u_{sh} \cos(\alpha-\theta) + v_{sh} \sin(\alpha-\theta) \tag{2.70}$$

$$\bar{v}_{sh} = - u_{sh} \sin(\alpha-\theta) + v_{sh} \cos(\alpha-\theta) \tag{2.71}$$

Also, the transformations between the body-oriented and shock-oriented coordinates are given by

$$\bar{s} = s \cos(\alpha-\theta) + n \sin(\alpha-\theta) \tag{2.72}$$

$$\bar{n} = - s \sin(\alpha-\theta) + n \cos(\alpha-\theta) \tag{2.73}$$

The derivative with respect to $\bar{n}$ is related to (s,n) coordinate as

$$\frac{\partial}{\partial \bar{n}} = \cos(\alpha-\theta) \frac{\partial}{\partial n} - \sin(\alpha-\theta) \frac{\partial}{\partial s} \tag{2.74}$$

Consequently, the shock conditions in the computational plane are expressed as

Continuity:

$$\rho_{sh} \bar{v}_{sh} = -\sin\alpha \tag{2.75}$$

Tangential-momentum:

$$\varepsilon^2 \mu_{sh} \{ [\cos(\alpha-\theta) + \bar{\eta} \frac{dn_{sh}}{d\xi} \sin(\alpha-\theta)] \frac{1}{n_{sh}} \frac{dg}{d\bar{\eta}} \frac{\partial \bar{u}}{\partial \eta}$$

$$+ \frac{\partial \bar{u}}{\partial \xi} \sin(\alpha-\theta) \}_{sh} + \bar{u}_{sh} \sin\alpha = \sin\alpha \cos\alpha \qquad (2.76)$$

Normal-momentum:

$$p_{sh} = p_\infty + \sin\alpha(\sin\alpha + \bar{v}_{sh}) \qquad (2.77)$$

Energy:

$$\varepsilon^2 (\frac{\mu}{Pr})_{sh} \{ [\cos(\alpha-\theta) + \bar{\eta} \frac{dn_{sh}}{d\xi} \sin(\alpha-\theta)] \frac{1}{n_{sh}} \frac{dg}{d\bar{\eta}} \frac{\partial T}{\partial \eta}$$

$$- \frac{\partial T}{\partial \xi} \sin(\alpha-\theta) \}_{sh} + T_{sh} \sin\alpha - \frac{\sin\alpha}{2} (\bar{u}_{sh} - \cos\alpha)^2$$

$$= \frac{\sin\alpha}{2} \{ \frac{4\gamma}{(\gamma+1)^2} \sin^2\alpha + [(\frac{2}{\gamma-1}) - \frac{4(\gamma-1)}{(\gamma+1)^2}] \frac{1}{M_\infty^2}$$

$$- \frac{4}{(\gamma+1)^2 M_\infty^4 \sin^2\alpha} \} \qquad (2.78)$$

Equation of state:

$$\rho_{sh} = \gamma p_{sh}/(\gamma-1)T_{sh} \qquad (2.79)$$

From Eqs. (2.76) and (2.78), it is noted that the first term in these two equations can be neglected at low altitudes where ε is very small. On the other hand, this term becomes important when ε is large.

Chapter 3

HIGH REYNOLDS NUMBER PERFECT GAS FLOW

3.1 Introduction

For a hypersonic flow over a slender body at lower altitudes where density, and hence, Reynolds numbers are high, the flow will become turbulent. The Reynolds stresses and turbulent heat flux should be considered in the analysis of such flowfields. These two effects dominate the surface properties. However, at present, it is impossible to relate these fluctuating terms correctly to the dependent variables in the equations. Direct numerical solutions of turbulent flows cannot be obtained without a proper modeling of the fluctuating terms.

Many turbulence models have been developed with varying degrees of complexity [33]. These models, generally, are developed by first postulating a mathematical model containing undetermined constants, and then by attempting to choose the constants to make predictions fit the experimental measurements. Empirical turbulence models, such as the algebraic eddy viscosity models are appealing because the storage capacity and computing time required are much less than that for a more sophisticated turbulence model. Also, these models provide results which are comparable to a more complex model [33].

Two algebraic turbulence models, Cebeci-Smith [18] and Baldwin-Lomax [20], have been used widely for calculation of the compressible turbulent flows [19,22,25,34-36]. Both are two-layer eddy-viscosity

models and have similar forms. The primary difference between them is the choice of length and velocity scales in the outer layer.

The boundary layer displacement thickness and boundary layer edge velocity are used as length and velocity scales, respectively, in the Cebeci-Smith model. The determination of the boundary layer edge is required within the solution. However, it is difficult to define the boundary layer edge in a hypersonic flow because there may not be a constant velocity region in the shock layer. Thus, the definition of the boundary layer edge is not well defined. Anderson and Moss used the ratio of the local total enthalpy to freestream total enthalpy to define the boundary layer edge [19]. It is based on the fact that the total enthalpy is constant within the inviscid part of the shock layer. It has been observed that with the presence of small numerical variations of the velocity or enthalpy profile in the shock layer, there could be sudden jumps and oscillations in the boundary layer thickness [37]. The length scale in the Cebeci-Smith model would be affected, hence the heat transfer to the body surface would experience oscillations that were not physically correct.

Another definition suggested by Anderson and Moss [25] is based on the ratio of the integral of the viscous dissipation term in the shock layer for situations where the total enthalpy is not constant in the inviscid region. However, the factor of the ratio is subjective.

By observing the shape of the total enthalpy profiles, Thompson et al. [34] defined the boundary layer thickness on the same physical basis as of Anderson and Moss [19] but in terms of the total enthalpy gradient. It was found that this definition gave reliable boundary

layer thickness consistently. It was superior to other definitions of the boundary layer edge.

It has been shown that the calculated heat transfer was sensitive to the definition used in establishing the boundary layer thickness [37]. Due to these difficulties with the Cebeci-Smith model, it is more appealing to use the Baldwin-Lomax model to predict the turbulent effects, since this model does not require the determination of the boundary layer edge. The velocity and length scales are based on the distribution of the vorticity. The maximum value of a vorticity function and its corresponding location, instead of the boundary layer quantities, are used to form the velocity and length scales for the outer layer. This model has become a popular algebraic eddy viscosity model.

Although the Baldwin-Lomax model avoids determining the boundary layer edge in the outer eddy viscosity formulation, several difficulties have been encountered. First of all, there is ambiguity in determining the peak of the vorticity function. Degani and Schiff [38] found that there might be more than one peak in the function. This can result in an incorrect determination of the length scale for the outer layer if a wrong maximum value has been picked up. This problem can be eliminated by selecting the peak near the body surface [22,36].

The second difficulty lies in determining the two additional constants, C_{cp} and C_{Kleb}, in the outer formulation. Baldwin and Lomax determined these constants by comparing results with the Cebeci-Smith model for transonic, constant pressure boundary layer flows [20]. Visbal and Knight [36] have shown that C_{cp} should be decreased and C_{Kleb}

increased for an equilibrium incompressible turbulent boundary layer
[36]. However, Knight suggested a higher value of C_{cp} for a compression
corner calculation at Mach 3.0 [21]. The values of C_{cp} and C_{Kleb} depend
on the flow Mach number [20,21,36,37]. There is no one fixed value for
all flow conditions. These values should be chosen carefully, otherwise
different heat transfer results will be predicted [37]. These
difficulties need to be investigated intensively before this model can
be relied on to hypersonic flow conditions.

In this chapter, a method for solving the flow over a blunt
slender body where the inviscid region encompasses a significant portion
of the total shock layer thickness is presented. The first order
continuity and normal momentum equations are solved simultaneously as a
coupled set rather than in a successive manner as has been utilized for
wide-angle bodies. Two of the most frequently employed algebraic
turbulence models, namely the Cebeci-Smith and Baldwin-Lomax models, are
implemented to examine their suitability for the hypersonic flow.

3.2 Basic Formulation

As indicated in Chap. 2, the steady perfect gas viscous shock-
layer equations [12] for an axisymmetric or two-dimensional body at zero
angle of attack are obtained from the compressible Navier-Stokes
equations, written in terms of a body-oriented coordinate system. They
are nondimensionalized by the variables which are of order one in the
region near the body surface (boundary layer) for large Reynolds
numbers. The same set of equations are then nondimensionalized by
variables which are of order one in the essentially inviscid region

outside the boundary layer. Terms in each set of equations up to second-order in the inverse square root of the Reynolds number are kept. A comparison of the two sets of equations is then made and one set of equations is obtained from them which is valid to second order in both the outer and inner regions. A solution of this set of equations is thus uniformly valid to second-order in the entire shock layer for arbitrary γ. Anderson and Moss [19] used the eddy viscosity approximation to replace the Reynolds stresses and turbulent heat flux to find the solution of the turbulent flow. These equations provided here again are in an orthogonal, body oriented, transformed coordinates form, Eqs. (2.25) through (2.37).

The second-order partial differential equations applicable to this study are expressed as [19]

$$\frac{\partial^2 W}{\partial \eta^2} + \frac{d^2 g/d\bar{\eta}^2 + \alpha_1 (dg/d\bar{\eta})}{(dg/d\bar{\eta})^2} \frac{\partial W}{\partial \eta} + \frac{\alpha_2}{(dg/d\bar{\eta})^2} W$$

$$+ \frac{\alpha_3}{(dg/d\bar{\eta})^2} + \frac{\alpha_4}{(dg/d\bar{\eta})^2} \frac{\partial W}{\partial \xi} = 0 \qquad (3.1)$$

where $dg/d\bar{\eta}$ and $d^2g/d\bar{\eta}^2$ are the first and second derivatives of the stretching function g. The quantity W represents u for the s-momentum equation and H for the energy equation. The coefficients α_1 to α_4 are

written as:

s-momentum, W = u:

$$\alpha_1 = \frac{1}{\mu(1+\epsilon^+)} \frac{\partial\mu(1+\epsilon^+)}{\partial\eta} \frac{dg}{d\bar{\eta}} + \frac{n_{sh}\kappa(1+2\epsilon^+)}{(1+\bar{\eta}n_{sh}\kappa)(1+\epsilon^+)} + \frac{jn_{sh}\cos\theta}{r + \bar{\eta}n_{sh}\cos\theta}$$

$$+ \frac{n'_{sh}n_{sh}\bar{\eta}\rho u}{\epsilon^2\mu(1+\epsilon^+)(1+\bar{\eta}n_{sh}\kappa)} - \frac{n_{sh}\rho v}{\epsilon^2\mu(1+\epsilon^+)} \tag{3.2}$$

$$\alpha_2 = -\frac{n_{sh}\kappa}{\mu(1+\epsilon^+)(1+\bar{\eta}n_{sh}\kappa)} \frac{\partial\mu(1+\epsilon^+)}{\partial\eta} \frac{dg}{d\bar{\eta}} - \frac{n_{sh}^2\kappa}{(1+\epsilon^+)(1+\bar{\eta}n_{sh}\kappa)} \times$$

$$\left(\frac{\kappa}{1+\bar{\eta}n_{sh}\kappa} + \frac{j\cos\theta}{r+\bar{\eta}n_{sh}\cos\theta}\right) - \frac{n_{sh}^2\kappa\rho v}{\epsilon^2(1+\bar{\eta}n_{sh}\kappa)\mu(1+\epsilon^+)} \tag{3.3}$$

$$\alpha_3 = -\frac{n_{sh}^2}{\epsilon^2(1+\bar{\eta}n_{sh}\kappa)\mu(1+\epsilon^+)} \left[\frac{\partial p}{\partial\xi} - \frac{n'_{sh}\bar{\eta}}{n_{sh}} \frac{dg}{d\bar{\eta}} \frac{\partial p}{\partial\eta}\right] \tag{3.4}$$

$$\alpha_4 = -\frac{n_{sh}^2\rho u}{\epsilon^2(1+\bar{\eta}n_{sh}\kappa)\mu(1+\epsilon^+)} \tag{3.5}$$

Energy, W = H:

$$\alpha_1 = \frac{1}{\frac{\mu}{Pr}(1+\epsilon^+\frac{Pr}{Pr,t})} \frac{dg}{d\bar{\eta}} \frac{\partial}{\partial\eta} \left[\frac{\mu}{Pr}(1+\epsilon^+\frac{Pr}{Pr,t})\right] + \frac{\kappa n_{sh}}{1+\bar{\eta}n_{sh}\kappa}$$

$$+ \frac{j n_{sh} \cos\theta}{r + \bar{\eta} n_{sh} \cos\theta} + \frac{n'_{sh} n_{sh} \bar{\eta} \rho u}{\varepsilon^2 \frac{\mu}{Pr}(1 + \varepsilon^+ \frac{Pr}{Pr,t})(1 + \bar{\eta} n_{sh} \kappa)}$$

$$- \frac{n_{sh} \rho v}{\varepsilon^2 \frac{\mu}{Pr}(1 + \varepsilon^+ \frac{Pr}{Pr,t})} \tag{3.6}$$

$$\alpha_2 = 0 \tag{3.7}$$

$$\alpha_3 = \frac{n_{sh}}{\frac{\mu}{Pr}(1 + \varepsilon^+ \frac{Pr}{Pr,t})} \left[\frac{dg}{d\bar{\eta}} \frac{\partial\phi}{\partial\eta} + n_{sh}\left(\frac{\kappa}{1 + \bar{\eta} n_{sh} \kappa} + \frac{j\cos\theta}{r + \bar{\eta} n_{sh} \cos} \right) \phi \right.$$

$$\left. + \frac{v}{\varepsilon^2} \frac{dg}{d\bar{\eta}} \frac{\partial p}{\partial\eta} - \frac{n_{sh} \kappa v \rho u^2}{\varepsilon^2 (1 + \bar{\eta} n_{sh} \kappa)} \right] \tag{3.8}$$

$$\alpha_4 = - \frac{n_{sh}^2 \rho u}{\varepsilon^2 \frac{\mu}{Pr}(1 + \varepsilon^+ \frac{Pr}{Pr,t})(1 + \bar{\eta} n_{sh} \kappa)} \tag{3.9}$$

where

$$\phi = \frac{\mu}{Pr} \left[Pr - 1 + \varepsilon^+ \frac{Pr}{Pr,t}(Pr,t - 1) \right] \frac{u}{n_{sh}} \frac{dg}{d\bar{\eta}} \frac{\partial u}{\partial\eta} - \frac{\mu u^2 \kappa}{1 + \bar{\eta} n_{sh} \kappa} \tag{3.10}$$

The remaining first-order equations are written as

Global continuity:

$$\frac{\partial}{\partial\xi}[n_{sh}(r + \bar{\eta} n_{sh} \cos\theta)^j \rho u] + \frac{dg}{d\bar{\eta}} \frac{\partial}{\partial\eta}\{(r + \bar{\eta} n_{sh} \cos\theta)$$

$$x \; [(1+\bar{\eta}n_{sh}\kappa)\rho v - n'_{sh}\bar{\eta}\rho u]\} = 0 \qquad (3.11)$$

n-momentum:

$$\frac{\rho u}{(1+\bar{\eta}n_{sh}\kappa)} \frac{\partial v}{\partial \xi} - \frac{n'_{sh}\,\bar{\eta}\rho u}{n_{sh}(1+\bar{\eta}n_{sh}\kappa)} \frac{\partial v}{\partial \eta} \frac{dg}{d\bar{\eta}} + \frac{\rho v}{n_{sh}} \frac{\partial v}{\partial \eta} \frac{dg}{d\bar{\eta}}$$

$$- \frac{\rho u^2 \kappa}{(1+\bar{\eta}n_{sh}\kappa)} + \frac{1}{n_{sh}} \frac{\partial p}{\partial \eta} \frac{dg}{d\bar{\eta}} = 0 \qquad (3.12)$$

State:

$$p = \rho T \; (\gamma-1)/\gamma \qquad (3.13)$$

The molecular viscosity is given by the Sutherland's law as

$$\mu = [(1+C)/(T+C)]T^{3/2} \qquad (3.14)$$

where

$$C = C^*/(\gamma-1)M_\infty^2 T_\infty^* \qquad (3.15)$$

and C^* is 110.33 K for air.

In the preceding equations, the prime denotes the differentiation with respect to ξ, and ϵ^+ is the eddy viscosity which is set equal to zero for a laminar flow. The independent variable of transformation is defined by

$$\eta = g(\frac{n}{n_{sh}}) = g(\bar{\eta}) \qquad (3.16)$$

The stretching function $g(\bar{\eta})$, Eq. (2.21), is given by ($\bar{\alpha} = 0$)

$$g(\bar{\eta}) = 1 - \frac{1}{\ln(\frac{\bar{\beta}+1}{\bar{\beta}-1})} \ln(\frac{\bar{\beta}-\bar{\eta}+1}{\bar{\beta}+\bar{\eta}-1}) \tag{3.17}$$

and its first and second derivatives are

$$\frac{dg}{d\bar{\eta}} = \frac{1}{\ln(\frac{\bar{\beta}+1}{\bar{\beta}-1})} \left[\frac{1}{(\bar{\beta}-\bar{\eta}+1)} + \frac{1}{(\bar{\beta}+\bar{\eta}-1)} \right] \tag{3.18}$$

$$\frac{d^2 g}{d\bar{\eta}^2} = \frac{1}{\ln(\frac{\bar{\beta}+1}{\bar{\beta}-1})} \left[\frac{1}{(\bar{\beta}-\bar{\eta}+1)^2} - \frac{1}{(\bar{\beta}+\bar{\eta}-1)^2} \right] \tag{3.19}$$

Equation (3.17) permits the mesh to be refined near the body with the values of $\bar{\beta}$ near 1 giving the largest amount of stretching. Equation (3.16) may be inverted to obtain the physical coordinate $\bar{\eta}$ from the transformed coordinate η:

$$\bar{\eta} = 1 - \bar{\beta} \left[\frac{(\frac{\bar{\beta}+1}{\bar{\beta}-1})^{1-\eta} - 1}{(\frac{\bar{\beta}+1}{\bar{\beta}-1})^{1-\eta} + 1} \right] \tag{3.20}$$

The transformation of Eq. (3.16) keeps the body at $\eta = 0$ and the shock at $\eta = 1$ with uniform mesh in the computational coordinate η.

3.3 Boundary Conditions

At low altitude, slip effects are not important. At the wall, no-slip and no-temperature-jump boundary conditions are used. The wall temperature and enthalpy are specified as constant.

The boundary conditions at the shock are calculated by using the Rankine-Hugoniot relations. The nondimensional forms are given as

Continuity:

$$\rho_{sh} \, \nabla_{sh} = - \sin\alpha \tag{3.21}$$

Tangential-momentum:

$$\mathbb{U}_{sh} = \cos\alpha \tag{3.22}$$

Normal-momentum:

$$P_{sh} = \frac{1}{\gamma M_{\infty}^2} + \sin^2\alpha \, (1 - \frac{1}{\rho_{sh}}) \tag{3.23}$$

State

$$P_{sh} = (\frac{\gamma-1}{\gamma}) \, \rho_{sh} T_{sh} \tag{3.24}$$

Density

$$\rho_{sh} = \frac{(\gamma+1)M_{\infty}^2\sin^2\alpha}{(\gamma-1)M_{\infty}^2\sin^2\alpha + 2} \tag{3.25}$$

where $\mathbb{U}_{sh}$ and ∇_{sh} are the velocity components in the tangential and normal directions, respectively, in the shock-oriented coordination system. These are related to the body-oriented coordinate as

$$u_{sh} = \mathbb{U}_{sh} \sin(\alpha+\beta) + \nabla_{sh} \cos(\alpha+\beta) \tag{3.26}$$

$$v_{sh} = - \mathbb{U}_{sh} \cos(\alpha+\beta) + \nabla_{sh} \sin(\alpha+\beta) \tag{3.27}$$

3.4 Turbulence Models

Two of the most widely used algebraic turbulence models, namely the Cebeci-Smith (CS) and Baldwin-Lomax (BL), have been implemented in this study. Algebraic turbulence models are more appealing because they require less computer storage and much less computational time as compared to the two-equation model of turbulence, such as κ-ϵ model. Both Cebeci-Smith and Baldwin-Lomax models of turbulence employ a two-layer eddy-viscosity formulation. The inner law is based upon Prandtl's mixing-length concept. The outer law employs either the Clauser-Klebanoff expression (in the Cebeci-Smith model) or an equivalent expression (in the Baldwin-Lomax model) for computing the eddy viscosity.

3.4.1 Cebeci-Smith Turbulence Model

The algebraic eddy viscosity (in nondimensional form) is given by

$$
\epsilon^+ = \begin{cases} \epsilon_i^+ & \bar{\eta} \leq \bar{\eta}_{crossover} \\ \\ \epsilon_o^+ & \bar{\eta} > \bar{\eta}_{crossover} \end{cases}
\tag{3.28}
$$

where $\bar{\eta}_{crossover}$ is the value of $\bar{\eta}$ at which values from the inner and outer formulas are equal.

The inner eddy viscosity is obtained from the Prandtl mixing-length concept

$$
\epsilon_i^+ = \frac{\rho \ell^2}{\epsilon^2 \mu n_{sh}} \left| \frac{\partial u}{\partial \eta} \frac{d g}{d \bar{\eta}} \right|
\tag{3.29}
$$

The mixing length ℓ is obtained by using the van Driest's proposal stated as [18,19]

$$\ell = K_1 n_{sh} \bar{\eta} [1 - \exp(-n^+/A^+)] \qquad (3.30)$$

where

$$n^+ = \frac{n_{sh}\bar{\eta}\rho}{\epsilon\mu} \left[\frac{\mu_w}{\rho n_{sh}} \left(\frac{\partial u}{\partial \eta} \frac{dg}{d\bar{\eta}} \right)_w \right]^{1/2} \qquad (3.31)$$

The quantity K_1 is the von Karman constant with a value of 0.4, and A^+ is a damping factor expressed (for flows with a pressure gradient) as [18,19]

$$A^+ = 26(1-11.8P^+)^{-1/2} \qquad (3.32)$$

where

$$P^+ = - \epsilon^2 \frac{\mu}{\rho u_\tau} \left[\left(\frac{\partial p}{\partial \xi}\right)_e - \frac{n'_{sh}}{n_{sh}} \bar{\eta}_e \left(\frac{dg}{d\bar{\eta}}\right)_e \left(\frac{\partial p}{\partial \eta}\right)_e \right] \qquad (3.33)$$

and

$$u_\tau = \epsilon \left[\frac{\mu_w}{\rho n_{sh}} \left(\frac{\partial u}{\partial \eta} \frac{dg}{d\bar{\eta}}\right)_w \right]^{1/2} \qquad (3.34)$$

For the outer region of the viscous layer, the eddy viscosity is approximated by the Clauser-Klebanoff expression [18,19]

$$\epsilon_o^+ = \frac{K_2 \rho u_e \delta_k \gamma_{1,\bar{\eta}}}{\epsilon^2 \mu} \qquad (3.35)$$

where

$$\delta_k = \int_0^\delta \left(1 - \frac{u}{u_e} \right) \frac{n_{sh}}{dg/d\bar{\eta}} \, d\eta \qquad (3.36)$$

$$K_2 = 0.0168 \qquad (3.37)$$

and

$$\gamma_{i,\bar{\eta}} = [1 + 5.5(\frac{n_{sh}\bar{\eta}}{\delta})^6]^{-1} \qquad (3.38)$$

The boundary layer thickness, δ, in Eqs. (3.36) and (3.38) is assumed to be the value of $\bar{\eta}$ at the point where

$$H_t / H_{t,\infty} = 0.995 \qquad (3.39)$$

Another criterion for obtaining δ, based on viscous dissipation, is the height where

$$\frac{\int_0^\delta \frac{F}{(dg/d\bar{\eta})} \, d\eta}{\int_0^1 \frac{F}{(dg/d\bar{\eta})} \, d\eta} = 0.995 \qquad (3.40)$$

where

$$F = \{ \, \epsilon^2 \mu \, [(1+\epsilon^+)\frac{1}{n_{sh}} \frac{dg}{d\bar{\eta}} \frac{\partial u}{\partial \eta} - \frac{\kappa u}{(1+\bar{\eta}n_{sh}\kappa)}]\}^2 / (1+\epsilon^+)\mu \qquad (3.41)$$

Thompson et al. [34] defined the boundary layer edge at a location where

$$d(H_t / H_{t,\infty})/d\bar{\eta} \leq 0.5 \qquad (3.42)$$

All three of these criteria have been used in this study.

3.4.2 Baldwin-Lomax Turbulence Model

This model employs a formulation similar to the Cebeci-Smith model for the inner-region eddy viscosity

$$\epsilon_i^+ = \frac{\rho \ell^2}{\epsilon^2 \mu} \, |\omega| \qquad (3.43)$$

where ℓ is given by Eq. (3.30) except that A^+ is replaced by $\tilde{A}^+$ which is defined as

$$\tilde{A}^+ = 26(|\tau|/\tau_w)^{-1/2} \tag{3.44}$$

In Eq. (3.44), τ is the local shear stress obtained from

$$\tau = \varepsilon^2 \mu \left((1+\varepsilon^+)\frac{1}{n_{sh}} \frac{dg}{d\bar{\eta}} \frac{\partial u}{\partial \eta} - \frac{\kappa u}{1+\bar{\eta}n_{sh}\kappa} \right) \tag{3.45}$$

The magnitude of the vorticity, $|\omega|$ is given by

$$|\omega| = \left| \frac{1}{(1+\bar{\eta}n_{sh}\kappa)} \left(\frac{\partial v}{\partial \xi} - \frac{\bar{\eta}n'_{sh}}{n_{sh}} \frac{dg}{d\bar{\eta}} \frac{\partial v}{\partial \eta} - \frac{(1+\bar{\eta}n_{sh}\kappa)}{n_{sh}} \frac{dg}{d\bar{\eta}} \frac{\partial u}{\partial \eta} - \kappa u \right) \right| \tag{3.46}$$

The outer-eddy-viscosity approximation of the Baldwin-Lomax model replaces the Clauser-Klebanoff formulation by the relation

$$\varepsilon_0^+ = \frac{K_2 C_{cp} \rho F_{wake} F_{KLEB}(\bar{\eta})}{\varepsilon^2 \mu} \tag{3.47}$$

where K_2 is a constant given by Eq. (3.37), C_{cp} is an additional constant given as 1.6 [20] and

$$F_{wake} = \bar{\eta}_{max} F_{max} \tag{3.48}$$

The quantities $\bar{\eta}_{max}$ and F_{max} are the values at the location of the maximum value in the vorticity function

$$F(\bar{\eta}) = n_{sh}\bar{\eta}|\omega|(1-\exp(-n^+/\tilde{A}^+)) \tag{3.49}$$

The Klebanoff intermittency factor, F_{KLEB}, is given by

$$F_{KLEB}(\bar{\eta}) = \left(1+5.5\left(\frac{C_{KLEB}\,\bar{\eta}}{\bar{\eta}_{max}}\right)^6 \right)^{-1} \tag{3.50}$$

where C_{Kleb} = 0.3

It has been found that the value of C_{cp} depends on the Mach number. Baldwin and Lomax [20] chose a value of 1.6 for C_{cp} by comparing with the Cebeci-Smith's turbulence model for transonic, constant pressure boundary layer flows. However, a value of 3.0 for C_{cp} is found more appropriate for hypersonic flow [37].

3.4.3 Transition Model

Both continuous and instantaneous transitions from a laminar to turbulent flow have been included in this study. Instantaneous transition is initialized when the local Reynolds number or momentum-thickness Reynolds number exceeds a preselected value. Continuous transition is effected by defining a streamwise transition intermittency factor $\gamma_{i,\xi}$ which modifies the composite eddy viscosity ε^+ over a specific distance along the body.

The factor $\gamma_{i,\xi}$ is evaluated by a relation developed by Dhawan and Narasimha [39] as

$$\gamma_{i,\xi} = 1-\exp(-0.412\bar{\xi})$$ (3.51)

where

$$\bar{\xi} = \frac{4(\xi-\xi_0)}{\xi_0(\bar{x}-1)}$$ (3.52)

The quantity ξ_0 is the location where the transition is started and $\bar{x}$ is approximately equal to two.

3.5 Method of Solution

The overall method of solution employed is an implicit finite-difference spatial-marching method, similar to the one employed by Davis, and Anderson and Moss [12,19]. However, the method is implemented in this study differently because convergence problems are encountered for slender bodies if the method of solution outlined in these references is employed.

To simplify the numerical computations, the viscous shock-layer equations are again transformed by normalizing most of the variables with their local shock values. It should be pointed out that the normal velocity, at the shock may change sign at some locations and may be near zero at others. The normalized v-profiles in such a region are not very well behaved and stability problems can occur if these profiles are used in the solution procedure. Therefore, it is desirable to remove the normalization procedure from the normal velocity profile.

When the normal coordinate is normalized with respect to the local shock standoff distance, a constant number of finite-difference grid points between the body and shock are used. The second order equations, Eqs. (3.1) through (3.10), are solved by using the finite difference method. The derivatives are replaced with finite-difference expressions in a such way that three-point central differences in the η-direction and two-point backward differences in the ξ-direction occur. The truncation terms of order $\Delta\xi_m$ and either $\Delta\eta_n\Delta\eta_{n-1}$ or $\Delta\eta_n-\Delta\eta_{n-1}$ are neglected. The subscript n denotes the grid point along a line normal to the body surface, whereas the subscript m denotes the grid station

along the body surface. Replacing the differential terms by the finite-difference expressions, the governing equations are expressed as

$$A_n W_{m,n-1} + B_n W_{m,n} + C_n W_{m,n+1} = D_n \qquad (3.53)$$

where

$$A_n = \frac{2}{\Delta\eta_{n-1}(\Delta\eta_n + \Delta\eta_{n-1})} - \frac{(\alpha_1)_{m,n}\Delta\eta_n}{\Delta\eta_{n-1}(\Delta\eta_n + \Delta\eta_{n-1})} \qquad (3.54)$$

$$B_n = \frac{2}{\Delta\eta_n \Delta\eta_{n-1}} + \frac{(\alpha_1)_{m,n}(\Delta\eta_n - \Delta\eta_{n-1})}{\Delta\eta_n \Delta\eta_{n-1}} + (\alpha_2)_{m,n} + \frac{(\alpha_4)_{m,n}}{\Delta\xi_m} \qquad (3.55)$$

$$C_n = \frac{2}{\Delta\eta_n(\Delta\eta_n + \Delta\eta_{n-1})} + \frac{(\alpha_1)_{m,n}\Delta\eta_{n-1}}{\Delta\eta_n(\Delta\eta_n + \Delta\eta_{n-1})} \qquad (3.56)$$

$$D_n = -(\alpha_3)_{m,n} + \frac{(\alpha_4)_{m,n} W_{m-1,n}}{\Delta\xi_m} \qquad (3.57)$$

Equation (3.53) along with the boundary conditions constitutes a system of the tridiagonal form, for which efficient computational procedures are available.

To avoid the instability problem encountered by the traditional approach [12,19] and from the hypersonic small disturbance theory [14] for a flow on a slender body, the two first-order equations -- the continuity and normal-momentum equations -- are solved simultaneously as a coupled set rather than in a successive manner for the pressure, p, and normal velocity, v. The density in these equations is eliminated through use of the equation of state. The resulting equations are

$$\frac{\partial}{\partial \xi} \left(n_{sh}(r+\bar{\eta}n_{sh}\cos\theta)\frac{p}{T}u + \frac{dg}{d\bar{\eta}}\frac{\partial}{\partial \eta} \left\{ (r+\bar{\eta}n_{sh}\cos\theta) \right. \right.$$

$$\left. \left. \times \left[(1+\bar{\eta}n_{sh}\kappa)\frac{pv}{T} - n'_{sh}\bar{\eta}\frac{pu}{T} \right] \right\} = 0 \right. \tag{3.58}$$

and

$$\frac{n_{sh}pu}{(1+\bar{\eta}n_{sh}\kappa)}\frac{\partial v}{\partial \xi} - \frac{n'_{sh}\bar{\eta}up}{(1+\bar{\eta}n_{sh}\kappa)}\frac{\partial v}{\partial \eta}\frac{dg}{d\bar{\eta}} + vp\frac{\partial v}{\partial \eta}\frac{dg}{d\bar{\eta}}$$

$$- \frac{n_{sh}\kappa u^2 p}{(1+\bar{\eta}n_{sh}\kappa)} + \left(\frac{\gamma}{\gamma-1}\right) T\frac{\partial p}{\partial \eta}\frac{dg}{d\bar{\eta}} = 0 \tag{3.59}$$

Equations (3.58) and (3.59) are expressed in the finite-difference form at points (m,n+1/2) and (m,n-1/2) using a box scheme discussed by Richtmyer [40]. The final forms are

$$A_{c,n+1/2}\, v_{m,n+1} + B_{c,n+1/2}\, v_{m,n} + C_{c,n+1/2}\, p_{m,n+1}$$

$$+ D_{c,n+1/2}\, p_{m,n} = E_{c,n+1/2} \tag{3.60}$$

$$A_{c,n-1/2}\, v_{m,n} + B_{c,n-1/2}\, v_{m,n-1} + C_{c,n-1/2}\, p_{m,n}$$

$$+ D_{c,n-1/2}\, p_{m,n-1} = E_{c,n-1/2} \tag{3.61}$$

$$A_{NM,n+1/2}\, v_{m,n+1} + B_{NM,n+1/2}\, v_{m,n} + C_{NM,n+1/2}\, p_{m,n+1}$$

$$+ D_{NM,n+1/2}\, p_{m,n} = E_{NM,n+1/2} \tag{3.62}$$

$$A_{NM,n-1/2}\, v_{m,n} + B_{NM,n-1/2}\, v_{m,n-1} + C_{NM,n-1/2}\, p_{m,n}$$

$$+ D_{NM,n-1/2} \; p_{m,n-1} = E_{NM,n-1/2} \qquad (3.63)$$

The coefficients of these equations are given in Appendix A. Eliminating p and v alternatively in the coupled equations, Eqs. (3.60)-(3.63), two tridiagonal equations for pressure and normal velocity are obtained as

$$K_1 \; p_{m,n+1} + K_2 \; p_{m,n} + K_3 \; p_{m,n-1} = K_4 \qquad (3.64)$$

$$K_5 \; v_{m,n+1} + K_6 \; v_{m,n} + K_7 \; v_{m,n-1} = K_8 \qquad (3.65)$$

The coefficients K_1 through K_8 are also given in Appendix A. Equations (3.64) and (3.65) are solved in the same way as the energy and s-momentum equations.

By integrating the continuity equation from $\eta=0$ to $\eta=1$, a quadratic equation for the shock standoff distance is obtained. The density is determined by the equation of state.

The solution is started at the stagnation streamline where the various flowfield quantities are expanded in terms of the distance, ξ, along the body surface [19,26]. These series expansions reduce the partial differential equations, Eqs. (3.1) through (3.12), to ordinary differential equations in terms of η. At a body location m, other than the stagnation streamline, a two-point backward difference scheme is used for the derivative with respect to ξ at the point (m,n). This again gives ordinary differential equations at location m in terms of η for Eqs. (3.1) through (3.12). The finite-difference form of these ordinary differential equations (obtained through the central differences) can be solved by using the Thomas Algorithm. Figure 3.1 gives the flow chart for the solution sequence of these equations.
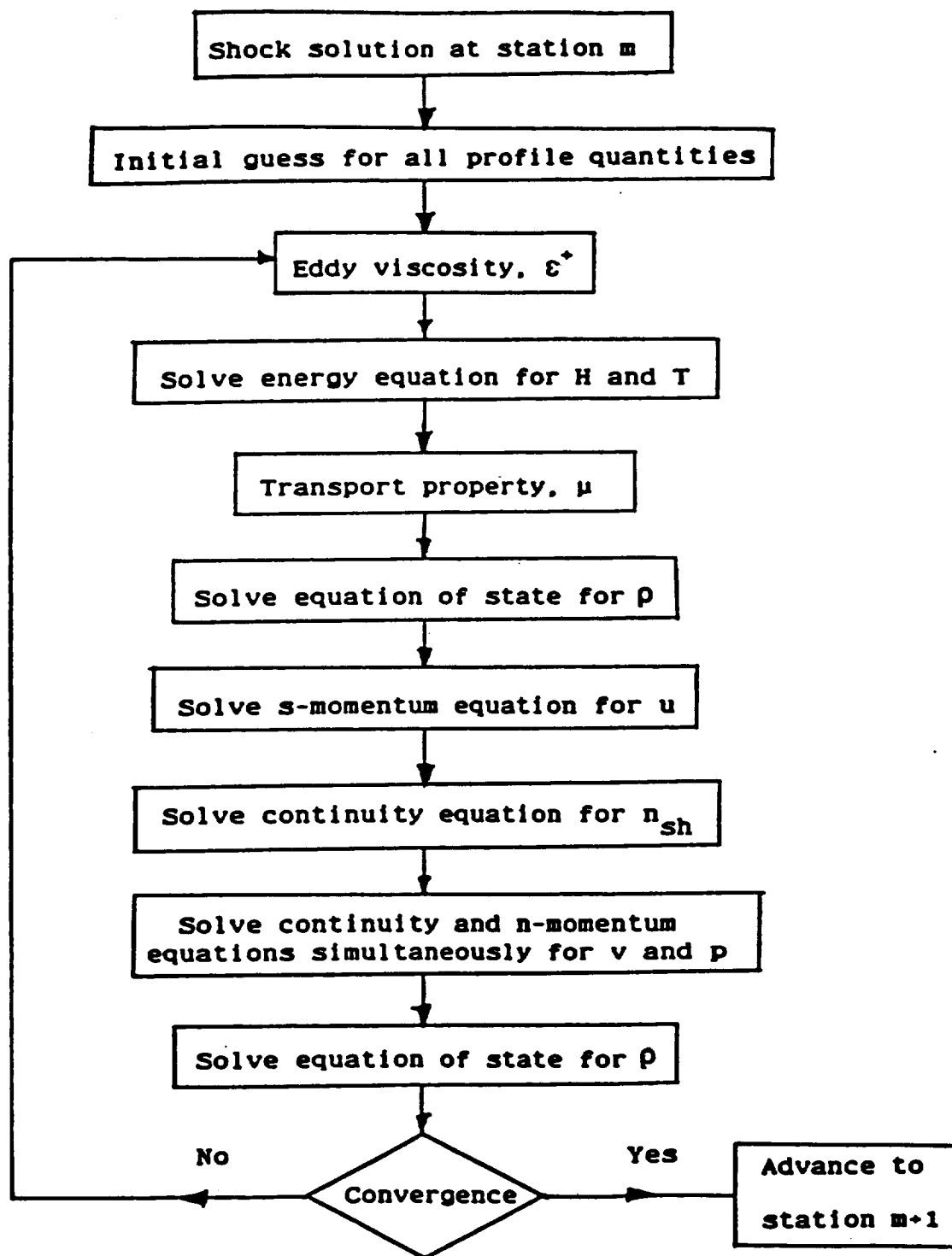
Fig. 3.1   Solution sequence of viscous shock-layer equations.

The Vigneron condition [41] (for the pressure gradient in the streamwise momentum equation) has been used for marching in the subsonic nose region. In this condition, a portion of the pressure gradient is treated implicitly by employing a two-point backward difference scheme. The remainder portion of the pressure gradient is forward differenced to allow for upstream influences.

The solution is iterated at location m until convergence is achieved. The solution advances to the next body station, m+1, and uses the previous converged solution profiles as initial values for starting the solution at m+1. This procedure is repeated until a global solution at all body locations is obtained.

The initial shock shape is created by the thin layer approximation for a short wide-angle body (35° sphere-cone, for example). The shock shape obtained from a full-layer solution to this body shape is then used as an initial guess for the slender bodies in a sequential manner by reducing the body angles in steps of 5 to 10 degrees. In place of the shock stand-off distance used previously [17,42], its derivative in the streamwise direction is smoothed after each global iteration.

Due to the change in sign of the normal velocity profile from station to station, an under-relaxation scheme [43]

$$F = \bar{\omega}F_1 + (1-\bar{\omega}) F_2 \tag{3.66}$$

has been employed in the present work. Here F_1 is the most recently calculated physical quantity and F_2 is the value obtained from the previous local iteration. A value of $\bar{\omega}$ of 0.2 to 0.4 gives convergence

in most cases. In general, an under-relaxation was required only for the pressure and normal velocity.

Depending upon the initial approximation to the shock shape (whether obtained by using the thin shock-layer form of normal-momentum equation or from a larger body angle solution), the first global pass solution may be improved by subsequent global iterations.

3.6 Results and Discussions

Numerical solutions to the previously discussed viscous shock-layer equations for the hypersonic flow over a long slender body have been obtained. Results for laminar, transitional, and turbulent flows of a perfect gas are compared with the experimental data and/or with numerical solutions in the literature. The solutions are chosen for small body angle (5° to 35°) hyperboloids and spher.e-cones at zero-degree angle of attack. The free stream Reynolds numbers are within the range from 1.2 X 10^4 to 3.5 X 10^6.

3.6.1 Comparison of the Present Method with Cascading Method

Figures 3.2 to 3.6 show the effect of solving the normal momentum and continuity equations simultaneously in a coupled way as compared to solving all the governing equations in a successive way [12,19]. Results of shock stand-off distance, wall pressure, and skin friction coefficient are shown in Figs. 3.2 to 3.4 for a hyperboloid with 20° half-body angle. It is clearly noticed that the solutions oscillate in the downstream region with the cascading approach. It is also noticed that this instability can be removed when coupling is implemented between the normal momentum and continuity equations.

Figures 3.5 and 3.6 show the results for shock stand-off distance

and Stanton number distribution for a 35° sphere-cone without coupling

the two first-order equations. Oscillation in the solution is noted in

the vicinity of the tangency point where the curvature is discontinuous.

The curvature is equal to one on the spherical part and zero on the

conical part. It is important to note that coupling the two first-order

equations can stabilize the solutions at this discontinuity.

3.6.2 <u>Comparison of the Present Method with other Predictions and Data</u>

<u>for Laminar flows</u>

The results obtained by the present method (VSL2D) are compared

with another method (VSL3D) in Figs. 3.7 to 3.10. The results of VSL3D

were obtained by Thompson [44]. Figure 3.7 gives the convergence

history of the streamwise derivative of the shock stand-off distance for

the present method. It is seen that solutions do not diverge with the

subsequent global passes. Figure 3.8 presents a comparison of the

boundary layer thickness, as obtained by the VSL2D and VSL3D methods.

The boundary layer thickness is defined as the location where $H_t/H_{t,\infty}$ =

0.995. The predictions of the boundary layer thickness are quite

different by the two methods. The VSL3D results show a big jump in the

boundary layer thickness. In spite of this difference, the laminar

heat transfer and skin-friction coefficients compare well as shown in

Figs. 3.9 and 3.10.

A comparison of surface heat transfer results for a long 5°

sphere-cone between the present viscous shock-layer (VSL) and

parabolized Navier-Stokes (PNS) predictions [45] is given in Fig. 3.11.

The VSL results are about five to ten percent higher for most of the
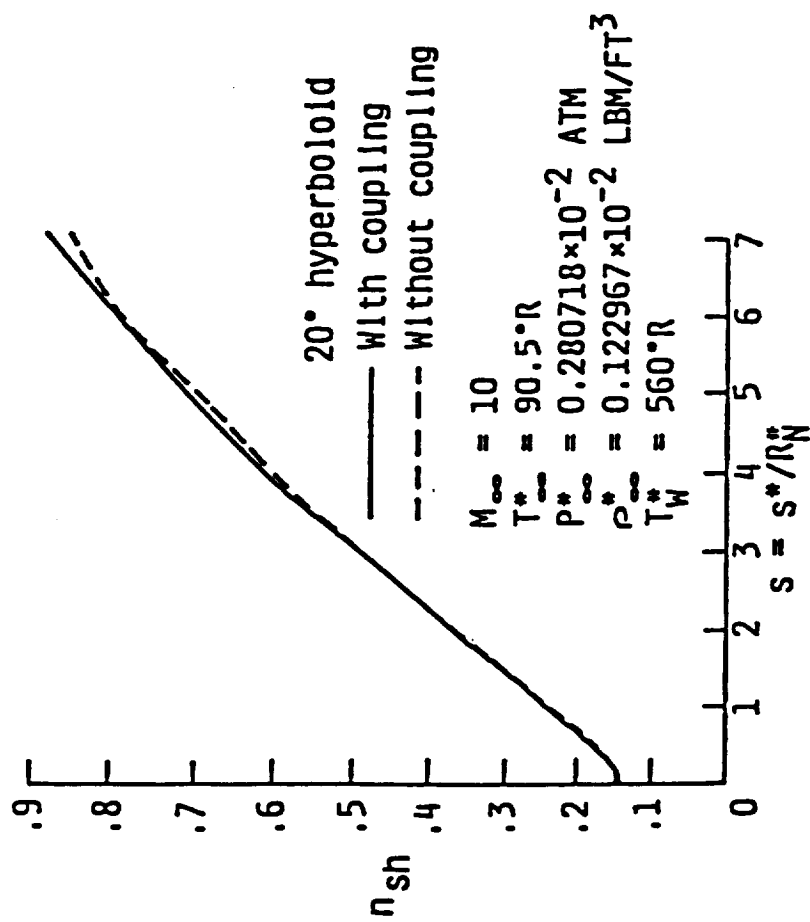
Fig. 3.2   Shock stand-off distance for a 20° hyperboloid.
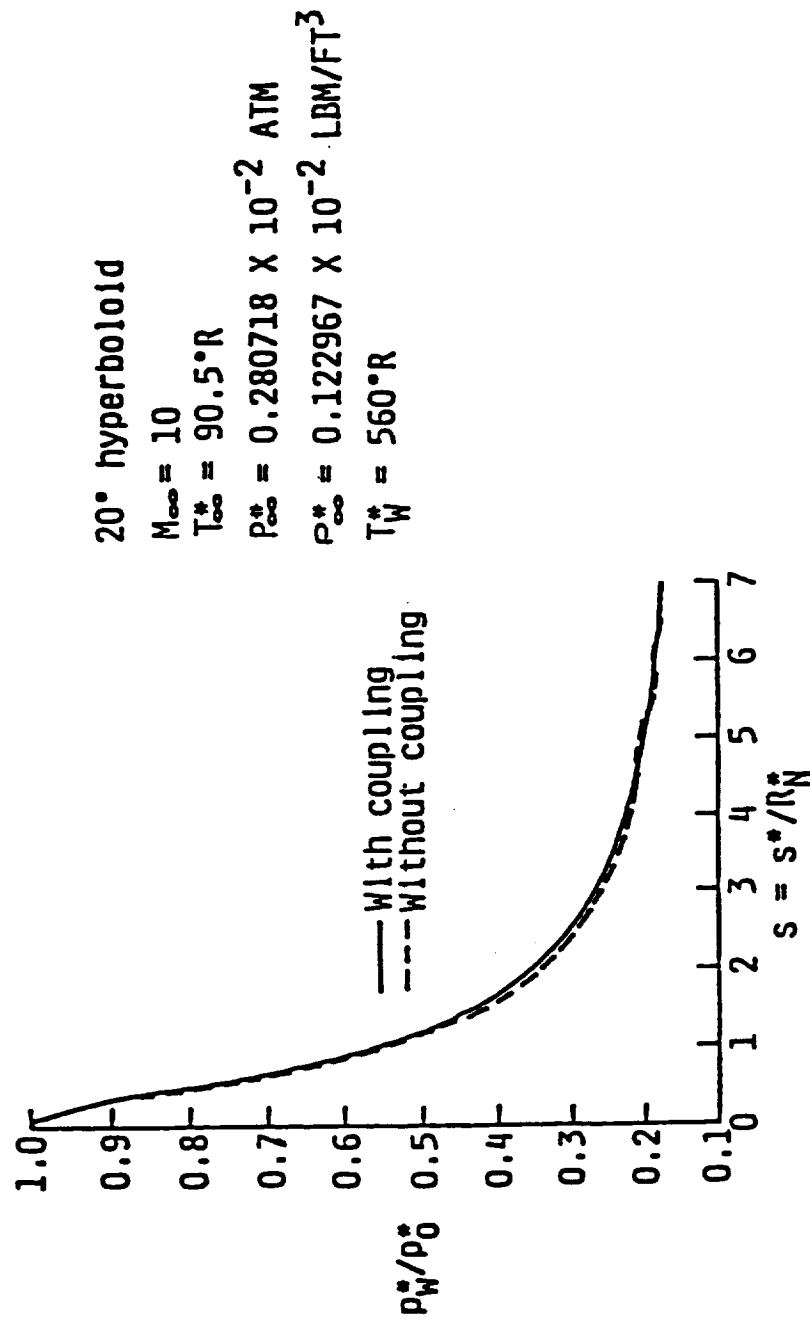
Fig. 3.3   Wall pressure distribution for a 20° hyperboloid.
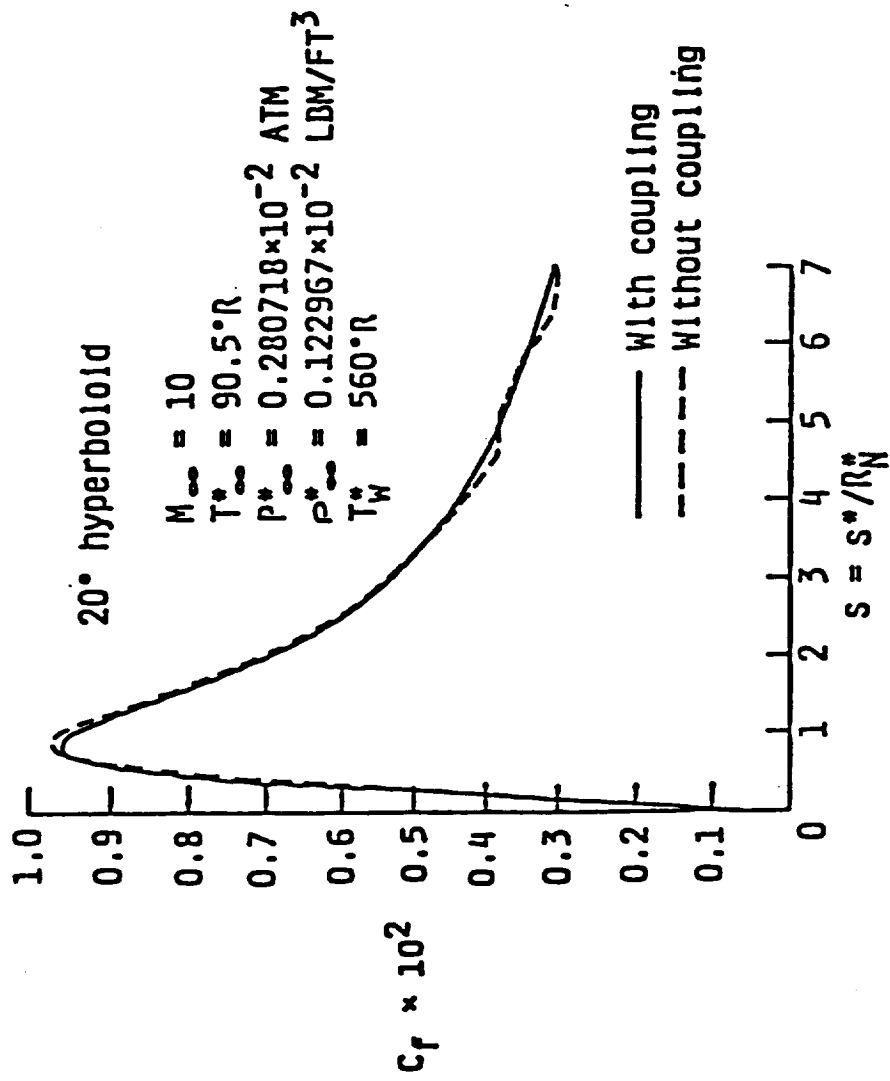
Fig. 3.4   Skin-friction coefficient for a 20° hyperboloid.
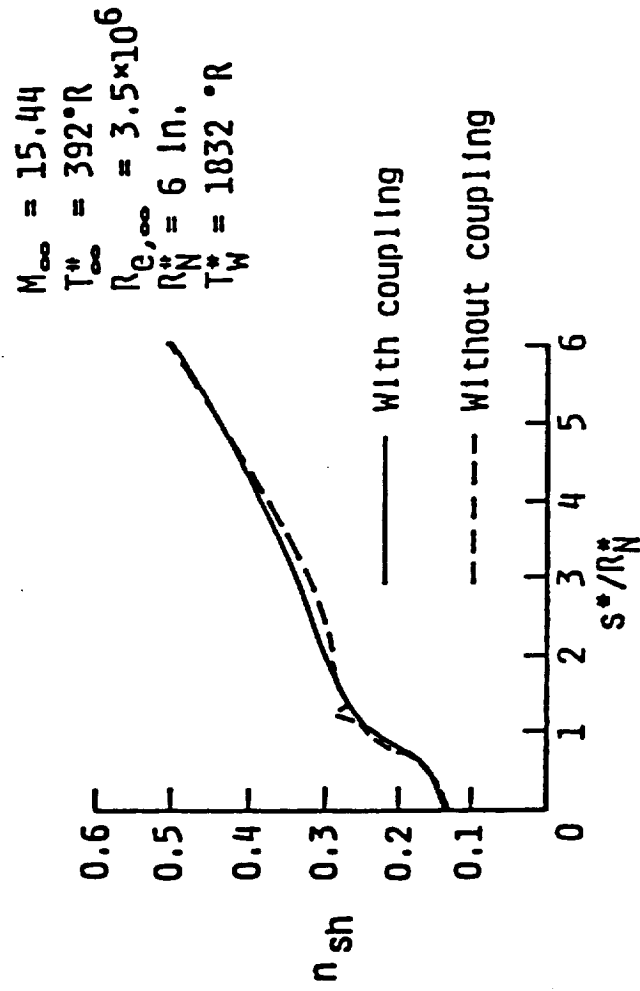
Fig. 3.5   Shock stand-off distance for a 35° sphere-cone.

Fig. 3.6   Stanton number distribution for a 35° sphere-cone.

Laminar flow
M_∞ = 15.44
T_∞^* = 392°R
Re_∞ = 3500000
R_N^* = 6 in.
T_W^* = 1832°R

——— 1st global pass
––– 2nd global pass
— — 3rd global pass

$S = S^*/R_N^*$

n_{sh}'

.48

.36

.24

.12

0

0   20   40   60   80   100
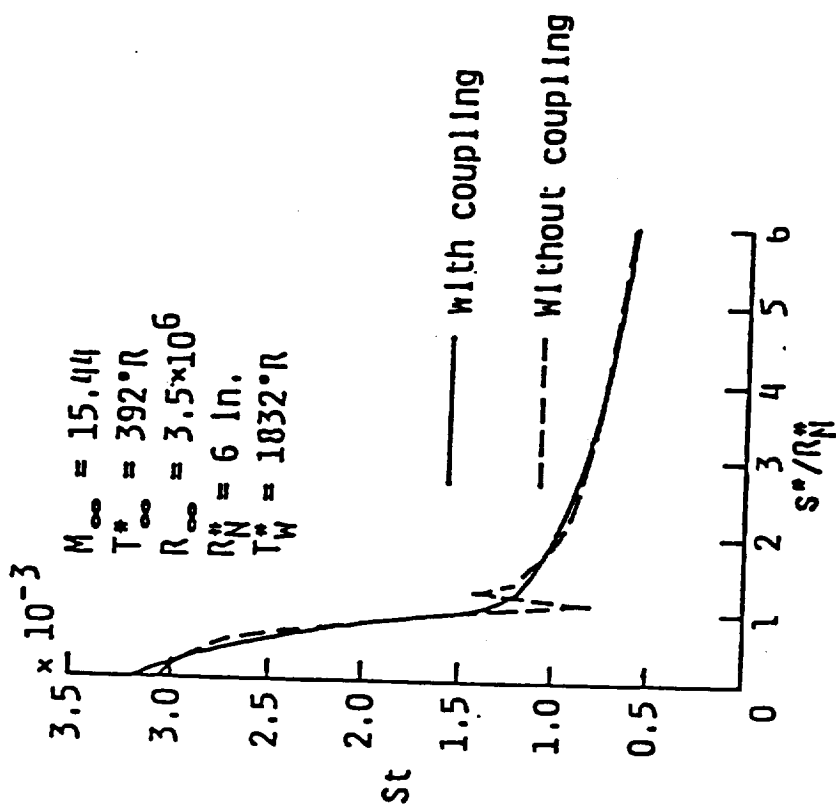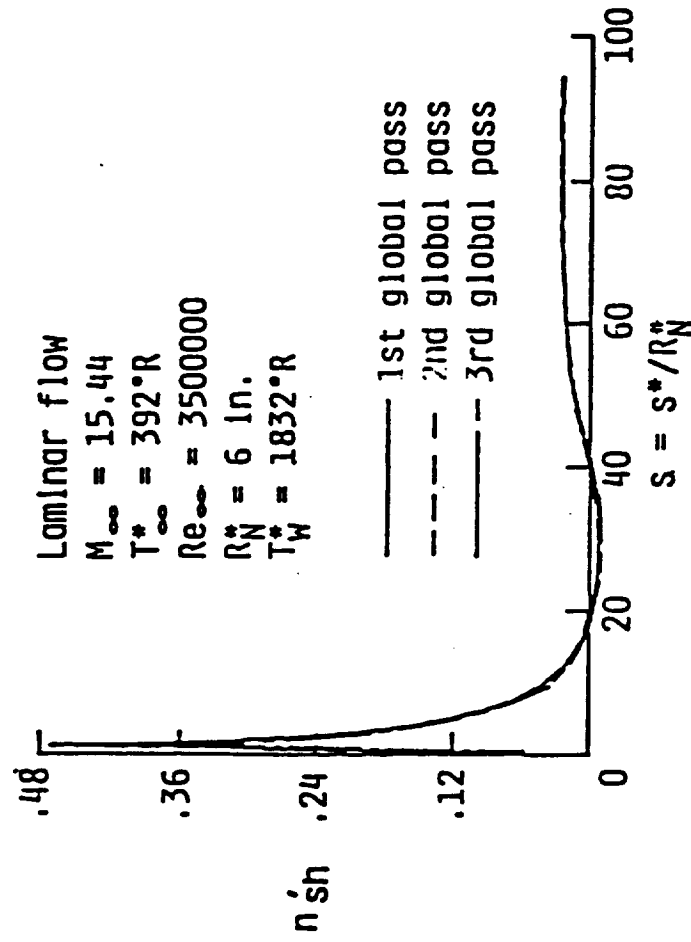
Fig. 3.7   Shock stand-off distance gradient for a 10°
sphere-cone with laminar flow.
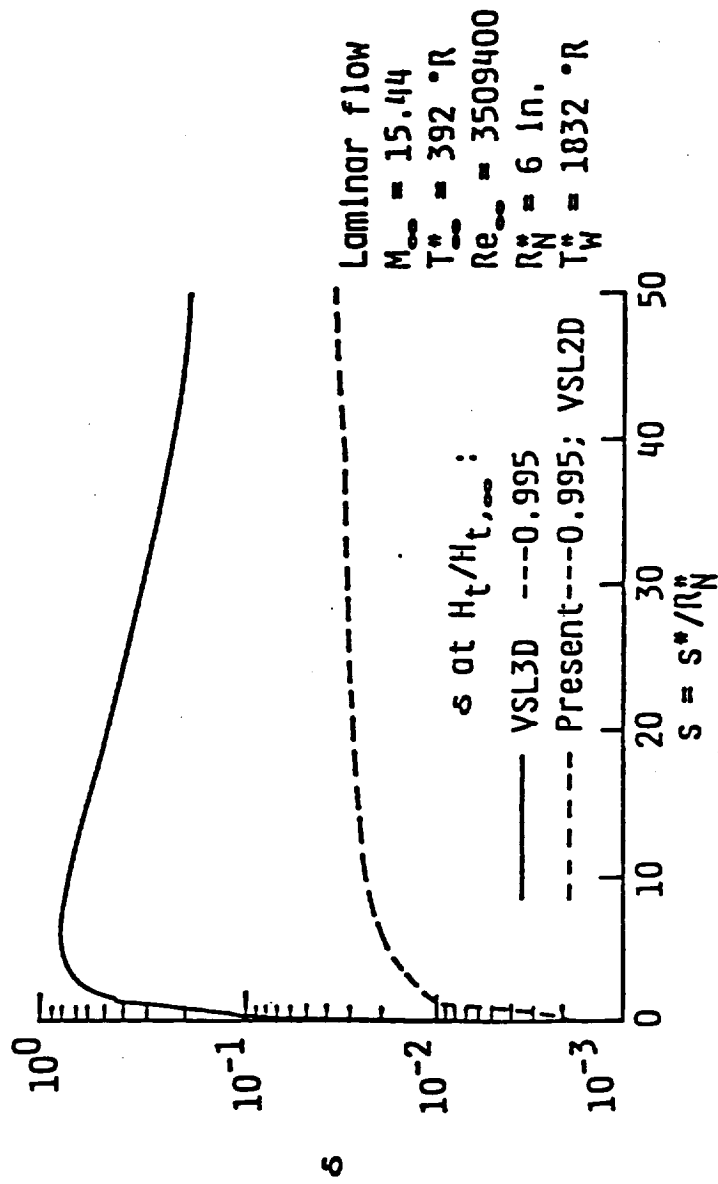
Fig. 3.8 Boundary-layer thickness for a 10° sphere-cone with laminar flow.
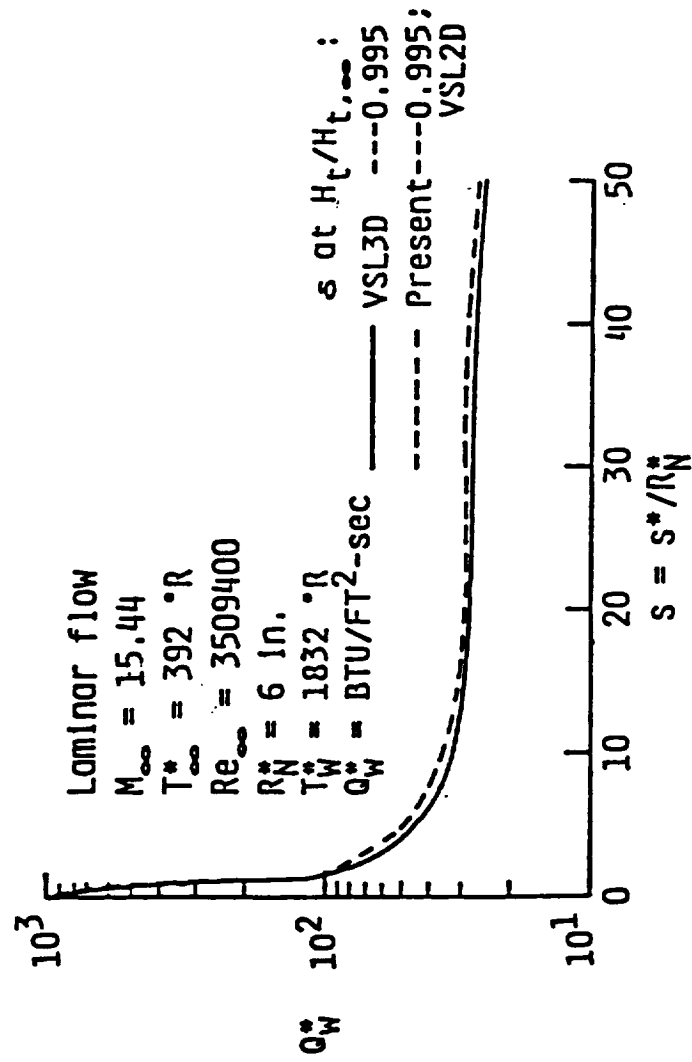
Fig. 3.9   Surface heat transfer rate distribution for a 10° sphere-cone with laminar flow.
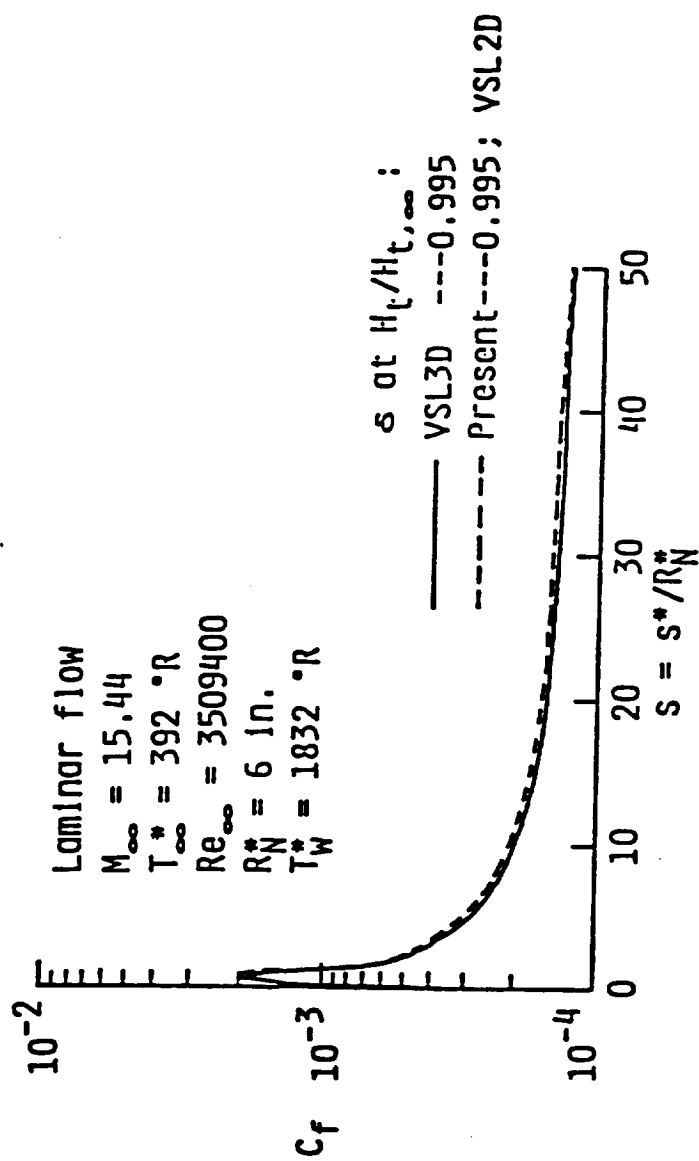
Fig. 3.10 Skin-friction coefficient for a 10° sphere-cone with laminar flow.

body length as compared to the PNS results. The PNS predictions employ fourth-order explicit and second-order implicit smoothing terms, whereas the present VSL calculations do not use any smoothing. Furthermore, the stability of PNS solutions restricts the reduction of the normal grid spacing adjacent to the wall (required for accurate heat transfer predictions) if a relatively large marching stepsize is required for a long body. Since the PNS requires a starting solution that describes the subsonic region, any starting solution errors distort the PNS results in the nose region. In the VSL method, the starting profiles are created as part of the solution and, thus, the method is self-starting.

Figures 3.12 to 3.15 show comparisons of results obtained from the present method with available experimental data. A comparison of the predicted pressure distributions on a 10° hyperboloid with the experimental data [46], as well as with the results of Hosny et al. [15], is given in Fig. 3.12. Both predictions compare quite well with the data. Hosny et al. [15] solved all governing equations in a coupled manner which may require more computational time at every point in the flow, especially if real gas properties are included. The present method with the coupling between the two first-order equations gives equally accurate results. The present approach may be more appealing for real gas calculations where local iterations are required to update the chemical composition along with the transport and thermodynamic properties.

The present method gives surface heat transfer rates which compare quite well with the data of Cleary [47] for a 15° sphere-cone as shown

$M_\infty = 25$
$ALT = 175000$ ft
$Re,\infty = 12610$
$R_N^* = 1.5$in.
$T_W^* = 540°R$

——— VSL (present)
– – – PNS

$X = X^*/R_N^*$

$\dfrac{Q_W^*}{P_\infty^* U_\infty^{*3}}$
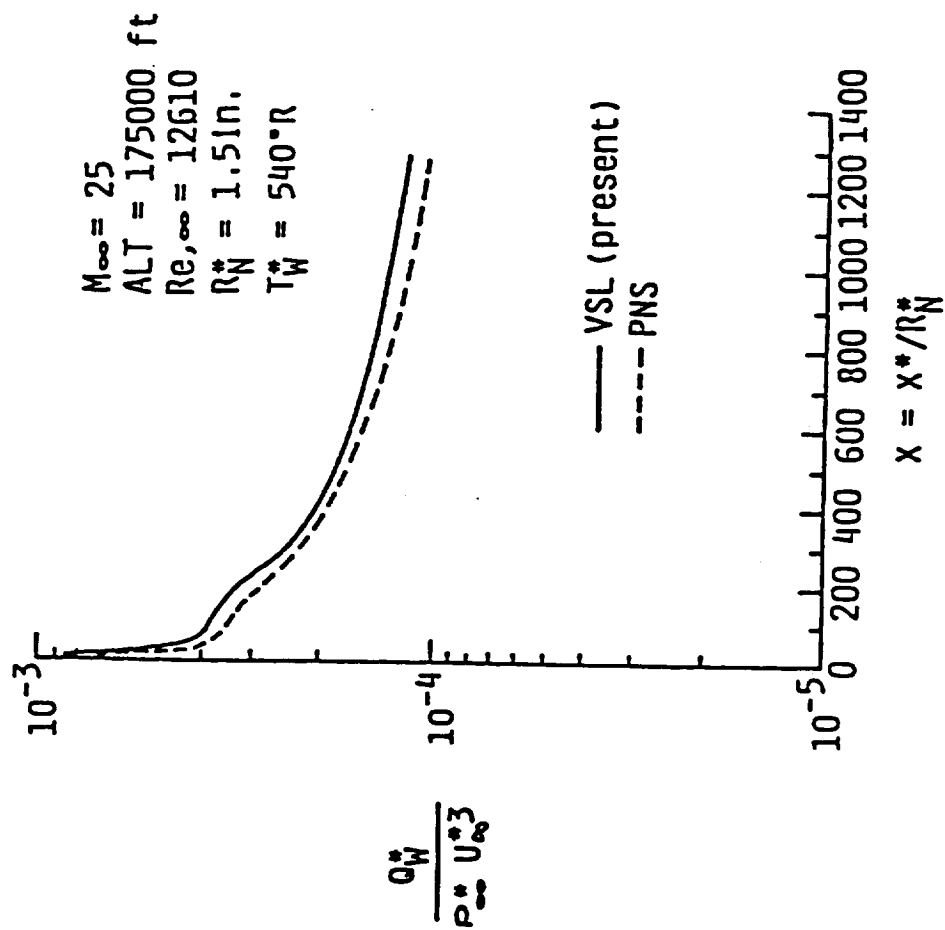
Fig. 3.11   Surface heat transfer rate distribution for a 5° sphere-cone with laminar flow.
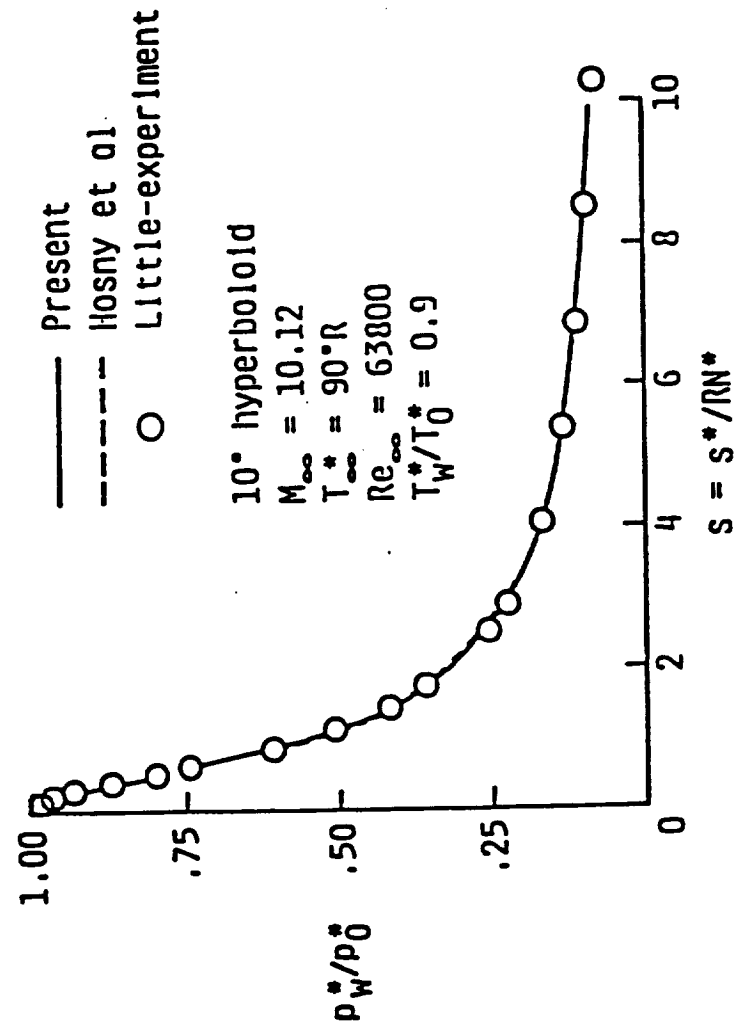
Fig. 3.12 Surface pressure distribution for a 10° hyperboloid with laminar flow.
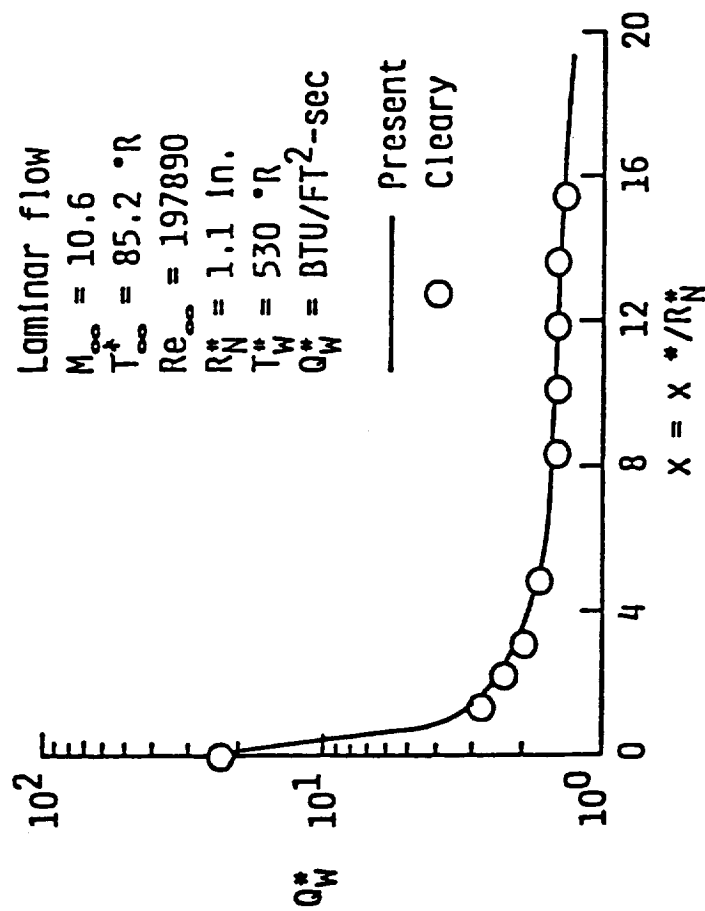
Fig. 3.13 Surface heat transfer rate distribution for a 15° sphere-cone with laminar flow.
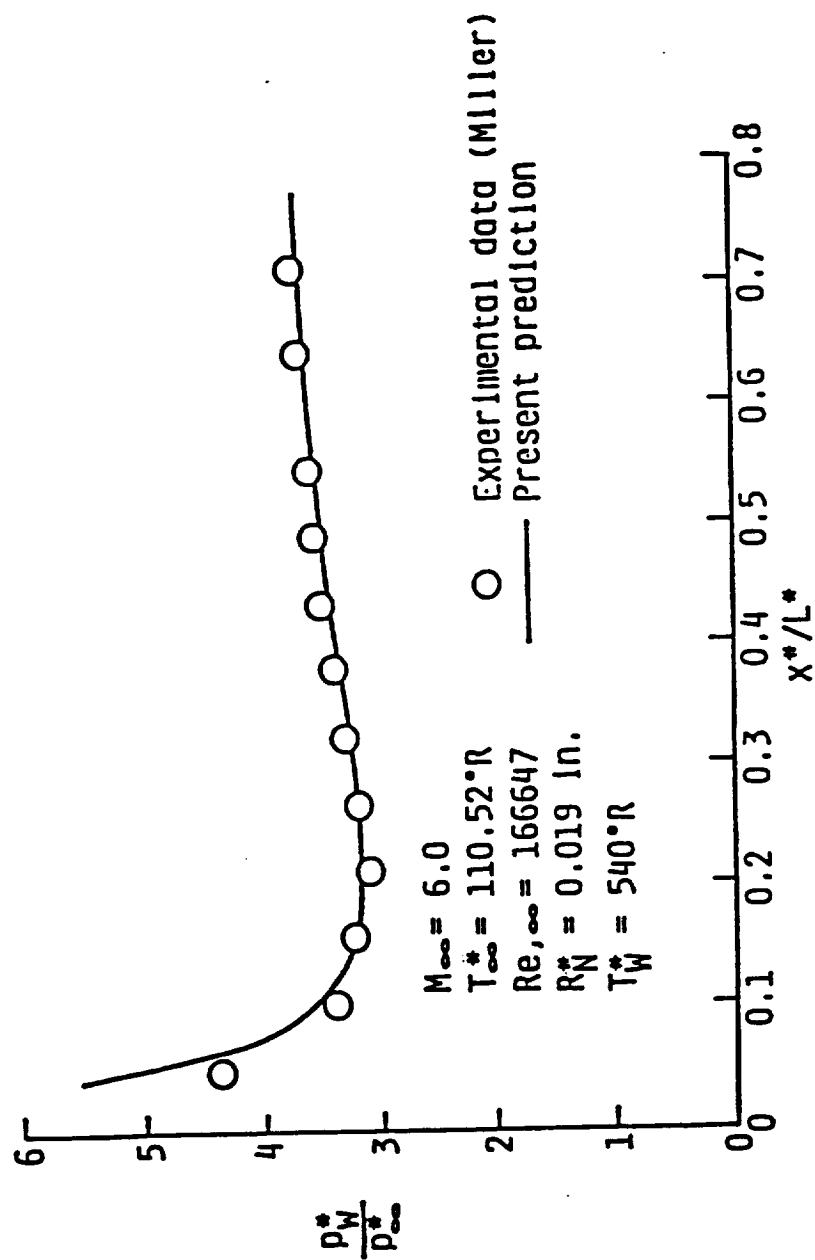
Fig. 3.14 Surface pressure distribution for a 12.84° sphere-cone with laminar flow.
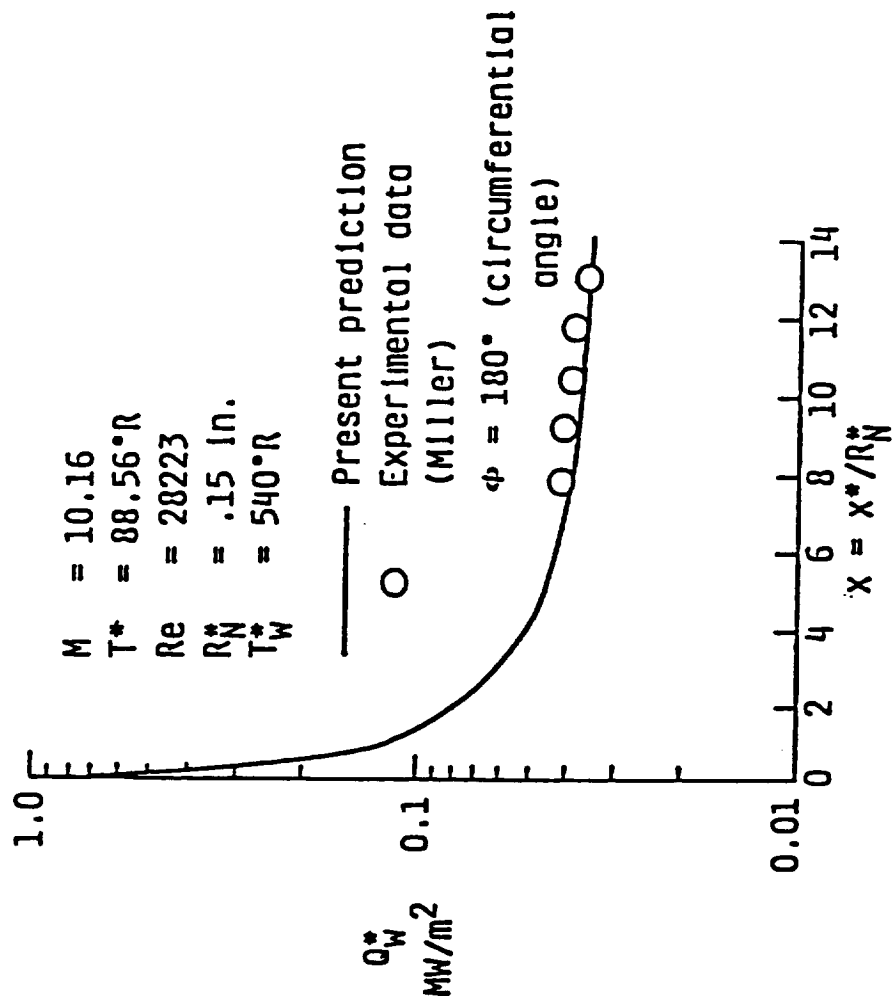
Fig. 3.15 Surface heat transfer rate distribution for a 12.84°
sphere-cone with laminar flow.

in Fig. 3.13. As shown in Figs. 3.14 and 3.15, the present predictions

for the wall pressure distribution and surface heat transfer rate on a

12.84° sphere-cone agree fairly well with the experimental values of

Miller [48,49].

3.6.3 Comparison of Predictions with different Turbulence Models and

Data for Long Slender Bodies

Cebeci-Smith [18] and Baldwin-Lomax [20] turbulence models are

implemented in the present method to predict turbulence effects.

Transition to turbulence is modeled by using the Dhawan and Narasimha

method [39].

Figures 3.16 to 3.18 show a comparison between the results for a

10° sphere-cone as obtained by the VSL2D and VSL3D [44] models. The

Cebeci-Smith turbulence model is implemented in both solutions. The

onset of transition is set at $s^*/R_N^* = 2.0$. The definition of the

boundary layer edge is based on the total enthalpy (i.e., $H_t/H_{t,\infty} =$

0.995). The results for the boundary layer thickness are shown in Fig.

3.16. Similar to the results for the laminar flow (Fig. 3.8), these

results also differ significantly with each other. However, this

difference influences the surface heat transfer rate and skin friction

coefficient predictions significantly for a turbulent flow as shown in

Figs. 3.17 and 3.18.

The length and velocity scales in the Cebeci-Smith model are

strongly dependent on the boundary layer edge location, and these

influence the surface properties. Due to this difficulty, Thompson et

al. [34] defined the boundary-layer edge location based on the gradient

of the total enthalpy $[\partial(H_t/H_{t,\infty})\,/\partial\bar{\eta}]$. With this definition, good

agreement between the VSL2D and VSL3D results is obtained for the

surface heat transfer rate (Fig. 3.19). The results obtained by using

the classical total enthalpy definition for the boundary-layer edge are

also shown in Fig. 3.19. It is noted that the new boundary layer

definition gives results comparable to the classical definition along a

long body [37].

The results for the turbulent flow over a 9° sphere-cone are

illustrated in Figs. 3.20 to 3.25. The hemispherical portion of the

model was roughened in order to insure attainment of turbulence flow

over this region [50]. Three different definitions, which are based on

the total enthalpy, the gradient of total enthalpy, and the dissipation

models, for the boundary layer edge locations have been used to

calculate the turbulent heating with the Cebeci-Smith model as given in

Fig. 3.20. It is seen clearly that predictions from the total enthalpy

and total enthalpy gradient models are comparable to the experimental

data. The boundary layer thickness based on the dissipation model does

not give heat transfer predictions comparable to the classical enthalpy

model.

The Baldwin-Lomax model uses the distribution of vorticity to form

the outer length scale. It is known that there may be more than one

peak in the vorticity function [38]. Figures 3.21 to 3.23 give the

distributions of the vorticity function at three different locations.

It is seen that there is more than one peak at each location. The

correct peak that should be picked is near the body surface. The

Baldwin-Lomax model proposed originally [20] was for constant pressure

Fig. 3.16 Boundary-layer thickness for a 10° sphere-cone with turbulent flow.

Turbulent flow

$M_\infty = 15.44$
$T^*_\infty = 392\ °R$
$Re_\infty = 3509400$
$R^*_N = 6$ in.
$T^*_W = 1832\ °R$
$Q^*_W = BTU/FT^1$-sec

σ at $H_t/H_{t,\infty}$:

Present---0.99 } VSL2D
Present---0.995
VSL3D ---0.995

$s = s^*/R^*_N$

Q^*_W
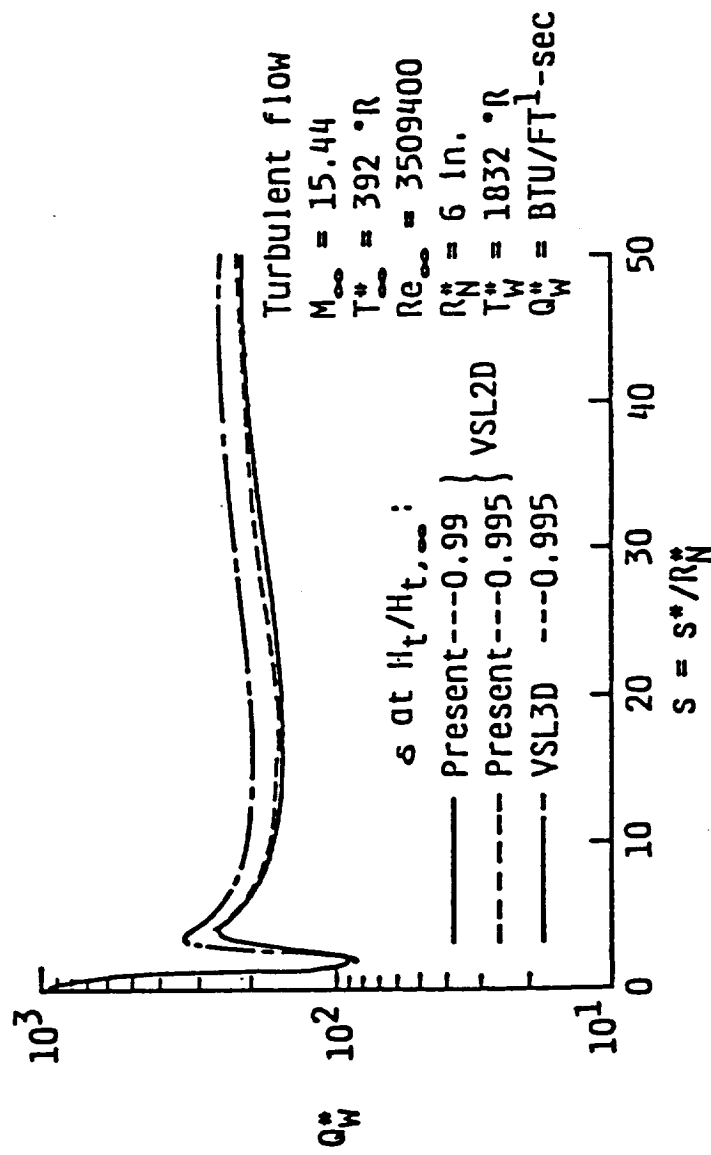
Fig. 3.17 Surface heat transfer rate distribution for a
10° sphere-cone with turbulent flow.
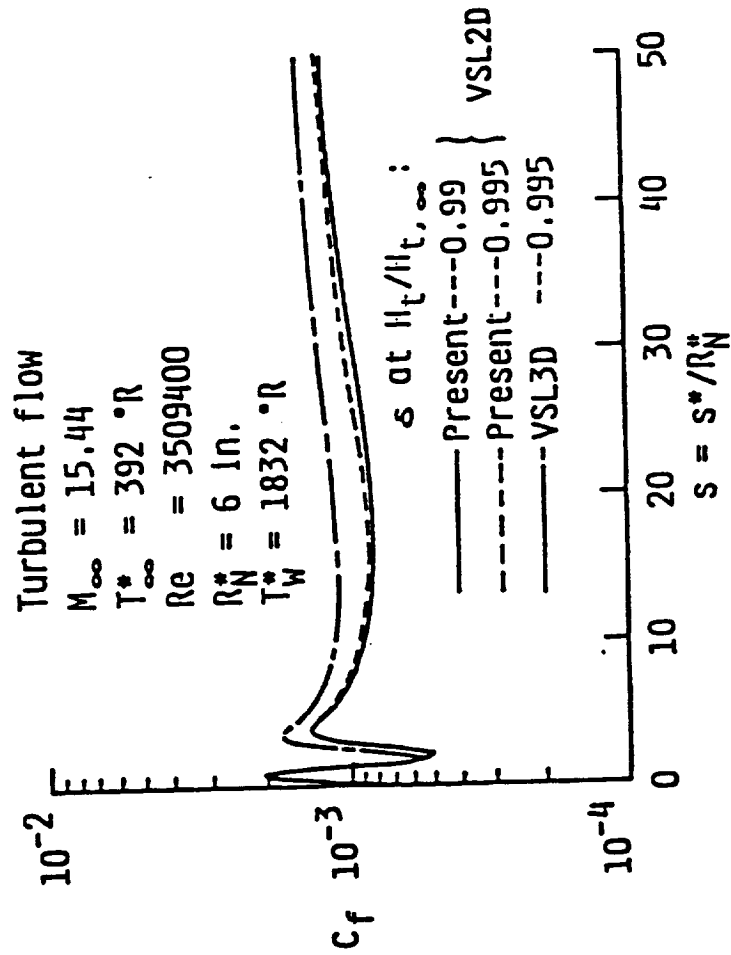
Fig. 3.18 Skin-friction coefficient for a 10° sphere-cone with turbulent flow.
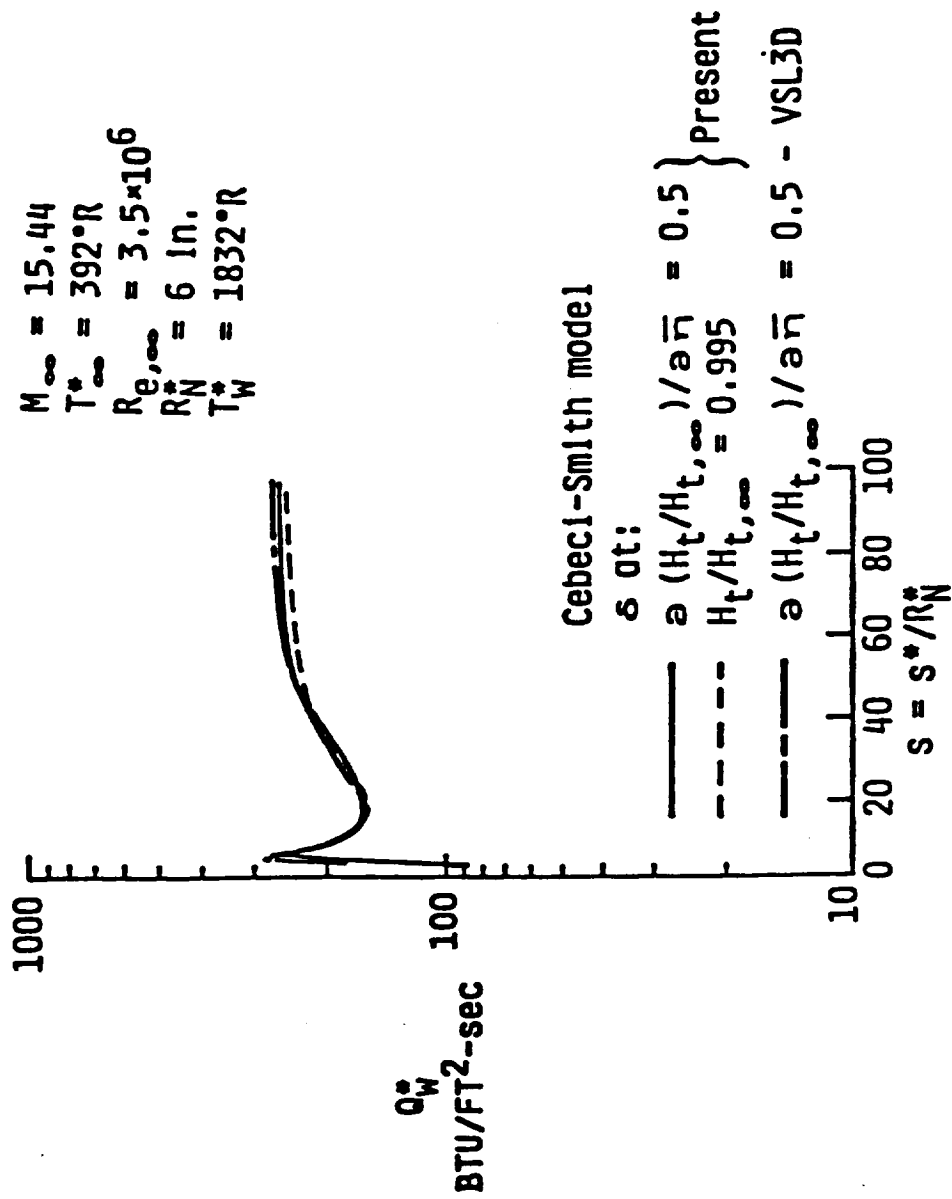
Fig. 3.19 Surface heat transfer rate distribution for a 10°
sphere-cone with turbulent flow.

boundary layers at transonic speeds. This model has been modified to include the effect of pressure gradient on the damping factor $\tilde{A}^+$ [37]. Results of surface heat transfer for both models are given in Fig. 3.24. When compared to the experimental data, the original model predicts well up to the tangency point ($s^*/R_N^* = 1.5$) in the favorable pressure gradient region, whereas the modified model gives good predictions in the adverse pressure-gradient region and beyond. It was, therefore, decided to combine the two models. The predictions for the combined pressure gradient models implemented in the Baldwin-Lomax model are given in Fig. 3.25. Here the original Baldwin-Lomax model is used up to the tangency point and the modified model is used afterwards. The combined model gives very good predictions when compared to the experimental data along the entire body length. Also included in this figure are the predictions obtained with the Cebeci-Smith model. The two models give almost the same surface heat transfer predictions.

The results for the Stanton number distributions for a 7° sphere-cone are given in Figs. 3.26 and 3.27. The transition to turbulence is initialized at $s^*/R_N^* = 4.8$ as given by the data of Carver [51]. Results by using the Cebeci-Smith turbulence model with two boundary layer edge definitions based on the total enthalpy and its gradient are shown in Fig. 3.26. Both definitions give surface heat transfer rate predictions within 15% to the experimental data. There is an increase in the value of Stanton number at a s^*/R_N^* location of about 15 by using the total enthalpy definition for the boundary layer thickness. This is probably due to the poor resolution of the gradients of various
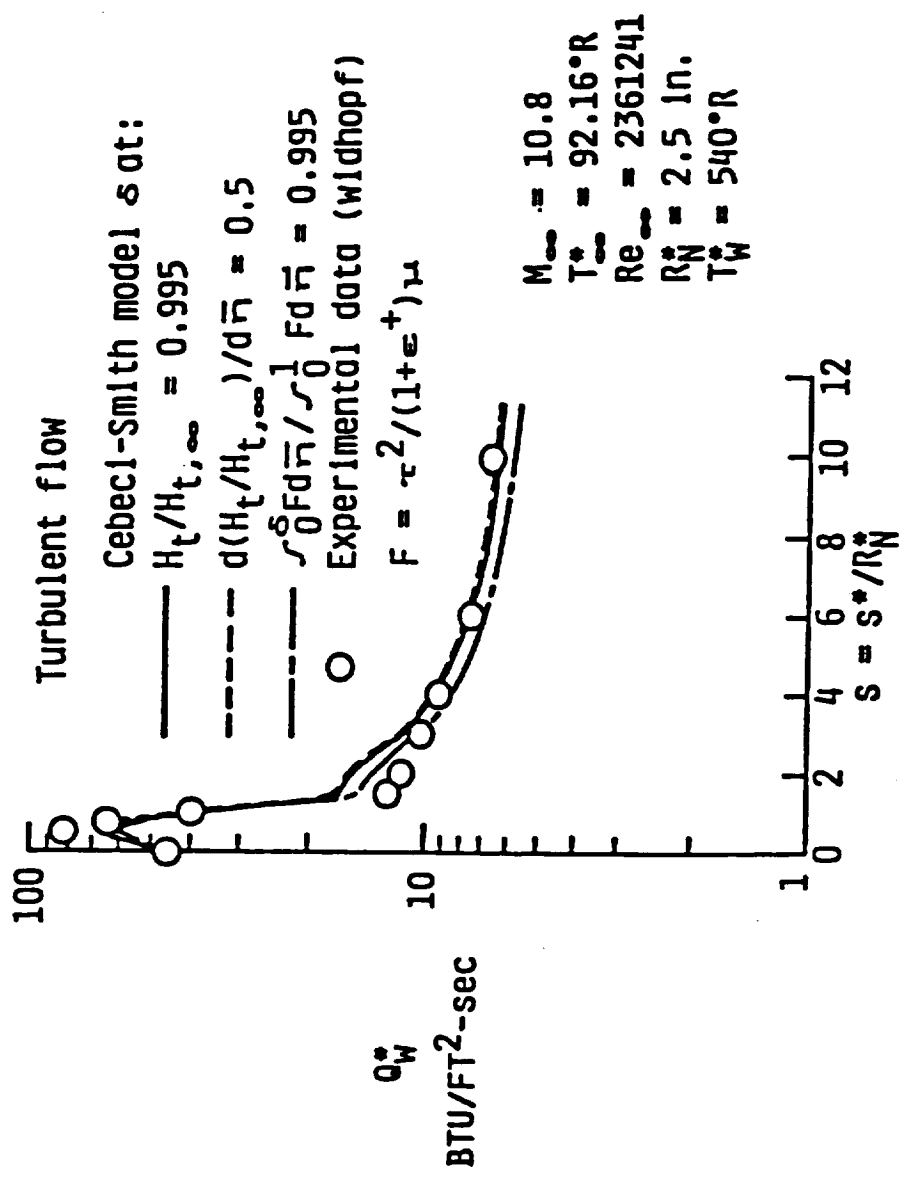
Fig. 3.20 Surface heat transfer rate distribution for a 9°
sphere-cone with turbulent flow.

$$M_\infty = 10.8$$
$$T_\infty^* = 92.18 \, °R$$
$$Re,\infty = 2.3 \times 10^6$$
$$R_N^* = 2.5 \, in.$$
$$T_W^* = 540 \, °R$$

$$s = 1.0$$

$$F(n) = n|\omega| [1-\exp(-n/\vec{A}^+)]$$
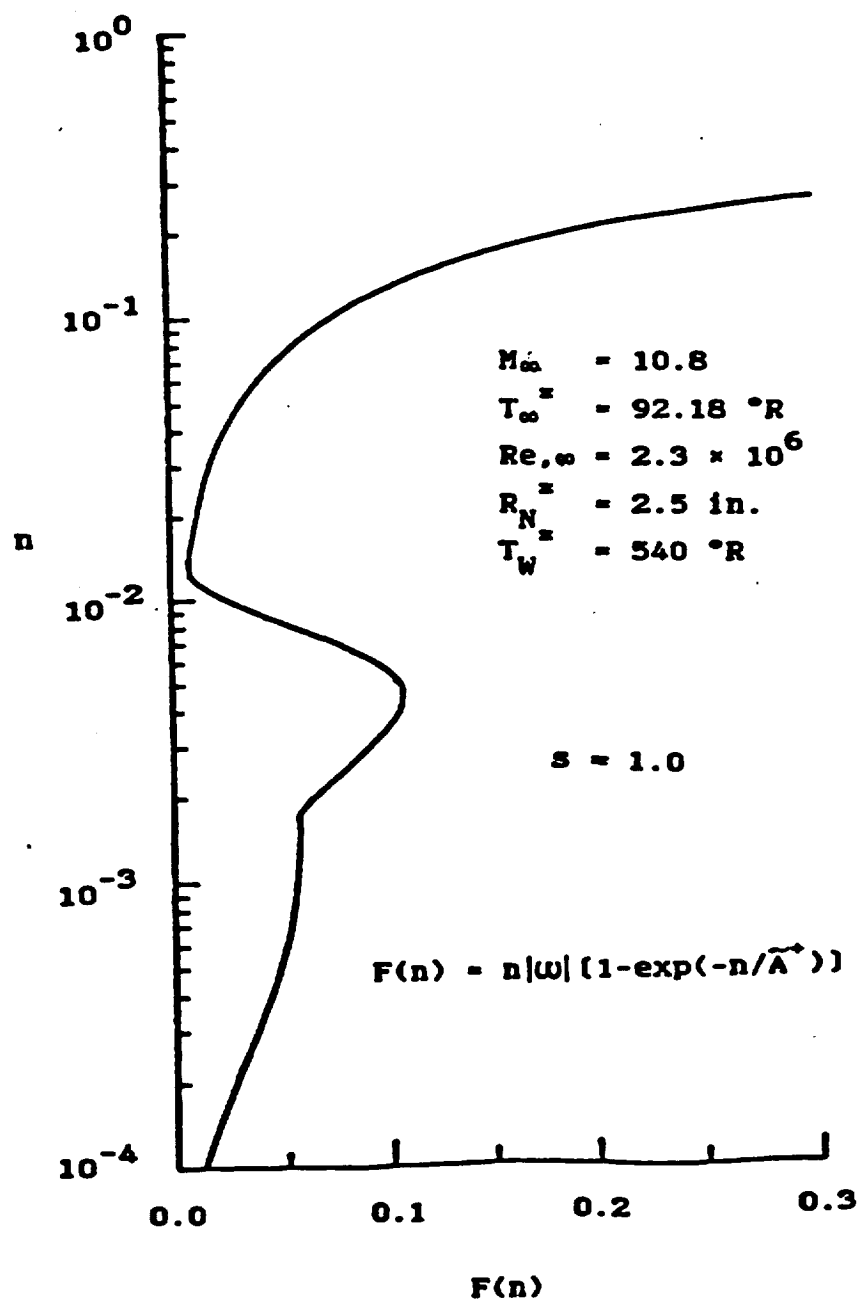
Fig. 3.21   Distribution of vorticity function at s = 1.0 for a 9° sphere-cone with turbulent flow.

M_∞ = 10.8

T_∞^x = 92.18 °R

$Re,_\infty$ = 2.3 × 10^6

R_N^x = 2.5 in.

T_W^x = 540 °R

S = 2.0137

$F(n) = n|\omega|(1-\exp(-n/\widetilde{A}^+))$

F(n)
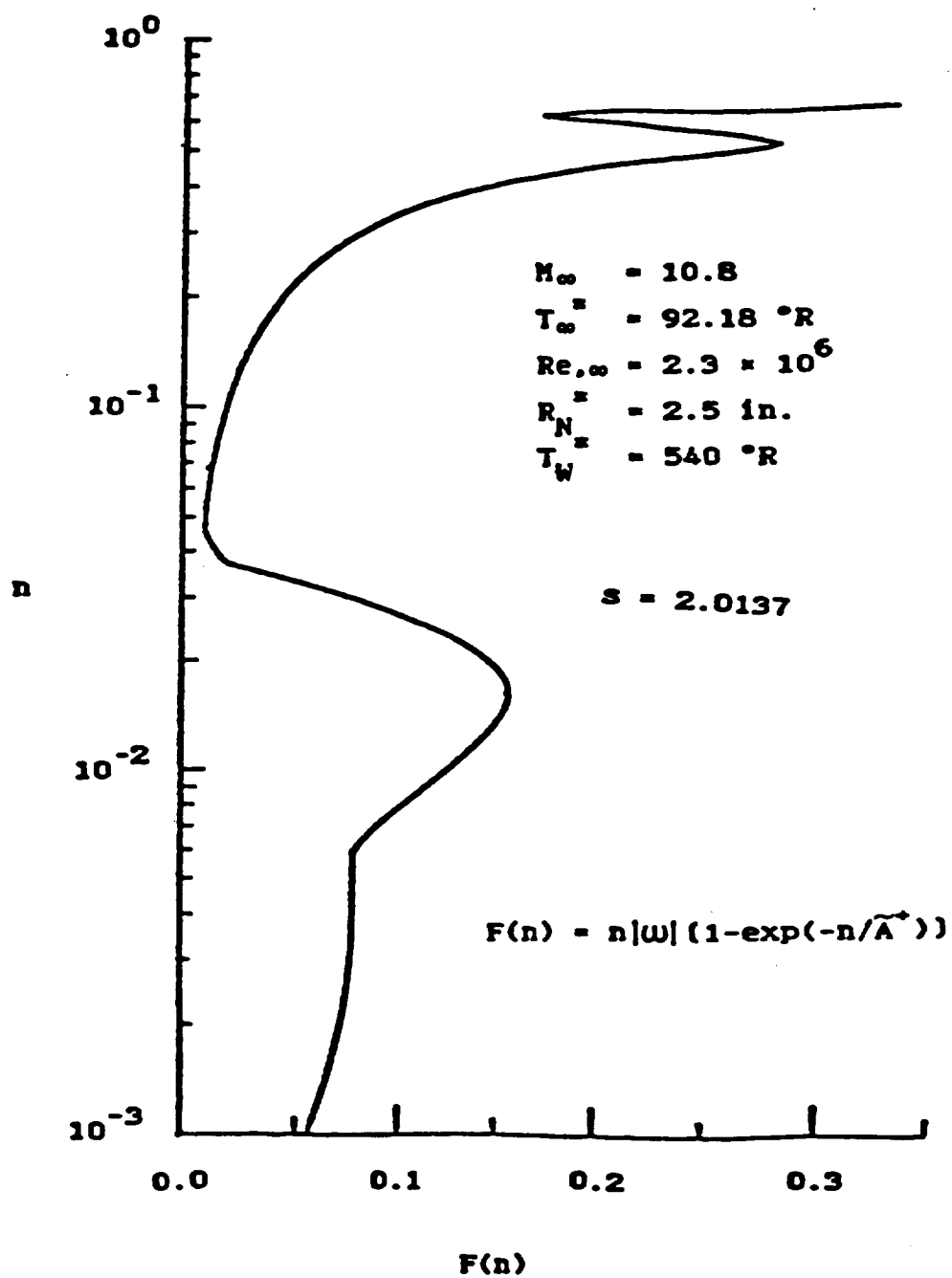
Fig. 3.22   Distribution of vorticity function at s = 2.0 for a 9° sphere-cone with turbulent flow.

M_∞ = 10.8

T_∞ = 92.18 °R

Re,∞ = 2.36 × 10^6

R_N = 2.5 in.

T_W = 540 °R

s = 10.0137

$$F(n) = n|\omega|\{1-\exp(-n/\widetilde{A}^+)\}$$
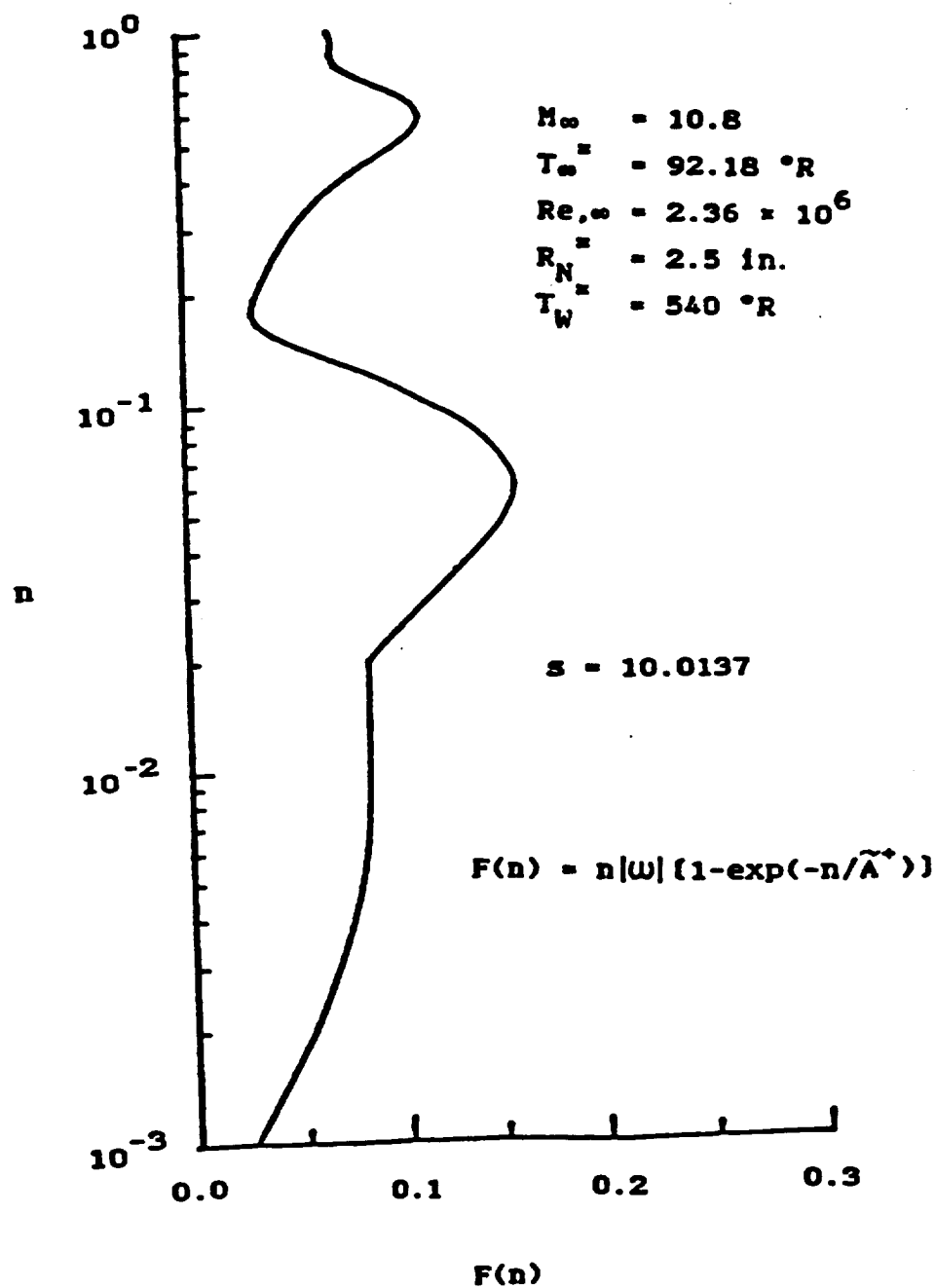
Fig. 3.23 Distribution of vorticity function at s = 10.0 for a 9° sphere-cone with turbulent flow.
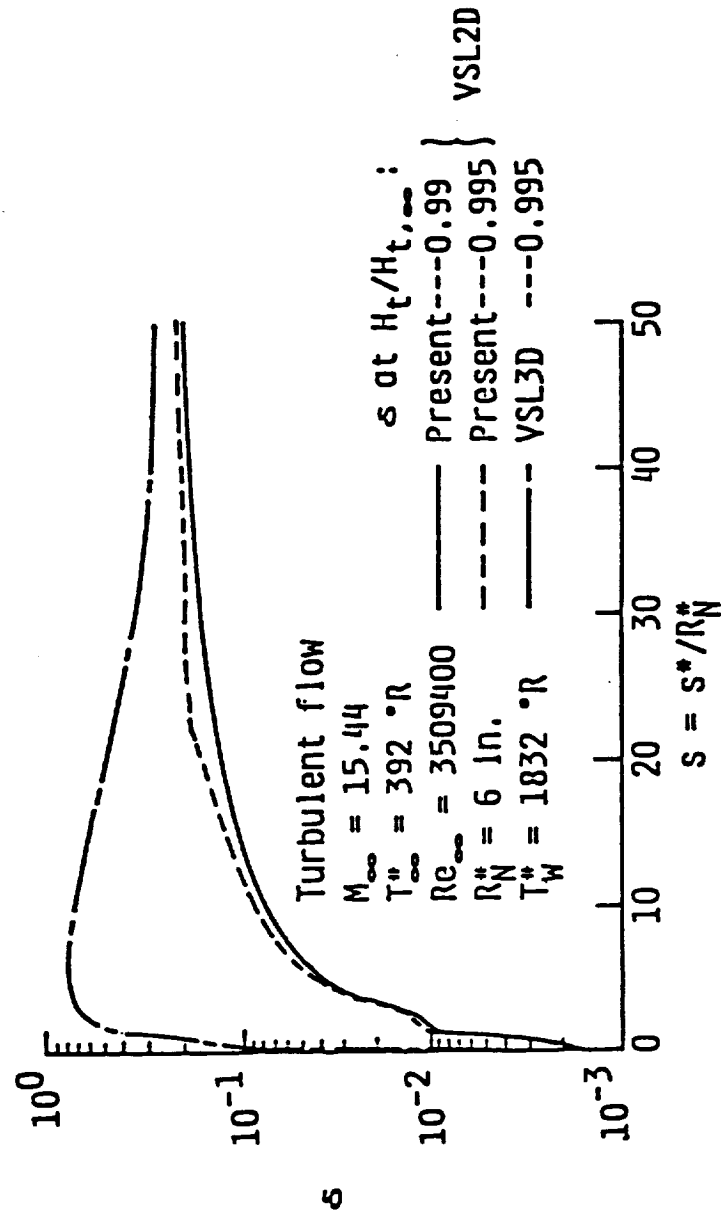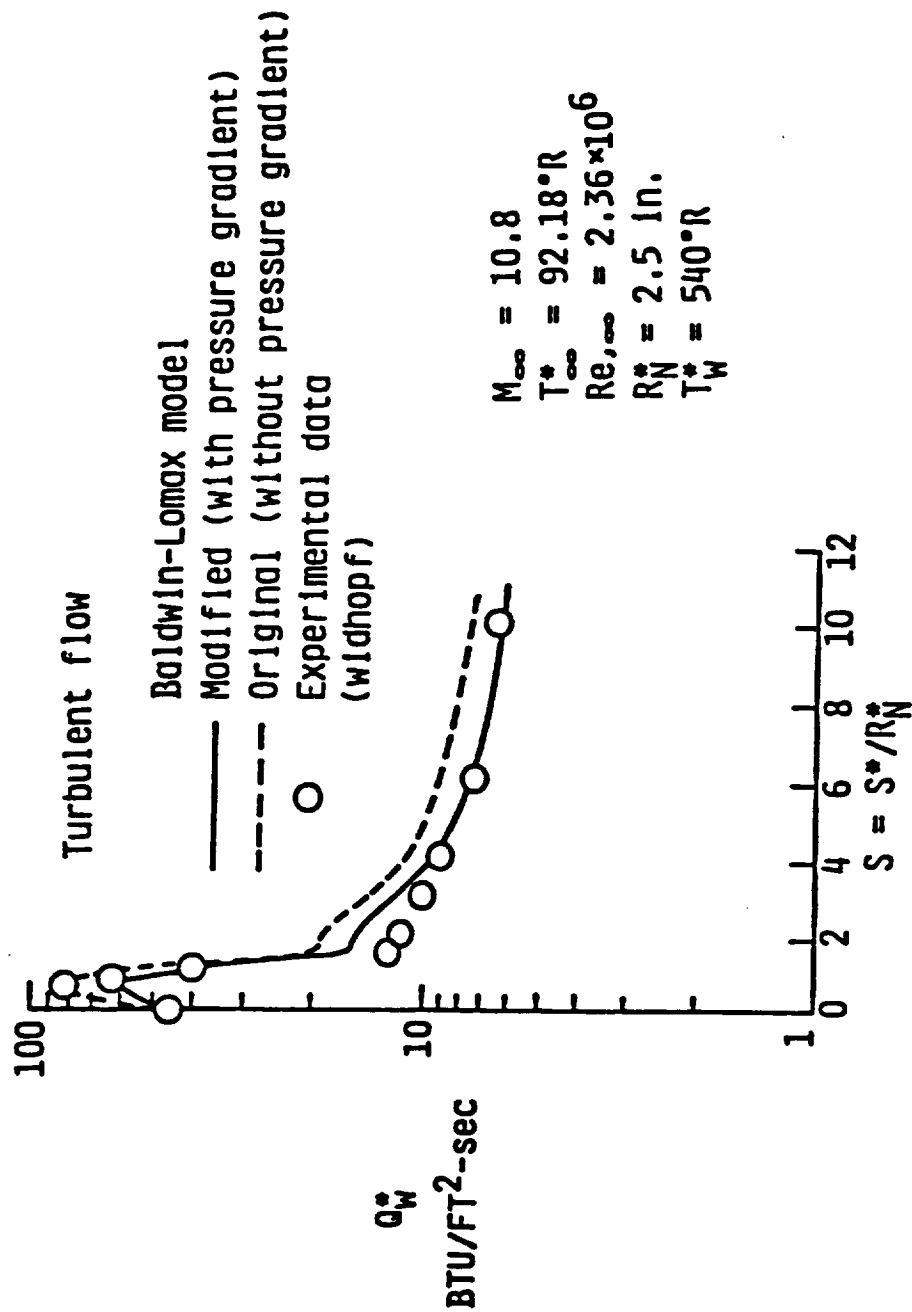
Fig. 3.24 Surface heat transfer rate distribution for a 9° sphere-cone with turbulent flow.
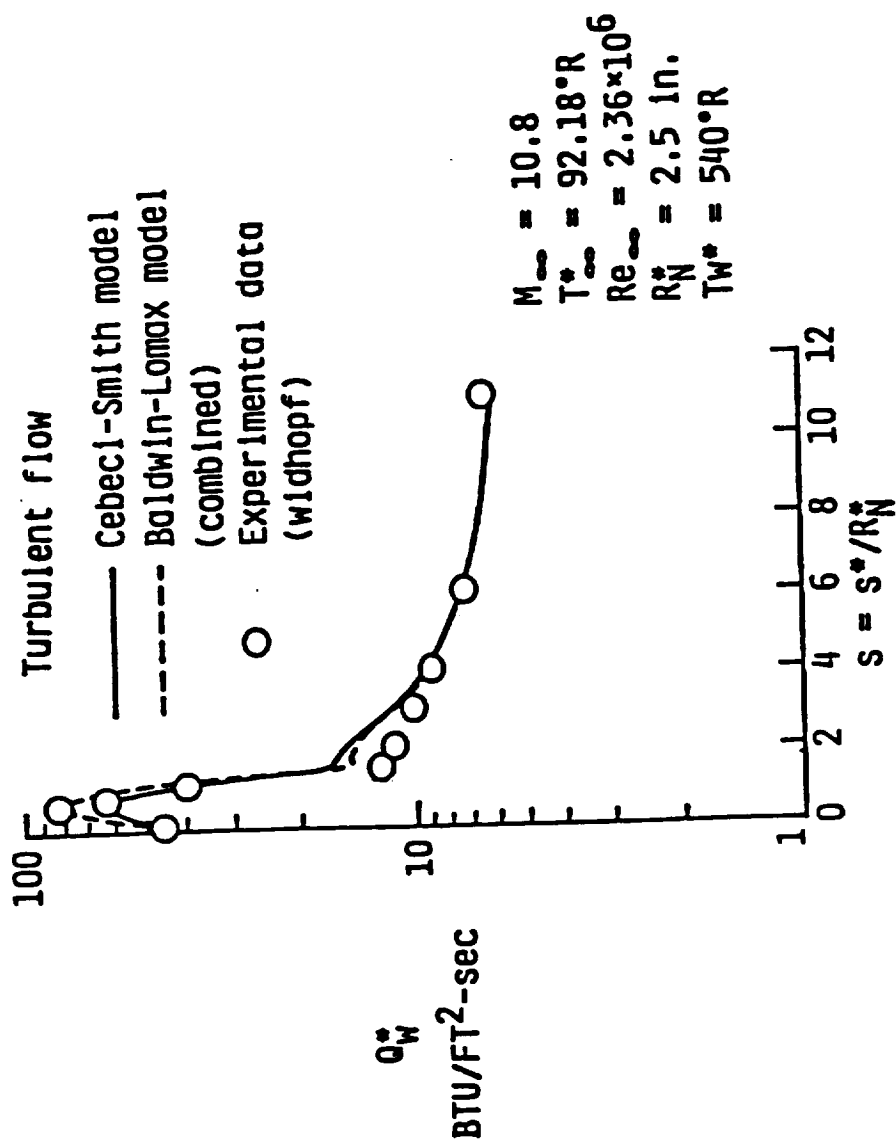
Fig. 3.25 Surface heat transfer rate distribution for a 9° sphere-cone with turbulent flow.

flowfield quantities at the boundary layer edge at this body location. This problem can be overcome through the use of adaptive grids. The observed increase in the heating data in Figs. 3.26 and 3.27 with increasing body location is probably due to the entropy-layer swallowing. This trend is also visible from the theoretical predictions. Once the swallowing is complete, the data and predictions would probably show a decreasing trend with increasing body distance.

Since the sensitivity of the surface heat transfer rate on the boundary layer thickness definition does not exist in the Baldwin-Lomax turbulence model, the Stanton number distribution was obtained using this model in Fig. 3.27. A comparison of predictions with the experimental data shows that a value of 3.0 for C_{cp} gives better results as compared to the values of 2.08 suggested for $M_\infty = 3$ by Knight [21] or the original value of 1.6 given for $M_\infty = 1$ [20]. This coefficient which appears in the Baldwin-Lomax outer formulation is dependent upon the flow Mach number. The value of 3 inferred here for C_{cp} at $M_\infty = 8$ along with the other suggested values for different Mach numbers point to a linear dependence of C_{cp} on the flow Mach number in the range $1 \leq M \leq 8$. Additional comparisons with data are necessary to verify this dependence.

The surface heat transfer results for a 5° sphere-cone obtained by using the Cebeci-Smith and the modified Baldwin-Lomax models of turbulence are illustrated in Fig. 3.28. The results of laminar flow calculations are shown in this figure. These calculations were performed using both the present method and the VSL3D method [34]. The
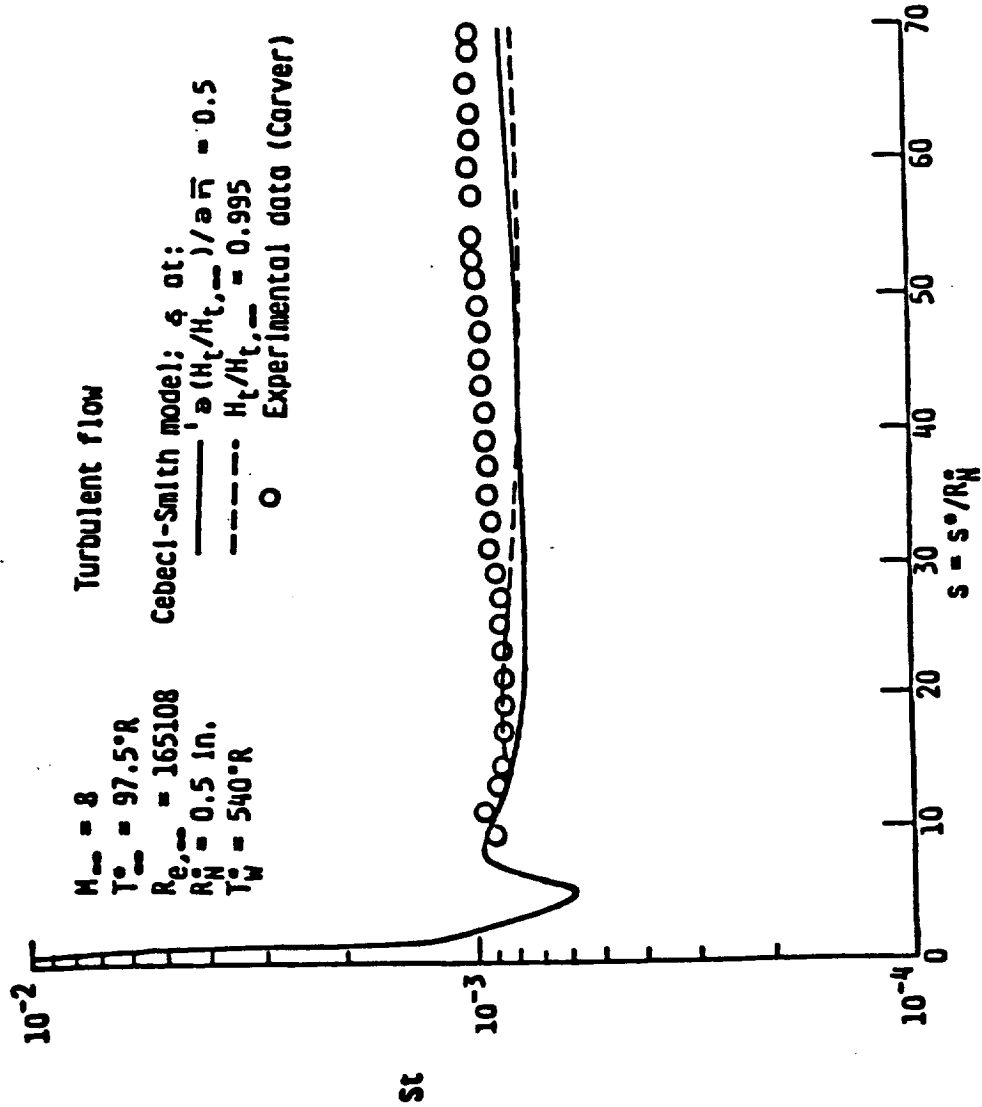
Fig. 3.26 Stanton number distribution for a 7° sphere-cone
with turbulent flow.
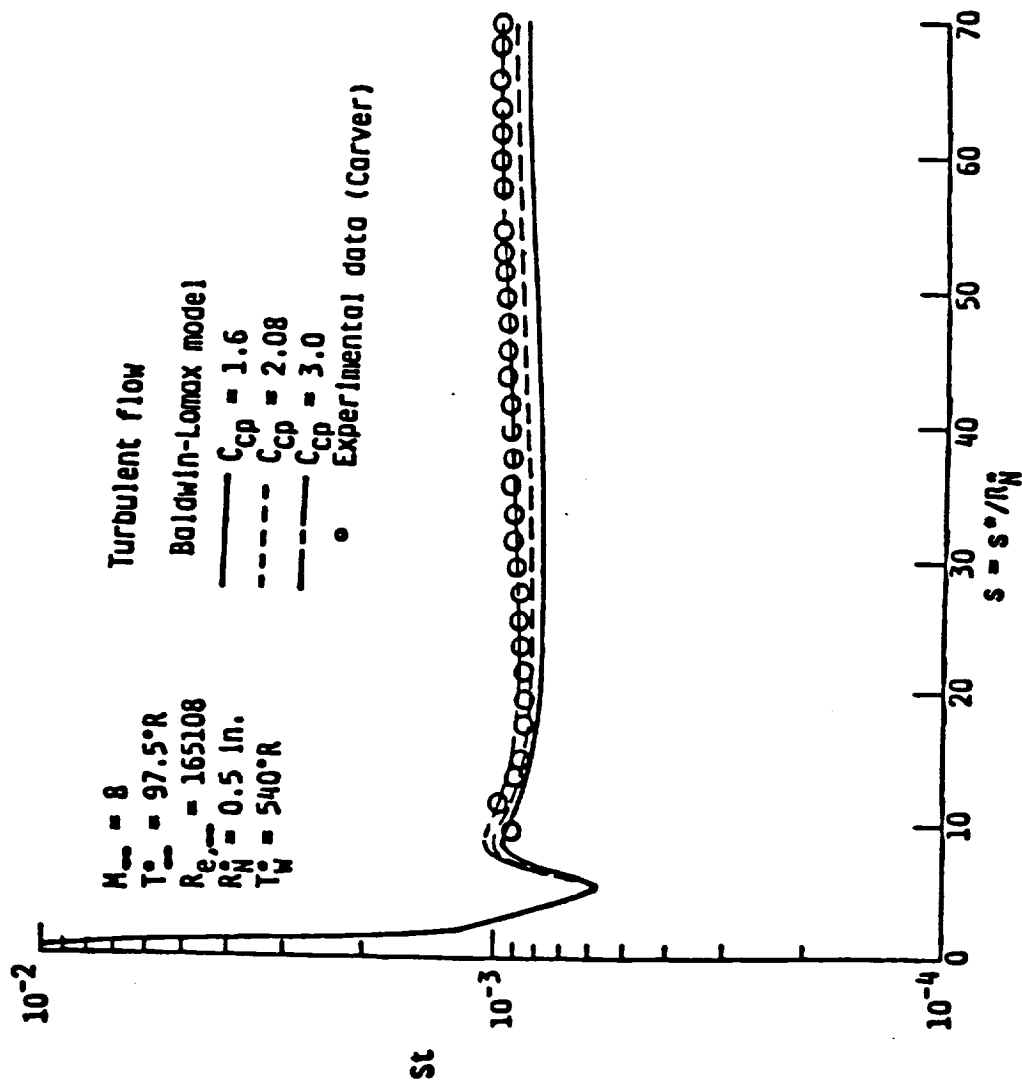
Fig. 3.27 Stanton number distribution for a 7° sphere-cone with turbulent flow.

$M_\infty = 15$
$T^*_\infty = 480°R$
$R^*_N = 1.5$ In.
$R_{e,\infty} = 18906$
$T^*_W = 540°R$

Turbulent flow

Laminar flow

C.S. $(a(H_t/H_{t,\infty})/a\bar{n} = 0.5)$ } Present
B.L. $(C_{cp} = 3.0)$
C.S. $(a(H_t/H_{t,\infty})/a\bar{n} = 0.5)$ — VSL3D

Q^*_W
BTU/FT^2-sec

100.0

10.0

1.0

0.1

0 20 40 60 80 100 120 140

x^*, FT
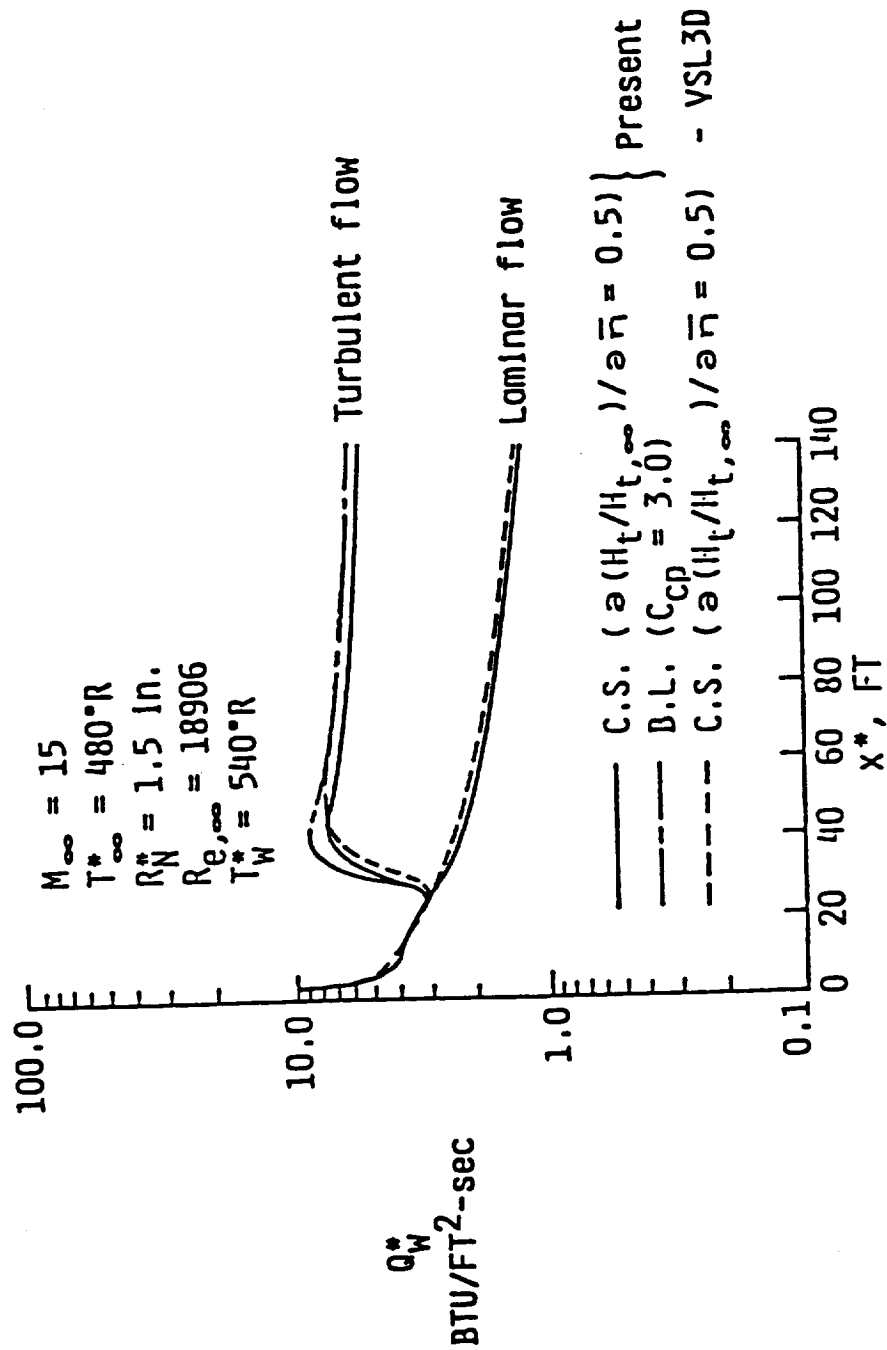
Fig. 3.28 Surface heat transfer rate distribution for a 5°
sphere-cone with turbution flow.

transition was initialized at an axial location of 23.8 ft. Even though the turbulent flow results from the two methods using the Cebeci-Smith model are different, the VSL3D results compare with the modified Baldwin-Lomax model very well from the end of transition.

3.7 Conclusions

Numerical solutions of viscous shock-layer equations are presented for hypersonic laminar and turbulent flows over long slender bodies. These results are obtained from a method which employs a spatial-marching implicit finite-difference technique. This technique is fast and uses partial coupling among the governing equations based on the hypersonic small disturbance theory. The partial coupling yields a simple and computationally efficient technique.

Detailed comparisons have been made with other predictions and experimental data for slender body flows to assess the accuracy of the present numerical technique. Results from the present method show that the coupling between the normal momentum and continuity equations is essential and adequate to obtain stable and fairly accurate solutions past long slender bodies.

The two widely used algebraic turbulence models, namely, the Cebeci-Smith and Baldwin-Lomax models have been analyzed with the present numerical technique for application to long slender bodies. Both of these models appear adequate for such flows. Due to the sensitivity of the Cebeci-Smith turbulence model to the boundary layer edge location, however, it is imperative that the numerical method should provide good resolution and accurate solutions near the boundary layer edge. This can be a problem for long slender bodies, especially,

if the numerical method (such as PNS) employs artificial viscosity to damp oscillations. For this reason, the Baldwin-Lomax turbulence model, which avoids the use of the conventional boundary layer thickness in its formulation, appears more convenient to implement.

A correction for the pressure-gradient effect has been made to the Baldwin-Lomax model. Constant C_{cp} in the outer-layer formulation has been modified to 3.0 for the Mach 8 case. Based upon this study and other investigations, a linear dependence of this constant on the flow Mach number is suggested. Further comparisons with the experimental data are needed to verify this dependence. An additional consideration in the implementation of the Baldwin-Lomax model concerns the appearance of two peaks associated with the two maxima in the vorticity functions used to form the outer-layer length scale. The second peak is avoided by choosing the first one in the region where the gradient of total enthalpy is less than or equal to 0.5, i.e., $\partial(H_t/H_{t,\infty})/\partial\bar{\eta} \leq 0.5$.

Chapter 4

LOW REYNOLDS NUMBER PERFECT GAS FLOW

4.1 Introduction

Most future hypersonic vehicles will be operating in the upper atmosphere, where "low density effects" will play a major role in establishing the lift, drag, moments, and aerodynamic heating on a hypersonic vehicle. An accurate knowledge of hypersonic aerothermodynamics under low density conditions is required for an accurate prediction of the aerothermal environment for the new generation of hypersonic vehicles.

The degree of rarefaction of a low density flow is usually expressed through the Knudsen number which is the ratio of the molecular mean free path in the gas to a characteristic dimension of the flowfield. The conventional continuum flow assumption is valid when this parameter is very small in comparison to unity. The opposite limit of very large Knudsen number corresponds to a free molecule flow in which intermolecular collisions may be neglected. The region between these limits is generally referred to as the transition flow regime [52].

At highly rarefied gas flow conditions, the conventional approach by continuum analysis is no longer valid. A more appropriate approach is by kinetic theory of gases which can correctly describe microscopic properties of molecules, such as the Boltzmann equation [30]. Although

there is only one dependent variable, the distribution function for the
molecular states in the Boltzmann equation, the number of independent
variables make this approach extremely difficult to obtain analytical or
numerical solutions. An alternative is to model the gas flow at the
molecular level. The Direct Simulation Monte Carlo (DSMC) method [53]
has been found to be most readily applicable to complex engineering
problems. However, this method still requires large computational times
and computer storage.

At the slightly rarefied gas conditions, significant levels of
molecular collisions are still present in the flowfield which make the
continuum approaches applicable except in a region next to the wall. It
is because the gradients of the macroscopic variables become so steep
that the mean free path becomes large compared to the local
characteristic length. This region is called the Knudsen layer in which
the determination of the flow properties requires the direct solution of
the Boltzmann equation matched to the solutions for the outer flow and
the wall boundary conditions. This is most conveniently done through
the use of a slip model in which slip and jump properties are used for
the boundary conditions for the conventional continuum flow equations.
These slip and jump boundary conditions for the gas and solid interface
are obtained from the balance equations for mass, momentum and energy
fluxes at the Knudsen layer edge [30-31, 54-55].

Not much attention seems to have been given to the problems
encountered with low-density aerothermodynamics. Davis [12] included
body and shock-slip in the viscous shock-layer analysis of a perfect-gas
flow around a hyperboloid. Davis [56] modified these slip relations for
a binary mixture. Tree et al. [57] analyzed the hypersonic ionizing

viscous shock-layer flow past axially symmetric bodies at low densities. Tiwari and Szema [58,59] investigated the effects of body and shock slip conditions on the aerothermodynamic environment of a Jovian entry body. Swaminathan et al. [60] and Song et al. [61] recently included the body- and shock-slip effects for three-dimensional flows. However, their surface slip condition for single species or multicomponent mixtures contained some errors as explained in Ref. 31. The shock-slip boundary conditions did not account for the derivatives of the shock quantities in the shock-oriented coordinate system. This introduced significant errors in analyzing flows past slender bodies as compared to the wide-angle bodies [62].

Gupta et al. [31] reanalysed the wall boundary conditions by using the approach of Scott [63] and provided appropriate relations for the various quantities with surface slip in a form which can readily be employed for multicomponent and binary mixtures as well as a single-species gas. These surface slip expressions have been implemented successfully in full Navier-Stokes equations [26,62]

Under the low Reynolds number (or low density) flow conditions, the viscous effects influence almost the entire shock layer and the shock itself is considerably thick as compared to the high Reynolds number (or high density) case. The complete Navier-Stokes equations are considered appropriate for the low Reynolds number applications. But computer storage and computational time make them are very expensive to solve for flows around long bodies. The viscous shock-layer equations have been shown to give good results for hypersonic flows on blunt slender long bodies at high Reynolds number. Thus, it is desirable to employ the viscous shock-layer equations instead of Navier-Stokes

equations at low Reynolds number cases to reduce the computational requirement.

In this chapter, the surface-slip relations developed by Gupta et al. [31] and the corrected form of the shock-slip boundary conditions [12] are implemented in the viscous shock-layer code for a perfect gas as described in Chap. 2. to obtain results for the low-density flight conditions for long slender bodies. A detailed comparison with experimental data and other numerical results gives an estimate of accuracy of the present predictions. Furthermore, the range of applicability of the viscous shock-layer solutions is ascertained by comparing these results with those obtained from the steady-state Navier-Stokes equations.

4.2 Flow Governing Equations

The conservation equations employed in this chapter are the steady perfect gas viscous shock-layer equations for an axisymmetric or two-dimensional body at zero angle of attack [12]. These equations are written in the same forms as Eqs. (2.25) through (2.37) except that the eddy viscosity, ε^+, is set to zero. Also, the stretching function $g(\bar{\eta})$, Eq. (2.21), is given by

$$g(\bar{\eta}) = 1 - [\bar{\alpha} + \frac{(1-\bar{\alpha})}{\ln(\frac{\bar{\beta}+1}{\bar{\beta}-1})} \ln \{\frac{\bar{\beta}-\bar{\eta}(2\bar{\alpha}+1)+1}{\bar{\beta}+\bar{\eta}(2\bar{\alpha}+1)-1}\}] \qquad (4.1)$$

The first and second derivatives of Eq. (4.1) are expressed as

$$\frac{dg}{d\bar{\eta}} = \frac{(1-\bar{\alpha})(2\bar{\alpha}+1)}{\ln(\frac{\bar{\beta}+1}{\bar{\beta}-1})} \left\{ \frac{1}{[\bar{\beta}-\bar{\eta}(2\bar{\alpha}+1)+1]} - \frac{1}{[\bar{\beta}+\bar{\eta}(2\bar{\alpha}+1)-1]} \right\} \qquad (4.2)$$

$$\frac{d^2 g}{d\bar{\eta}^2} = \frac{(1-\bar{\alpha})(2\bar{\alpha}+1)^2}{\ln(\frac{\bar{\beta}+1}{\bar{\beta}-1})} \left\{ \frac{1}{[\bar{\beta}-\bar{\eta}(2\bar{\alpha}+1)+1]^2} - \frac{1}{[\bar{\beta}+\bar{\eta}(2\bar{\alpha}+1)-1]^2} \right\} \qquad (4.3)$$

Equation (4.1) permits the mesh to be refined either near the body only ($\bar{\alpha} = 0$) or refined equally near both the body and bow shock ($\bar{\alpha} = 1/2$) when the shock becomes thick under the low density flight conditions. The parameter $\bar{\beta}$ controls the amount of refinement with values near 1 giving the largest amount of stretching. The physical coordinate $\bar{\eta}$ can be obtained from inverting Eq. (4.1) and is expressed as

$$\bar{\eta} = \frac{1}{(2\bar{\alpha}+1)} \left[1 - \bar{\beta} \left\{ \frac{(\frac{\bar{\beta}+1}{\bar{\beta}-1})^{\frac{1-\eta-\bar{\alpha}}{1-\bar{\alpha}}} - 1}{(\frac{\bar{\beta}+1}{\bar{\beta}-1})^{\frac{1-\eta-\bar{\alpha}}{1-\bar{\alpha}}} + 1} \right\} \right] \qquad (4.4)$$

This transformation keeps the body at $\eta = 0$ and the shock at $\eta = 1$ with uniform mesh in the computational coordinate η.

4.3 Shock- and Surface-Slip Boundary Conditions

At high altitudes, the continuum flow assumption breaks down in the region next to the wall. The no-slip and no-temperature jump boundary conditions are no longer valid. As such, the slip and temperature jump boundary conditions should be used. The relations for the body and shock slip conditions are provided in this section.

4.3.1 Surface Slip Conditions

The surface slip conditions for a single-species gas as given in Gupta et al. [31] are used as the boundary conditions on the body surface. Since no mass injection is considered in this chapter, the normal component of velocity at the surface is taken to be zero. The nondimensional forms of surface slip conditions in the computational plane, Eqs. (2.59) through (2.61), are given here again as

Velocity slip:

$$u_s = \sqrt{\frac{\pi}{2}} \left(\frac{2-\bar{\theta}}{\bar{\theta}}\right) \frac{\epsilon^2 \mu_s}{\sqrt{P_s \rho_s}} \left[\frac{1}{n_{sh}} \frac{dg}{d\bar{\eta}} \frac{\partial u}{\partial \eta} - \frac{\kappa u}{(1+\bar{\eta}h_{sh}\kappa)}\right]_s \tag{4.5}$$

Pressure slip:

$$P_s = P_w + \frac{4}{5\sqrt{2\pi}} \left(\frac{\gamma}{\gamma-1}\right) \left(\frac{2-\bar{\theta}}{\bar{\theta}}\right) \frac{\epsilon^2}{Pr} \frac{\mu_s}{T_s} \sqrt{\frac{P_s}{\rho_s}} \left(\frac{1}{n_{sh}} \frac{dg}{d\bar{\eta}} \frac{\partial T}{\partial \eta}\right)_s \tag{4.6}$$

Temperature slip:

$$T_s = T_w + \frac{1}{2}\sqrt{\frac{\pi}{2}} \left(\frac{\gamma}{\gamma-1}\right)\left(\frac{2-\bar{\theta}}{\bar{\theta}}\right) \frac{\epsilon^2}{Pr} \frac{\mu_s}{\sqrt{P_s \rho_s}} \left(\frac{1}{n_{sh}} \frac{dg}{d\bar{\eta}} \frac{\partial T}{\partial \eta}\right)_s \tag{4.7}$$

In the derivation of the relation for the temperature slip, it is assumed that the internal energy is frozen during the reflection from

the wall. The parameter $\bar{\theta}$ is the accommodation coefficient which is taken to be 1 in this study.

4.3.2 Shock Slip Conditions

The boundary conditions at the shock are the modified Rankine-Hugoniot relations developed by Cheng [32]. These relations are obtained by integrating the one-dimensional Navier-Stokes equation across the shock. Since velocity components tangent and normal to the shock are not the same as those tangent and normal to the body surface, transformations are needed to relate these quantites. The transformations are given by

$$\bar{u}_{sh} = u_{sh} \cos(\alpha-\theta) + v_{sh}\sin(\alpha-\theta) \tag{4.8}$$

$$\bar{v}_{sh} = - u_{sh} \sin(\alpha-\theta) + v_{sh}\cos(\alpha-\theta) \tag{4.9}$$

where $\bar{u}_{sh}$ and $\bar{v}_{sh}$ are the components of velocity tangent and normal to the shock interface, respectively. The nondimensional forms of the shock slip conditions in the computational plane, Eqs. (2.75) through (2.78), are given here again by

Continuity:

$$\rho_{sh}\,\bar{v}_{sh} = -\sin\alpha \tag{4.10}$$

Tangential-momentum:

$$\varepsilon^2\mu_{sh}\{[\cos(\alpha-\theta) + \bar{n}\,\frac{dn_{sh}}{d\xi}\,\sin(\alpha-\theta)]\,\frac{1}{n_{sh}}\,\frac{dg}{d\bar{n}}\,\frac{\partial\bar{u}}{\partial\eta}$$

$$+ \frac{\partial\bar{u}}{\partial\xi}\,\sin(\alpha-\theta)\}_{sh} + \bar{u}_{sh}\,\sin\alpha = \sin\alpha\,\cos\alpha \tag{4.11}$$

Normal-momentum:

$$P_{sh} = P_{\infty} + \sin\alpha(\sin\alpha + \nabla_{sh})$$

(4.12)

Energy:

$$\epsilon^2 \left(\frac{\mu}{Pr}\right)_{sh} \left\{\left[\cos(\alpha-\theta) + \bar{\eta}\,\frac{dn_{sh}}{d\xi}\,\sin(\alpha-\theta)\right]\frac{1}{n_{sh}}\,\frac{dg}{d\bar{\eta}}\,\frac{\partial T}{\partial \eta}\right.$$

$$\left. - \frac{\partial T}{\partial \xi}\,\sin(\alpha-\theta)\right\}_{sh} + T_{sh}\,\sin\alpha - \frac{\sin\alpha}{2}\,(\Box_{sh} - \cos\alpha)^2$$

$$= \frac{\sin\alpha}{2}\,\left\{\frac{4\gamma}{(\gamma+1)^2}\,\sin^2\alpha + \left[\left(\frac{2}{\gamma-1}\right) - \frac{4(\gamma-1)}{(\gamma+1)^2}\right]\frac{1}{M_\infty^2}\right.$$

$$\left. - \frac{4}{(\gamma+1)^2 M_\infty^4 \sin^2\alpha}\right\}$$

(4.13)

Equation of state:

$$\rho_{sh} = \gamma p_{sh}/(\gamma-1)T_{sh}$$

(4.14)

The errors in the expressions used by Davis [12] have been corrected in this study and this is discussed also by Lee et al. [62].

4.4 Method of Solution

The method of solution is similar to that implemented in Chap. 3. The two second-order equations, s-momentum and energy, are replaced with central differences in the η-direction and two-point backward differences in the ξ-direction. The two first-order equations, continuity and normal-momentum, are solved simultaneously in a coupled way. The solution is started at the stagnation point. The velocity slip and temperature jump on the surface and at the shock are iterated along with the corresponding governing equations. The solution is iterated at location m until the convergence is achieved. The solution

is then advanced to the m+1 station. Figure 4.1 presents the flow chart for obtaining solutions with body-slip only, shock-slip only, and with body and shock-slip.

Solutions to the steady-state Navier-Stokes equations, which are given in Appendix B, have been obtained by first expressing them in the body-oriented coordinate system. This procedure is the same as the one employed with the viscous shock-layer equations. After obtaining a solution of the viscous shock-layer equation, the higher-order terms are evaluated using these flowfield results. These terms are held constant during the solution for the first approximation to the Navier-Stokes equations. The solution with this approximation is obtained at the end of the first global pass. At the beginning of the second global pass, the higher-order terms are reevaluated from the first global-pass solutions. These terms are held constant again during the solution for the second approximation obtained at the end of the second global pass. This procedure is repeated until the flowfield results corresponding to successive global passes converge within a specified limit [23].

4.5 Results and Discussions

Numerical solutions of the viscous shock-layer (VSL) equations for the low-density hypersonic flow over long slender bodies are obtained. The surface slip [31] and the recently corrected shock-slip boundary conditions [62] are implemented in the implicit finite-difference method used to solve the governing equations. Detailed comparisons with the experimental data are included for several conditions. Extensive results are provided for long slender bodies with temperature surface conditions ranging from adiabatic to highly cooled. Also included are
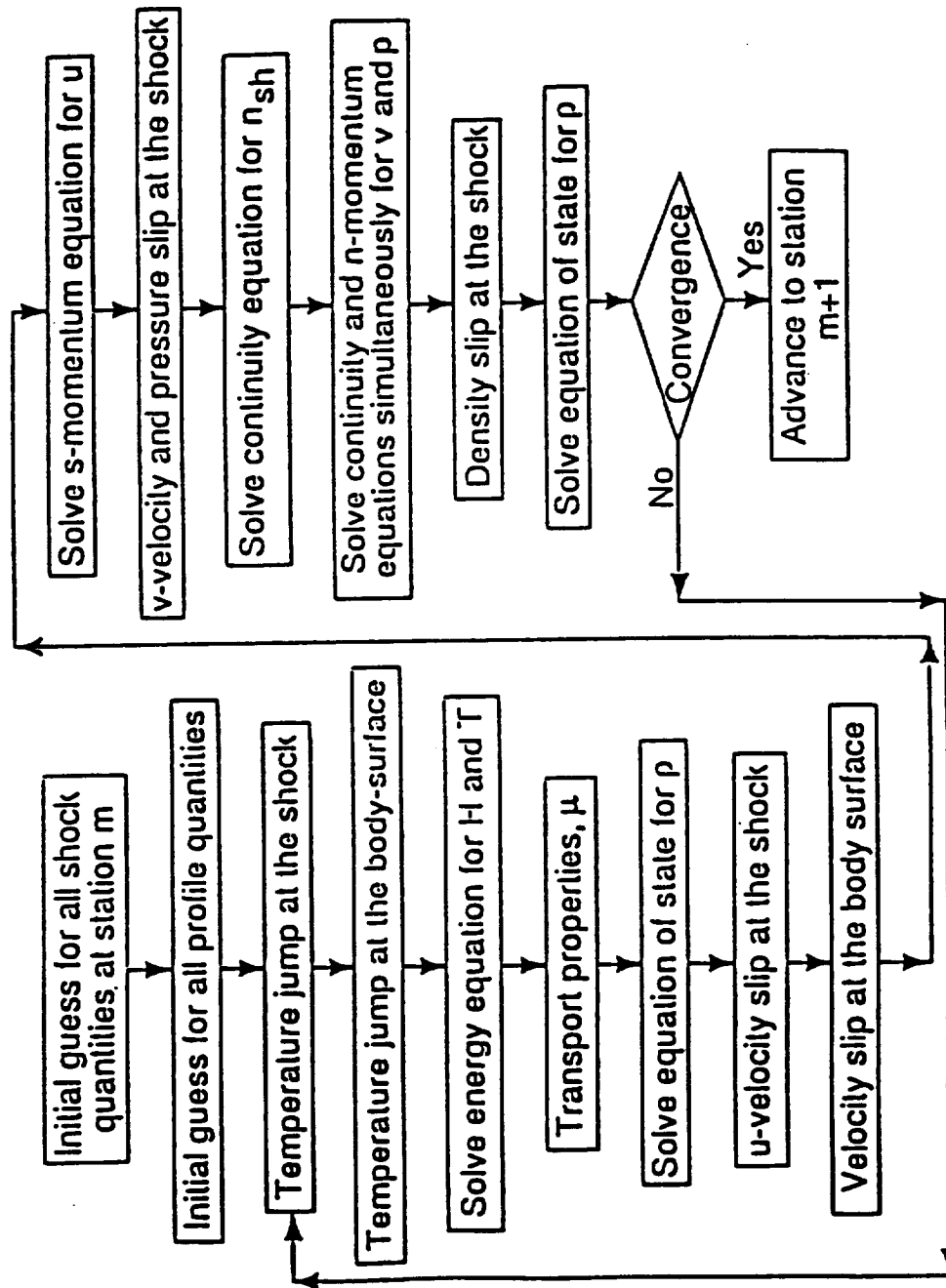
Fig. 4.1 Solution sequence with shock and body slip.

calculations from the steady-state Navier-Stokes equations. These results provide an indication of the range of applicability of the viscous shock-layer solutions.

4.5.1 Comparison with Experimental Data

There are only a few experimental data for the low-density, high-energy flows available in the literature. The data of Little [46] are still considered quite good for such flows. These data, however, are limited to the measurements of pressure, drag, and skin friction. These data were used extensively for comparison with the theoretical predictions by Davis [12]. The same data have been employed for comparison with the present results also. Figures 4.2 to 4.6 give comparisons between the viscous shock-layer predictions and the experimental data [46] for a 10° hyperboloid. With shock and body slip, surface pressure predictions by the present method agree quite well with the experimental data as shown in Fig. 4.2. Comparisons of drag coefficients on a 10° hyperboloid for a range of values of the rarefaction parameter ε are shown in Figs. 4.3 to 4.6. Predictions of Davis [12] are also given in these figures. It is clear that the present predictions with the shock and body slips are in much better agreement with the experimental data than the predictions of Davis. Large differences in the present calculations and those of Davis are seen with increasing values of ε. These differences may be due to the errors in the slip conditions as mentioned in Sec. 4.1.

Comparison between the predicted Stanton number distribution and experimental data [64] for a 10° sphere-cone is provided in Fig. 4.7. The present calculations with shock and body slip are in good agreement
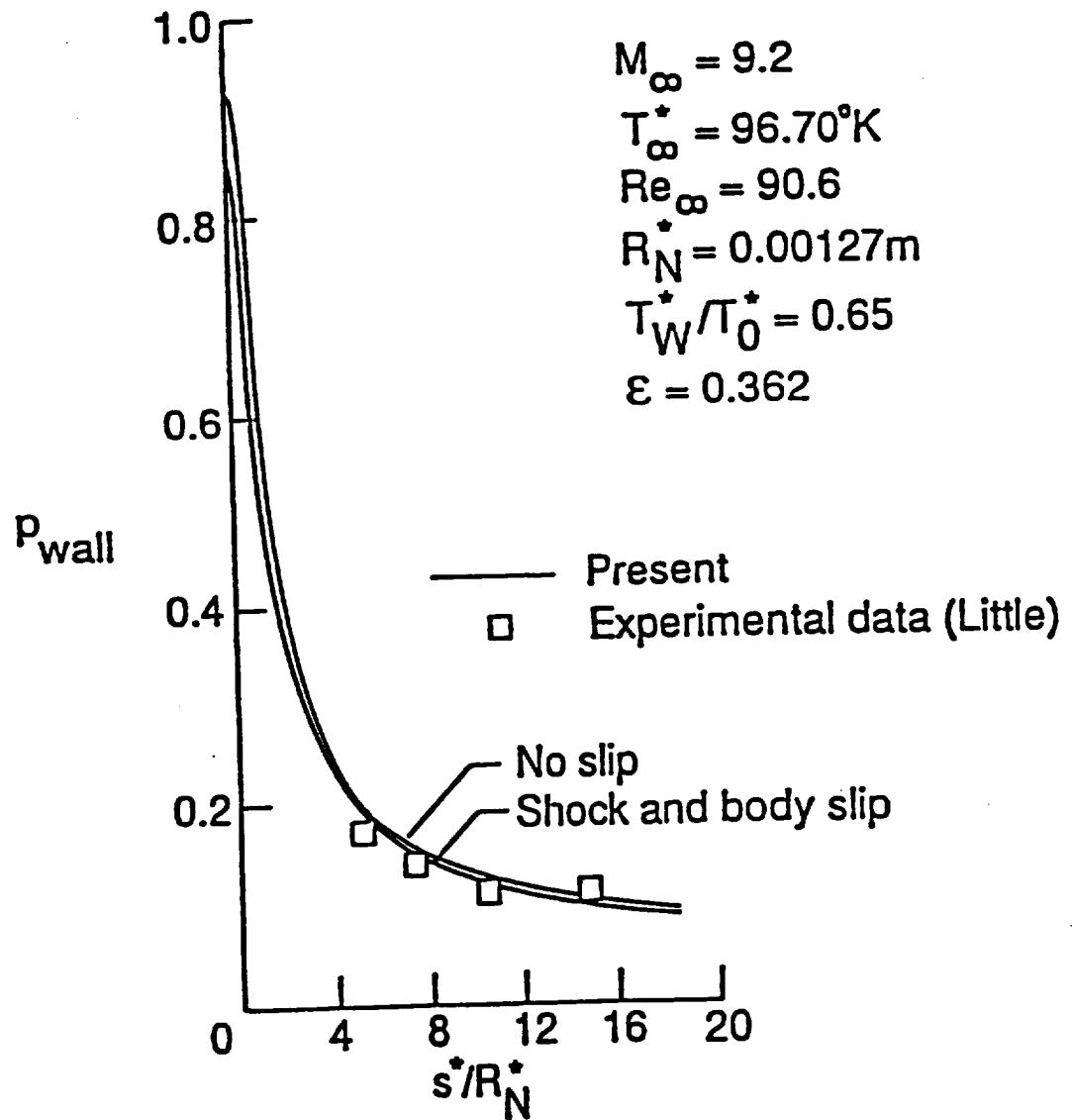
Fig. 4.2 Surface pressure distribution for a 10° hyperboloid with ε = 0.362.
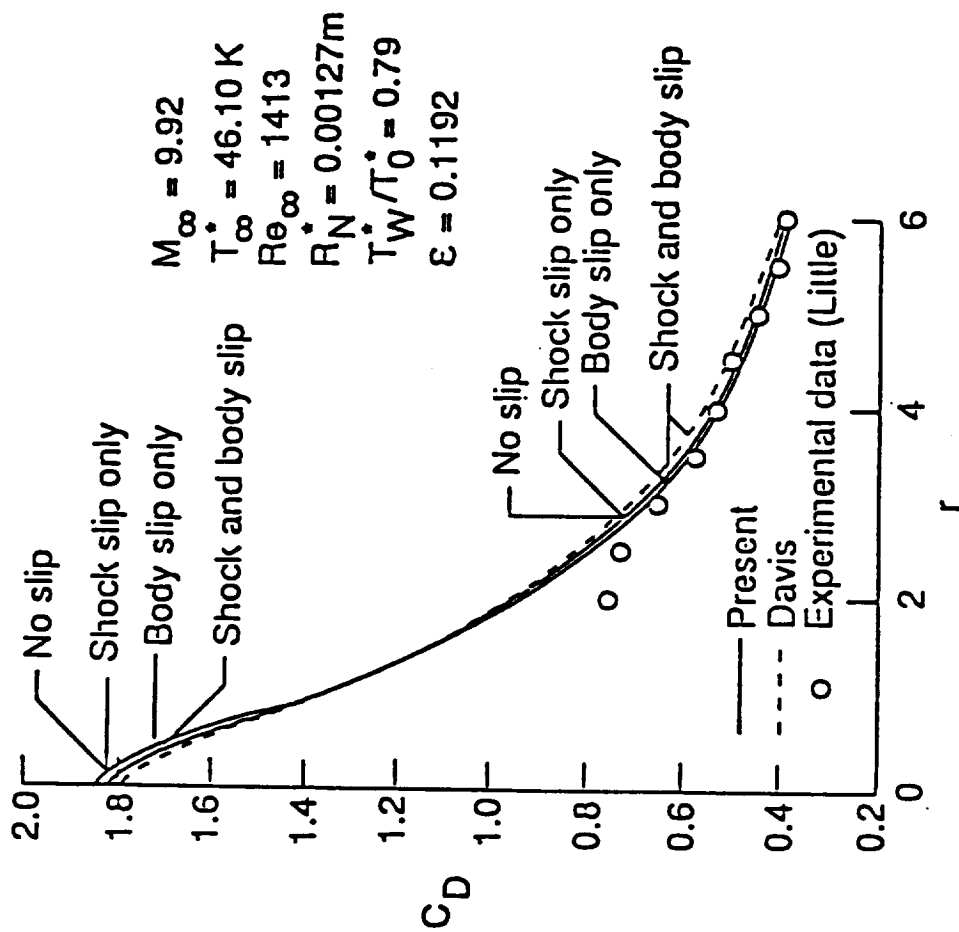
Fig. 4.3 Drag coefficient distribution for a 10° hyperboloid
with ε = 0.1192.
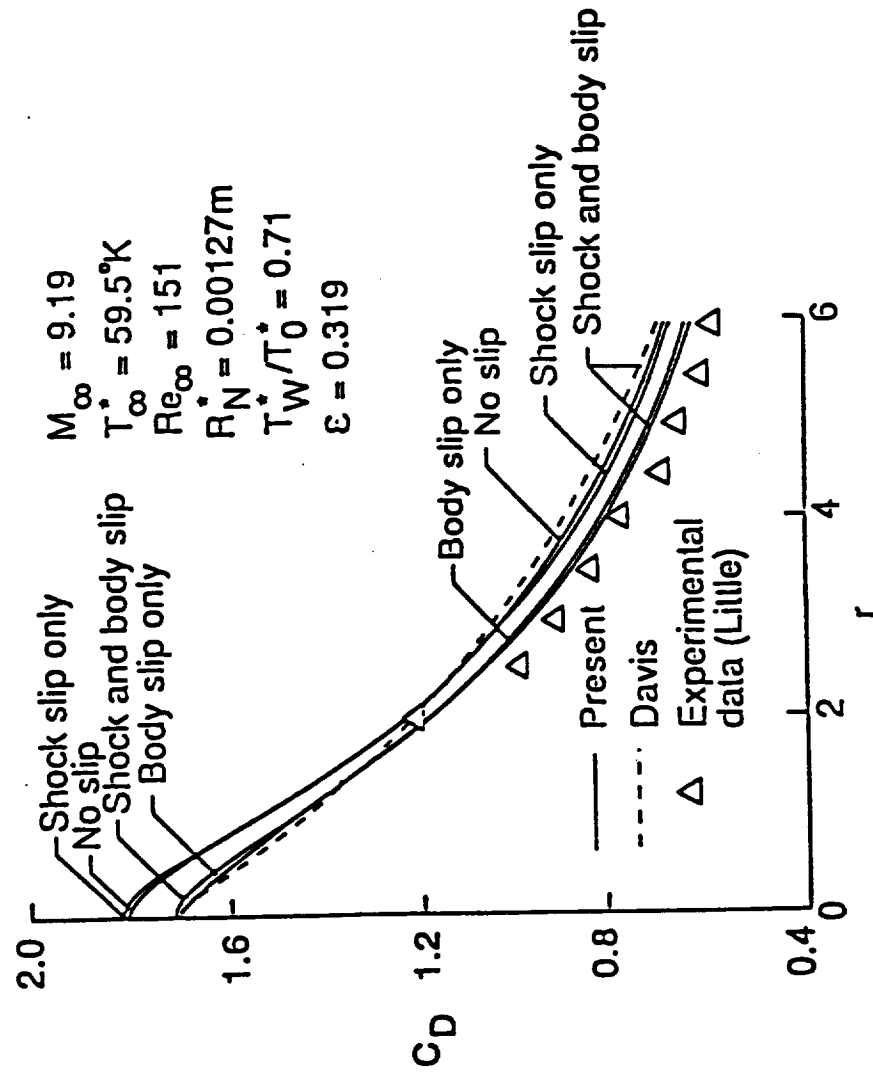
Fig. 4.4   Drag coefficient distribution for a 10° hyperboloid
with ε = 0.319.
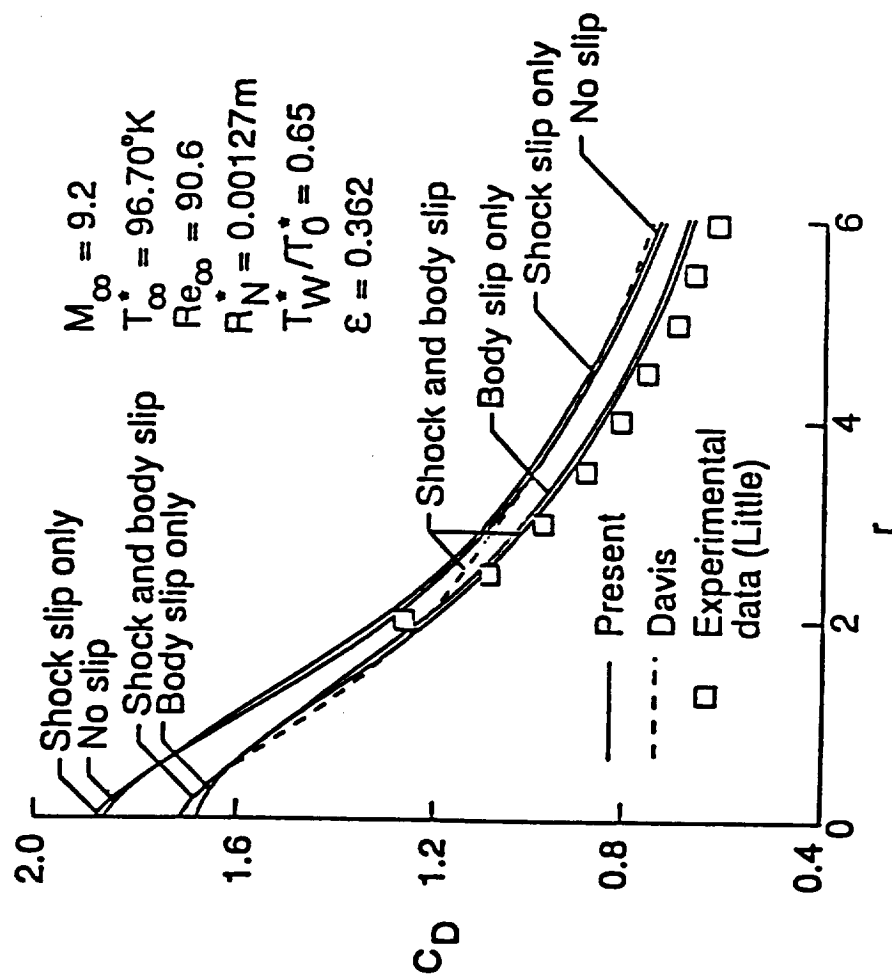
Fig. 4.5 Drag coefficient distribution for a 10° hyperboloid with ε = 0.362.

Fig. 4.6   Drag coefficient distribution for a 10° hyperboloid with ε = 0.690.

$M_\infty = 18.2$
$T_\infty^* = 45°K$
$Re_\infty^* = 1017$
$R_N^* = 0.00191m$
$T_W^*/T_0^* = 0.11$
$\varepsilon = 0.1935$

— — — — — No slip
————— Shock slip only
— · — · — Body slip only
— ·· — ·· — Shock and body slip
O Experimental data (Boylan)

St

s^*/R_N^*
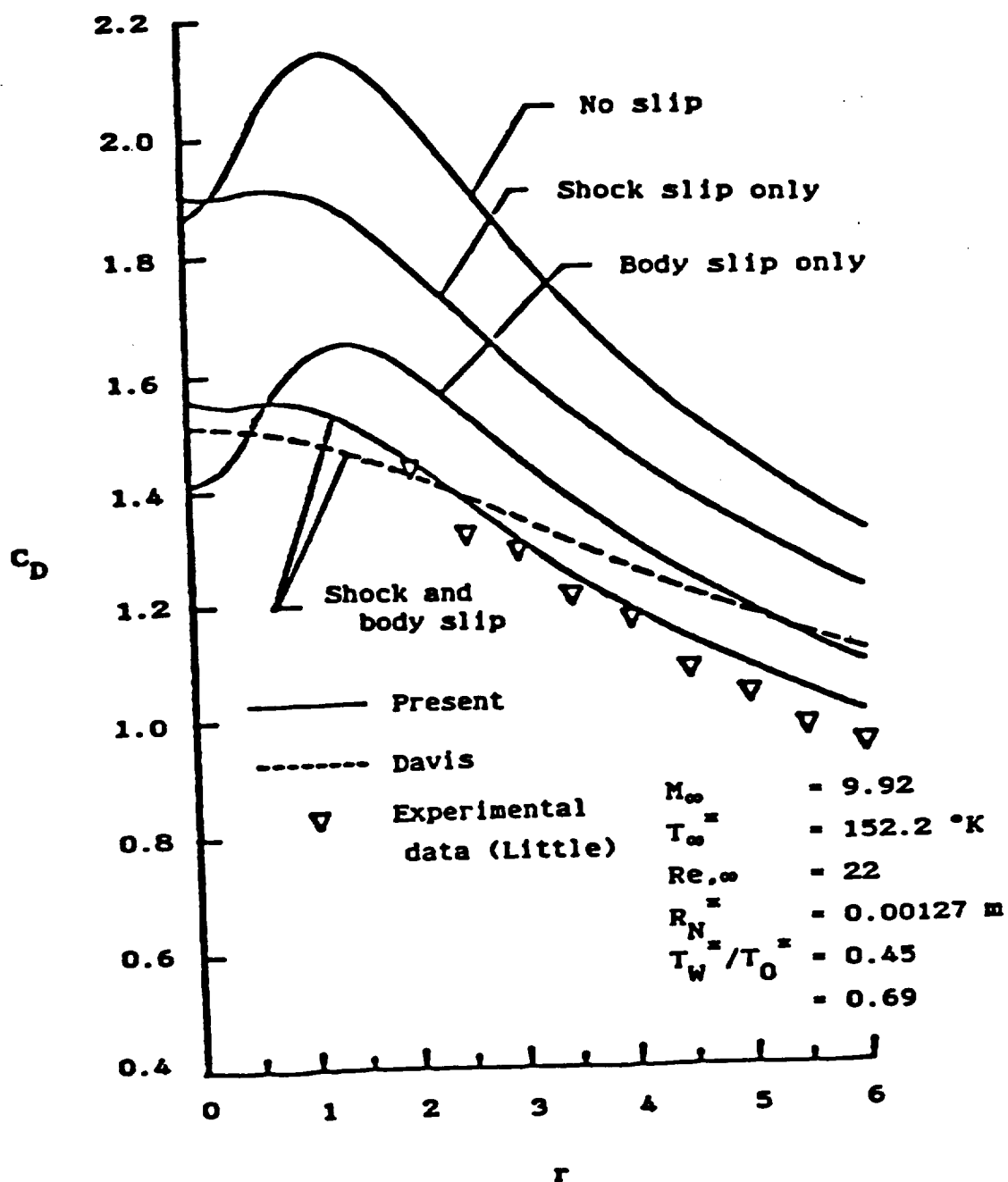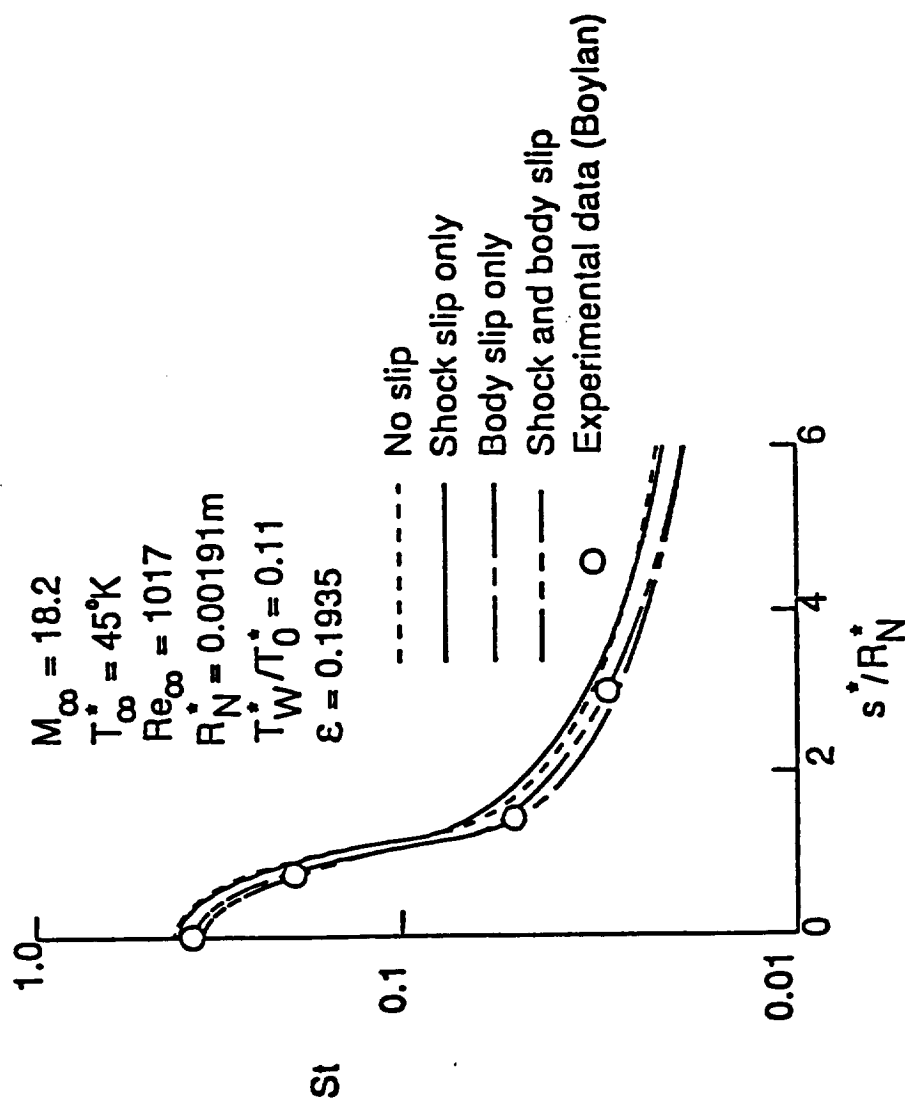
Fig. 4.7   Stanton number distribution for a 10° sphere-cone
with $\varepsilon = 0.194$.

with the data except for the stagnation point. The experimental heat transfer rate at the stagnation point were determined to be biased upward due to particle impact caused by the arc heater [65].

4.5.2 Comparison with Predicted Results

Results obtained for a 22.5° hyperboloid in the stagnation region by the present viscous shock-layer equations and the steady-state Navier-Stokes equations are compared with those obtained by Anderson and Moss [23] in Table 4.1. The results from these calculations compare fairly well, especially for C_p. A maximum difference of less than ten percent occurs between the two results at $Re,_\infty$ of 90 in the heat transfer coefficient, C_H. This may be due to the grid clustering employed near the shock and body in the present calculations.

Figures 4.8. and 4.9 show comparisons for the Stanton number and skin friction coefficient, respectively as obtained by the present viscous shock-layer method and that obtained by Davis [12]. Also shown are the present results obtained from the steady-state Navier-Stokes equations. The calculations are carried out for the stagnation point only for different values of the Reynolds number parameter, ϵ, which is a measure of the degree of rarefaction. Larger values of ϵ imply increased rarefaction effects. The two viscous shock-layer predictions have similar trends. However, significant differences are noticed for large values of ϵ. The discrepancies may be due to the errors contained in the slip equations used by Davis [12] and the current grid clustering near the shock and body. Figures 4.8 and 4.9 also show that the viscous shock-layer predictions deviate from the Navier-Stokes results for large values of ϵ. For $\epsilon = 1$, the present viscous shock layer predictions

Table 4.1 Viscous shock-layer and Navier-Stokes calculations in the stagnation region of a 22.5° hyperboloid.

Re_∞	T_W/T_0	T_∞,R	ε	M_∞	Present VSL No slip		Present VSL Body & Shock slip		Present NS Body & Shock slip		Anderson & Moss VSL Body & Shock slip		Anderson & Moss NS Body & Shock slip	
					C_H	C_p	C_H	C_p	C_H	C_p	C_H	C_p	C_H	C_p
31160	0.08	474	0.024	19.10	0.037	1.84	0.037	1.74	0.037	1.74	–	1.77	–	1.80
1035	0.79	83	0.140	9.92	0.039	1.85	0.036	1.82	0.039	1.85	–	1.82	–	1.87
90	0.65	174	0.366	9.20	0.281	1.86	0.158	1.72	0.208	1.99	0.169	1.74	0.225	2.00

give a Stanton number of 0.68, whereas the Navier-Stokes results yield a value of about 0.9. It is clear that the Navier-Stokes predictions have the right trend in approaching a value of 1 for the free-molecule flow limit. These results suggest that the viscous shock-layer approximation may not be valid for large values of ε.

Figures 4.10 and 4.11 show comparisons of predicted skin-friction coefficient and Stanton number distributions, respectively, as obtained by the present viscous shock-layer method and that by Gordon [16]. The comparison between these two results is quite good when the coarse grid structure of Gordon [16] is used. The method of Gordon is fully coupled and requires solving a 5 x 5 matrix at every point in the flowfield for a perfect gas. The complexity and stability problems in a fully coupled solution will be increased in analyzing a multi-species high-temperature air flow. Also, the computational times will be considerably large for long slender bodies by this method. The present approach, with coupling between the normal momentum and continuity equations only, may be more appealing for such flow conditions. Figures 4.10 and 4.11 also give results with and without slip for a variable grid near the shock and body surface. It is clearly seen that the computational grid-size as well as the slip effects are important in this case.

4.5.3 Calculations for Different Altitudes and Surface Temperatures and Range of Validity of Viscous Shock-Layer Results

An extensive test for the present computational method and the surface and shock-slip boundary conditions is provided through the results given in Figs. 4.12 and 4.13. The flow analyzed in these figures is a high Mach number (M_∞ = 20) flow over highly cooled (T_W =
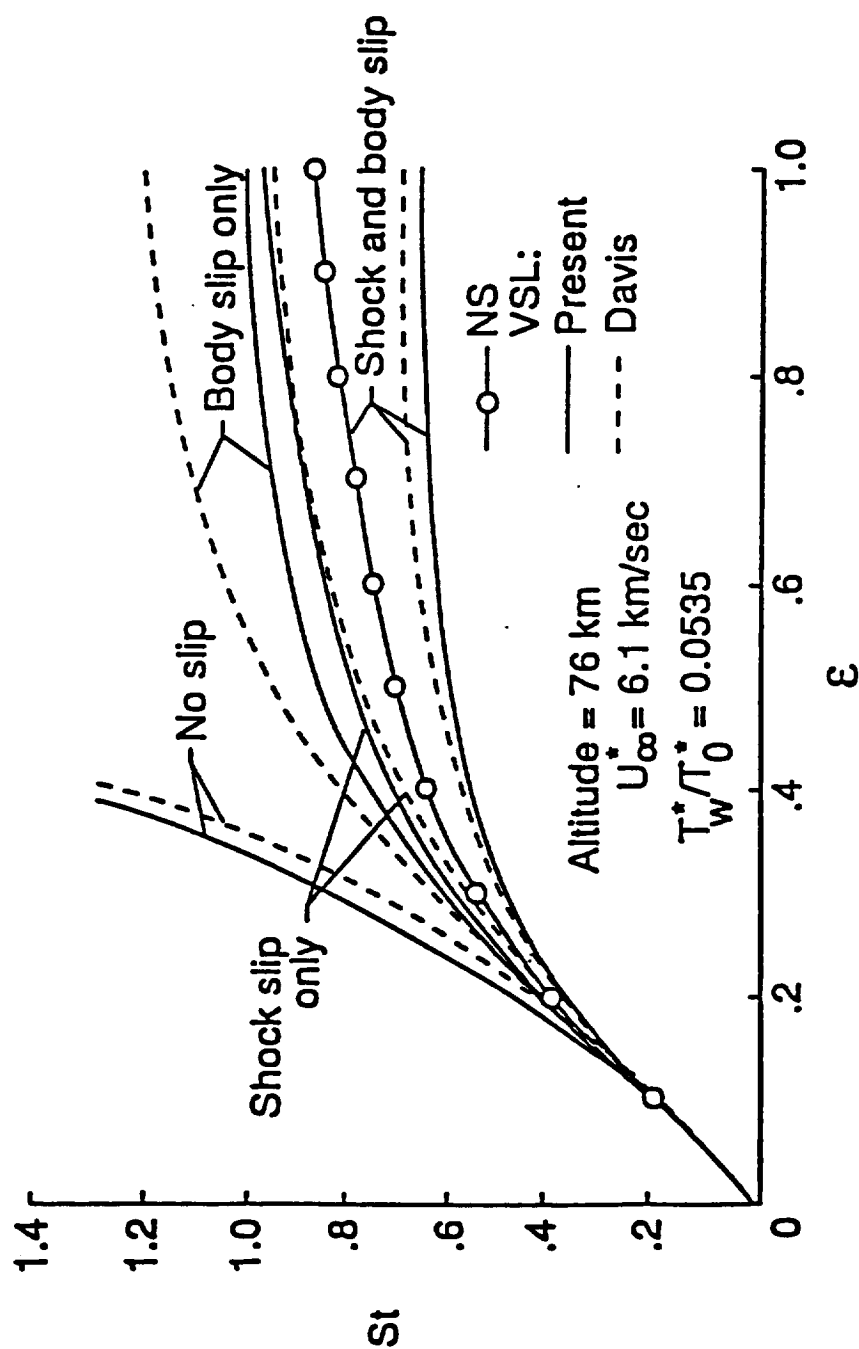
Fig. 4.8 Stanton number at the stagnation point of a 22.5° hyperboloid as a function of epsilon.
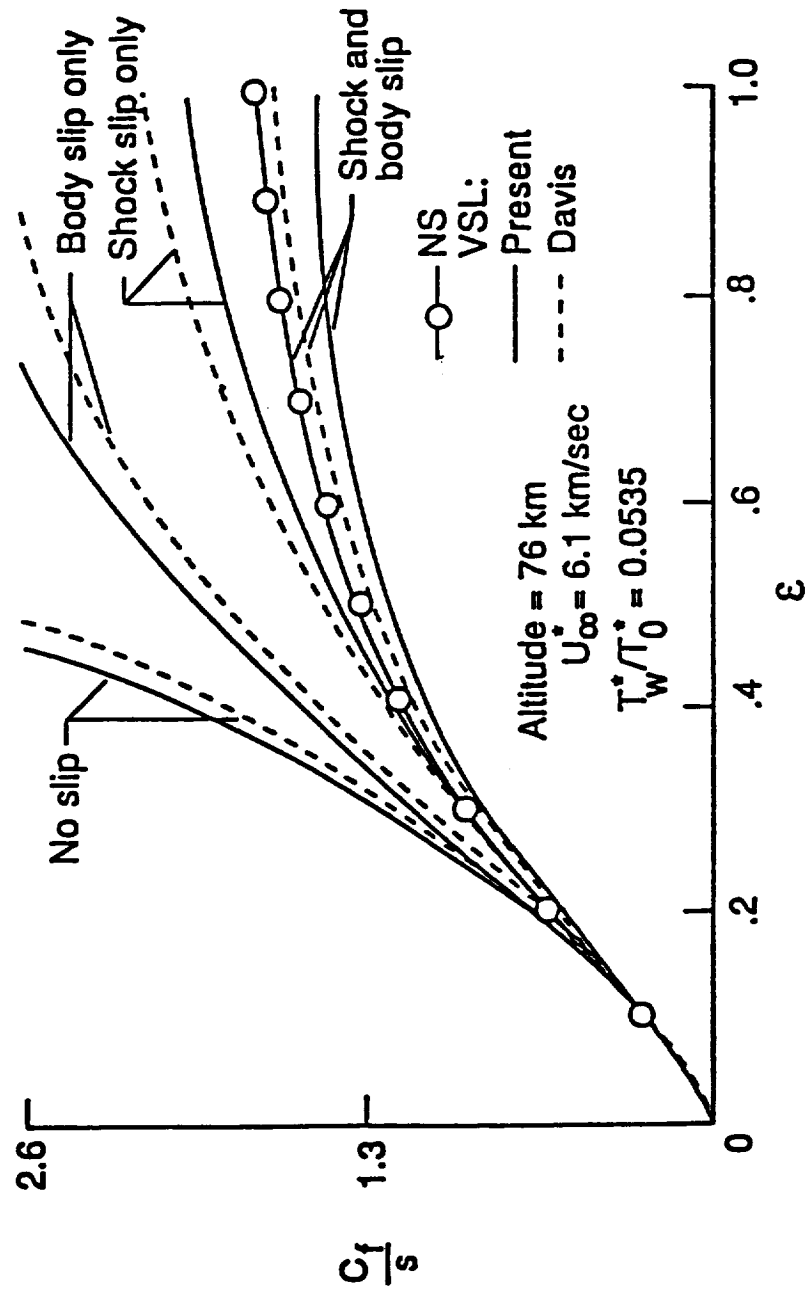
Fig. 4.9   Skin-friction coefficient at the stagnation point of a
22.5° hyperboloid as a function of epsilon.
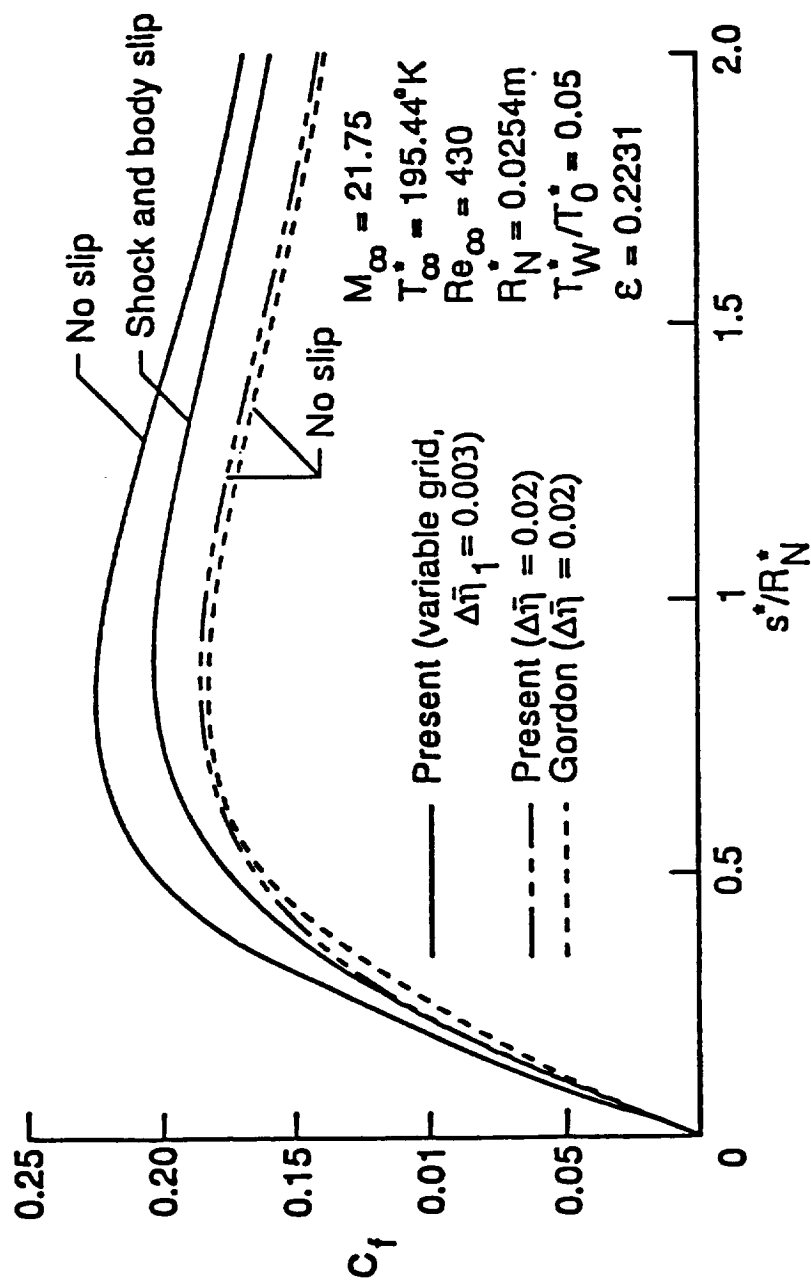
Fig. 4.10 Skin-friction coefficient distribution for a 22.5°
hyperboloid with ε = 0.223.
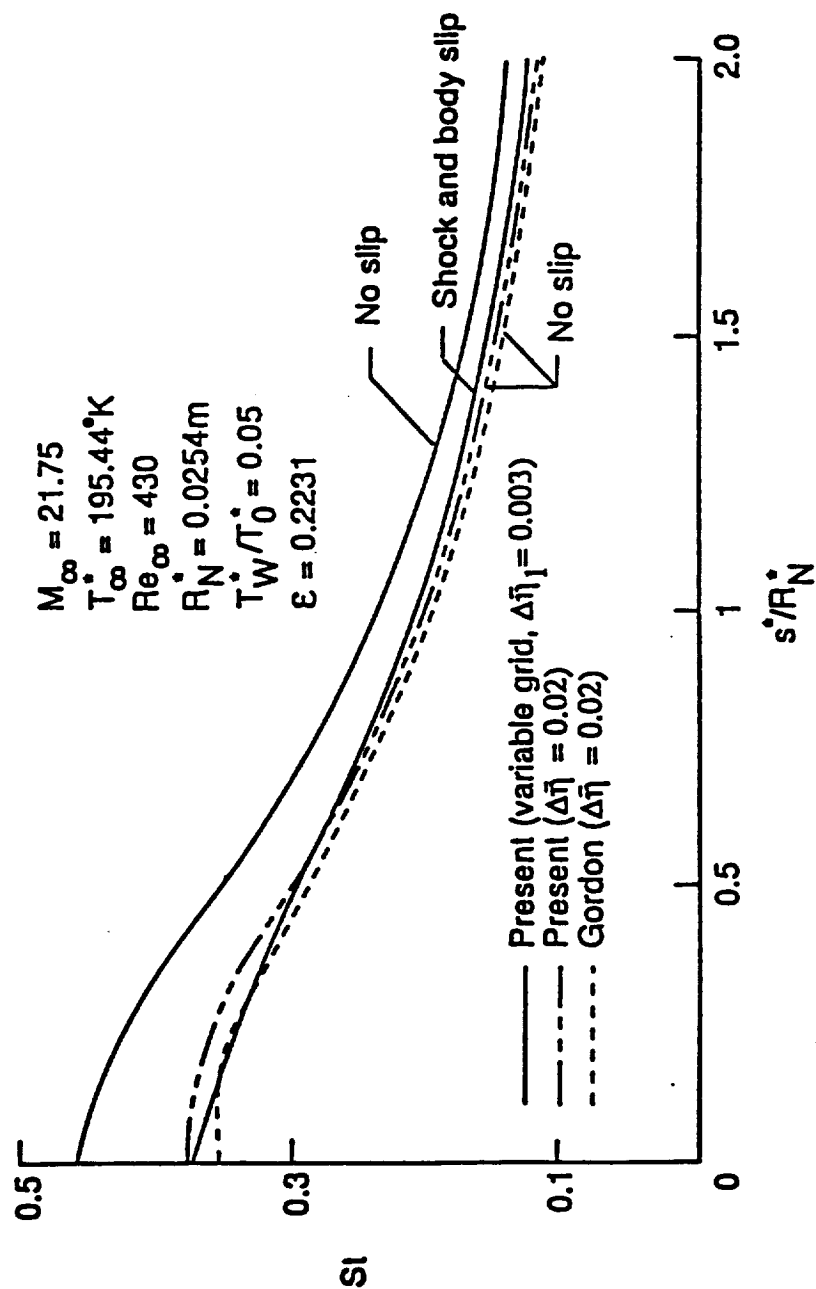
Fig. 4.11 Stanton number distribution for a 22.5° hyperboloid with ε = 0.223.

300 K), 2.54 cm nose radius, five and ten degree sphere cones. The free-stream conditions for very high-to-low altitude flight cases are given in Table 4.2. Figure 4.12 gives the Stanton number distribution for a 5° sphere-cone obtained by using the viscous shock-layer equations for different body locations. The slip effects become insignificant at body locations greater than about ninety nose-radii or at altitudes less than about 60 km for a wall temperature of 300 K. The Stanton number values with and without slip for a 10° sphere-cone as shown in Fig. 4.13 are higher than those for a 5° sphere-cone at the corresponding body locations for a given altitude except for the stagnation point (s = 0). At this location, the Stanton number values are almost the same for the 5° and 10° sphere-cones. Figures 4.12 and 4.13 also indicate that for a given altitude and body location, the slip effects are higher on the conical flank portion for a 5° sphere-cone than for a 10° sphere-cone. Further, the effect of slip increases with increasing altitude for a given cone angle and body location.

Figures 4.14 to 4.20 show the effect of surface temperature on stagnation-point pressure and heat-transfer coefficients. Both the viscous shock-layer and Navier-Stokes solutions are provided in these figures. The results presented in Figs. 4.14 to 4.17 show that the viscous shock-layer values of C_p with no slip gradually increase from a value of 1.84 at about 30.5 km altitude to a value of 1.88 at 100 km altitude. The value of C_p stays constant at 1.84 for an adiabatic wall. The viscous shock layer predictions for C_p with slip continuously decrease with increasing altitude for a cooled surface. This trend is

Table 4.2 Freestream conditions[+]

Altitude km	Density kg/m³	T_∞^*, K	U_∞^*, km/s	a_∞^*, m/s	Re_∞	c	$\lambda_\infty^{*\dagger}$, m	Kn_∞
15.24	1.876×10^{-1}	216.65	5.90	295.07	1977845	.0031	3.179×10^{-7}	1.252×10^{-5}
30.48	1.710×10^{-2}	226.98	6.04	302.03	177565	.0103	3.524×10^{-6}	1.388×10^{-4}
45.72	1.702×10^{-3}	267.07	6.55	327.61	16805	.0320	3.676×10^{-5}	1.447×10^{-3}
60.96	2.716×10^{-4}	253.89	6.39	319.42	2723	.0815	2.277×10^{-4}	8.964×10^{-3}
76.20	3.625×10^{-5}	195.46	5.61	280.26	396	.2231	1.606×10^{-3}	6.325×10^{-2}
83.82	9.885×10^{-6}	180.65	5.39	269.44	111	.4271	5.785×10^{-3}	2.278×10^{-1}
91.44	2.384×10^{-6}	184.94	5.45	272.64	27	.8698	2.412×10^{-2}	9.497×10^{-1}

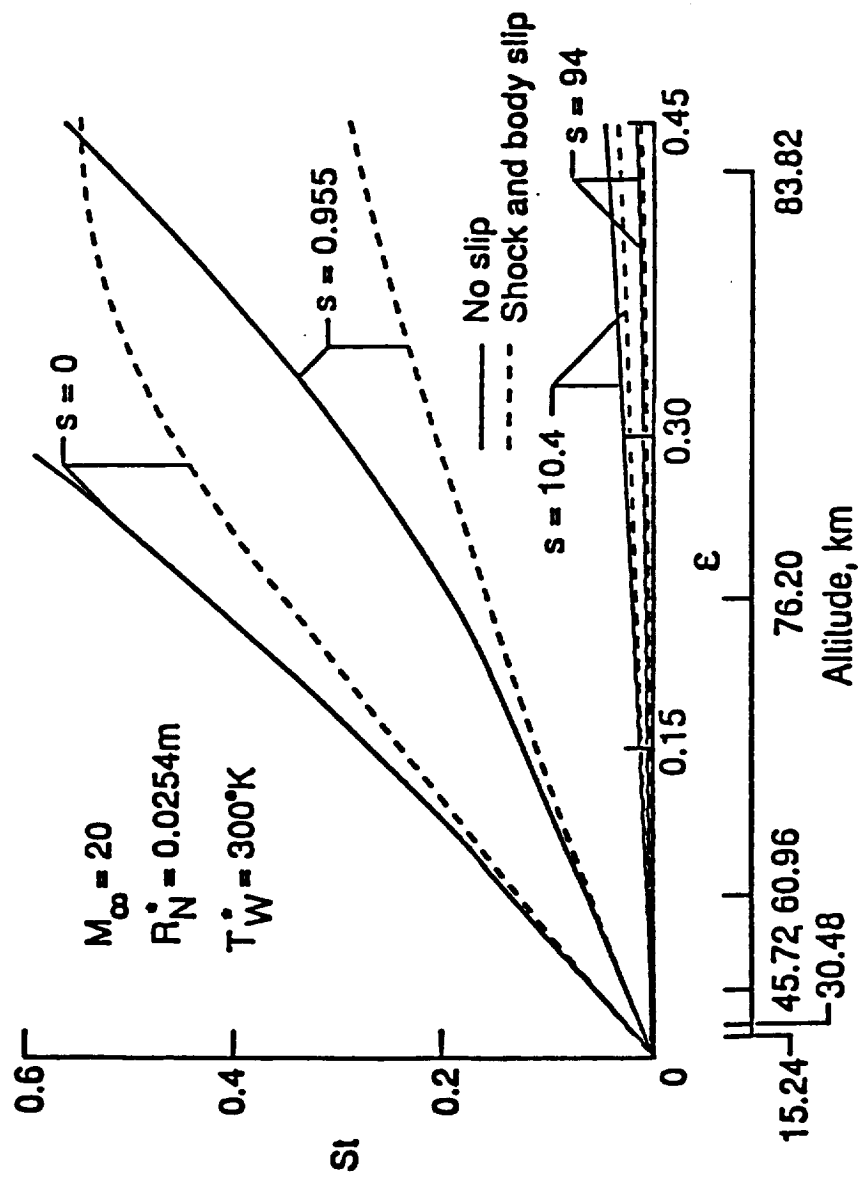† $R_N^* = 0.0254$ m, $T_W^* = 300$ K, $W^* = 28.96$ g/mole, $M_\infty = 20$, $S_\infty = 16.73$

Fig. 4.12 Stanton number distribution for a 5° sphere-cone as a function of epsilon.
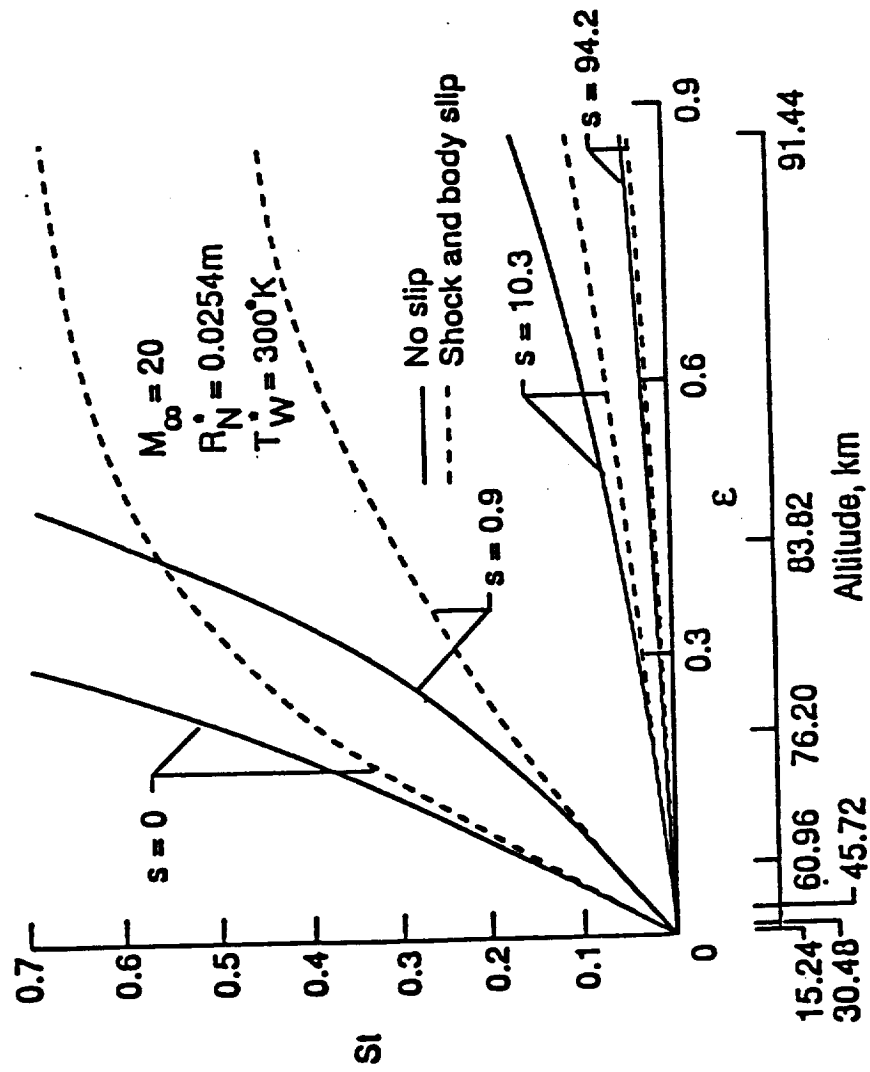
Fig. 4.13 Stanton number distribution for a 10° sphere-cone as a function of epsilon.

similar to the one given by the results of Davis [12]. This trend, however, indicates that viscous shock-layer results with slip do not approach the free molecule flow value at higher altitudes. The Navier-Stokes results with the body and shock slip do provide the right behavior of approaching the free molecule flow value at higher altitudes. These results, however, first show a decrease in the value of C_p and then an increase as the altitude increases further.

This behavior, also obtained by Jain and Adimurthy [66], is consistent with the trend observed by Potter and Bailey [67]. Good agreement between the Navier-Stokes results and the data of Potter and Bailey [67] was reported by Jain and Adimurthy [66]. As can be noticed from Figs. 4.14 to 4.17, the dip in the pressure coefficient curve is reduced by increasing the wall temperature. For an adiabatic surface (implying no temperature slip), there is no dip in the C_p curve, and it increases monotonically towards the free-molecule flow value with the increasing in the altitude. It may be mentioned here that the free-molecule flow value of C_p as well as its asymptotic value at lower altitudes is also influenced by the wall temperature. The free-molecule flow value is obtained from the equations of Bird's [46]. The predicted value of C_p from Navier-Stokes and viscous shock-layer solutions with slip approach the asymptotic value of 1.84, which is predicted by the inviscid modified Newtonian formulation, at lower altitudes with the increase in surface temperature. Obviously, this asymptotic value is obtained for a very high Reynolds number flow in absence of any slip effects. Reducing the slip effects by increasing the wall temperature also gives this asymptotic value at moderately high altitudes.

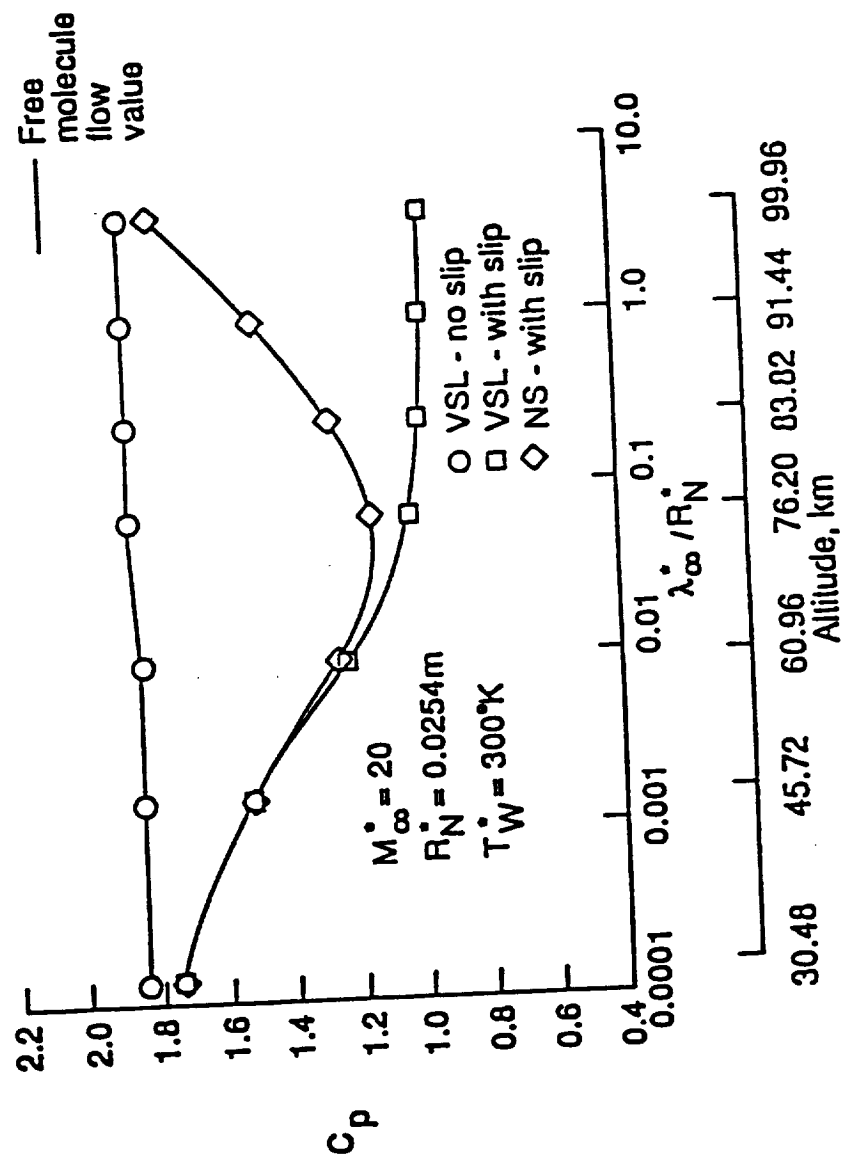
Fig. 4.14 Stagnation-point pressure coefficient for a 10° sphere-cone versus Knudsen number and altitude with $T_W^* = 300$ °K.
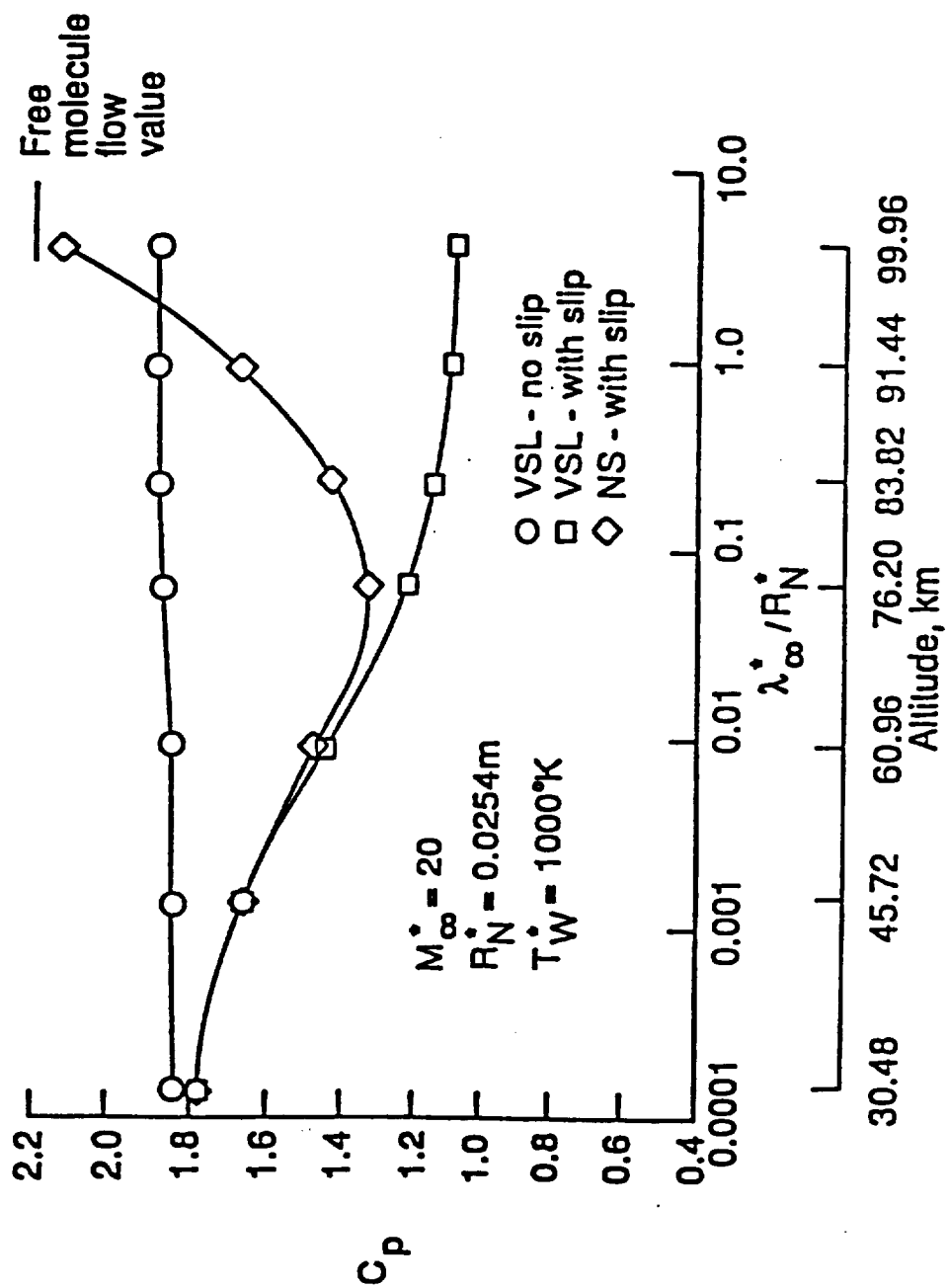
Fig. 4.15 Stagnation-point pressure coefficient for a 10°
sphere-cone versus Knudsen number and altitude
with $T_W^* = 1000$ °K.

Fig. 4.16 Stagnation-point pressure coefficient for a 10° sphere-cone versus Knudsen number and altitude with $T_W^* = 5000$ °K.
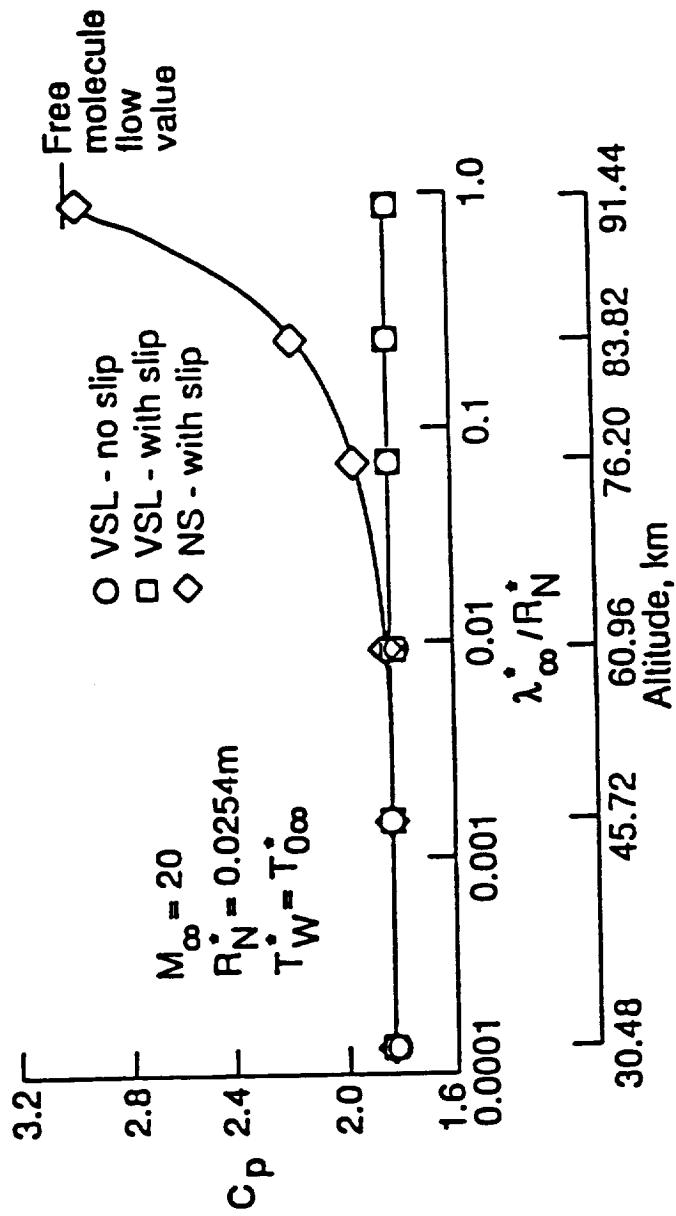
Fig. 4.17 Stagnation-point pressure coefficient for a 10° sphere-cone versus Knudsen number and altitude with $T_W^* = T_{aw}^*$.
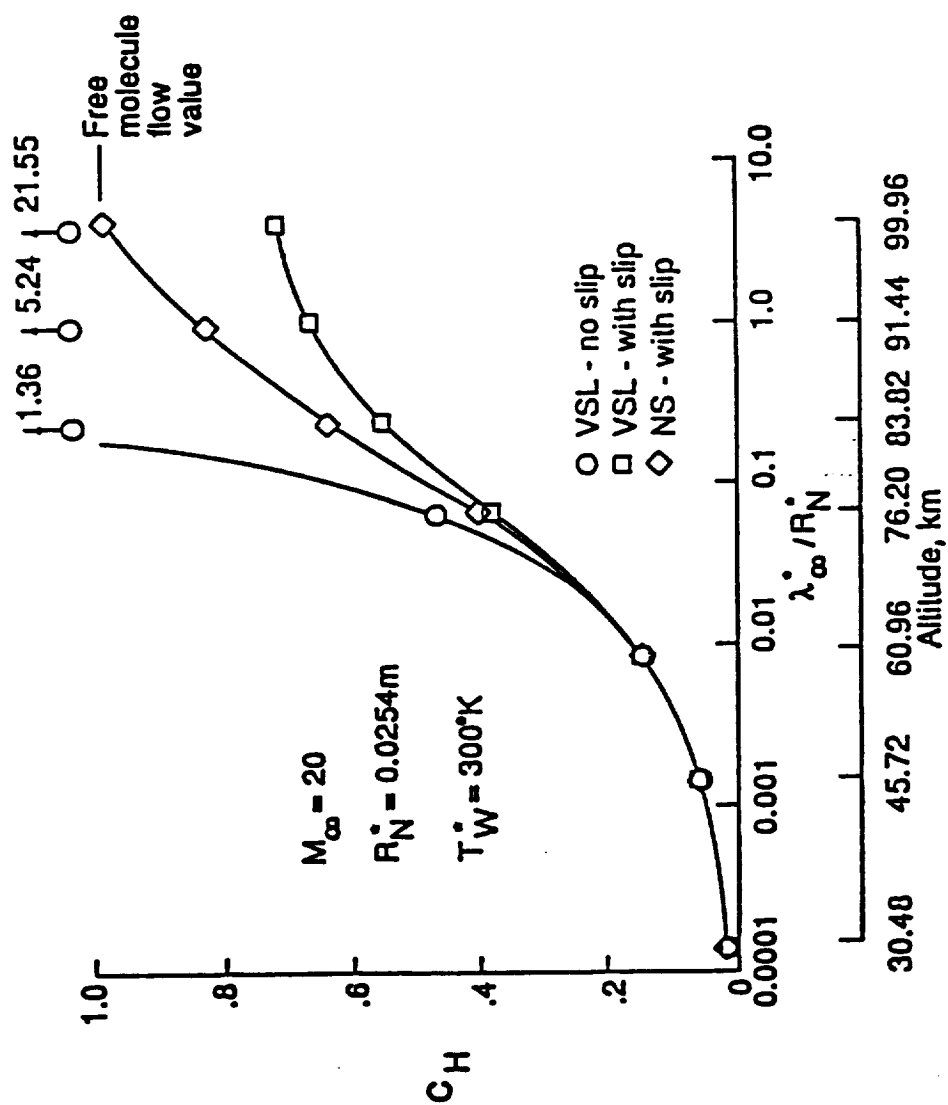
Fig. 4.18 Stagnation-point heat-transfer coefficient for a 10° sphere-cone versus Knudsen number and altitude with $T_W^* = 300$ °K.
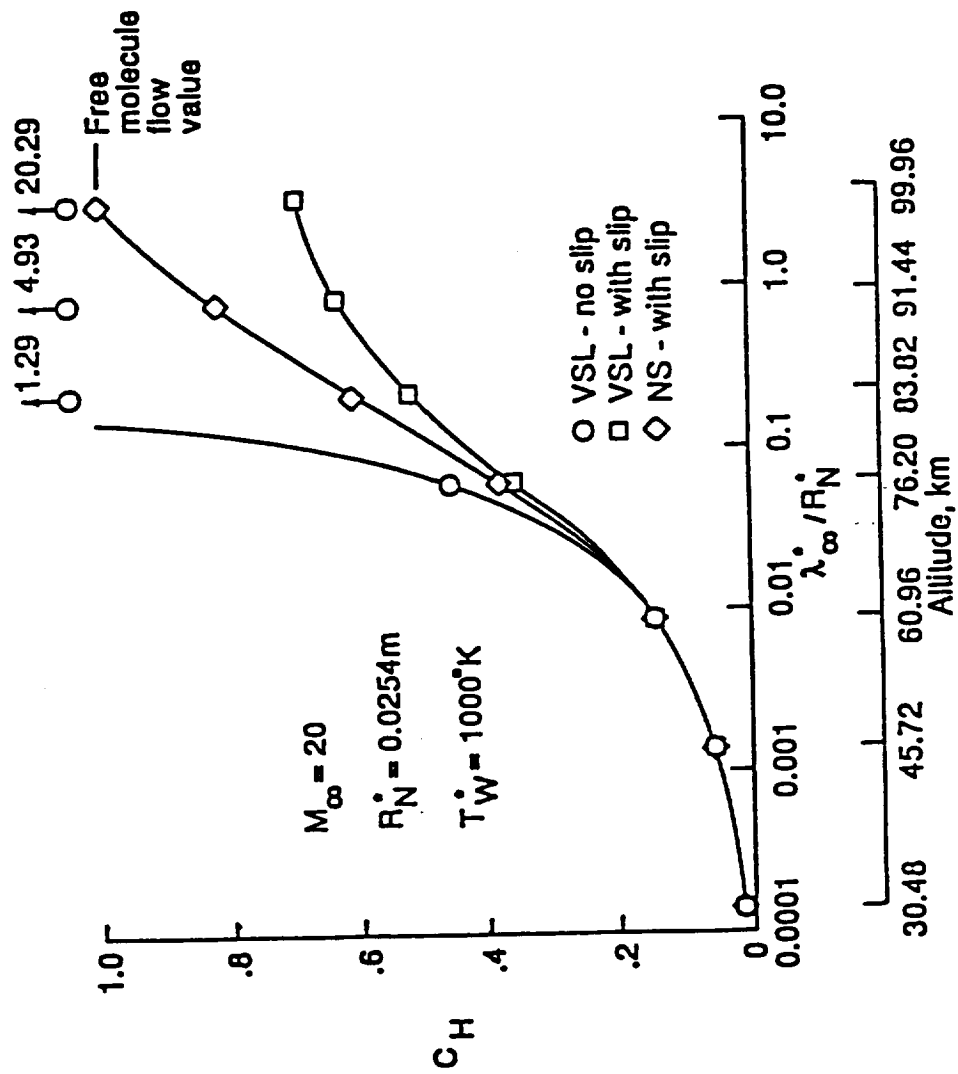
Fig. 4.19 Stagnation-point heat-transfer coefficient for a 10° sphere-cone versus Knudsen number and altitude with $T_W^* = 1000$ °K.

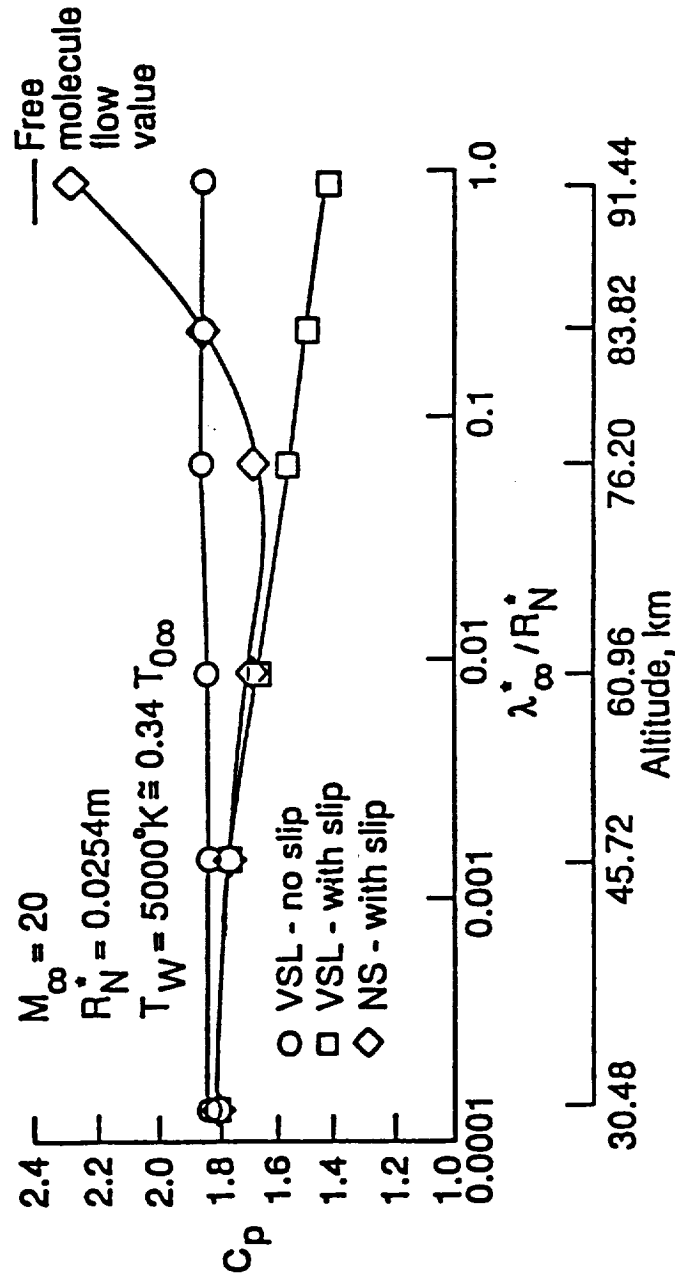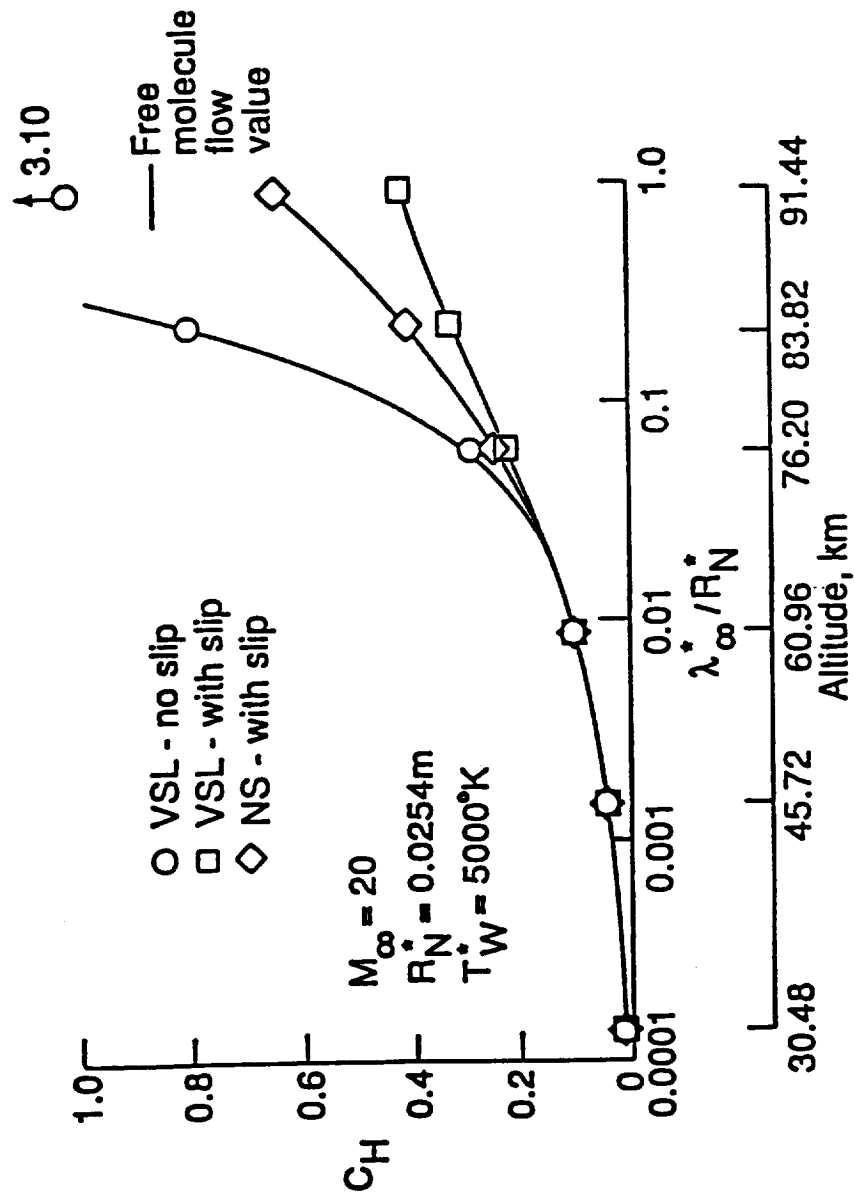Fig. 4.20   Stagnation-point heat-transfer coefficient for a 10° sphere-cone versus Knudsen number and altitude with $T_W^* = 5000$ °K.

The results for the stagnation-point heat transfer coefficient as
a function of the freestream Knudsen number (or altitude) are presented
in Figs. 4.18 to 4.20 for different surface temperatures. Results for a
given surface temperature show that the viscous shock-layer formulation
with or without slip does not give physically realistic results at very
high altitudes. The Navier-Stokes results with slip do approach the
free-molecule flow value of approximately unity at very high altitudes.
With an increase in surface temperature, the surface heat-transfer rate
is decreased as expected. The effect of slip is noticeable down to an
altitude of about 60 km for the various surface temperature considered
here. Discrepancies of less than ten percent are noticeable below
approximately 75 km altitude.

Results of Figs. 4.14 to 4.20 suggest that the viscous shock-layer
calculations with slip begin to deviate from the Navier-Stokes results
with slip for freestream Knudsen number $(\lambda_\infty^* / R_N^*)$ greater than about
0.06. For C_p, the deviation begins at $\lambda_\infty^* / R_N^* = 0.01$. It may not be
appropriate to use the viscous shock-layer model even with body and
shock slip at higher altitudes.

4.6 Conclusions

Results have been obtained for the surface pressure, drag, heat
transfer, and skin-friction coefficients for hyperboloids and sphere-
cone-shaped slender bodies under varying degrees of low-density flow
conditions. Recently obtained surface-slip and corrected shock-slip
conditions are employed to account for the low-density effects. The
method of solution used for the viscous shock-layer equations is a

partially coupled spatial-marching implicit finite-difference technique. The flow cases analyzed include highly cooled surfaces in very high Mach number flows. The viscous shock-layer predictions compare quite favorably with experimental data. Results are also obtained from the steady-state Navier-Stokes equations by successive approximations by using the viscous shock-layer results to evaluate higher order terms for the first approximation. Comparison between the Navier-Stokes and viscous shock-layer results indicates that viscous shock-layer equations even with body and shock slip do not give physically consistent results in the stagnation region above approximately 75 km altitude for the conditions considered in this study.

Chapter 5

CHEMICAL NONEQUILIBRIUM FLOWS

5.1 Introduction

One of dominant aspect of hypersonic flow is high-temperature effects. Strong compression of the gas forward of the vehicle and heat generation due to viscous dissipation lead to increase gas temperature in the shock layer. At high temperature, the gas will become chemically reacting. The specific heat per unit mass is considerably increased, the specific heat ratio will no longer equal to 1.4 and will no longer be a constant. The assumption of a calorically perfect gas is not appropriate; the effects of chemical reactions must be taken into account.

From the example of atmospheric entry of the Apollo command vehicle given by Anderson [68], the shock layer temperature predicted on the basis of an equilibrium chemically reacting gas is a factor of 5 less than the temperature predicted on the basis of a calorically perfect, nonreacting gas which gives an unrealistically high value of temperature in a high Mach number flow. Two major physical characteristics which cause a high-temperature gas to deviate from calorically perfect gas behavior, as stated in [68], are vibrational excitation and chemical reactions.

All chemical processes take place by molecular collisions. As the temperature of the gas is increased, and hence the molecular collisions

become more violent, it is probable that the diatomic molecules of oxygen, O_2, and nitrogen, N_2, will be dissociated and nitric oxide, NO, will be formed or dissociated by collisions with other particles. In turn, collisions take time to occur. Hence, the chemical changes in a gas require a finite time to occur. Equilibrium flows assume that the gas has had enough time for the necessary collisions to occur. However, there are some flight conditions frequently encountered in atmospheric entry where the gas is not given the necessary time to come to a state of equilibrium. Under these conditions, flows are characterized by a chemical nonequilibrium process in the shock layer. The experimental wall temperature measurements and resulting heat-transfer rates obtained during the first flights of the Space Shuttle have been lower than the predicted equilibrium values at least over the first 40 percent of the Shuttle length and for much of the altitude range of interest [69-72]. The flight data from the Catalytic Surface Experiment [71,73] have verified that the lower rates can be attributed primarily to the fairly noncatalytic nature of the Shuttle thermal protection system and not to the unknowns in the freestream or flowfield quantities, and that the nonequilibrium effects persist to altitudes as low as 50 km for the orbiter.

Although measurement data can be obtained from the Space Shuttle flights, it is very expensive for each flight. Moreover, a small scale laboratory experiment cannot simulate the chemical nonequilibrium flow around a hypersonic vehicle. An adequate design capability for future transportation systems relies on numerical predictions. Among the numerical methods available for solving the nonequilibrium flow over a

hypersonic vehicle, the viscous shock-layer approach not only has the advantage of requiring much less computing cost as compared to the Navier-Stokes solutions, but it also provides accurate predictions. This method has been used widely as a tool for engineering calculations [24,60,61,72,74,75].

The viscous shock-layer equations for a perfect gas and for a chemically reacting binary mixture were developed by Davis [12,56]. Based on this analysis, Moss [24] developed a code using the viscous-shock-layer equations for a multicomponent gas mixture with chemical equilibrium or nonequilibrium. It is shown that accurate results can be obtained by this nonequilibrium code [24,72,74,76,77]. However, the difficulties encountered in the case of a perfect gas are also encountered in the nonequilibrium flow over a slender long body.

Appropriate shock and wall boundary conditions must be prescribed for the viscous shock-layer equations for chemically reacting flows. In addition to surface temperature and velocity, wall species concentrations are needed. However, the surface heating rate in a hypersonic nonequilibrium flow environment is strongly affected by the surface catalytic activity (the recombination of the dissociated oxygen and nitrogen atoms). For a dissociated nonequilibrium flow over a finite-catalytic wall, the heating rate and the wall species concentration is a function of the surface reaction rate coefficient (or energy-transfer recombination coefficient) [78]. The temperature-dependent and constant values of the coefficients for oxygen and nitrogen surface recombination have been determined by Scott [79]. These values have been incorporated in the viscous-shock-layer code available in [72]; however, the resulting heating predictions are only

in fair agreement with the STS-2 experimental data. Based on STS-2 data, a new oxygen reaction rate expression has been developed by Zoby et al. [77], and it has been shown that a better heating comparison with experimental data can be obtained [75,77].

Thermodynamic properties and transport properties are required for each species considered in a multicomponent gas mixtures. All these properties are obtained from the polynomial curve-fit formulas based on measured data. Measurements made on the Orbiter during reentry have provided an extensive and reliable data base to improve these relations.

The primary objective of this study is to investigate the effects of chemical nonequilibrium conditions in hypersonic flows over long slender bodies. For this, modifications in the existing code by Moss [24] are needed. The modifications included are:(1) the two first order equations, continuity and normal momentum, are solved simultaneously as a coupled set, and (2) the thermodynamic and transport curve fit relations are modified. The effects of different wall recombination coefficients on the predicted heat transfer are investigated. Also, this chapter includes a parametric study on the effects of body-angle, nose radius, and Mach number.

5.2 Analysis

The conservation equations that describe a reacting multicomponent gas mixture can be found in the literature [27,28]. The viscous shock-layer equations for nonequilibrium multicomponent gas mixture developed by Moss [24] are obtained from the conservation equations employing the same procedure as for the perfect gas [12]. For a blunt axisymmetric

body at zero angle of attack, the global continuity, s-momentum, and n-momentum equations in the orthogonal, body-oriented transformed coordinates and in nondimensional form are written in the same form as Eqs. (2.25) through (2.29), (2.35) and (2.36) except the eddy viscosity, ε^+, is set to zero. For a chemical nonequilibrium flow, the energy equation is formulated in terms of the temperature instead of total enthalpy. In addition to these conservation equations, the species continuity equation and equation of state are needed to complete the set of equations. The energy and species continuity equations in the computational plane are written in the form of Eq. (2.25). The W in this equation represents T for the energy equation and C_i for the species continuity equation. The coefficients α_1 to α_4, Eqs. (2.42) to (2.49), are given here again by

Energy, W = T:

$$\alpha_1 = \frac{1}{\kappa}\frac{\partial\kappa}{\partial\eta}\frac{dg}{d\overline{\eta}} + \frac{n_{sh}\kappa}{1+\overline{\eta}n_{sh}\kappa} + \frac{jn_{sh}\cos\theta}{r+\overline{\eta}n_{sh}\cos\theta} - \frac{n_{sh}}{\kappa}\sum_{i=1}^{N_s}J_iC_{p,i}$$

$$+ \frac{n_{sh}n'_{sh}\rho C_p u\overline{\eta}}{\varepsilon^2\kappa(1+\overline{\eta}n_{sh}\kappa)} - \frac{n_{sh}\rho C_p v}{\varepsilon^2\kappa} \qquad (5.1)$$

$$\alpha_2 = 0 \qquad (5.2)$$

$$\alpha_3 = \frac{n_{sh}^2\mu}{\kappa}\left(\frac{1}{n_{sh}}\frac{\partial u}{\partial\eta}\frac{dg}{d\overline{\eta}} - \frac{\kappa u}{1+\overline{\eta}n_{sh}\kappa}\right)^2 - \frac{n_{sh}^2\overline{\eta}}{\varepsilon^2\kappa}\sum_{i=1}^{N_s}h_i\dot{w}_i$$

$$+ \frac{un_{sh}^2}{\varepsilon^2 \kappa (1+\bar{\eta} n_{sh}\kappa)} \frac{\partial p}{\partial \xi} - \frac{n_{sh}^2}{\varepsilon^2 \kappa} \left(\frac{u}{1+\bar{\eta} n_{sh}\kappa} \frac{n_{sh}'\bar{\eta}}{n_{sh}} - \frac{v}{n_{sh}} \right) \frac{dg}{d\bar{\eta}} \frac{\partial p}{\partial \eta} \quad (5.3)$$

$$\alpha_4 = - \frac{n_{sh}^2 \rho C_p u}{\varepsilon^2 \kappa (1+\bar{\eta} n_{sh}\kappa)} \quad (5.4)$$

Species continuity, $W = C_i$:

$$\alpha_1 = \frac{1}{PL_i} \frac{\partial PL_i}{\partial \eta} \frac{dg}{d\bar{\eta}} + \left(\frac{n_{sh}\kappa}{1+\bar{\eta} n_{sh}\kappa} + \frac{n_{sh}\cos\theta}{r+\bar{\eta} n_{sh}\cos\theta} \right)$$

$$+ \frac{n_{sh} n_{sh}'\bar{\eta} \rho u}{\varepsilon^2 PL_i (1+\bar{\eta} n_{sh}\kappa)} - \frac{n_{sh}\rho v}{\varepsilon^2 PL_i} \quad (5.5)$$

$$\alpha_2 = 0 \quad (5.6)$$

$$\alpha_3 = \frac{1}{PL_i} \frac{\partial PM_i}{\partial \eta} \frac{dg}{d\bar{\eta}} + \frac{PM_i}{PL_i} \left(\frac{n_{sh}\kappa}{1+\bar{\eta} n_{sh}\kappa} + \frac{n_{sh}\cos\theta}{r+\bar{\eta} n_{sh}\cos\theta} \right) + \frac{\dot{w}_i n_{sh}^2}{\varepsilon^2 PL_i} \quad (5.7)$$

$$\alpha_4 = - \frac{n_{sh}^2 \rho u}{\varepsilon^2 PL_i (1+\bar{\eta} n_{sh}\kappa)} \quad (5.8)$$

where

$$PL_i = \frac{\mu}{Pr} \Delta b_{ii} \quad (5.9)$$

$$PM_i = \frac{\mu}{Pr} \sum_{\substack{k=1 \\ k \neq i}}^{N_s} \Delta b_{ik} \frac{\partial C_k}{\partial \eta} \frac{dg}{d\bar{\eta}}$$ (5.10)

$$\Delta b_{ik} = \begin{cases} Le,_i & i=k \\ \\ Le,_i - [\frac{M_i^*}{\overline{M}^*} Le,_{ik} + (1 - \frac{M_i^*}{M_k^*}) \sum_{\substack{j=1 \\ j \neq i}}^{N_s} Le,_{ij} C_j] & i \neq k \end{cases}$$ (5.11)

In Eq. (5.11), $Le,_{ik}$ are the multicomponent Lewis numbers and $\overline{M}^*$ is

molecular weight which is given by

$$\overline{M}^* = \frac{1}{\sum_{i=1}^{N_s} \frac{C_i}{M_i^*}}$$ (5.12)

The mass flux, J_i, due to concentration gradients can be written as [29]

$$J_i = \frac{\mu}{n_{sh} Pr} \sum_{k=1}^{N_s} \Delta b_{ik} \frac{\partial C_k}{\partial \eta} \frac{dg}{d\bar{\eta}}$$ (5.13)

The equation of state is given by

$$p = \rho T R^* / \overline{M}^* C_{p,\infty}^*$$ (5.14)

The term $\dot{w}_i$ which appears in the energy and species continuity

equations represents the rate of production of species i due to chemical

reactions. As discussed by Blottner [6,29] and Davis [56], the way of the production terms are written is very important in achieving convergence of the iteration procedure. Consequently, for the energy equation, the production terms are written as [56]

$$(\frac{\dot{w}_i}{\rho})_{k+1} = (\frac{\dot{w}_i}{\rho})_k + \frac{\partial}{\partial T} (\frac{\dot{w}_i}{\rho})_k (T_{k+1} - T_k) \qquad (5.15)$$

where k denotes the iteration for which the solution is known and k+1 the iteration for which a solution is required. It is found that if an expression of this type is not used which allows T to appear as an unknown in the energy equation, the method will not converge at low altitude conditions where the gas is approaching equilibrium conditions [29]. The term $\sum_{i=1}^{N_s} h_i \dot{w}_i$ which appears in the energy equation, Eq. (5.3), is written as follows:

$$\sum_{i=1}^{N_s} h_i \dot{w}_i = \overline{\dot{w}}_1 + T\overline{\dot{w}}_2 \qquad (5.16)$$

As for the species continuity equations, the production term is written as

$$\frac{\dot{w}_i}{\rho} = \dot{w}_i^0 - C_i \dot{w}_i^1 \qquad (5.17)$$

Hence, Eqs. (5.15) and (5.17) express the production terms as a function of temperature for the energy equation and in terms of the species mass fraction for the species equations.

5.3 Boundary Conditions

At the wall, the no-slip and no-temperature-jump boundary conditions are used in this study. No mass injection is considered, the normal component of velocity at the surface is taken to be zero. Also, the surface total enthalpy is given as

$$\bar{H} = \sum_{i=1}^{N_S} h_i C_i \tag{5.18}$$

For a nonequilibrium flow, the wall species concentration is dictated by the catalytic recombination rate k_w^* in the recombination equation which is given by

$$\frac{\partial C_i}{\partial \eta} \frac{dg}{d\bar{\eta}} - \frac{k_{w,i} \rho P_r^n sh}{Le \, \mu \, \epsilon^2} C_i = 0 \tag{5.19}$$

where $k_{w,i} = k_{w,i}^* / U_\infty^*$. The catalytic recombination rate is determined from the catalytic recombination coefficient (or catalytic efficiency) γ_i by [78]

$$\gamma_i = \sqrt{\frac{2\pi M_i^*}{R^* T^*}} \, k_{w,i}^* \tag{5.20}$$

For a noncatalytic wall, the catalytic recombination rate of atoms is

equal to zero [31]; hence, Eq. (5.19) becomes

$$(\frac{\partial C_i}{\partial \eta})_w = 0 \tag{5.21}$$

for all the species of a multicomponent mixture. For a fully catalytic wall, the catalytic recombination rate of each atom is equal to one [31].

For a finite rate catalytic wall, the recombination coefficient for oxygen and nitrogen based on arcjet experimental heat-transfer data were determined by Scott [79] such as

$$\gamma_0 = 16.0 \ e^{-10271/T_w^*} \tag{5.22}$$

and

$$\gamma_N = 0.071 \ e^{-2219/T_w^*} \tag{5.23}$$

However, it has been noticed that the resulting heating predictions are only in fair agreement with the STS-2 experimental data by incorporating these coefficients [72,75]. Zoby et al. [77] developed a recombination coefficient for oxygen based on experimental flight, STS-2, heat-transfer data. It is given by

$$\gamma_0 = 0.00941 \ e^{-658.9/T_w^*} \tag{5.24}$$

Boundary conditions immediately behind the shock are calculated by using the Rankine-Hugoniot relations. The nondimensional shock

relations are the same as Eqs. (3.21) to (3.23) and include

Energy:

$$h_{sh} = h_{\infty} + \frac{\sin^2\alpha}{2}\left(1 - \frac{1}{\rho_{sh}^2}\right) \tag{5.25}$$

State:

$$p_{sh} = \rho_{sh}T_{sh}\left(\frac{R^*}{M_{sh}^* C_{p,\infty}^*}\right) \tag{5.26}$$

Enthalpy:

$$h_{sh} = \sum_{i=1}^{N_S} h_{i,sh}\, C_{i,sh} \tag{5.27}$$

The chemistry across the shock wave is assumed to be frozen.

5.4 Chemical Composition

In this study, the chemical reaction is confined to a system of neutral air species (O, O_2, N, N_2 and NO). When chemical reactions proceed at a finite rate, the rate of production terms $\dot{w}_i$ are required. For a multicomponent gas with N_s reacting chemical species and N_r chemical reactions, the chemical equation describing the overall change from reactants to products may be written in the general form
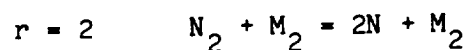
$$\sum_{i=1}^{N_j} \alpha_{i,r} X_i^* \underset{K_{b,r}^*}{\overset{K_{f,r}^*}{\underset{\longleftarrow}{\longrightarrow}}} \sum_{i=1}^{N_j} \beta_{i,r} X_i^* \tag{5.28}$$

where $r = 1, 2, \ldots, N_r$ and N_j is equal to the sum of the reacting species (N_s) plus the number of catalytic bodies. The quantities $\alpha_{i,r}$ and $\beta_{i,r}$ are the stoichiometric coefficients for reactants and products, respectively, whereas $K^*_{f,r}$ and $K^*_{b,r}$ are the forward and backward rate constants. The quantities X^*_i denote the concentrations in moles per unit volume. The rate of change of any species as a result of a particular reaction is [80]

$$\left(\frac{dX^*_i}{dt^*}\right)_r = (\beta_{i,r} - \alpha_{i,r})\, (K^*_{f,r} \prod_{j=1}^{N_j} X^{*\alpha_{j,r}}_j$$

$$- K^*_{b,r} \prod_{j=1}^{N_j} X^{*\beta_{j,r}}_j) \tag{5.29}$$

In order to find the net mass rate of production of the ith species per unit volume, Eq. (5.29) must be summed over all reactions r. Thus, the rate of production of chemical species, $\dot{w}^*_i$, can be expressed as

$$\dot{w}^*_i = M^*_i \sum_{r=1}^{N_r} \left(\frac{dX^*_i}{dt^*}\right)_r \tag{5.30}$$

The chemical reactions used in this study are as follows:

$r = 1 \qquad O_2 + M_1 = 2O + M_1$

$r = 2 \qquad N_2 + M_2 = 2N + M_2$

$$r = 3 \qquad N_2 + N = 2N + N$$

$$r = 4 \qquad NO + M_3 = N + O + M_3$$

$$r = 5 \qquad NO + O = O_2 + N$$

$$r = 6 \qquad N_2 + O = NO + N$$
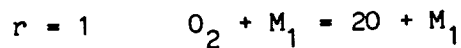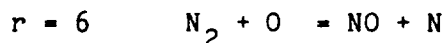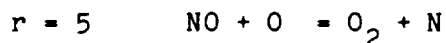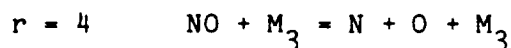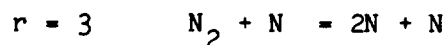
where M_1, M_2 and M_3 are the catalytic third bodies [6]. The reaction constants for these equations are expressed in the modified Arrhenius form, where the forward rate is given as

$$K^*_{f,r} = T^{*C2^*_r} \exp\left(\log_e CO_r - \frac{C^*_r \times 10^3}{T^*}\right), \frac{1}{s} \left(\frac{mole}{cm^3}\right)^{-\alpha_r} \qquad (4.31)$$

and the backward rate is given as

$$K^*_{b,r} = T^{*D2^*_r} \exp\left(\log_e DO_r - \frac{D1^*_r \times 10^3}{T^*}\right), \frac{1}{s} \left(\frac{mole}{cm^3}\right)^{-\beta_r} \qquad (5.32)$$

where

$$\alpha_r = \sum_{i=1}^{N_j} \alpha_{i,r} - 1 \qquad (5.33)$$

and

$$\beta_r = \sum_{i=1}^{N_j} \beta_{i,r} - 1 \qquad (5.34)$$

The values for the coefficients in Eqs. (5.31) and (5.32) are taken from the compilation of experimentally determined rate constants given by Blottner et al. [81]. For a specified temperature, density, and species composition, Eqs. (5.29) to (5.32) are used to determine the production rate of a multicomponent gas.

5.5 Thermodynamic and Transport Properties

The thermodynamic properties $C_{p,i}$ and h_i and the transport properties μ_i, K_i and D_{ij} are required for each species considered.

Since the multicomponent gas mixtures are considered to be mixtures of thermally perfect gases, the thermodynamic and transport properties for each species are calculated by using the local temperature and pressure. Then the mixture properties are determined in terms of the individual species properties.

5.5.1 Thermodynamic Properties

Values for the thermodynamic properties as a function of temperature are obtained by using polynomial curve fits for each chemical species. The following polynomial equations are used:

Specific Heat

$$\frac{C_{p,i}^*}{R^*} = a_1 + a_2 T^* + a_3 T^{*2} + a_4 T^{*3} + a_5 T^{*4} \tag{5.35}$$

Enthalpy

$$\frac{h_i^*}{R^* T^*} = a_1 + \frac{a_2 T^*}{2} + \frac{a_3 T^{*2}}{3} + \frac{a_4 T^{*3}}{4} + \frac{a_5 T^{*4}}{5} + \frac{a_6}{T^*} \tag{5.36}$$

The development of these curve fits and a tabulation of the polynomial constant (a_1 to a_7) are presented in [82]. These curve-fit formulas are tabulated up to 15,000 K. However, there are many flow conditions where the temperatures in the shock layer are much higher than 15,000 K. Hence, these curve fit formulas have been extended to a temperature range of up to 35,000 K by Shinn [83] based on the tabulated values given by Browne [84,85].

5.5.2 Transport Properties

Transport properties for viscosity and thermal conductivity are required for each species considered in the shock layer gas. These properties are obtained by using polynomial curve fits to the data of Esch et al. [86]. The mixture viscosity is obtained by using the semiempirical formula of Wilke [27]. The mixture thermal conductivity is obtained by a method analogous to that used for viscosity [24]. A binary diffusion model with Lewis number equal to 1.4 is used.

In addition, the transport properties of the individual species are also obtained from the polynomial curve-fits in temperature to the values given by Yos [87]. These data are believed to be more accurate at the higher temperatures which are encountered in nonequilibrium calculations. With these individual species properties, transport properties for the gas mixture are obtained by using the methods of Armaly and Sutton [88] for viscosity and Mason and Saxena [89] for thermal conductivity.

5.6 Method of Solution

The method of solution is essentially the same as that used for solving the viscous shock-layer equations for one component perfect gas. The solution for the multicomponent gas mixture proceeds in exactly the same way as given in Chap. 3 for the one component gas except a species equation is included now.

Three second-order equations, species continuity, s-momentum and energy, are replaced with central differences in the η-direction and two-point backward differences in the ξ-direction. The two first-order equations, continuity and n-momentum, are solved simultaneously. The

density in these two equations are replaced by Eq. (5.14). Then these two equations can be written in the same forms as Eqs. (3.60) to (3.63). The coefficients for a multicomponent gas mixture in these equations are given in Appendix A. All these equations along with the boundary conditions constitute a system of the tridiagonal form such as Eqs. (3.53), (3.64) and (3.65). The shock stand-off distance is evaluated by integrating the continuity equation and density is obtained from the equation of state.

For specified free-stream conditions and body geometry, a stagnation streamline solution is obtained. With the stagnation streamline solution providing the initial conditions, the conditions at the shock providing the outer boundary conditions, and the conditions at the wall taken as the inner boundary conditions, the numerical solution is marched downstream to the desired body location ξ. At any body station m, the converged profiles at station m-1 are used as the initial guess for the profiles at station m. The solution is then iterated locally until convergence is achieved. The solution is advanced subsequently to the m+1 station. Figure 5.1 presents the procedure for solving the governing equations for any location m.

5.7 Results and Discussions

Numerical solution to the previously discussed viscous shock-layer equations with chemical nonequilibrium are presented and discussed. First, comparisons of present results are made with data of STS-2 [90] to investigate the effects of modifications of the chemical nonequilibrium code and the heating effects of different finite-rate oxygen surface recombination expressions. Second, results of three

Shock solution at station m

Initial guess for all profile quantities

Solve species continuity for C_i

Solve energy equation for T

Solve equation of state for ρ

Thermodynamic and transport properties

Solve s-momentum equation for u

Solve continuity equation for n_{sh}

Solve continuity and n-momentum equation simultaneously for v and p

Solve equation of state for ρ

Convergence
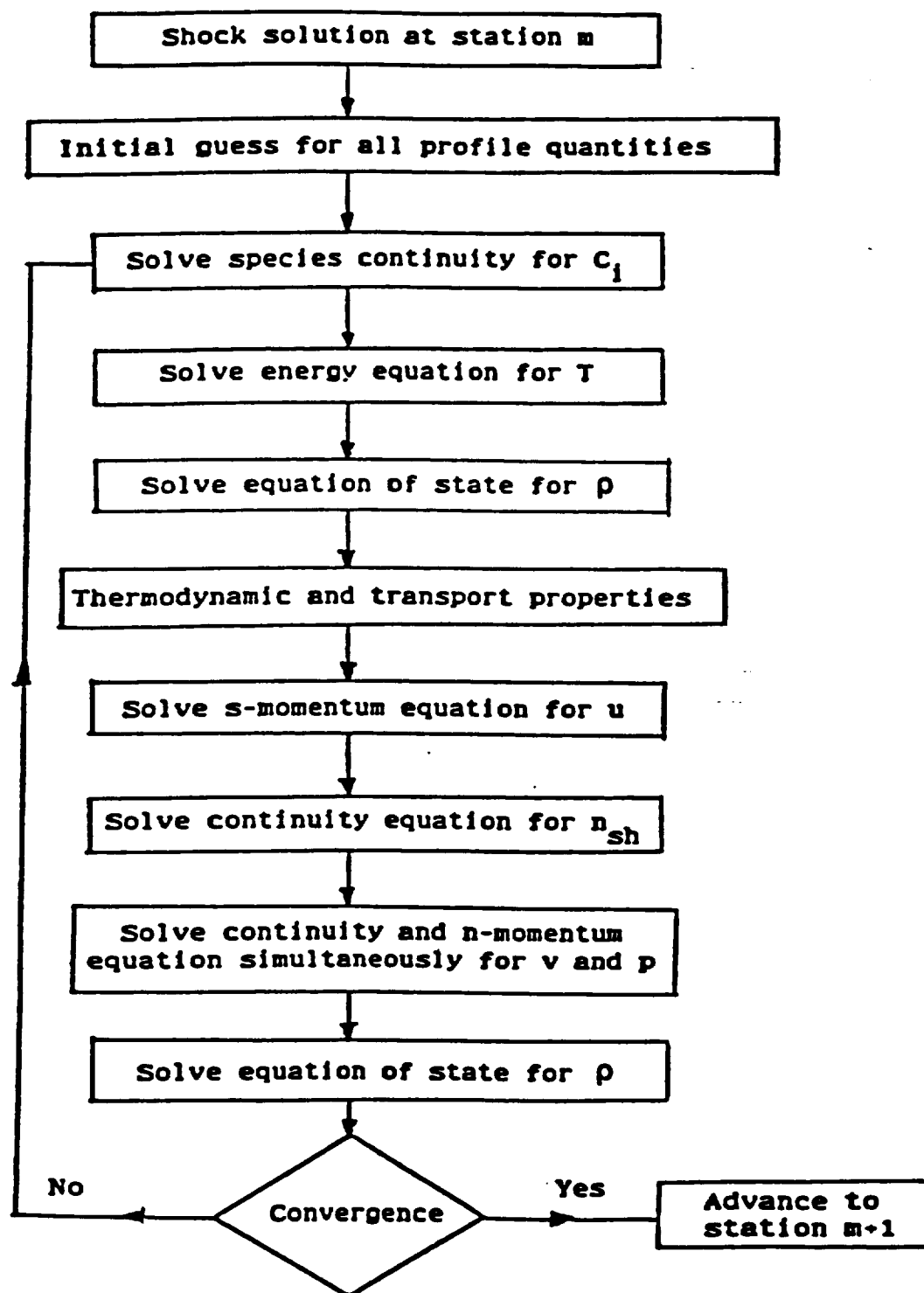
No

Yes

Advance to station m+1

Fig. 5.1 Solution sequence with nonequilibrium chemistry.

different small body-angle sphere cones are presented which demonstrate the effects of surface catalysis and body angle. Finally, the effects of nose bluntness, Mach number and the thermodynamic and transport curve fit relations on surface heat transfer rate are investigated.

In the original code of Moss [24], the convergence criteria for each body station was that the relative difference be less than 0.001 for both the temperature and tangential velocity derivatives at the wall. In this study, the temperature, tangential velocity, pressure and species concentration profiles are added into the convergence criteria where the relative difference is less than 0.001 for all these profiles.

5.7.1 Comparison of the Present Method with Cascading Method

Figures 5.2 and 5.3 show the results of shock standoff distance and surface heat transfer distribution over a 35° sphere cone with finite rate chemistry. Without coupling the two first-order equations, continuity and normal-momentum, oscillation exists in the vicinity of the tangency point; this is the same as with the perfect gas model (Figs. 3.5 and 3.6). This oscillation can be removed by solving the two first-order equations simultaneously in a coupled way.

5.7.2 Comparison of the Present Method with Measured Data

Present predicted heating rates are compared with the STS-2 laminar heating data [90] for three different altitudes in Figs. 5.4 to 5.6. The viscous shock-layer equations are applied to the windward symmetry plane by using the concept of an equivalent axisymmetric body at zero degree angle of attack [72,77,91,92]. Results for an altitude of 71.29 km are given in Fig. 5.4. With coupling the global continuity and normal momentum equations, the predicted heating rates are lower
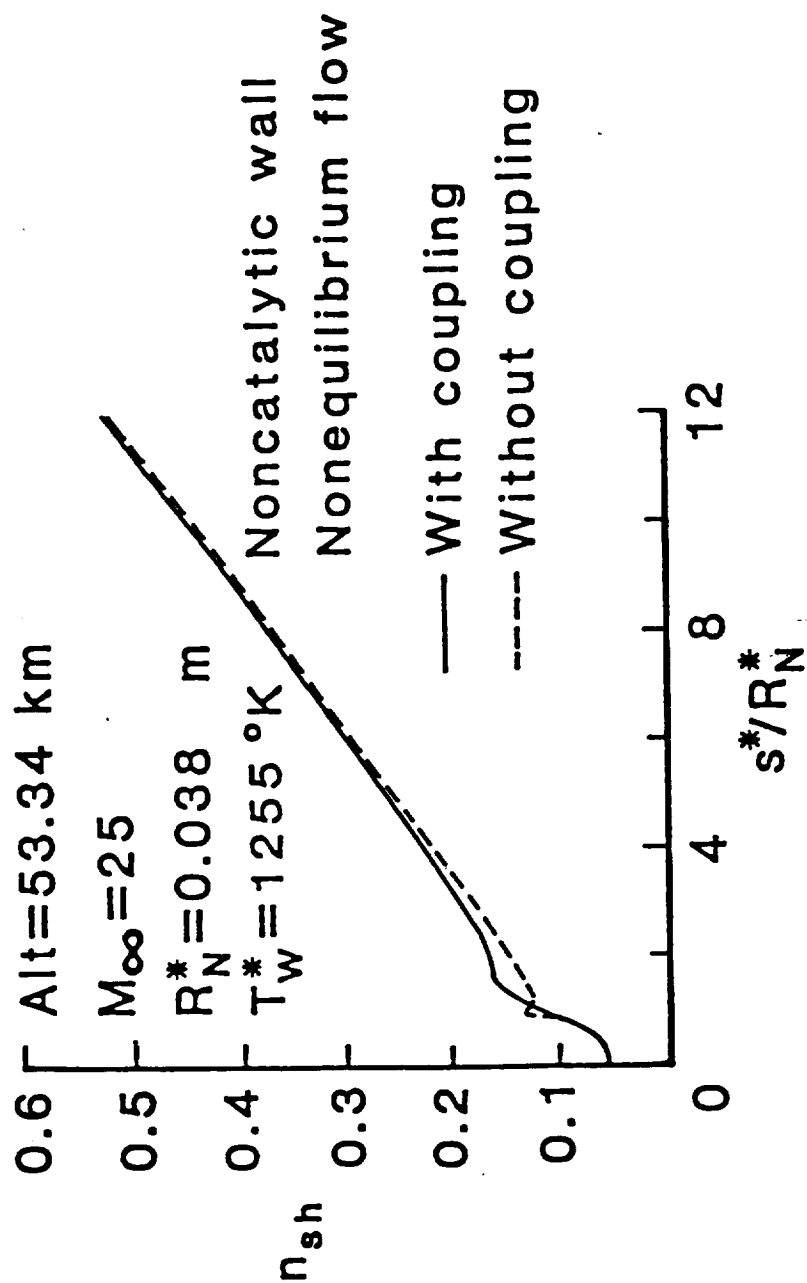
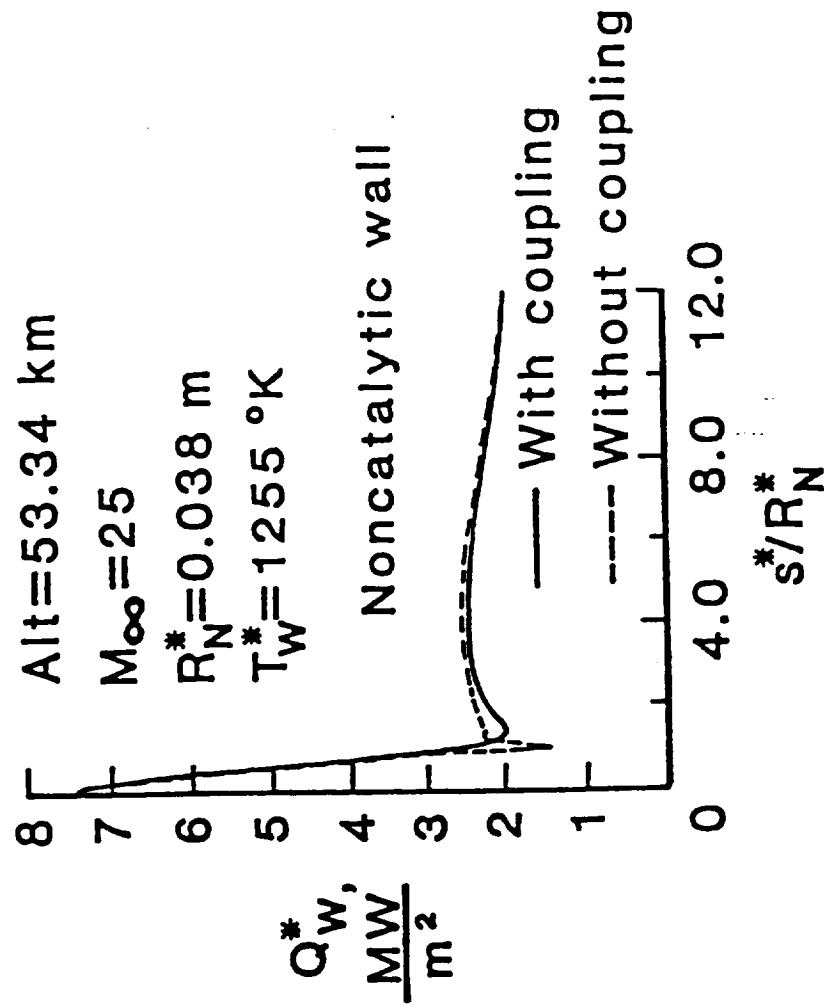Fig. 5.2 Shock stand-off distance for a 35° sphere-cone with nonequilibrium chemistry.

Fig. 5.3 Surface heat transfer rate distribution for a '35° sphere-cone with nonequilibrium chemistry.

than that without the coupling. Since the body angle is not small, the coupling effect is not significant. It is also shown that the predicted heating rates using the oxygen surface reaction rate expression of Zoby et al. [77] yield better comparison with the experimental data than that using the Scott's relation [79]. The prediction using Scott's expression are 30 to 40 percent lower than the experimental data. The present "equivalent" axisymmetric body results agree quite well with the three-dimensional results which are obtained by Thompson [75]. Figures 5.5 and 5.6 give the comparisons of surface heating rate between predictions and STS-2 data at altitudes 60.56 km and 52.97 km, respectively. With finite catalytic wall conditions, the present predictions are in good agreement with the data over the length of the vehicle.

The results presented in Figs. 5.4 to 5.6 show that the flowfield in the shock layer at high altitude is quite far from that predicted by assuming the condition of chemical equilibrium. With decreasing altitudes, the data and the finite rate chemistry predict the results that approach the equilibrium value. However, near the stagnation region some degree of nonequilibrium flow persists to altitudes as low as 50 km, as shown in Fig. 5.6.

5.7.3 Effects of Surface Catalysis and Body Angle

Results for three sphere cones with body half-angles of 20°, 10°, and 6° are presented to illustrate the effects of body angle and surface catalysis. Freestream conditions are those for 53.34 km altitude and a Mach number of 25. The bodies have the same nose radius which equals 0.0381 m. Both noncatalytic and fully catalytic surfaces are examined
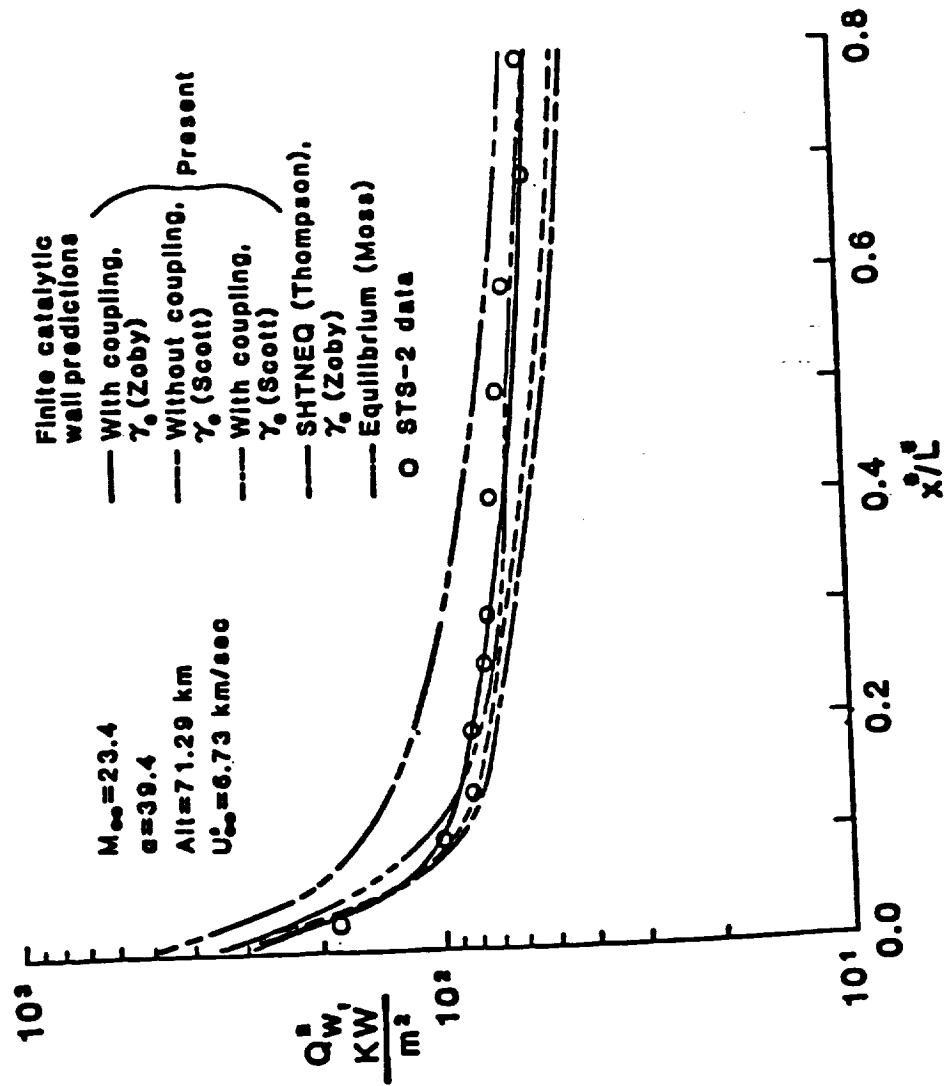
Fig. 5.4   Comparison of predicted and experimental heating
rate distribution at an altitude of 71.29 Km.
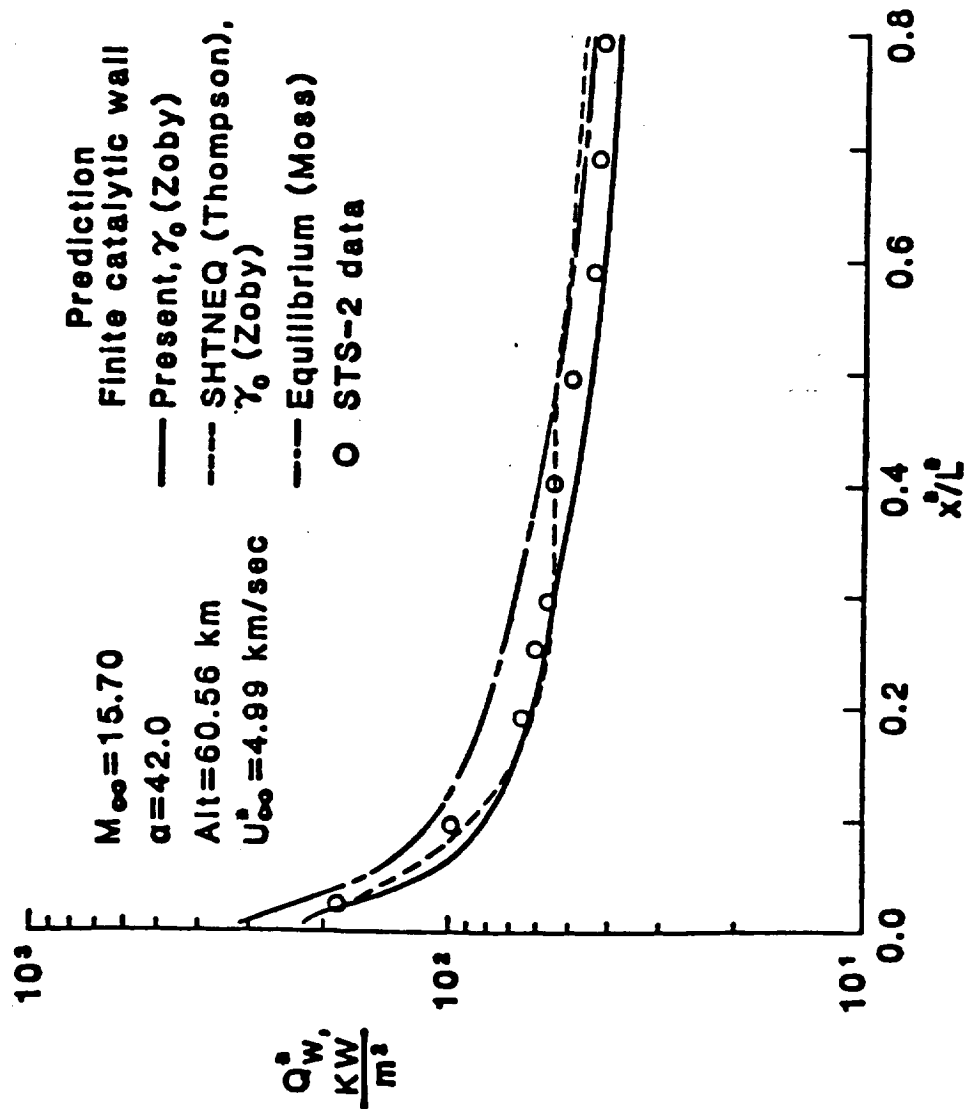
Fig. 5.5   Comparison of predicted and experimental heating
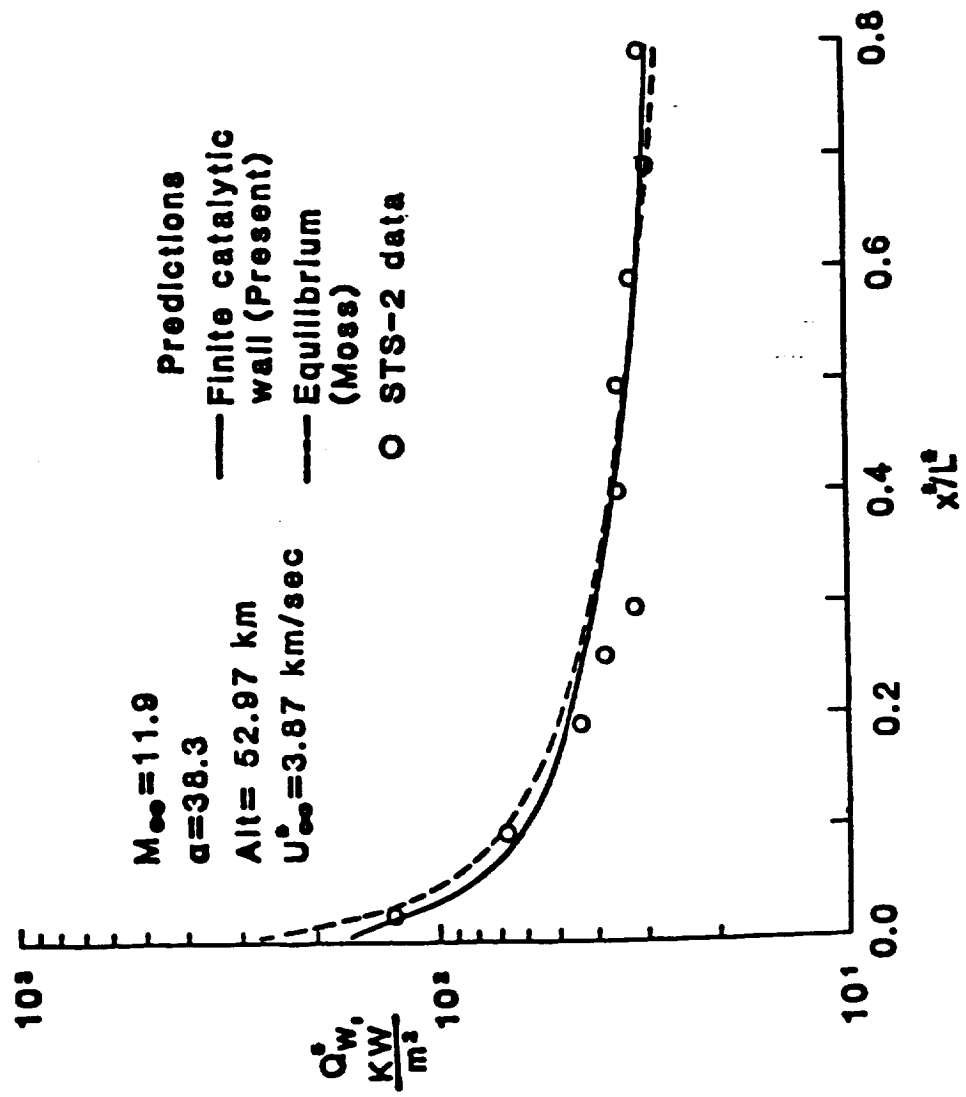   rate distribution at an altitude of 60.56 Km.

Fig. 5.6   Comparison of predicted and experimental heating
rate distribution at an altitude of 52.97 Km.

to show the limiting effects of wall catalycity on heating. Figure 5.7

gives the convergence history of the shock standoff distance for a 10°

sphere-cone using the present method. It does not matter whether the

initial shock shape is created from the perfect gas solution for the

same body-angle (the solid line and the dash line) or from the chemical

nonequilibrium solution for larger body-angle (the chain line), the

shock standoff distance will converge to the same shock shape.

The predicted heat-transfer distributions for 20°, 10°, and 6°

sphere cones are given in Figs. 5.8 through 5.13. In order to present

these results clearly, it is necessary to show them in two figures for

each body-angle. The first of these two figures is an enlarged view of

the nose region while the second extends up to 400 nose radii. From

these figures, it is seen that the heating rates with the noncatalytic

surface may decrease more than 50 percent in comparison to that with the

fully catalytic surface on the spherical region. The differences in the

heating rates decrease in the downstream regions. With a noncatalytic

surface an appreciable amount of dissociation is present at the wall,

then a diffusion-inhibiting blanket of unrecombined atoms can pile up

near the surface and thereby reduce the heat transfer to the wall by

diffusion; this could result in a reduction of heat transfer to the

surface. On the other hand, with a fully catalytic surface the atomic

species which result from the dissociation in the high temperature air

will recombine with oxygen and nitrogen molecules at the surface. Since

the diffusion flux of atoms toward the wall must be equal to the rate of

disappearance of atoms at the wall due to recombination there, the heat

transfer to wall by diffusion is maximum with a fully catalytic wall.
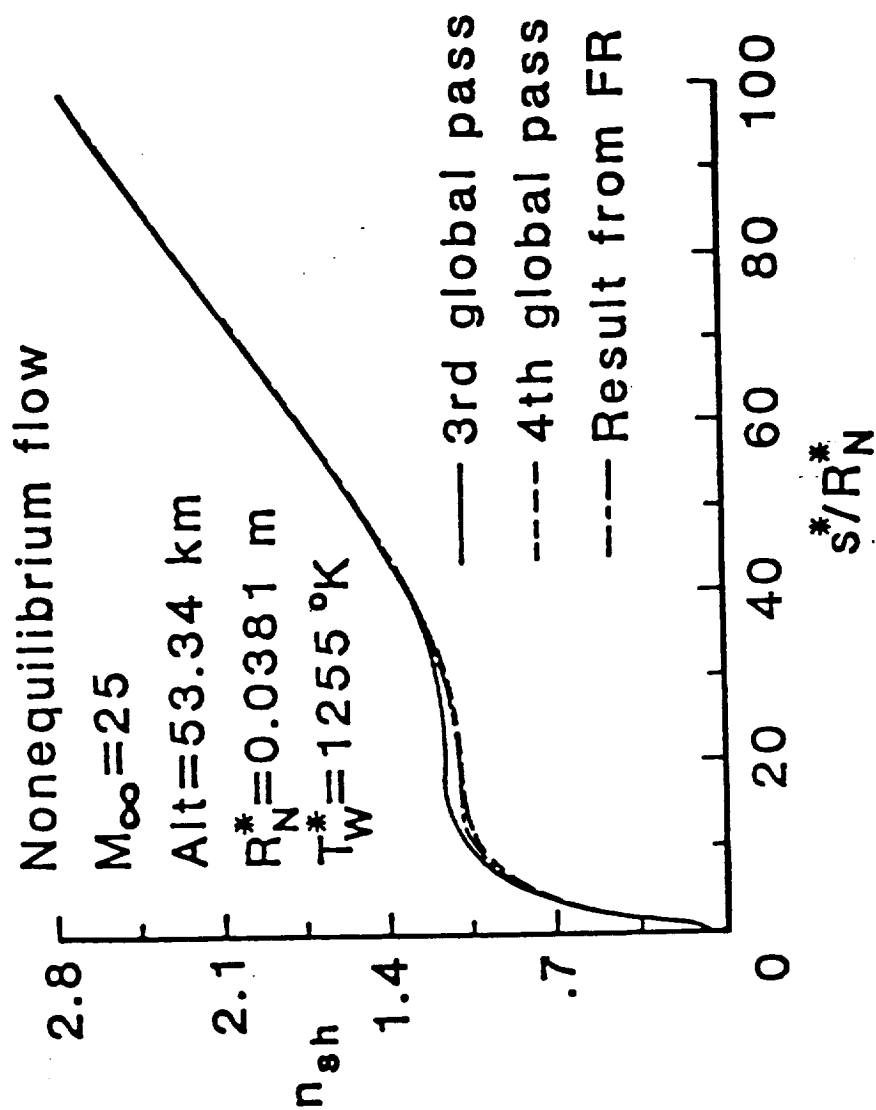
Fig. 5.7   Shock stand-off distance for a 10° sphere-cone with nonequilibrium chemistry.

Fig. 5.8   Nonequilibrium surface heat transfer rate
distribution for a 20° sphere-cone (fore-cone).

Fig. 5.9   Nonequilibrium surface heat transfer rate distribution for a 20° sphere-cone (aft-cone).

Fig. 5.10 Nonequilibrium surface heat transfer rate
distribution for a 10° sphere-cone (fore-cone).

Fig. 5.11   Nonequilibrium surface heat transfer rate
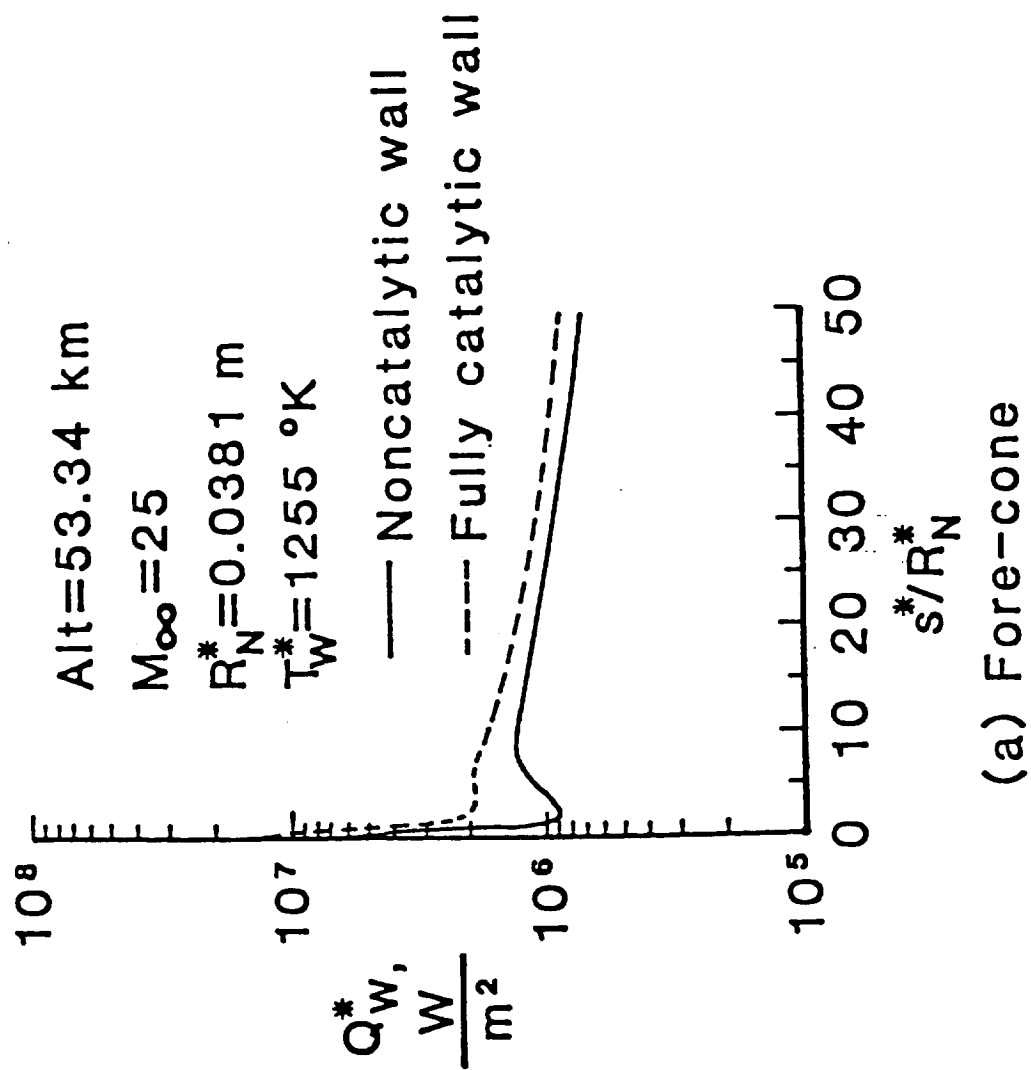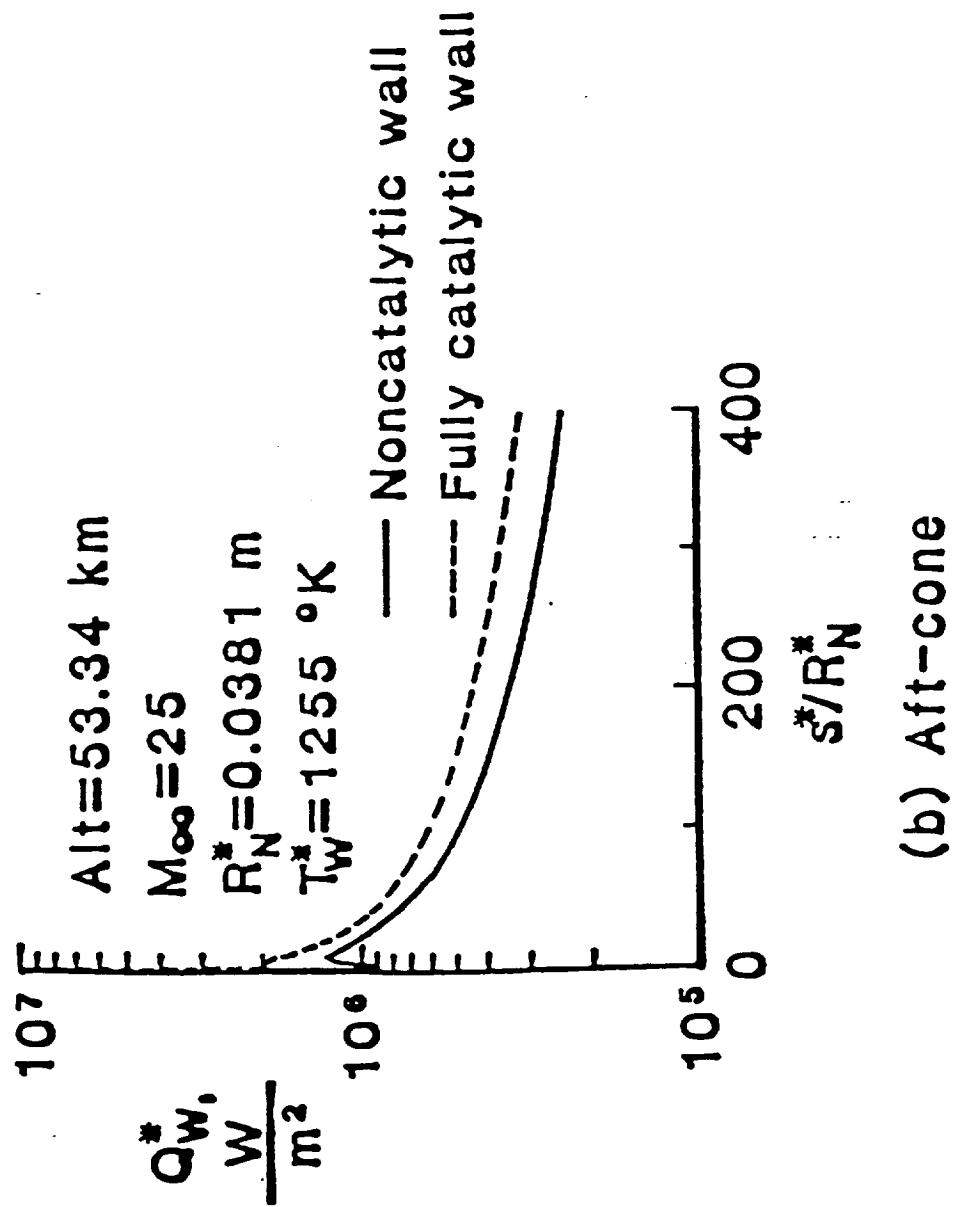distribution for a 10° sphere-cone (aft-cone).
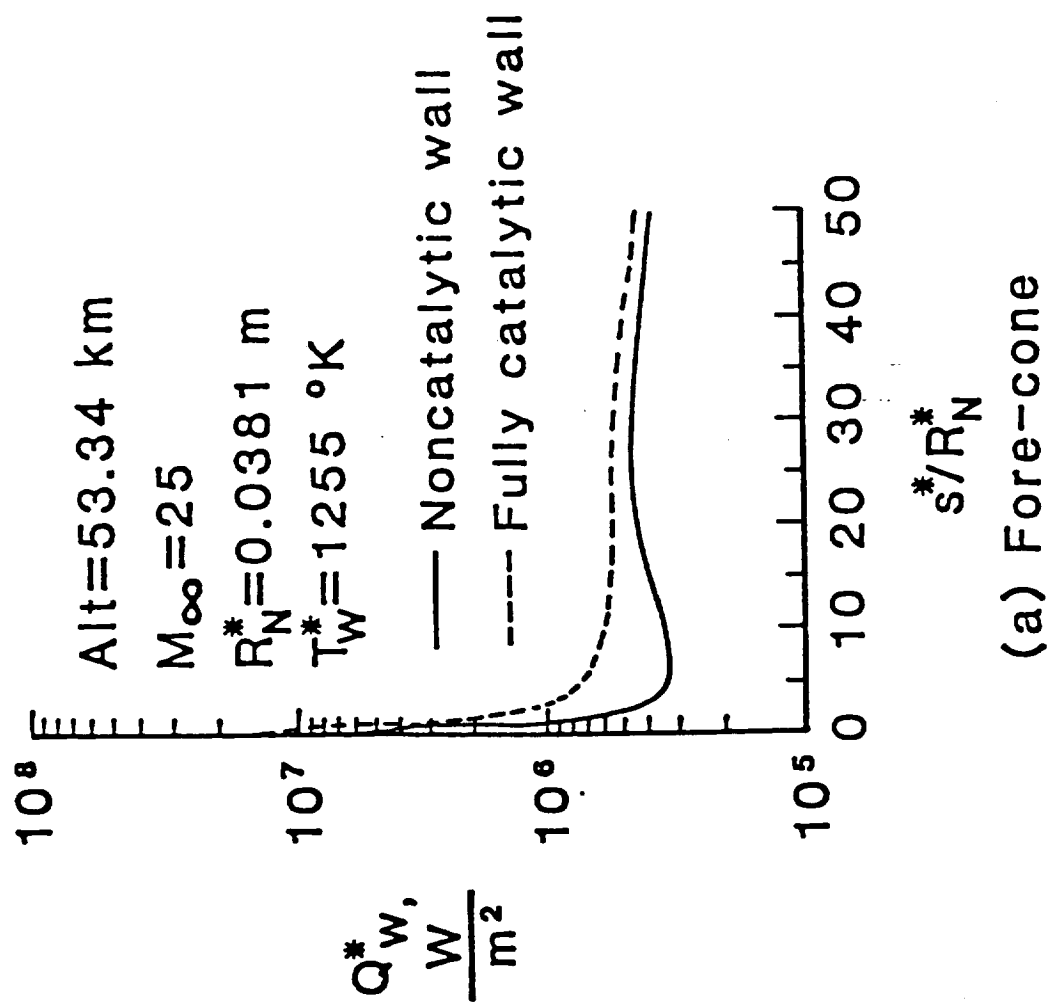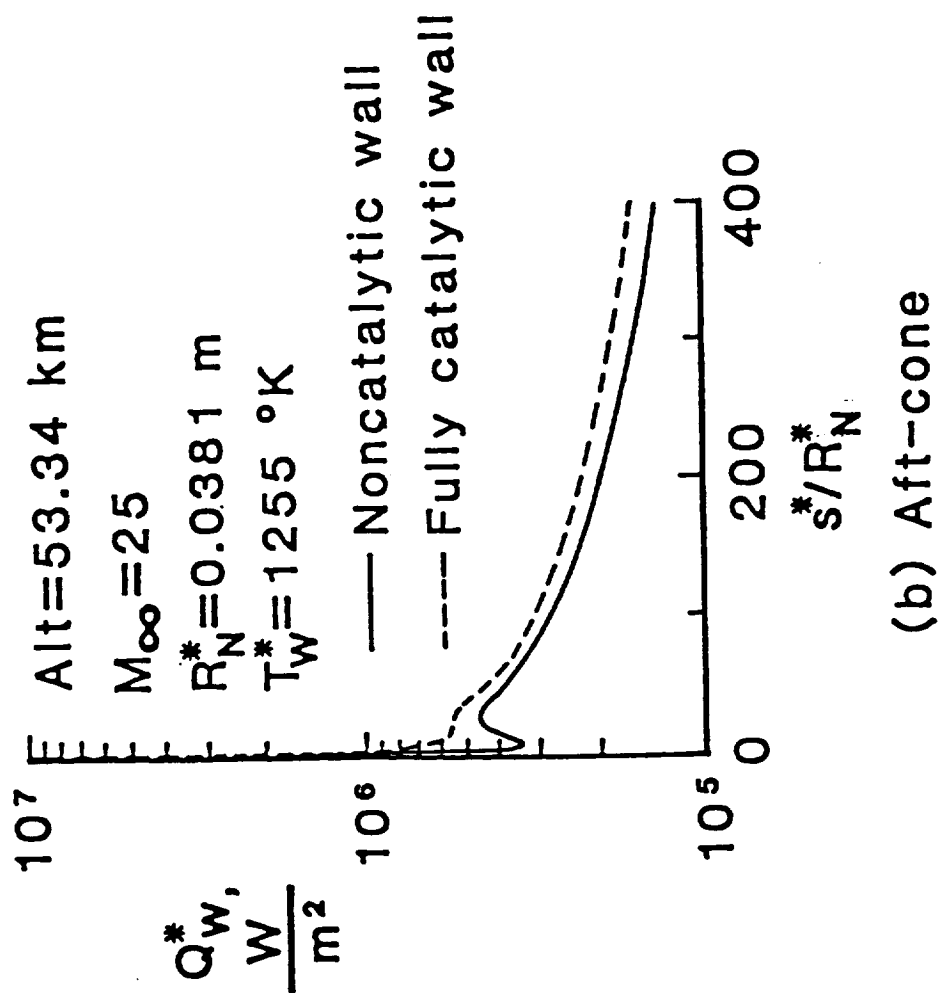
Fig. 5.12 Nonequilibrium surface heat transfer rate
distribution for a 6° sphere-cone (fore-cone).

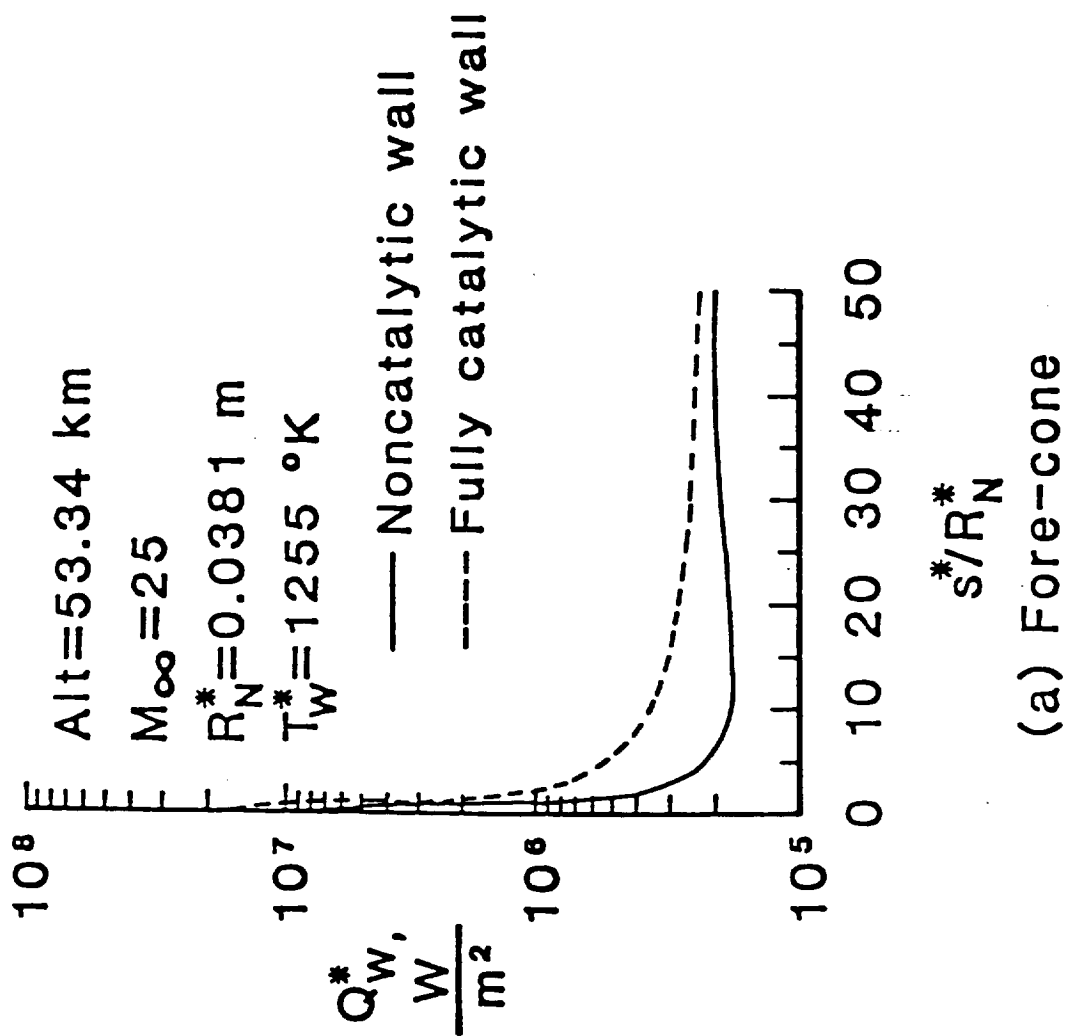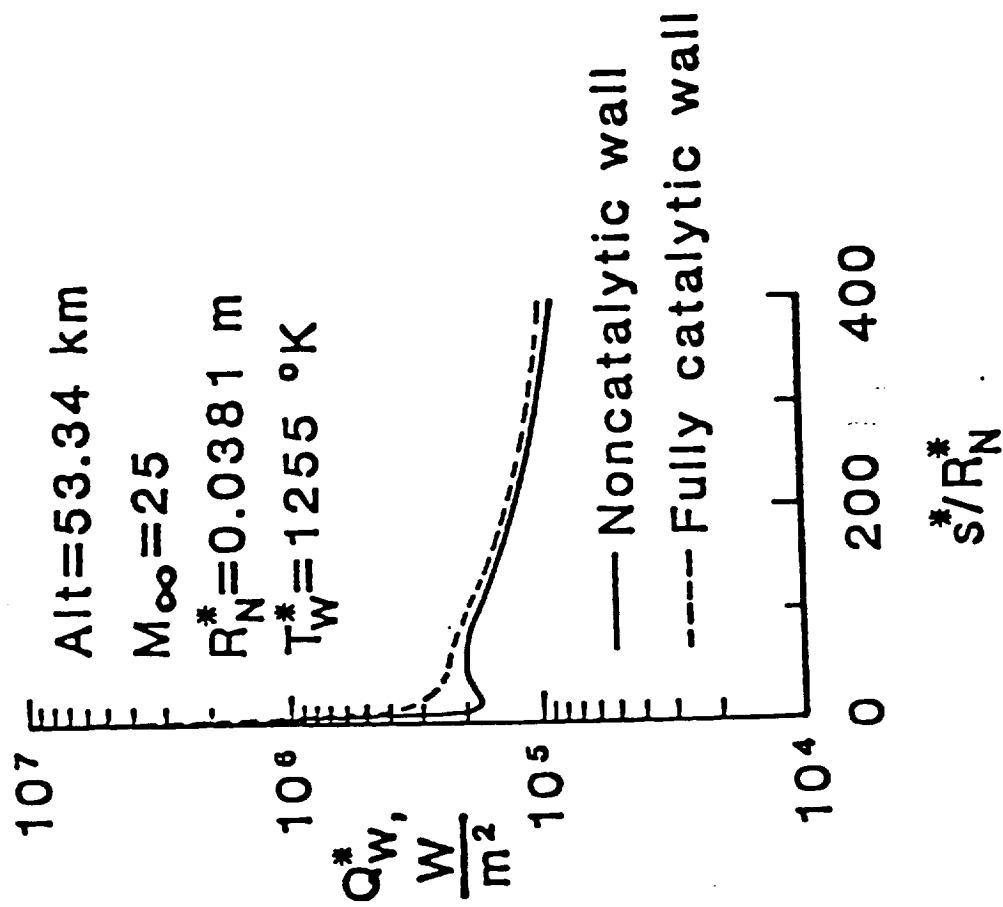Fig. 5.13 Nonequilibrium surface heat transfer rate distribution for a 6° sphere-cone (aft-cone).

For a real surface, some degree of catalysis is usually present, hence, the heating rate for a finite catalytic surface is between these two limits.

The results for the ratio of surface heating rate with noncatalytic wall to that with fully catalytic wall for the three bodies are shown in Figs. 5.14 and 5.15. The ratio demonstrates the maximum potential for a surface heating-rate reduction in the presence of dissociated nonequilibrium flow over a finite-catalytic surface. All the three curves have the same trend. The ratios keep decreasing up to the tangency point, then increase up to a maximum value in the recompression region, and finally, decrease to a constant value on the far downstream region. It is noticed that the location of the maximum point moves downstream as the body-angle decreases; i.e., the recompression region moves downstream as the body-angle decreases.

For stations beyond 100 nose radii (Fig. 5.15), the results indicate less nonequilibrium effects for the slender 6° cone than the 10° and 20° cones. As shown in Figs. 5.16 and 5.17, these can be attributed to more dissociated species present throughout the flowfield for energy transport by diffusion to the surface for the wider angle cone. In this body region for the lower cone angles, conditions sufficient to produce dissociated species exist only in a small region of the boundary layer. In the fore-cone region (Fig. 5.14), the largest cone angle produces the smallest nonequilibrium effects as indicated by higher values of the ratio. (This result does not imply the local or total heating rate to the larger cone angle is less.) As shown in Figs. 5.18 and 5.19, this trend may be explained for a given nose radius, the

flow over the smaller cone angle compared to the larger cone angle expands rapidly and results in freezing of the flow chemistry and larger percentages of dissociated species.

Figures 5.20 to 5.22 show the effects of body-angle on the surface heating rates and wall pressure. Figures 5.20 and 5.21 give the heating rates for a noncatalytic wall and for a fully catalytic wall, respectively. The wall pressure distributions are illustrated in Fig. 5.22. Since the wall catalyticity has negligible effect on the wall pressure, the results are presented only for the noncatalytic wall. Decreasing the body angle can reduce the wall pressure and heat transfer to the surface. Hence, the desirable geometries for hypersonic vehicles are slender long bodies in order to reduce the heat transfer rate and drag force on the bodies. It is noticed in Fig. 5.22 that the recompression regions start at $s^*/R_N^* = 3.0$, 10.0, and 28.0 for the 20°, 10° and 6° sphere cone, respectively, under the condition investigated.

5.7.4 Effects of Nose Bluntness and Mach Number

A study of the effects of nose bluntness and Mach number on the shock standoff distance, surface heat transfer and mass concentration of O_2 at the stagnation point of a 45° sphere cone is conducted and results are discussed here. Freestream conditions are selected at 90 km, nose radii are 0.305 m to 2.286 m, and Mach numbers are 30 to 36. Only noncatalytic surface boundary condition is considered.

Figures 5.23 to 5.24 show the effects of nose bluntness on the shock standoff distance and surface heating rate for a Mach number of 36. It is seen that the shock standoff distance increases and surface
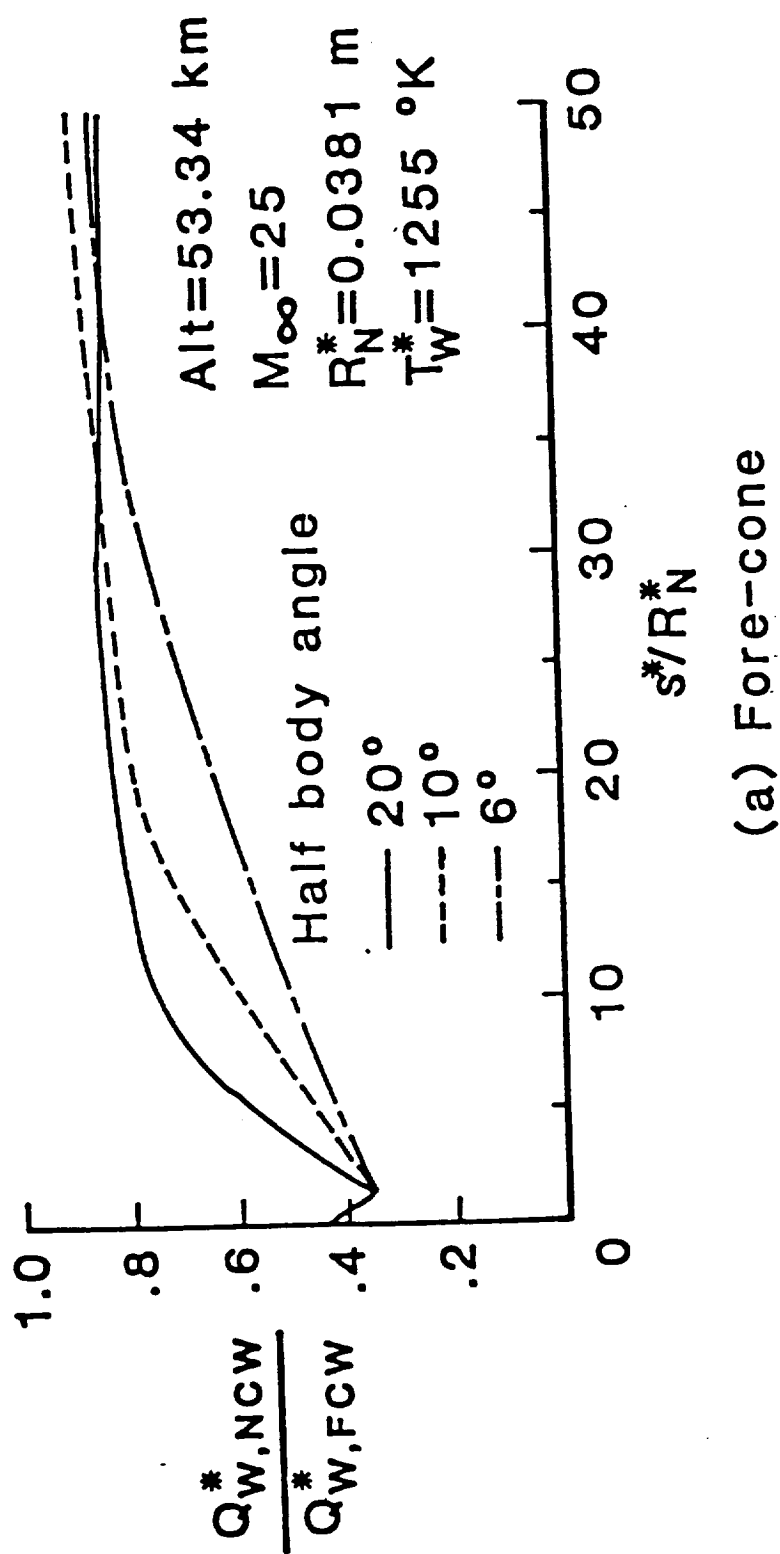
Fig. 5.14   Effect of body angle on noncatalytic to fully catalytic heating ratio distribution (fore-cone).
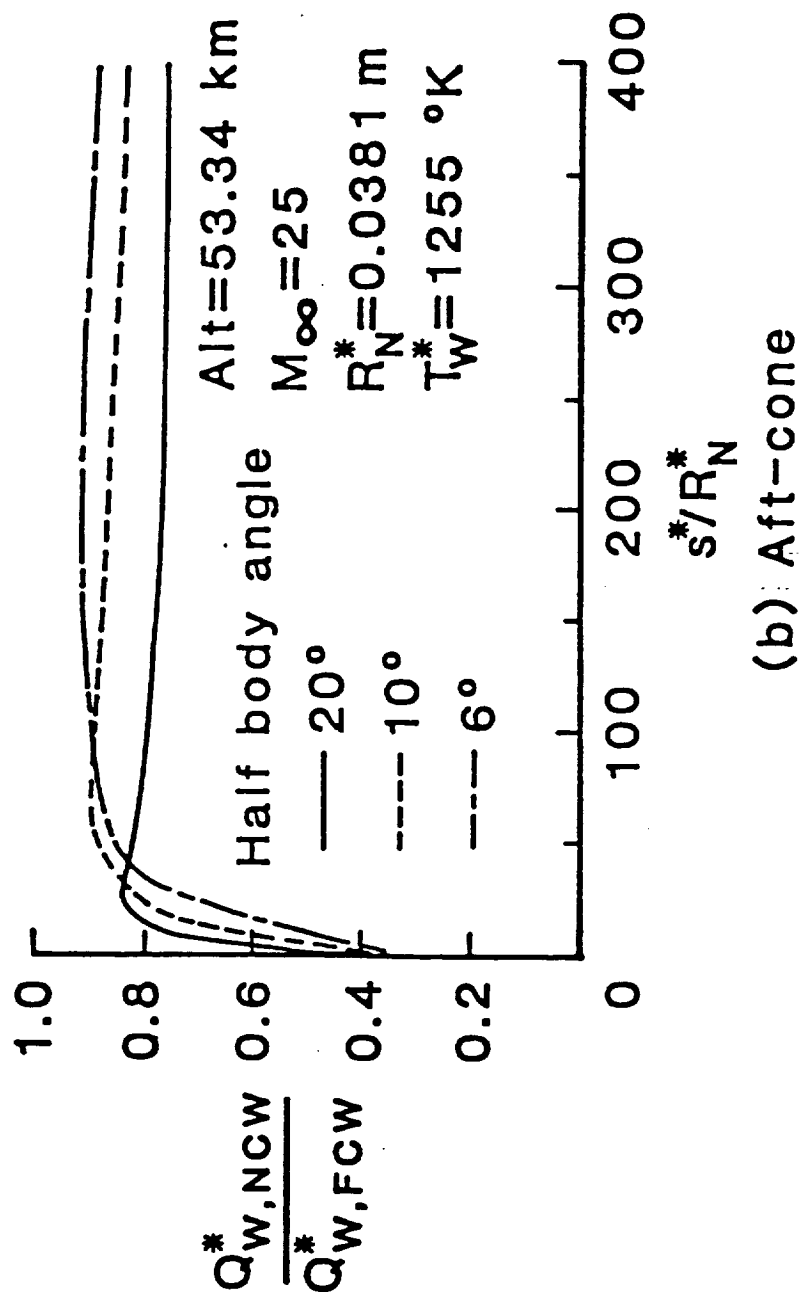
Fig. 5.15 Effect of body angle on noncatalytic to fully catalytic heating ratio distribution (aft-cone).
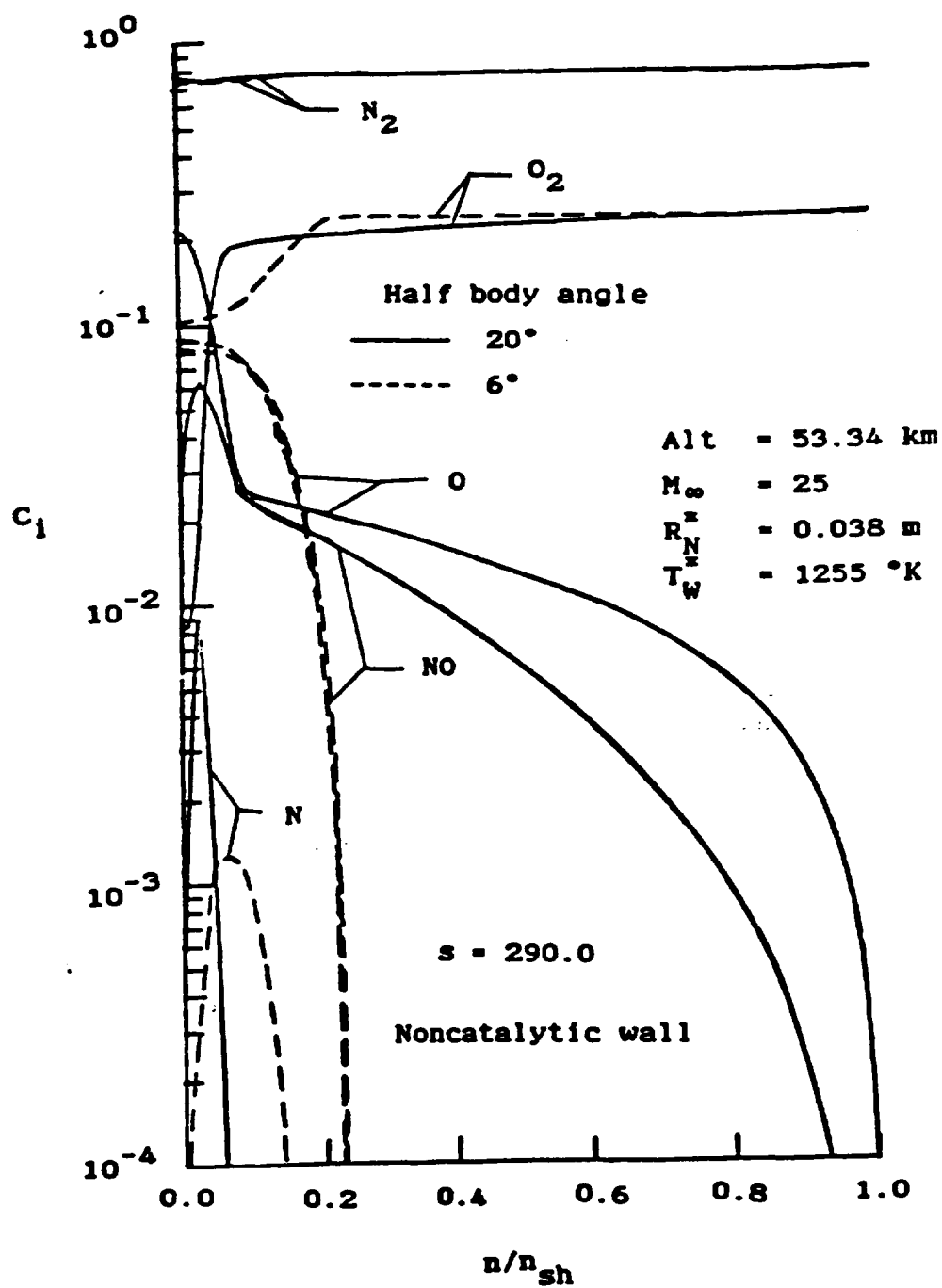
Fig. 5.16 Species concentration profiles at s = 290.0 for a noncatalytic wall.
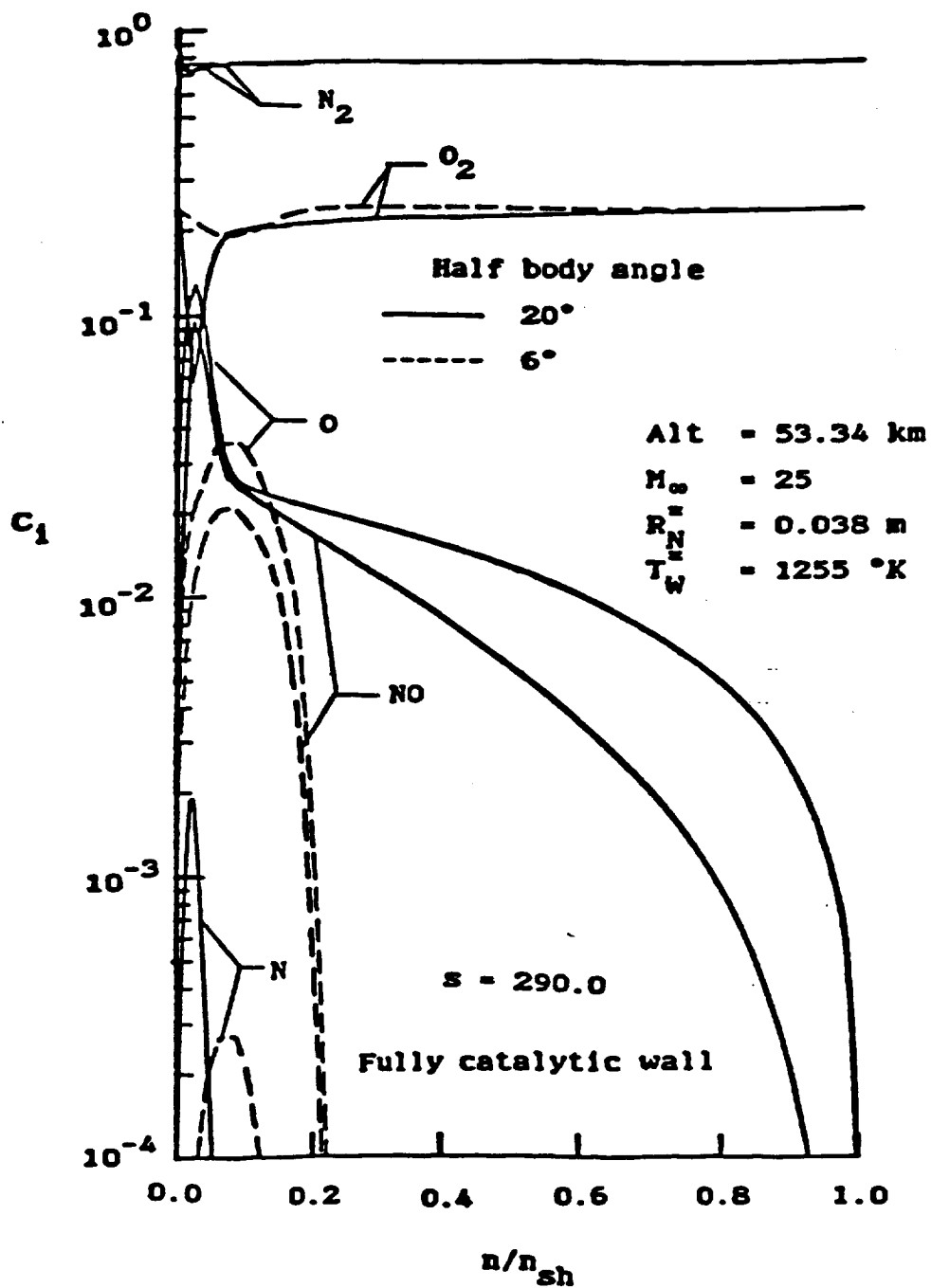
Fig. 5.17 Species concentration profiles at s = 290.0 for a fully catalytic wall.
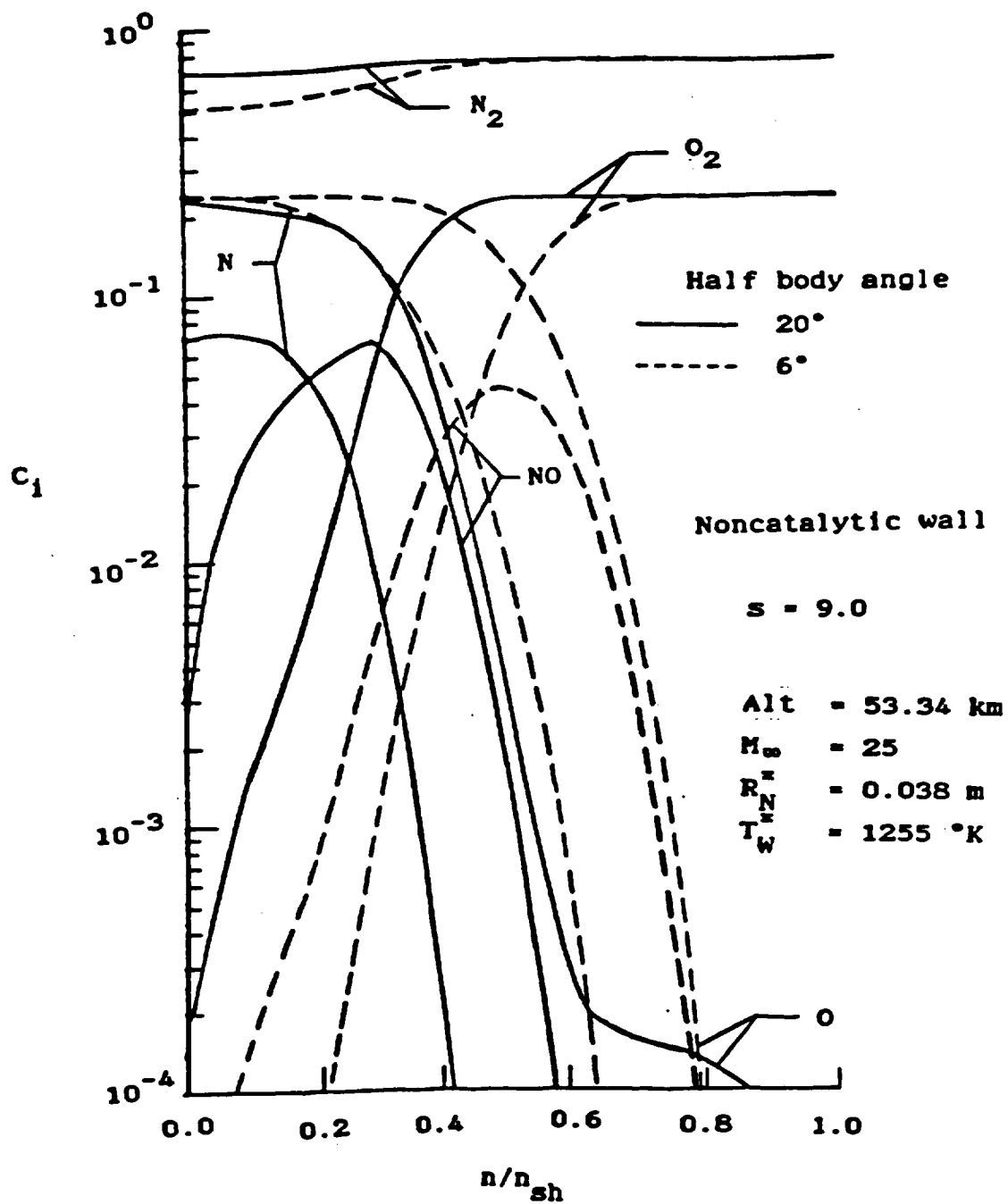
Fig. 5.18 Species concentration profiles at s = 9.0 for a noncatalytic wall.
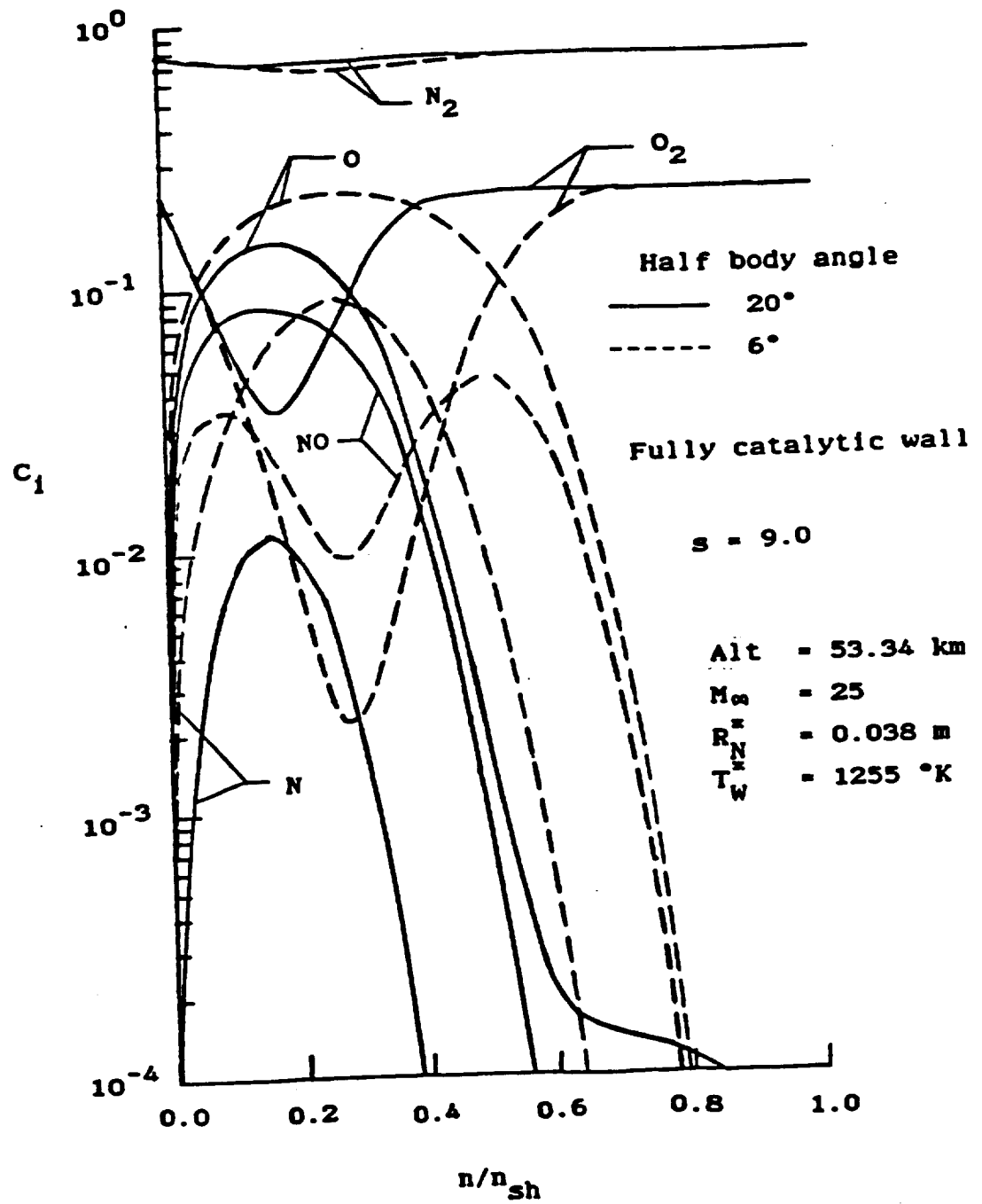
Fig. 5.19 Species concentration profiles at s = 9.0 for a fully catalytic wall.

heating rate decreases as the nose radius increases. Figure 5.25 shows the concentration profile of O_2 for three different nose radii. Since the shock standoff distance increases as the nose radius increases, both the oxygen and nitrogen molecules have more time to dissociate. Consequently, the atomic oxygen and nitrogen concentrations are higher in the shock layer. Moreover, the amount of energy absorbed by the dissociation phenomena has reduced the temperature in the shock layer such that the heat transfer to the wall is decreased.

Figures 5.26 and 5.27 show the effects of Mach number on the shock standoff distance and surface heating rate for a nose radius equal to 0.914 m. The shock standoff distance decreases and the surface heating rate increases as Mach number increases. At higher Mach numbers, the density and pressure increase across the shock wave are larger and hence the mass flow behind the shock wave can readily squeeze through a smaller area. Moreover, the temperature increase across the shock wave is larger as Mach number increases. As a result, a larger amount of energy transfers in the shock layer; i.e., the amount of heat transfer to the surface is larger. Figure 5.28 shows the concentration profile of oxygen molecules for three different Mach numbers. At the higher Mach numbers, oxygen dissociation increases due to the larger shock layer temperature.

It is noted from Fig. 5.26 that the shock standoff distance changes less and less as Mach number increases; i.e., the shock standoff distance becomes relatively insensitive to changes in free stream Mach number at high Mach numbers. This is an example of the Mach number independence principle.
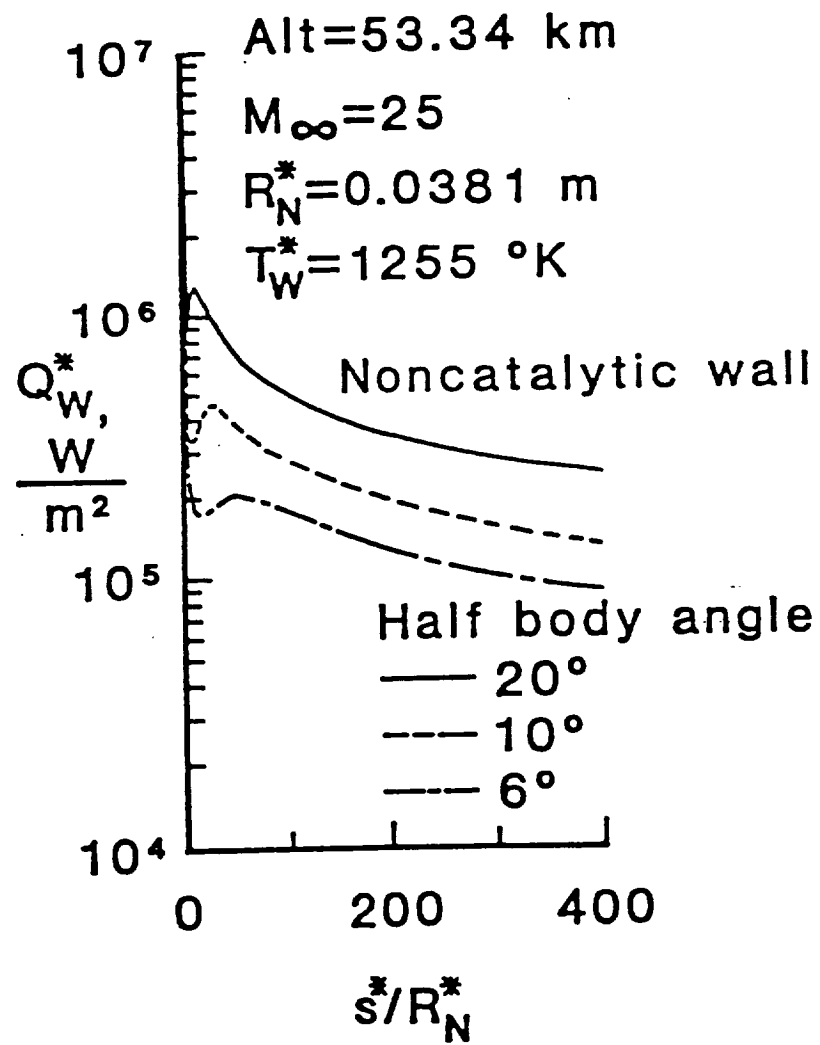
Fig. 5.20 Effect of body angle on nonequilibrium heating rate with noncatalytic wall.
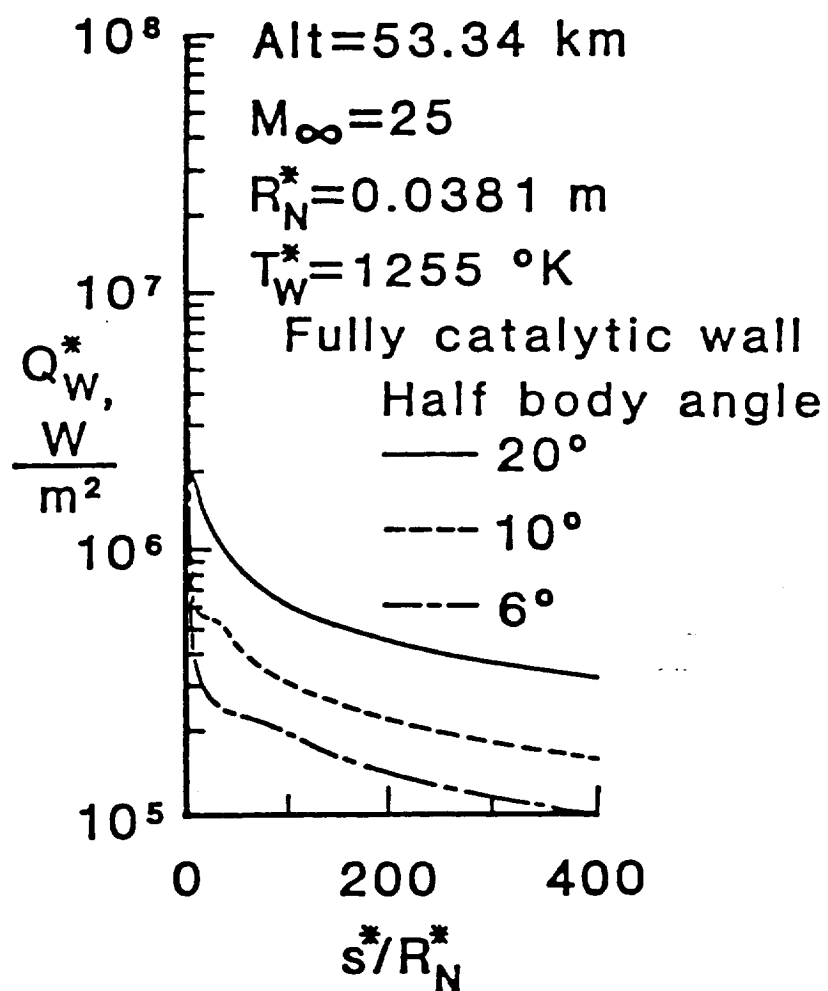
Fig. 5.21 Effect of body angle on nonequilibrium heating rate with fully catalytic wall.
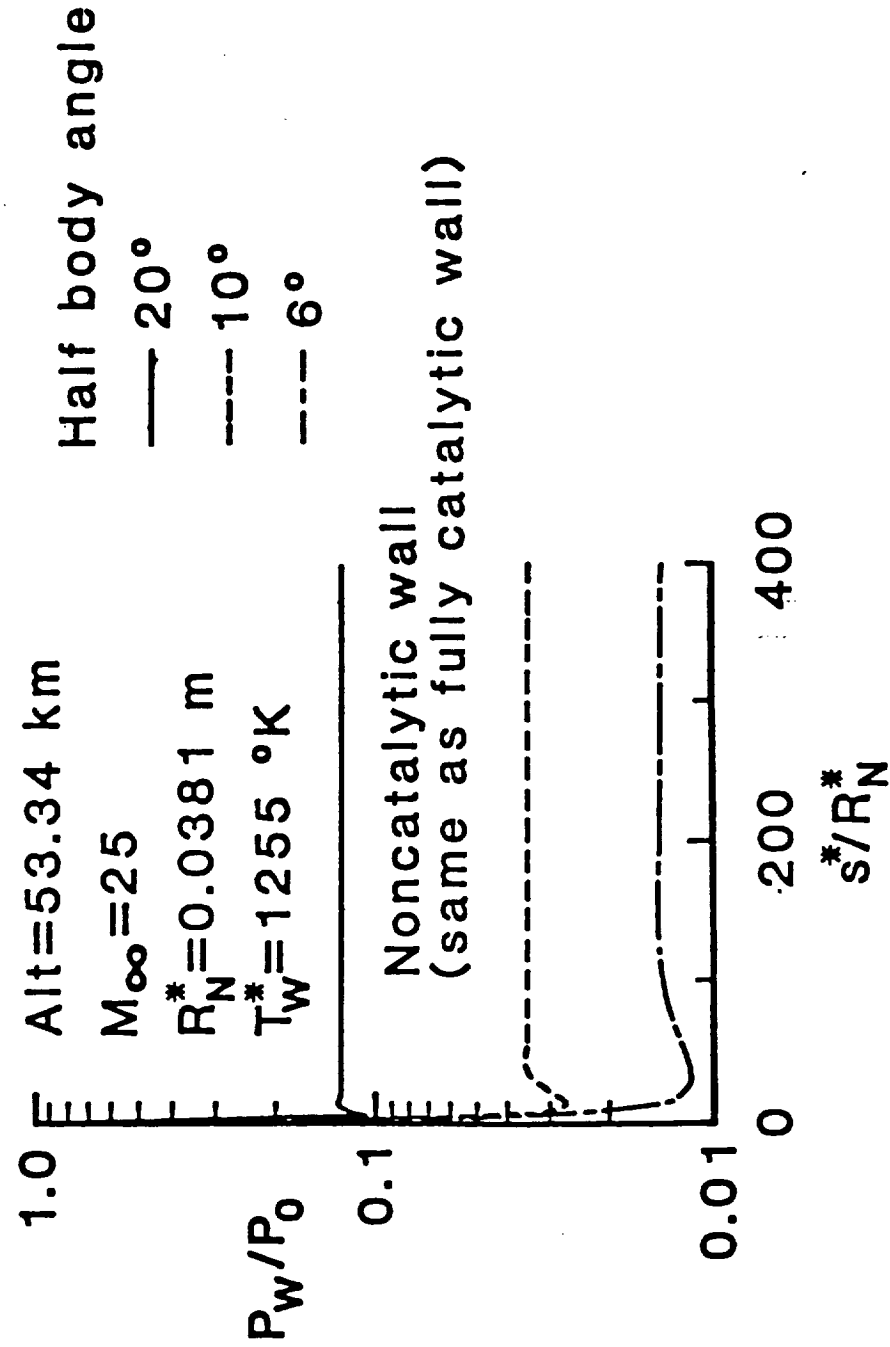
Fig. 5.22 Effect of body angle on surface pressure distribution.
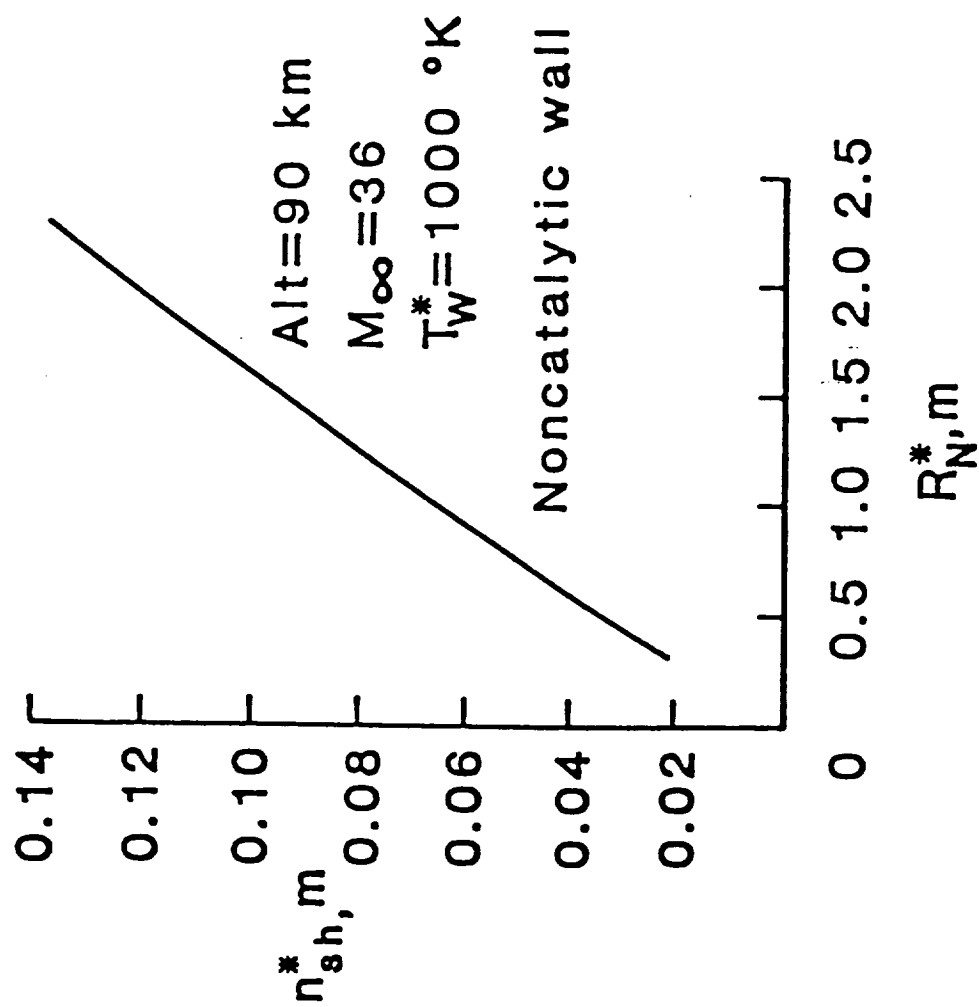
Fig. 5.23 Effect of nose radius on shock stand-off distance at the stagnation point.
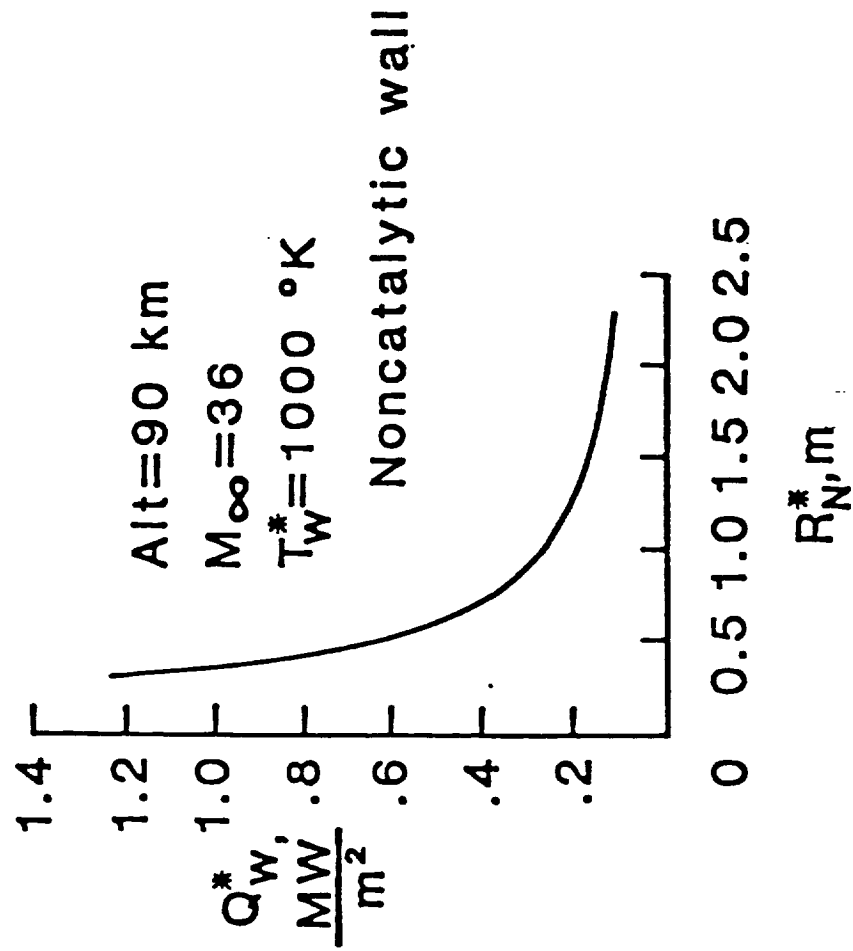
Fig. 5.24 Effect of nose radius on surface heat transfer rate at the stagnation point.
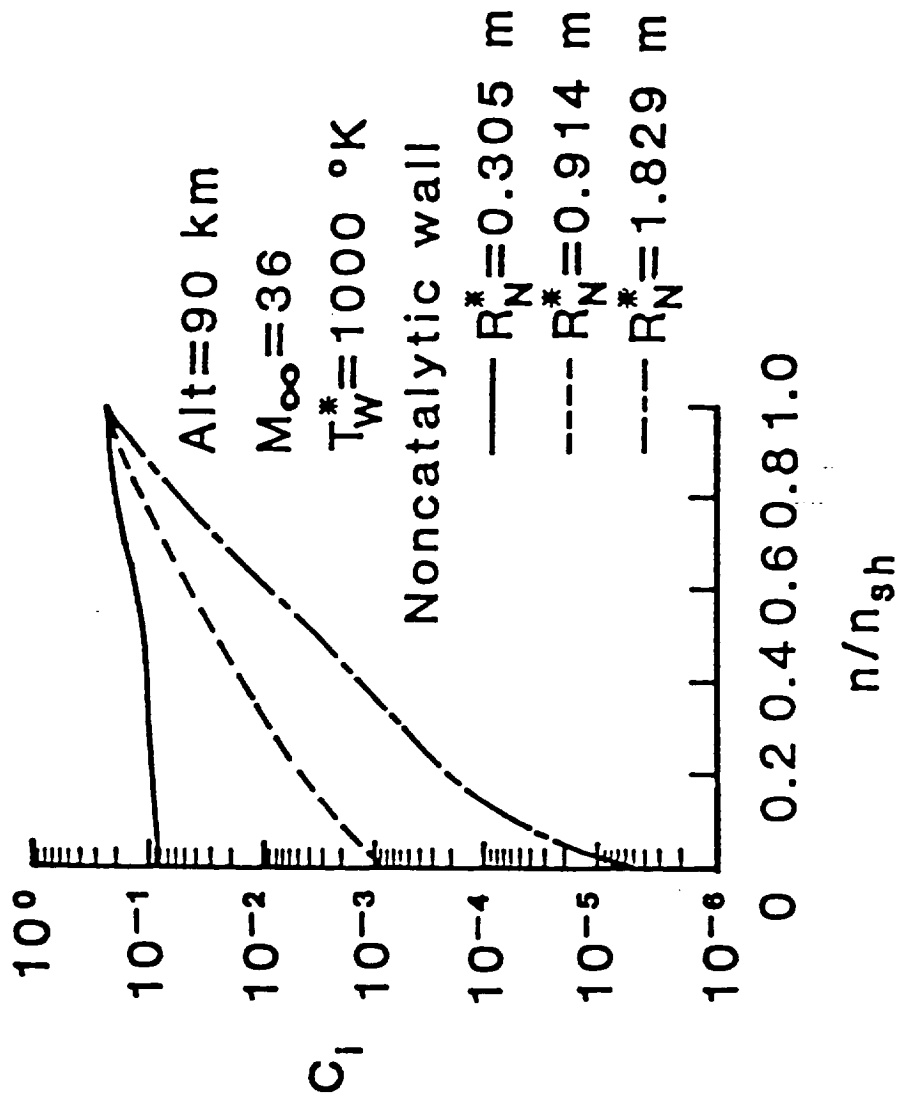
Fig. 5.25 Effect of nose radius on concentration
distribution of O_2 at the stagnation point.
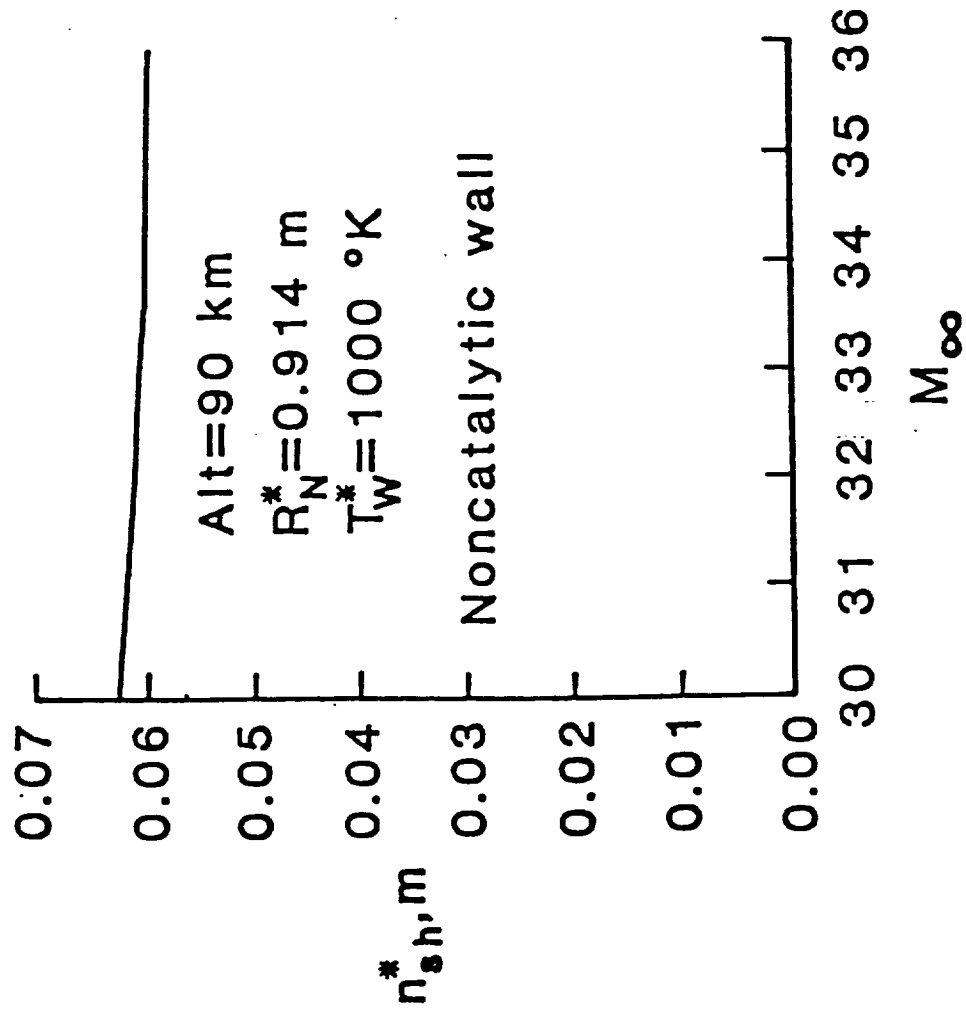
Fig. 5.26 Effect of Mach number on shock stand-off distance
at the stagnation point.
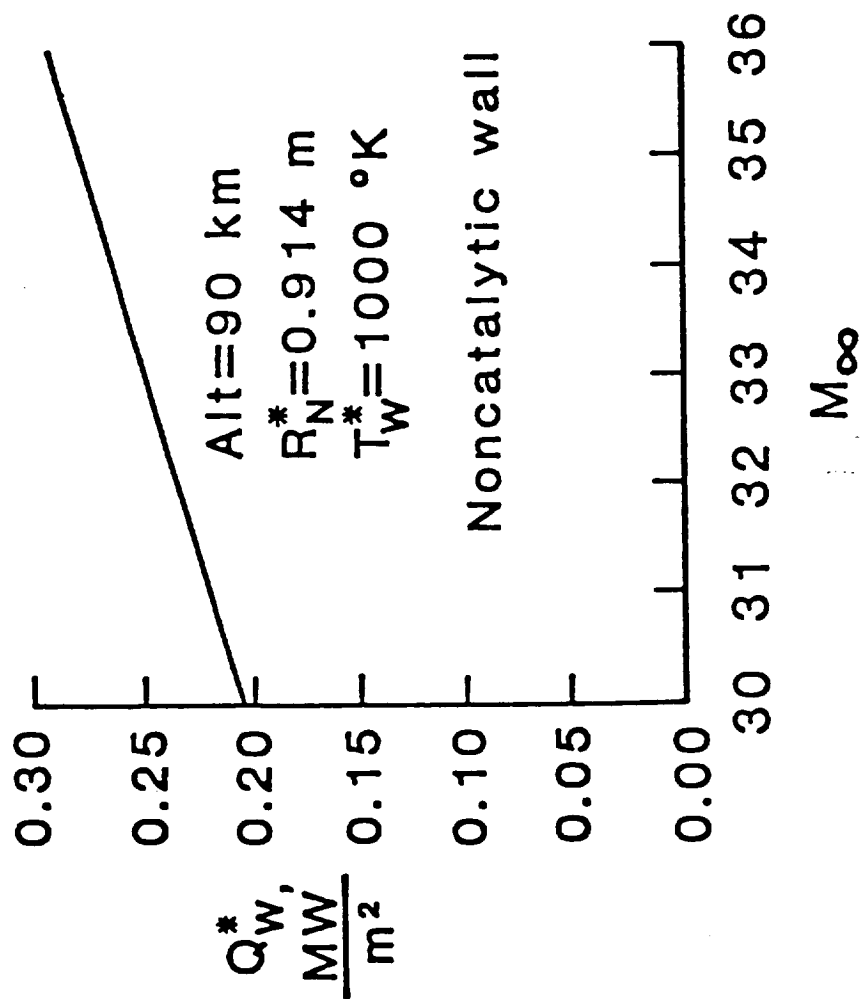
Fig. 5.27 . Effect of Mach number on surface heat transfer
rate at the stagnation point.
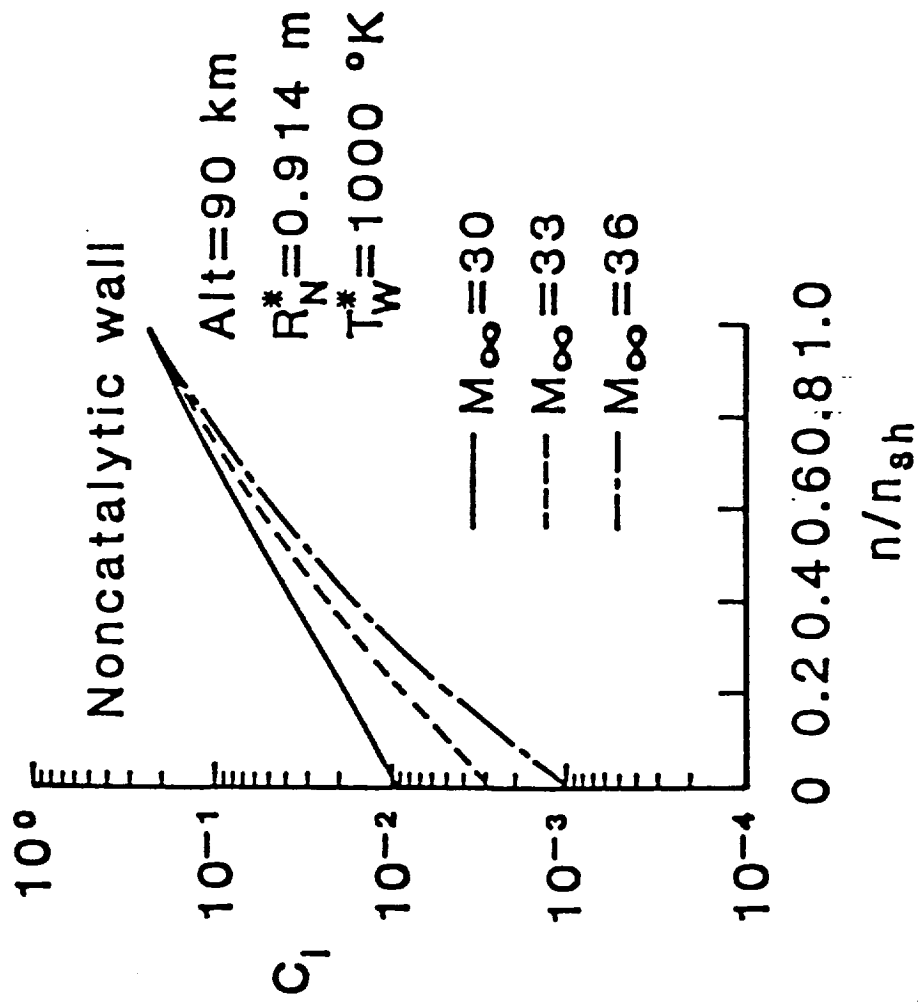
Fig. 5.28 Effect of Mach number on concentration
distribution of O_2 at the stagnation point.

5.7.5 Effects of the Thermodynamic and Transport Curve Fit Relations

The polynomial curve-fit formulas for thermodynamic and transport properties in [72] are based on Esch's data [82,86]. The mixture viscosity and thermal conductivity is obtained by Wilke's formula [27]. Values for the coefficients in these formulas are tabulated only up to 15,000 K. However, under certain conditions the temperatures in the shock layer are considerable higher than 15,000 K. Therefore, new polynomial curve-fit formulas for species transport properties have been developed from the data of Yos [87,93]. The gas mixture transport properties are obtained using the method of Armaly and Sutton [88] for the viscosity and Mason and Saxena [89] for the thermal conductivity. The polynomial curve-fit formulas for thermodynamic properties have been extended to an upper temperature range up to 35,000 K by Shinn [83]. These provide accurate predictions at higher temperatures encountered in nonequilibrium calculations [26,74,75]. The Prandtl number in the shock layer is set equal to a constant [24,26] or is calculated from the local thermodynamic and transport properties [75,76]. A study of the effects of the thermodynamic and transport properties on the surface heating rates of a 6° sphere cone is presented. Freestream conditions are those for an altitude of 53.34 km, a nose radius is 0.0381 m and a Mach number is 25. A noncatalytic surface boundary condition is considered.

Surface heating rate results with Yos' as well as with Esch's transport property data are given in Fig. 5.29. The results obtained by Thompson [34] are also shown in the figure for comparison. The Prandtl number is computed using local thermodynamic and transport properties.
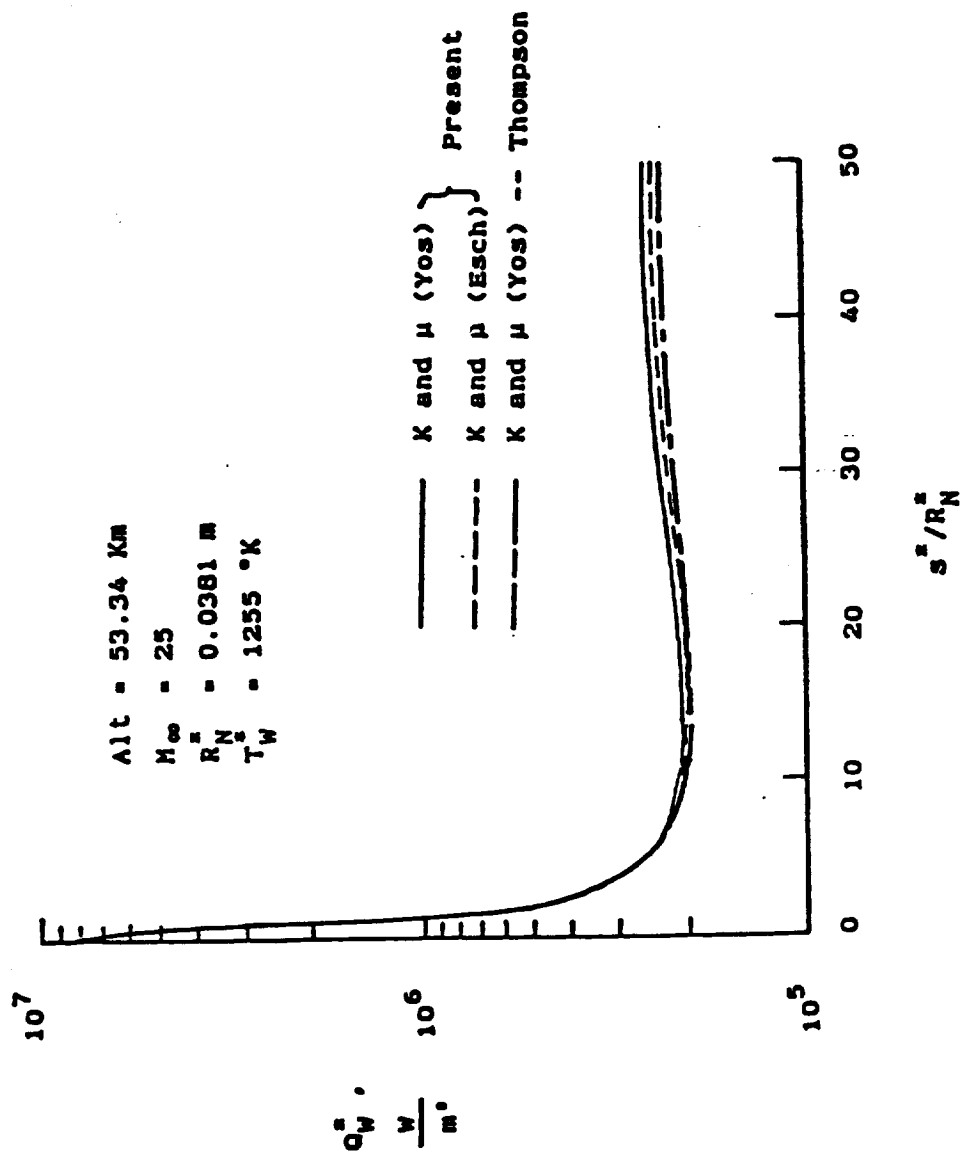
Fig. 5.29 Effect of the transport curve fit relations on surface heat transfer rate for a 6° sphere-cone.
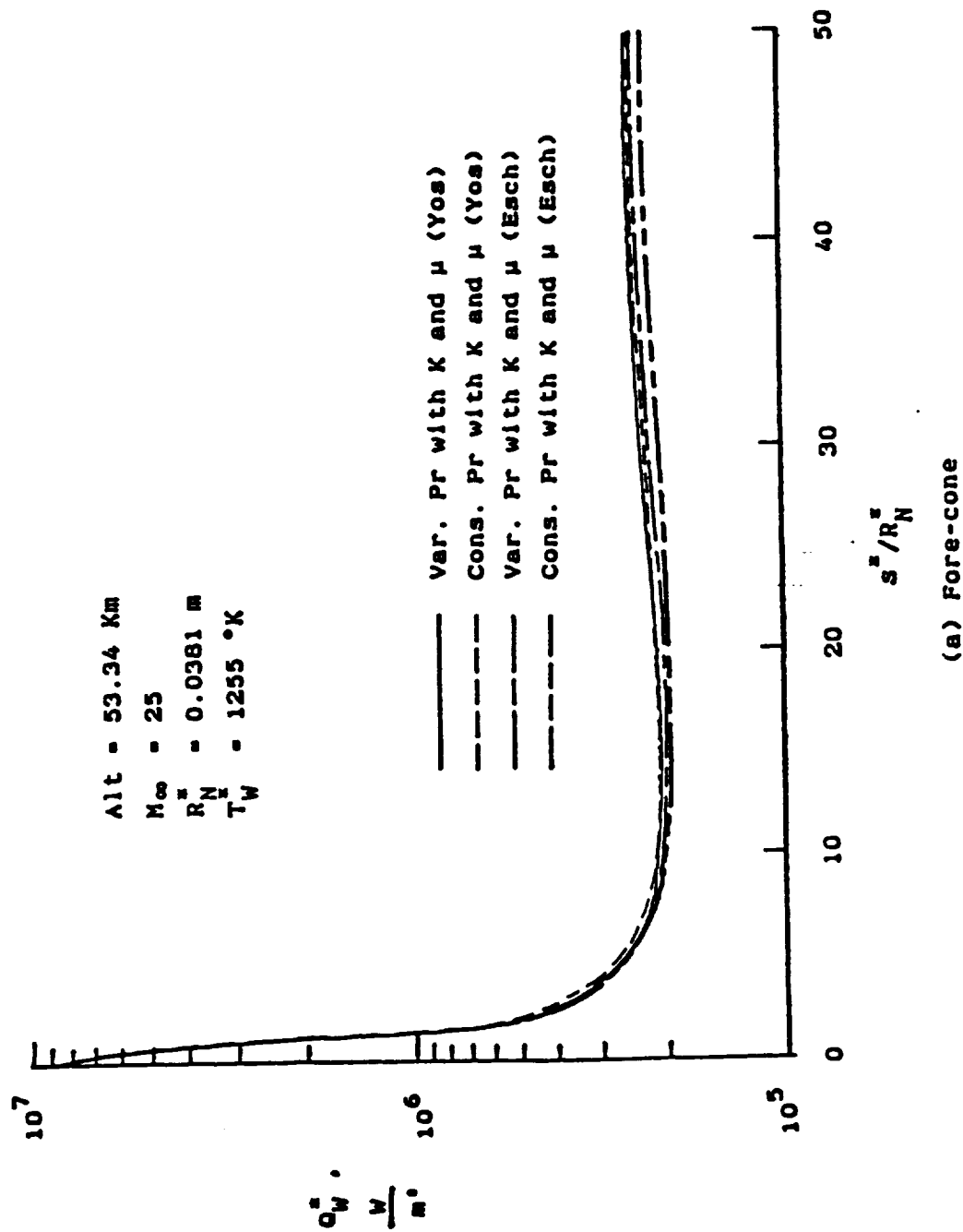
Fig. 5.30 Effect of the transport curve fit relations on surface
heat transfer rate for a 6° sphere-cone (fore-cone).
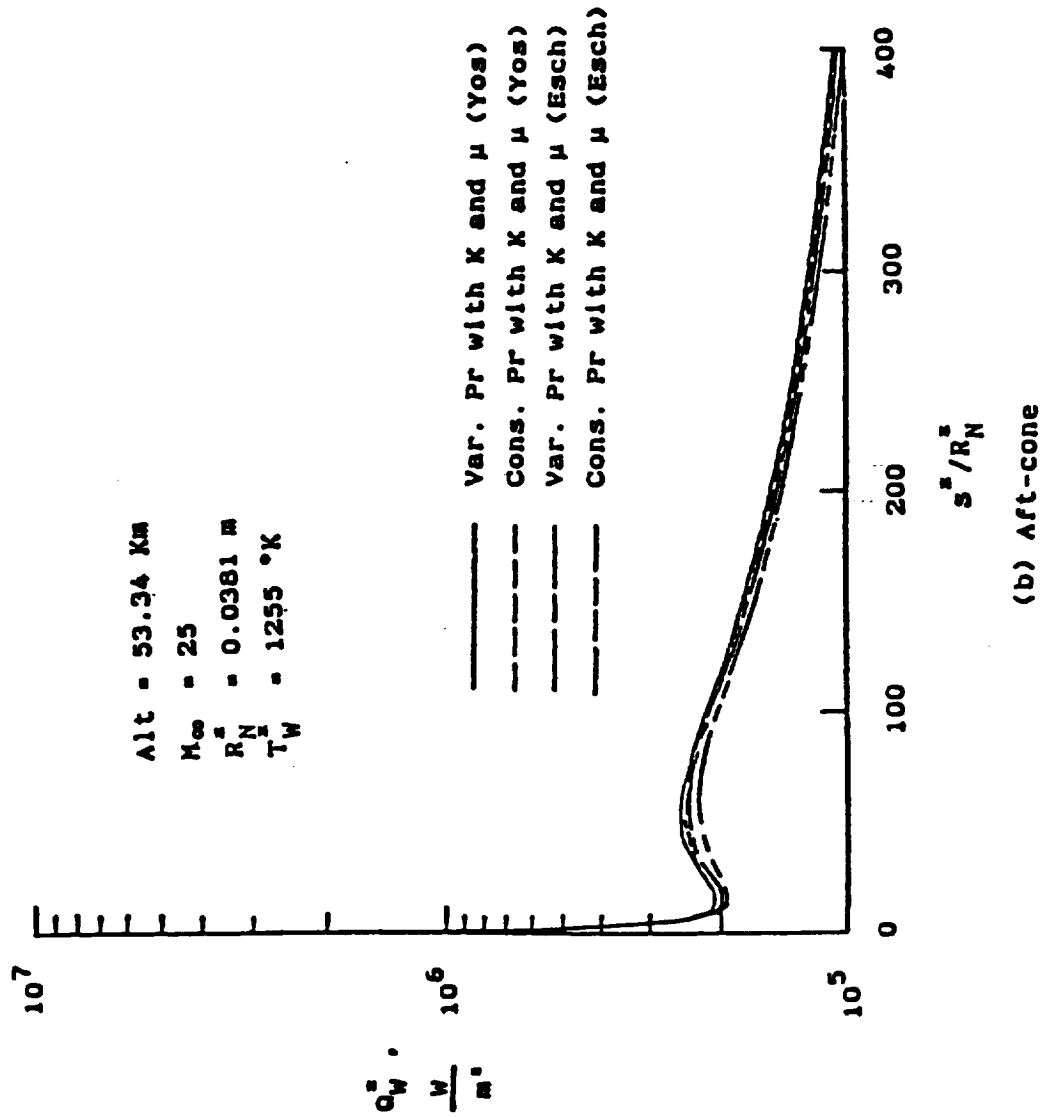
Fig. 5.31 Effect of the transport curve fit relations on surface heat transfer rate for a 6° sphere-cone (aft-cone).

C-3

The maximum differences between the two sets of results are about five percent. The differences between Thompson's results and the present results, which are obtained using Yos' data, are about nine percent. The reason for the discrepancy may be due to using different shock shape and normal-direction grid size. The outer boundary conditions depend on the shock shape, and the gradients of the flowfield quantities depend on the grid size.

Figures 5.30 and 5.31 show the surface heat transfer rates for variable as well as constant Prandtl number. Both Yos' and Esch's data have been used to compute the individual transport properties. The constant Prandtl number is set equal to 0.72. The predictions for the constant Prandtl number with Esch's data are always lower than the other predictions. On the other hand, the predictions for the variable Prandtl number with Yos' data are the highest values. Using Yos' data, higher surface heat transfer predictions are obtained for constant or variable Prandtl number than that using Esch's data. The differences between that using the variable Prandtl number with Yos' data and that using a constant Prandtl number with the Esch's data are about ten percent in the recompression region and about five percent on the other locations.

5.8 Conclusions

Numerical solutions of the viscous shock-layer equations under nonequilibrium chemistry conditions are presented for hypersonic flow over long slender bodies. The method of solution used for the viscous shock-layer equations is a partially coupled spatial-marching implicit finite-difference technique. The flow cases analyzed include

noncatalytic, finite catalytic, and fully catalytic surfaces. Results from the present method show that the coupling between the global continuity and normal momentum equations is essential and adequate to obtain stable solutions past long slender bodies. The comparisons of the present predictions with the STS-2 laminar heating data indicate that the oxygen surface reaction rate expression of Zoby can give better agreement with the flight data than the extrapolation of ground based experimental recombination data. It is shown that near the stagnation region of the vehicle, some degree of nonequilibrium flow persists to altitudes as low as 50 km.

It is shown that surface catalytic effects as well as body angles influence significantly the surface heat transfer rates. For a noncatalytic surface, the heating rates can decrease more than 50 percent in comparison to that for a fully catalytic surface near the stagnation region. These effects become less significant in the downstream region. It is also shown that the heating rate due to diffusion for a smaller body-angle sphere cone is not as important as for a larger body-angle in the downstream region.

In order to reduce surface heat transfer rate and drag force on the bodies, the desirable geometries of hypersonic vehicles are slender bodies with blunt noses. Although increasing the nose bluntness can decrease the surface heating rate, it will increase the pressure drag coefficients. Optimization should be made between the drag and heat transfer rate.

With thermodynamic and transport properties from Esch's data and for a constant Prandtl number, the present method always predicts lower heating rate than that from Yos' data. For higher temperature

conditions, the polynomial curve-fit formulas for species transport and thermodynamic properties based on Yos' and Browne's data can give better predictions of surface heat transfer.

Chapter 6

CONCLUDING REMARKS

A method for solving the viscous shock-layer equations for hypersonic flows over long slender bodies is presented. These equations are solved by employing a spatial-marching, implicit finite-difference technique. The two first-order equations, continuity and normal momentum, are solved simultaneously as a coupled set. This method yields a simple and computationally efficient technique.

A wide range of flow conditions has been considered in this study. This includes conditions from high Reynolds number at low altitudes to low Reynolds number at high altitudes. At low altitudes, the hypersonic flow over a slender body usually becomes turbulence. Two algebraic turbulence models, Cebeci-Smith and Baldwin-Lomax, have been used with the present numerical technique for application to long slender bodies. At high altitudes, the low density effects become important. Recently obtained surface-slip and corrected shock-slip conditions are employed to account for these effects. At higher altitudes, the gas becomes chemically reacting. Under certain conditions, the flows are characterized by chemical nonequilibrium conditions in the shock layer. Numerical solutions under these conditions are also obtained for long slender bodies.

Results for different conditions are obtained for axisymmetric bodies at an angle of attack of zero degree. Detailed comparisons have

been made with other predictions and experimental data for slender body
flows to assess the accuracy of the present numerical technique. The
results show that the coupling between the continuity and normal
momentum equations is essential and adequate to obtain stable and
accurate solutions past long slender bodies. This is true for both the
chemically nonreacting and reacting flows.

It is shown that both the Cebeci-Smith and Baldwin-Lomax models
are adequate for application to long slender bodies. Due to the
sensitivity of the Cebeci-Smith turbulence model to the boundary layer
edge location, it is imperative that the numerical method provide good
resolution and accurate solutions near the boundary layer edge. The
Baldwin-Lomax turbulence model, which avoids the use of conventional
boundary layer thickness in its formulation, appears more convenient to
implement. However, it has been shown that the constant, C_{cp}, depends
on the flow Mach number. Based upon this study and other
investigations, a linear dependence of this constant with Mach number is
suggested. Further comparisons with experimental data are needed to
verify this dependence.

Using the corrected slip models, the viscous shock-layer
predictions compare quite favorably with experimental data. The slip
effects become insignificant in the downstream region or at altitudes
less than about 60 km for geometry and conditions considered in this
study. Significant slip effects are observed primarily in the
stagnation region. Comparison between Navier-Stokes and viscous shock-
layer results indicates that viscous shock-layer equations, even with
body and shock slip, do not give physically consistent results in the

stagnation region above approximately 75 km altitude for the conditions considered here.

The present prediction with finite-rate chemistry yields good comparison with the STS-2 laminar heating data. Near the stagnation region of the vehicle, some degree of nonequilibrium flow can persist to altitudes as low as 50 km. Under chemical nonequilibrium conditions, the surface catalytic effects can influence significantly the surface heat transfer. For a noncatalytic surface, the heating rates can decrease more than 50 percent in comparison to that for a fully catalytic surface near the stagnation region. These effects become less significant in the downstream region. The heating rate due to diffusion for a smaller body-angle sphere cone is not as important as for a larger body-angle sphere cone in the downstream region.

For further study, it is recommended that the present method be used to study the following physical problems

1. incorporate surface and shock slip conditions in the finite rate chemistry code to investigate the low density effects.

2. increase the number of species, including ionized species.

3. incorporate a convenient radiative transfer model to investigate the effects of radiative heat transfer in the shock layer.

4. analyze the effects of angle of attack by developing three-dimensional viscous shock-layer equations.

5. modify the viscous shock-layer equations with equilibrium chemistry for long slender bodies.

REFERENCES

1. Williams, R. M., "National Aero-Space Plane: Technology for America's Future," Aerospace America, November 1986, pp. 18-22.

2. Martin, J. A., et al., "Special Section - Orbit-on Demand Vehicle," Aerospace America, February 1985, pp. 46-48.

3. Marsh, A, K., "USAF Studies Transatmosphere Vehicle," Aviation Week and Space Technology, Vol. 119, No. 19, November 1983 pp. 45.

4. Anderson, J. D., Jr., Fundamentals of Aerodynamics, McGraw-Hill Book Co., New York, 1984.

5. Anderson, J. D., "A Survey of Modern Research in Hypersonic Aerodynamics," AIAA Paper 84-1578, June 1984.

6. Blottner, F, G., "Viscous Shock Layer at the Stagnation Point with Nonequilibrium Air Chemistry," AIAA Journal, Vol. 7, No. 12, December 1969, pp. 2281-2288.

7. Wright, R. L. and Zoby, E, V., "Flight Boundary Layer Transition Measurements on a Slender Cone at Mach 20," AIAA Paper 77-719, June 1977.

8. Van Dyke, M., "A Review and Extension of Second-Order Hypersonic Boundary Layer Theory," Rarefied Gas Dynamics, Fluid Symposium Supplement 2, edited by J. A. Lauermann, Vol. II, Academic Press, New York, 1963.

9. Marchand, E. O., Lewis, C. H., and Davis, R. T., "Second-Order Boundary-Layer Effects on a Slender Blunt Cone at Hypersonic Conditions," AIAA Paper 68-54, New York, January 1968.

10. Jain, A. C. and Adimurthy, V., "Hypersonic Merged Stagnation Shock Layers, Part II, Cold Wall Case," AIAA Journal, Vol. 12, No. 3, March 1974, pp. 348-354.

11. Graves, R. A., "Solutions to the Navier-Stokes Equations for Supersonic Flow over Blunt Bodies with Massive Wall Blowing," Ph.D. Dissertation, George Washington University, November 1977.

12. Davis, R. T., "Numerical Solution of the Hypersonic Viscous Shock Layer Equations," AIAA Journal, Vol. 8, No. 5, May 1970, pp. 843-851.

13. Werle, M, J., Srivastava, B. N., and Davis, R. T., "Numerical Solutions to the Full Viscous Shock Layer Equations Using an ADI Technique," Department of Aerospace Engineering, University of Cincinnati, Report No. AFL-74-7-13, August 1974.

14. Truitt, R. W., Hypersonic Aerodynamic, The Ronald Press Co., New York, 1959.

15. Hosny, W. M., Davis, R. T., and Werle, M, J., "Improvements to the Solution of Viscous Shock Layer Equations," Arnold Engineering Development Center Report No. TR-79-25, August 1979.

16. Gordon, R. and Davis, R. T., "An Improved Method for Solving the Viscous Shock Layer Equations," Department of Aerospace Engineering and Engineering Mechanics, University of Cincinnati, Technical Report, September 1985.

17. Waskiewicz, J. D. and Lewis, C. H., "Recent Developments in Viscous Shock-Layer Theory," Aerospace and Ocean Engineering Department, Virginia Polytechnic Institute and State University, Report No. AERO-079, March 1978.

18. Cebeci, T. and Smith, A. M. O., Analysis of Turbulent Boundary Layers, Academic Press, New York, 1974.

19. Anderson, E. C. and Moss, J. N., "Numerical Solution of the Hypersonic Viscous-Shock-Layer Equations for Laminar, Transitional, and Turbulent Flows of a Perfect Gas Over Blunt Axially Symmetric Bodies," NASA TN D-7865, February 1975.

20. Baldwin, B. S. and Lomax, H., "Thin Layer Approximation and Algebraic Model for Separated Turbulent Flows," AIAA Paper 78-0257, January 1978.

21. Knight, D. D., "A Hybrid Explicit-Implicit Numerical Algorithm for the Three-Dimensional Compressible Navier-Stokes Equation," AIAA Paper 83-0223, January 1983.

22. Shirazi, S. A., and Truman, C. R., "Comparison of Algebraic Turbulence Models for PNS Predicitions of Supersonic Flow Past a Sphere-Cone," AIAA Paper 87-0544, January 1987.

23. Anderson, E. C. and Moss, J. N., "Numerical Solution of the Steady-State Navier-Stokes Equations for Hypersonic Flow About Blunt Axisymmetric Bodies," NASA TM X-71977, June 1974.

24. Moss, J. N., "Reacting Viscous-Shock-Layer Solutions with Multicomponent Diffusion and Mass Injection," NASA TR-R-411, June 1974.

25. Anderson, E. C. and Moss, J. N., "Viscous-Shock-Layer Solution for Turbulent Flow of Radiation Gas Mixtures in Chemical Equilibrium," NASA TM-X-72764, August 1975.

26. Gupta, R. N. and Simmonds, A. L., "Hypersonic Low-Density Solutions of the Navier-Stokes Equations with Chemical Nonequilibrium and Multicomponents Surface Slip," AIAA Paper 86-1349, June 1986.

27. Bird, R. B., Stewart, W. E., and Lightfoot, E. N., Transport Phenomena, John Wiley & Sons, Inc., 1960.

28. Williams, F. A., Combustion Theory, Addison-Wesley Pub. Co., Inc., 1965.

29. Blottner, F. G., "Finite Difference Methods of Solution of the Boundary-Layer Equations," AIAA Journal, Vol. 8, No. 2, February 1970, pp. 193-205.

30. Shidlovskiy, V. P. (Scripta Technica, Inc., Transl.), Introduction to the Dynamics of Rarefied Gases, American Elsevier Pub. Co., Inc., 1967.

31. Gupta, R. N., Scott, C. D., and Moss, J. N., "Slip-Boundary Equations for Multicomponent Nonequilibrium Airflow," NASA TP-2452, November 1985.

32. Cheng, H. K., "The Blunt-Body Problem in Hypersonic Flow at Low Reynolds Number," Institute Aerospace Science Paper No. 63-92, Cornell Aeronautical Laboratory Report No. AF-1285-A-10, June 1963.

33. Coakley, T. J., "Turbulence Modeling Methods for the Compressible Navier-Stokes Equations," AIAA Paper 83-1693, July 1983.

34. Thompson, R. A., Zoby, E. V., Wurster, K. E., and Gnoffo, P. A., "An Aerothermodynamic Study of Slender Conical Vehicles," AIAA Paper 87-1475, June 1987.

35. York, B. and Knight, D., "Calculation of a Class of Two-Dimensional Turbulent Boundary Layer Flows Using the Baldwin-Lamax Model," AIAA Paper 85-0126, January 1985.

36. Visbal, M. and Knight, D., "The Baldwin-Lomax Turbulence Model for Two-Dimensional Shock-Wave/Boundary-Layer Interactions," AIAA Journal, Vol. 22, No. 7, July 1984, pp. 921-928.

37. Gupta, R. N., Lee, K. P., Moss, J. N., Zoby, E. V., and Tiwari, S. N., "Viscous Shock-Layer Analysis of the High-Reynolds-Number Hypersonic Flow Past Long Slender Bodies," AIAA Paper 87-2487, August 1987.

38. Degani, D. and Schiff, L. B., "Computation of Supersonic Viscous Flows Around Pointed Bodies Having Crossflow Separation," Journal of Computational Physics, Vol. 66, January 1986, pp. 173-196.

39. Dhawan, S. and Narasimha, R., "Some Properties of Boundary Layer Flow During Transition from Laminar to Turbulent Motion," *Journal of Fluid Mechanics*, Vol. 3, Part 4, January 1958, pp. 418-436.

40. Richtmyer, R. D., *Difference Methods for Initial-Value Problems*, Interscience, New York, 1957.

41. Vigneron, Y. C., Rakich, J. V., and Tannehill, J. C., "Calculation of Supersonic Viscous Flow over Delta Wings with Sharp Supersonic Leading Edges," AIAA Paper 78-1137, July 1978.

42. Murray, A. L. and Lewis, C. H., "Hypersonic Three-Dimensional Viscous Shock Layer Flows Over Blunt Bodies," *AIAA Journal*, Vol. 16, No. 12, December 1978, pp. 1279-1286.

43. Srivastava, B. N., Werle, M. J., and Davis, R. T., "Viscous Shock Layer Solutions for Hypersonic Sphere-Cones," Arnold Engineering Development Center Report No. TR-77-20, January 1977.

44. Thompson, R. A., Private Communication, NASA Langley Research Center, Hampton, Virginia.

45. Gnoffo, P. A., "Hypersonic Flows Over Biconics Using a Variable-Effective-Gamma, Parabolized-Navier-Stokes Code," AIAA Paper 83-166, July 1983.

46. Little, H. R., "An Experimental Investigation of Surface Conditions on Hyperboloids and Paraboloids at a Mach Number of 10," M. S. Thesis, University of Tennessee, June 1969.

47. Cleary, J. W., "Effects of Angle of Attack and Bluntness on Laminar Heating-Rate Distributions of a 15 Degree Cone at a Mach Number of 10.6," NASA TN D-5450, October 1969.

48. Miller, C. G., III and Gnoffo, P. A., "Pressure Distributions and Shock Shapes for $12.84°/7°$ On-Axis and Bent-Nose Biconics in Air at Mach 6," NASA TM-83222, December 1981.

49. Miller, C. G., III, "Experimental and Predicted Heating Distributions for Biconics at Incidence in Air at Mach 10," NASA TP-2334, November 1984.

50. Widhopf, G. F., "Turbulent Heat Transfer Measurements On a Blunt Cone at Angle of Attack," Aerospace Corporation, San Bernardino, California, Aerospace Report No. TR-0059-(S6816-66)-1, February 1971.

51. Carver, D. B., "Heat Transfer, Surface Pressure and Flow Field Surveys on Conic and Biconic Models with Boundary Layer Trips at Mach 8 - Phases IV snf VI," Calspan/Arnold Engineering Development Center Division, Report No. AEDC-TSR-80-V14, March 1980.

52. Bird, G. A., "Low Density Aerothermodynamics," AIAA Paper 85-0994, June 1985.

53. Bird, G. A., Molecular Gas Dynamics, Oxford University Press, London, 1976.

54. Patterson, G. N., Molecular Flow of Gases, Wiley, New York, 1965.

55. Scott, C. D., "Reacting Shock Layers with Slip and Catalytic Boundary Conditions," AIAA Journal, Vol. 13, No. 10, October 1975, pp. 1271-1278.

56. Davis, R. T., "Hypersonic Flow of a Chemically Reacting Binary Mixture Past a Blunt Body," AIAA Paper 70-805, June 1970.

57. Tree, I. K., Melson, N. D., and Lewis, C. H., "Low Reynolds Number Hypersonic Ionizing Viscous Shock-Layer Over the Jovian Probe," AIAA Paper 79-1080, June 1979.

58. Tiwari, S. N. and Szema, K. Y., "The Significance of Shock and Body Slip Conditions on Jovian Entry Heating," NASA CR-123456, January 1979.

59. Tiwari, S. N. and Szema, K. Y., "Effects of Precursor Heating on Radiating and Chemically Reacting Viscous Flow Around a Jovian Entry Body," NASA CR-3186, October 1979.

60. Swaminathan, S., Song, D. J., and Lewis, C. H., "Effects of Slip and Chemical Reaction Models on Three-Dimensional Nonequilibrium Viscous Shock-Layer Flows," Journal of Spacecraft and Rockets, Vol. 21, November-December 1984, pp. 521-527.

61. Song, D. J. and Swaminathan, S., "High Altitude Effects on Three-Dimensional Nonequilibrium Viscous Shock-Layer Flows," Journal of Spacecraft and Rockets, Vol. 22, November-December 1985, pp. 614-619.

62. Lee, K. P., Gupta, R. N., Moss, J. N., Zoby, E. V., and Tiwari, S. N., "Viscous Shock-Layer Solutions for the Low-Density Hypersonic Flow Past Long Slender Bodies," AIAA Paper 88-0460, January 1988.

63. Scott, C. D., "Wall Boundary Equations with Slip and Catalysis for Multicomponent, Nonequilibrium Gas Flows," NASA TM X-58111, December 1973.

64. Boylan, D. E., "Laminar Heat Transfer on Sharp and Blunt Ten-Degree Cones in Conical and Parallel Low Density Flow," Arnold Engineering Development Center Report No. TR-73-106, August 1973.

65. Boylan, D. E., Private Communication, Severdrup Technology, Inc., Tullahoma, Tennessee, February 1987.

66. Jain, A. C. and Adimurthy, V., "Hypersonic Merged Stagnation Shock Layers, Part I: Adiabatic Wall Case," AIAA Journal, Vol. 12, No. 3, March 1974, pp. 342-347.

67. Potter, J. L. and Balley, A. B., "Pressures in the Stagnation Region of Blunt Bodies in the Viscous Layer to Merged Layer Regimes of Rarefied Flow," Arnold Engineering Development Center Report No. TDR-63-168, September 1963.

68. Anderson, J. D., Jr., Modern Compressible Flow: With Historical Perspective, McGraw-Hill Book Co., New York, 1982, pp. 334-390.

69. Scott, C. D., "Effects of Nonequilibrium and Catalysis on Shuttle Heat Transfer," AIAA Paper 83-1485, June 1983.

70. Scott, C. D. and Derry, S. H., "Catalytic Recombination and the Space Shuttle Heating," Entry Vehicle Heating and Thermal Protection Systems, edited by P. E. Bauer and H. E. Collicott, Vol. 85 of AIAA Progress in Astronautics and Aeronautics, New York, 1983, pp. 123-149.

71. Rakich, J. V., Stewart, D. A., and Lanfranco, M. J., "Results of a Flight Experiment on the Catalytic Efficiency of the Space Shuttle Heat Shield," AIAA Paper 82-0944, June 1982.

72. Shinn, J. L., Moss, J. N., and Simmonds, A. L., "Viscous-Shock-Layer Heating Analysis for the Shuttle Windward Plane with Surface Finite Catalytic Recombination Rates," AIAA Paper 82-0842, June 1982.

73. Stewart, D. A., Rakich, J. V., and Lanfranco, M. J., "Catalytic Surface Effects Experiment on the Space Shuttle," Thermophysics of Atmospheric Entry, edited by T. E. Horton, Vol. 82 of AIAA Progress in Astronautics and Aeronatics, New York, 1982, pp. 248-272.

74. Shinn, J. L. and Jones, J. J., "Chemical Nonequilibrium Effects on Flowfields for Aeroassisted Orbital Transfer Vehicles," Journal of Spacecraft and Rockets, Vol. 22, No. 1, January-February 1985, pp. 54-59.

75. Thompson, R. A., "Comparison of Nonequilibrium Viscous-Shock-Layer Solutions with Windward Surface Shuttle Heating Data," AIAA Paper 87-1473, June 1987.

76. Shinn, J. L. and Simmonds, A. L., "Comparison of Viscous-Shock-Layer Heating Analysis with Shuttle Flight Data in Slip Flow Regime," AIAA Paper 84-0226, January 1984.

77. Zoby, E. V., Gupta, R. N., and Simmonds, A. L. "Temperature-Dependent Reaction Rate Expressions for Oxygen Recombination," Thermal Design of Aeroassisted Orbital Transfer Vehicles, edited by H. F. Nelson, Vol. 96 of AIAA Progress in Astronautics and Aeronautics, New York, 1985, pp. 445-465.

78. Goulard, R., "On Catalytic Recombination Rates in Hypersonic Stagnation Heat Transfer," Jet Propulsion, Vol. 28, November 1958, pp. 737-745.

79. Scott, C. D., "Catalytic Recombination of Oxygen and Nitrogen in High Temperature Reusable Surface Insulation," Aerothermodynamics and Planetary Entry, edited by A. L. Crosbie, Vol. 77 of AIAA Progress in Astronautics and Aeronautics, New York, 1981, pp. 192-212.

80. Vincenti, W. G. and Kruger, C. H., Jr., Introduction to Physical Gas Dynamics, John Wiley & Sons, Inc., 1965.

81. Blottner, F. G., Johnson, M., and Ellis, M., "Chemically Reacting Viscous Flow Program for Multi-Component Gas Mixtures," Sandia Laboratories Report SC-RR-70-754, December 1971.

82. Esch, D. D., Siripong, A., and Pike, R. W., "Thermodynamic Properties in Polynomial Form for Carbon, Hydrogen, Nitrogen, and Oxygen Systems From 300 to 15000 ^{o}K," Reacting Fluids Laboratory, Department of Chemical Engineering, Louisiana State University Report No. NASA-FFL-TR-70-3, November 1970.

83. Shinn, J. L., Personal Communication, Aerothermodynamics Branch, NASA Langley Research Center, Hampton, Virginia, 1985.

84. Browne, W. G., "Thermodynamic Properties at Some Atoms and Atomic Ions," General Electric Co., Missile & Space Vehicle Department, Engineering Physics Techical Memo No. 2, 1962.

85. Browne, W. G., "Thermodynamic Properties of Some Diatoms and Diatomic Ions at High Temperature," General Electric Co., Missile & Space Vehicle Department, Engineering Physics Techical Memo No. 8, May 1962.

86. Esch, D. D., Pike, R. W., Engel, C. K., Farmer, R. C., and Balhoff, J. F., "Stagnation Region Heating of a Phenolic-Nylon Ablator During Return From Planetary Missions," NASA CR-112026, September 1971.

87. Yos, J. M., "Single Species Transport Properties for High Temperatures Gases," Personal Communication to R. N. Gupta, Systems Division, AVCO, Wilmington, MS, June 1985.

88. Armaly, B. F. and Sutton, K., "Viscosity of Multicomponent Partially Ionized Gas Mixtures," AIAA Paper 80-1495, July 1980.

89. Mason, E. A. and Saxena, S. C., "Approximate Formula for the Thermal Conductivity of Gas Mixtures," Physics of Fluids, Vol. 1, No. 5, September-October 1958, pp. 361-369.

90. Throckmorton, D. A., "Benchmark Determination of Shuttle Orbiter Entry Aerodynamic Heat-Transfer Data," Journal of Spacecraft and Rockets, Vol. 20, No. 3, May-June 1983, pp. 219-224.

91. Zoby, E. V., "Approximate Heating Analysis for the Windward Symmetry Plane of Shuttle-Like Bodies at Large Angle of Attack," Thermophysics of Atmospheric Entry, edited by T. E. Horton, Vol. 82 of AIAA Progress in Astronautics and Aeronautics, New York, 1982, pp. 229-247.

92. Gupta, R. N., Moss, J. N., Simmonds, A. L., Shinn, J. L., and Zoby, E. V., "Space Shuttle Heating Analysis with Variation in Angle of Attack and Surface Condition," Journal of Spacecraft and Rockets, Vol. 21, March-April 1984, pp. 217-219.

93. Gupta, R. N., Yos, J. M., Thompson, R. A., and Lee, K. P., "A Review of Reaction Rates and Thermodynamic and Transport Properties of an 11-Species Air Model for Chemical and Thermal Nonequilibrium Calculations to 30000K," NASA RP-1232, August 1990.

94. Browne, W. G., "Thermodynamic Properties of Some Diatomic and Linear Polyatomic Molecules," General Electric Co., Missile & Space Vehicle Department, Engineering Physics Techical Memo No. 3, 1962.

APPENDIX A

COEFFICIENTS OF CONTINUITY AND NORMAL MOMENTUM
EQUATIONS AS A COUPLED SET

The coefficients of Eqs. (3.60)-(3.65) are given in this appendix.
For a perfect gas, the coefficients in Eqs. (3.60)-(3.63) are given as

$$A_{c,n+1/2} = \frac{(r + \bar{\eta}_{n+1/2} n_{sh} \cos\theta)(1 + \bar{\eta}_{n+1/2} n_{sh} \kappa)}{\Delta \eta_n} \left(\frac{dg}{d\bar{\eta}}\right)_{n+1/2} \qquad (A.1)$$

$$B_{c,n+1/2} = - \frac{(r + \bar{\eta}_{n+1/2} n_{sh} \cos\theta)(1 + \bar{\eta}_{n+1/2} n_{sh} \kappa)}{\Delta \eta_n} \left(\frac{dg}{d\bar{\eta}}\right)_{n+1/2} \qquad (A.2)$$

$$C_{c,n+1/2} = \frac{n_{sh}(r + \bar{\eta}_{n+1/2} n_{sh} \cos\theta) u_{m,n+1/2}}{2\Delta \xi_{m-1} \, P_{m,n+1/2}} +$$

$$[\frac{(r + \bar{\eta}_{n+1/2} n_{sh} \cos\theta)(1 + \bar{\eta}_{n+1/2} n_{sh} \kappa) \, v_{m,n+1/2}}{\Delta \eta_n \, P_{m,n+1/2}} -$$

$$\frac{n'_{sh}(r + \bar{\eta}_{n+1/2} n_{sh} \cos\theta)\bar{\eta}_{n+1/2} u_{m,n+1/2}}{\Delta \eta_n \, P_{m,n+1/2}}] \left(\frac{dg}{d\bar{\eta}}\right)_{n+1/2} \qquad (A.3)$$

$$D_{c,n+1/2} = \frac{n_{sh}(r+\bar{\eta}_{n+1/2}n_{sh}\cos\theta)u_{m,n+1/2}}{2\Delta\xi_{m-1}\ P_{m,n+1/2}} -$$

$$[\frac{(r+\bar{\eta}_{n+1/2}n_{sh}\cos\theta)(1+\bar{\eta}_{n+1/2}n_{sh}\kappa)\ v_{m,n+1/2}}{\Delta\eta_n\ P_{m,n+1/2}} -$$

$$\frac{n'_{sh}(r+\bar{\eta}_{n+1/2}n_{sh}\cos\theta)\ \bar{\eta}_{n+1/2}u_{m,n+1/2}}{\Delta\eta_n\ P_{m,n+1/2}}]\ (\frac{d\bar{g}}{d\bar{\eta}})_{n+1/2} \qquad (A.4)$$

$$E_{c,n+1/2} = \frac{n_{sh}(r+\bar{\eta}_{n+1/2}n_{sh}\cos\theta)\ u_{m,n+1/2}}{2\Delta\xi_{m-1}\ P_{m,n+1/2}}(p_{m-1,n+1} + p_{m-1,n})$$

$$- \frac{n_{sh}(r+\bar{\eta}_{n+1/2}n_{sh}\cos\theta)}{2\Delta\xi_{m-1}}$$

$$x\ \{u_{m,n+1} + u_{m,n} - u_{m-1,n+1} - u_{m-1,n} - (\frac{u_{m,n+1/2}}{T_{m,n+1/2}})$$

$$x\ [T_{m,n+1} + T_{m,n} - T_{m-1,n+1} - T_{m-1,n}]\} -$$

$$\frac{n_{sh}u_{m,n+1/2}}{2\Delta\xi_{m-1}}\ [(r+\bar{\eta}_{n+1}n_{sh}\cos\theta)_m + (r+\bar{\eta}_n n_{sh}\cos\theta)_m -$$

$$(r+\bar{\eta}_{n+1}n_{sh}\cos\theta)_{m-1} - (r+\bar{\eta}_n n_{sh}\cos\theta)_{m-1}] +$$

$$\frac{(r+\overline{\eta}_{n+1/2}{}^n{}_{sh}\cos\theta)(1+\overline{\eta}_{n+1/2}{}^n{}_{sh}\kappa)v_{m,n+1/2}}{\Delta\eta_n\ T_{m,n+1/2}}(\frac{dg}{d\overline{\eta}})_{n+1/2}$$

$$x\ (T_{m,n+1}-T_{m,n})+\frac{n'_{sh}\overline{\eta}_{n+1/2}(r+\overline{\eta}_{n+1/2}{}^n{}_{sh}\cos\theta)}{\Delta\eta_n}$$

$$x\ (\frac{dg}{d\overline{\eta}})_{n+1/2}[u_{m,n+1/2}-u_{m,n}-(\frac{u_{m,n+1/2}}{T_{m,n+1/2}})$$

$$x\ (T_{m,n+1}-T_{m,n})]+n'_{sh}{}^n{}_{sh}\overline{\eta}_{n+1/2}u_{m,n+1/2}\cos\theta\ -$$

$$v_{m,n+1/2}{}^n{}_{sh}[\kappa(r+\overline{\eta}_{n+1/2}{}^n{}_{sh}\cos\theta)+\cos\theta(1+\overline{\eta}{}^n{}_{sh}\kappa)]\quad\text{(A.5)}$$

$$A_{NM,n+1/2}=\frac{n_{sh}u_{m,n+1/2}p_{m,n+1/2}}{2\Delta\xi_{m-1}(1+\overline{\eta}_{n+1/2}{}^n{}_{sh}\kappa)}\ -$$

$$[\frac{n'_{sh}\overline{\eta}_{n+1/2}u_{m,n+1/2}p_{m,n+1/2}}{\Delta\eta_n(1+\overline{\eta}_{n+1/2}{}^n{}_{sh}\kappa)}-\frac{p_{m,n+1/2}v_{m,n+1/2}}{\Delta\eta_n}]$$

$$x\ (\frac{dg}{d\overline{\eta}})_{n+1/2}\qquad\qquad\text{(A.6)}$$

$$B_{NM,n+1/2}=\frac{n_{sh}u_{m,n+1/2}p_{m,n+1/2}}{2\Delta\xi_{m-1}(1+\overline{\eta}_{n+1/2}{}^n{}_{sh}\kappa)}+[\frac{n'_{sh}\overline{\eta}_{n+1/2}u_{m,n+1/2}p_{m,n1/2}}{\Delta\eta_n(1+\overline{\eta}_{n+1/2}{}^n{}_{sh}\kappa)}\ -$$

$$\frac{P_{m,n+1/2}V_{m,n+1/2}}{\Delta\eta_n}](\frac{dg}{d\bar{\eta}})_{n+1/2} \quad (A.7)$$

$$C_{NM,n+1/2} = (\frac{\gamma-1}{\gamma})\frac{T_{m,n+1/2}}{\Delta\eta_n}(\frac{dg}{d\bar{\eta}})_{n+1/2} \quad (A.8)$$

$$B_{NM,n+1/2} = -(\frac{\gamma-1}{\gamma})\frac{T_{m,n+1/2}}{\Delta\eta_n}(\frac{dg}{d\bar{\eta}})_{n+1/2} \quad (A.9)$$

$$E_{NM,n+1/2} = \frac{n_{sh}P_{m,n+1/2}u^2_{m,n+1/2}\kappa}{(1+\bar{\eta}_{n+1/2}n_{sh}\kappa)} +$$

$$\frac{n_{sh}u_{m,n+1/2}P_{m,n+1/2}}{2\Delta\xi_{m-1}(1+\bar{\eta}_{n+1/2}n_{sh}\kappa)} (v_{m-1,n+1} + v_{m-1,n}) \quad (A.10)$$

For a multicomponent mixture, the coefficients $A_{c,n+1/2}$, $B_{c,n+1/2}$, $C_{c,n+1/2}$ and $D_{c,n+1/2}$ are the same as Eqs. (A.1) to (A.4) and $E_{c,n+1/2}$ is equal to Eq. (A.5) plus the following terms

$$-\frac{n_{sh}(r+\bar{\eta}_{n+1/2}n_{sh}\cos\theta)u_{m,n+1/2}}{2\Delta\xi_{m-1} M_{m,n+1/2}} (M_{m,n+1} + M_{m,n} - M_{m-1,n+1}$$

$$- M_{m-1,n}) - \frac{(r+\bar{\eta}_{n+1/2}n_{sh}\cos\theta)(1+\bar{\eta}_{n+1/2}n_{sh}\kappa)v_{m,n+1/2}}{\Delta\eta_n M_{m,n+1/2}} (\frac{dg}{d\bar{\eta}})_{n+1/2}$$

$$x \; (M_{m,n+1} - M_{m,n}) + \frac{n'_{sh}\bar{n}_{n+1/2}(r + \bar{n}_{n+1/2} n_{sh} \cos\theta) u_{m,n+1/2}}{\Delta n_n \; M_{m,n+1/2}}$$

$$x \; (M_{m,n+1} - M_{m,n}) \hspace{5cm} (A.11)$$

$A_{NM,n+1/2}$, $B_{NM,n+1/2}$ and $E_{NM,n+1/2}$ are same as Eqs. (A.6), (A.7) and (A.10). The terms $C_{NM,n+1/2}$ and $D_{NM,n+1/2}$ are expressed as

$$C_{NM,n+1/2} = \left(\frac{R^*}{M_{m,n+1/2} \; C_{p,\infty}^*}\right)\frac{T_{m,n+1/2}}{\Delta n_n} \left(\frac{dg}{d\bar{n}}\right)_{n+1/2} \hspace{2cm} (A.12)$$

$$D_{NM,n+1/2} = - \left(\frac{R^*}{M_{m,n+1/2} \; C_{p,\infty}^*}\right)\frac{T_{m,n+1/2}}{\Delta n_n} \left(\frac{dg}{d\bar{n}}\right)_{n+1/2} \hspace{2cm} (A.13)$$

The coefficients K_1 to K_8 in Eqs. (3.64) and (3.65) are given by

$$K_1 = (A_{c,n+1/2} C_{NM,n+1/2} - A_{NM,n+1/2} C_{c,n+1/2})(B_{c,n-1/2} A_{NM,n-1/2}$$

$$- B_{NM,n-1/2} A_{c,n+1/2}) \hspace{4cm} (A.14)$$

$$K_2 = (A_{c,n+1/2} D_{NM,n+1/2} - A_{NM,n+1/2} D_{c,n+1/2})(B_{c,n-1/2} A_{NM,n-1/2} -$$

$$B_{NM,n-1/2} A_{c,n-1/2}) - (A_{c,n+1/2} B_{NM,n+1/2} - A_{NM,n+1/2} B_{c,n+1/2})$$

$$x \ (B_{c,n-1/2}C_{NM,n-1/2} - B_{NM,n-1/2}C_{c,n-1/2}) \qquad (A.15)$$

$$K_3 = - \ (A_{c,n+1/2}B_{NM,n+1/2} - A_{NM,n+1/2}B_{c,n+1/2})(B_{c,n-1/2}D_{NM,n-1/2}$$

$$- \ B_{NM,n-1/2}D_{c,n-1/2}) \qquad (A.16)$$

$$K_4 = - \ (A_{c,n+1/2}E_{NM,n+1/2} - A_{NM,n+1/2}E_{c,n+1/2})(B_{c,n-1/2}A_{NM,n-1/2} -$$

$$B_{NM,n-1/2}A_{c,n-1/2}) - (A_{c,n+1/2}B_{NM,n+1/2} - A_{NM,n+1/2}B_{c,n+1/2})$$

$$x \ (B_{c,n-1/2}E_{NM,n-1/2} - B_{NM,n-1/2}E_{c,n-1/2}) \qquad (A.17)$$

$$K_5 = (C_{c,n+1/2}A_{NM,n+1/2} - C_{NM,n+1/2}A_{c,n+1/2})(D_{c,n-1/2}C_{NM,n-1/2}$$

$$- \ D_{NM,n-1/2}C_{c,n-1/2}) \qquad (A.18)$$

$$K_6 = (C_{c,n+1/2}B_{NM,n+1/2} - C_{NM,n+1/2}B_{c,n+1/2})(D_{c,n-1/2}C_{NM,n-1/2} -$$

$$D_{NM,n-1/2}C_{c,n-1/2}) - (C_{c,n+1/2}D_{NM,n+1/2} - C_{NM,n+1/2}D_{c,n+1/2})$$

$$x \ (D_{c,n-1/2}A_{NM,n-1/2} - D_{NM,n-1/2}A_{c,n-1/2}) \qquad (A.19)$$

$$K_7 = - \ (C_{c,n+1/2}D_{NM,n+1/2} - C_{NM,n+1/2}D_{c,n+1/2})(D_{c,n-1/2}B_{NM,n-1/2}$$

$$- D_{NM,n-1/2}B_{c,n-1/2}) \qquad (A.20)$$

$$K_8 = (C_{c,n+1/2}E_{NM,n+1/2} - C_{NM,n+1/2}E_{c,n+1/2})(D_{c,n-1/2}C_{NM,-1/2} -$$

$$D_{NM,n-1/2}C_{c,n-1/2}) - (C_{c,n+1/2}D_{NM,n+1/2} - C_{NM,n+1/2}D_{c,n+1/2})$$

$$x \ (D_{c,n-1/2}E_{NM,n-1/2} - D_{NM,n-1/2}E_{c,n-1/2}) \qquad (A.21)$$

APPENDIX B

NAVIER-STOKES EQUATIONS IN THE BODY ORIENTED
COORDINATE SYSTEM

The steady-state form of the Navier-Stokes equations is taken from Anderson and Moss [23]. For an axisymmetric or two-dimensional body at zero angle of attack, these equations in the body-oriented coordinate can be written in the form of Eq. (2.25). All the coefficients in Eqs. (2.26) to (2.34) are the same except Eqs. (2.28), (2.32) and (2.36) are need to modify. This modification is given in this appendix.

For the steady-state Navier-Stokes equations, coefficient α_3 appearing in Eq. (2.25) should be replaced by α_3', which is defined as:

s-momentumu

$$\alpha_3' = \alpha_3 + \frac{n_{sh}^2}{\epsilon^2 \mu} (HOT)_s \qquad (B.1)$$

Energy Equation

$$\alpha_3' = \alpha_3 + \frac{n_{sh}^2}{\epsilon^2 (\mu/Pr)} [u(HOT)_s + (HOT)_e] \qquad (B.2)$$

where α_3 in Eqs. (B.1) and (B.2) is given by Eqs. (2.28) and (2.32), respectively. Abbreviation HOT in Eqs. (B.1) and (B.2) represents higher-order terms, and subscripts `s' and `e' imply terms in the s-momentum and energy equations, respectively.

The normal momentum equation, Eq. (2.36), for the Navier-Stokes model is modified to

$$(LHS)_{Eq. (2.12)} - (HOT)_n = 0 \tag{B.3}$$

where the first term in Eq. (B.3) implies the entire left-hand side of Eq. (2.36), and the second term represents the higher-order terms in the n-momentum equation.

The higher-order terms appearing in Eqs. (B.1) through (B.3) are defined as:

$$(HOT)_s = \frac{\epsilon^2}{(1+\bar{\eta}n_{sh}\kappa)} \left[\frac{\partial C_1}{\partial \xi} - \bar{\eta} \frac{n'_{sh}}{n_{sh}} \frac{\partial C_1}{\partial \eta} \frac{dg}{d\bar{\eta}}\right] - \frac{\epsilon^2}{(1+\bar{\eta}n_{sh}\kappa)}$$

$$\times \left[\frac{\partial C_2}{\partial \xi} - \bar{\eta} \frac{n'_{sh}}{n_{sh}} \frac{\partial C_2}{\partial \eta} \frac{dg}{d\bar{\eta}}\right] + \frac{\epsilon^2}{n_{sh}} \frac{\partial C_3}{\partial \eta} \frac{dg}{d\bar{\eta}} + \frac{\epsilon^2 \mu}{(1+\bar{\eta}n_{sh}\kappa)}$$

$$\times \left[\frac{2\kappa}{1+\bar{\eta}n_{sh}\kappa} + \frac{\cos\theta}{r+\bar{\eta}n_{sh}\cos\theta}\right] \times \left[\frac{\partial v}{\partial \xi} - \bar{\eta} \frac{n'_{sh}}{n_{sh}} \frac{\partial v}{\partial \eta} \frac{dg}{d\bar{\eta}}\right]$$

$$+ \frac{2\epsilon^2\mu}{(1+\bar{\eta}n_{sh}\kappa)(r+\bar{\eta}n_{sh}\cos\theta)} \left[\frac{\partial(r+\bar{\eta}n_{sh}\cos\theta)}{\partial\xi} - \bar{\eta}n'_{sh}\cos\theta\right]$$

$$\times \left\{\left(\frac{1}{1+\bar{\eta}n_{sh}\kappa}\right)\left[\frac{\partial u}{\partial\xi} - \bar{\eta}\frac{n'_{sh}}{n_{sh}}\frac{\partial u}{\partial\eta}\frac{dg}{d\bar{\eta}}\right] - \frac{u}{(1+\bar{\eta}n_{sh}\kappa)(r+\bar{\eta}n_{sh}\cos\theta)}\right.$$

$$\times \left.\left[\frac{\partial(r+\bar{\eta}n_{sh}\cos\theta)}{\partial\xi} - \bar{\eta}n'_{sh}\cos\theta\right] + v\left[\frac{\kappa}{1+\bar{\eta}n_{sh}\kappa} - \frac{\cos\theta}{r+\bar{\eta}n_{sh}\cos\theta}\right]\right\}$$

$$(HOT)_n = \frac{\epsilon^2}{(1+\bar{\eta}n_{sh}\kappa)}\left[\frac{\partial C_4}{\partial\xi} - \bar{\eta}\frac{n'_{sh}}{n_{sh}}\frac{\partial C_4}{\partial\eta}\frac{dg}{d\bar{\eta}}\right] + \frac{\epsilon^2 C_4}{(1+\bar{\eta}n_{sh}\kappa)(r+\bar{\eta}n_{sh}\cos\theta)}$$

$$\left[\frac{\partial(r+\bar{\eta}n_{sh}\cos\theta)}{\partial\xi} - \bar{\eta}n'_{sh}\cos\theta\right] + \frac{\epsilon^2}{n_{sh}}\frac{\partial C_5}{\partial\eta}\frac{dg}{d\bar{\eta}} - \frac{\epsilon^2}{n_{sh}}\frac{\partial C_6}{\partial\eta}\frac{dg}{d\bar{\eta}}$$

$$+ \frac{\epsilon^2\kappa C_9}{1+\bar{\eta}n_{sh}\kappa} + \frac{\epsilon^2 C_{10}\cos\theta}{r+\bar{\eta}n_{sh}\cos\theta} \qquad\qquad (B.5)$$

$$(HOT)_e = \frac{\epsilon^2}{(1+\bar{\eta}n_{sh}\kappa)(r+\bar{\eta}n_{sh}\cos\theta)}\left[\frac{\partial C_7}{\partial\xi} - \bar{\eta}\frac{n'_{sh}}{n_{sh}}\frac{\partial C_7}{\partial\eta}\frac{dg}{d\bar{\eta}}\right]$$

$$- \frac{\epsilon^2}{(1+\bar{\eta}n_{sh}\kappa)(r+\bar{\eta}n_{sh}\cos\theta)}\left[\frac{\partial C_8}{\partial\xi} - \bar{\eta}\frac{n'_{sh}}{n_{sh}}\frac{\partial C_8}{\partial\xi}\frac{dg}{d\bar{\eta}}\right]$$

$$+ \frac{9}{8}\frac{\epsilon^2 C_1^2}{\mu} + 2\epsilon^2\mu\left[\frac{1}{n_{sh}}\frac{\partial v}{\partial\eta}\frac{dg}{d\bar{\eta}}\right]^2 + 2\epsilon^2\mu\left\{\frac{u}{(1+\bar{\eta}n_{sh}\kappa)(r+\bar{\eta}n_{sh}\cos\theta)}\right.$$

$$\times \left[\frac{\partial(r+\bar{\eta}n_{sh}\cos\theta)}{\partial\xi} - \bar{\eta}\, n'_{sh}\cos\theta\right] + \left(\frac{v\cos\theta}{(r + \bar{\eta}\, n_{sh}\cos\theta)}\right)\}^2$$

$$+ \epsilon^2\mu\{\left[\frac{1}{(1+\bar{\eta}n_{sh}\kappa)}\left(\frac{\partial v}{\partial\xi} - \bar{\eta}\frac{n'_{sh}}{n_{sh}}\frac{\partial v}{\partial\eta}\frac{dg}{d\bar{\eta}}\right)\right]^2$$

$$+ \frac{2}{(1+\bar{\eta}n_{sh}\kappa)}\left(\frac{\partial v}{\partial\xi} - \bar{\eta}\frac{n'_{sh}}{n_{sh}}\frac{\partial v}{\partial\eta}\frac{dg}{d\bar{\eta}}\right)\left(\frac{1}{n_{sh}}\frac{\partial u}{\partial\eta}\frac{dg}{d\bar{\eta}} - \frac{u\kappa}{1+\bar{\eta}n_{sh}\kappa}\right)\}$$

$$- \epsilon^2 C_{11} \qquad\qquad (B.6)$$

Variables C_1 through C_{11} appearing in Eqs. (B.4) through (B.6) are given by :

$$C_1 = \frac{4}{3}\mu\{\frac{1}{(1+\bar{\eta}n_{sh}\kappa)}\left[\frac{\partial u}{\partial\xi} - \bar{\eta}\frac{n'_{sh}}{n_{sh}}\frac{\partial u}{\partial\eta}\frac{dg}{d\bar{\eta}}\right] + \frac{v\kappa}{(1+\bar{\eta}n_{sh}\kappa)} \qquad (B.7)$$

$$C_2 = \frac{2}{3}\mu\{\frac{1}{n_{sh}}\frac{\partial v}{\partial\eta}\frac{dg}{d\bar{\eta}} + \frac{v\cos\theta}{r + \bar{\eta}n_{sh}\cos\theta} + \frac{u}{(1+\bar{\eta}n_{sh}\kappa)(r+\bar{\eta}n_{sh}\cos\theta)}$$

$$\times\left[\frac{\partial(r+\bar{\eta}n_{sh}\cos\theta)}{\partial\xi} - \bar{\eta}\, n'_{sh}\cos\theta\right]\} \qquad\qquad (B.8)$$

$$C_3 = \frac{\mu}{(1+\bar{\eta}n_{sh}\kappa)}\left[\frac{\partial v}{\partial\xi} - \bar{\eta}\frac{n'_{sh}}{n_{sh}}\frac{\partial v}{\partial\eta}\frac{dg}{d\bar{\eta}}\right] \qquad\qquad (B.9)$$

$$C_4 = \mu\{\frac{1}{(1+\bar{\eta}n_{sh}\kappa)}\left[\frac{\partial v}{\partial\xi} - \bar{\eta}\frac{n'_{sh}}{n_{sh}}\frac{\partial v}{\partial\eta}\frac{dg}{d\bar{\eta}}\right] + \frac{1}{n_{sh}}\frac{\partial u}{\partial\eta}\frac{dg}{d\bar{\eta}} - \frac{u\kappa}{1+\bar{\eta}n_{sh}\kappa}\} \qquad (B.10)$$

$$C_5 = \frac{4}{3} \frac{\mu}{n_{sh}} \frac{\partial v}{\partial \eta} \frac{dg}{d\bar{\eta}}$$

(B.11)

$$C_6 = \frac{2}{3} \mu \{\frac{1}{(1+\bar{\eta}n_{sh}\kappa)} [\frac{\partial u}{\partial \xi} - \bar{\eta} \frac{n'_{sh}}{n_{sh}} \frac{\partial u}{\partial \eta} \frac{dg}{d\bar{\eta}}] + [\frac{u}{(1+\bar{\eta}n_{sh}\kappa)(r+\bar{\eta}n_{sh}\cos\theta)}]$$

$$\times [\frac{\partial(r+\bar{\eta}n_{sh}\cos\theta)}{\partial \xi} - \bar{\eta} n'_{sh} \cos\theta] + v(\frac{\kappa}{1+\bar{\eta}n_{sh}\kappa} + \frac{\cos\theta}{r+\bar{\eta}n_{sh}\cos\theta})]\}$$

(B.12)

$$C_7 = \frac{\mu}{Pr} (\frac{r+\bar{\eta}n_{sh}\cos\theta}{1+\bar{\eta}n_{sh}\kappa})(\frac{\partial H}{\partial \xi} - \bar{\eta} \frac{n'_{sh}}{n_{sh}} \frac{\partial H}{\partial \eta} \frac{dg}{d\bar{\eta}})$$

(B.13)

$$C_8 = \frac{\mu u}{Pr} (\frac{r+\bar{\eta}n_{sh}\cos\theta}{1+\bar{\eta}n_{sh}\kappa}) (\frac{\partial u}{\partial \xi} - \bar{\eta} \frac{n'_{sh}}{n_{sh}} \frac{\partial u}{\partial \eta} \frac{dg}{d\bar{\eta}})$$

(B.14)

$$C_9 = 2\mu \{\frac{1}{n_{sh}} \frac{\partial v}{\partial \eta} \frac{dg}{d\bar{\eta}} - \frac{v\kappa}{(1+\bar{\eta}n_{sh}\kappa)} - \frac{1}{(1+\bar{\eta}n_{sh}\kappa)} [\frac{\partial u}{\partial \xi}$$

$$- \bar{\eta} \frac{n'_{sh}}{n_{sh}} \frac{\partial u}{\partial \eta} \frac{dg}{d\bar{\eta}}]\}$$

(B.15)

$$C_{10} = 2\mu \{(\frac{1}{n_{sh}} \frac{\partial v}{\partial \eta} \frac{dg}{d\bar{\eta}}) - \frac{v \cos\theta}{r+\bar{\eta}n_{sh}\cos\theta} - \frac{u}{(1+\bar{\eta}n_{sh}\kappa)(r+\bar{\eta}n_{sh}\cos\theta)}$$

$$\times [\frac{\partial(r+\bar{\eta}n_{sh}\cos\theta)}{\partial \xi} - \bar{\eta} n'_{sh} \cos\theta]\}$$

(B.16)

$$C_{11} = \frac{2}{3} \mu \left\{ \frac{1}{(1+\bar{\eta}n_{sh}\kappa)} \left[\frac{\partial u}{\partial \xi} - \bar{\eta} \frac{n'_{sh}}{n_{sh}} \frac{\partial u}{\partial \eta} \frac{dg}{d\bar{\eta}} \right] + \left[\frac{u}{(1+\bar{\eta}n_{sh}\kappa)(r+\bar{\eta}n_{sh}\cos\theta)} \right] \right.$$

$$\times \left[\frac{\partial(r+\bar{\eta}n_{sh}\cos\theta)}{\partial \xi} - \bar{\eta} \, n'_{sh} \, \cos\theta \right] + \frac{1}{n_{sh}} \frac{\partial v}{\partial \eta} \frac{dg}{d\bar{\eta}}$$

$$\left. + v \left[\frac{\kappa}{1+\bar{\eta}n_{sh}\kappa} + \frac{\cos\theta}{r+\bar{\eta}n_{sh}\cos\theta} \right] \right\}^2 \qquad (B.17)$$

REPORT DOCUMENTATION PAGE

Public reporting burden for this collection of information is estimated to average 1 hour per response, including the time for reviewing instructions, searching existing data sources, gathering and maintaining the data needed, and completing and reviewing the collection of information. Send comments regarding this burden estimate or any other aspect of this collection of information, including suggestions for reducing this burden, to Washington Headquarters Services, Directorate for Information Operations and Reports, 1215 Jefferson Davis Highway, Suite 1204, Arlington, VA 22202-4302, and to the Office of Management and Budget, Paperwork Reduction Project (0704-0188), Washington, DC 20503.

1. AGENCY USE ONLY (Leave blank)	2. REPORT DATE March 1992	3. REPORT TYPE AND DATES COVERED Contractor Report

4. TITLE AND SUBTITLE

Viscous-Shock-Layer Analysis of Hypersonic
Flows Over Long Slender Vehicles

5. FUNDING NUMBERS

G NAG1-346

WU 506-40-91-02

6. AUTHOR(S)

Kam-Pui Lee and Roop N. Gupta

7. PERFORMING ORGANIZATION NAME(S) AND ADDRESS(ES)

Old Dominion University
Norfolk, VA 23508

8. PERFORMING ORGANIZATION REPORT NUMBER

9. SPONSORING/MONITORING AGENCY NAME(S) AND ADDRESS(ES)

NASA Langley Research Center
Hampton, VA 23665-5225

10. SPONSORING/MONITORING AGENCY REPORT NUMBER

NASA CR-189614

11. SUPPLEMENTARY NOTES   Langley Technical Monitor: E. Vincent Zoby
The information presented in this report was offered as a thesis by Kam-Pui Lee
in partial fulfillment of the requirements for the Degree of Doctor of
Philosophy, Old Dominion University, August 1988.

12a. DISTRIBUTION/AVAILABILITY STATEMENT

Unclassified-Unlimited

Subject Category 34

12b. DISTRIBUTION CODE

13. ABSTRACT (Maximum 200 words)

An efficient and accurate method for solving the viscous-shock-layer equations
for hypersonic flows over long slender bodies is presented. The two
first-order equations, continuity and normal momentum, are solved
simultaneously as a coupled set. The flow conditions included are from
high Reynolds numbers at low altitudes to low Reynolds numbers at
high altitudes. For high Reynolds number flows, both chemical
nonequilibrium and perfect-gas cases are analysed with surface catalytic
effects and different turbulence models, respectively. At low Reynolds
number flow conditions, corrected slip models are implemented with
perfect-gas case. Detailed comparisons are included with other predictions
and experimental data.

14. SUBJECT TERMS

| VSL Analysis | Coupled Solutions | Low Density Flows |
| Long Slender Bodies | Finite-rate Perfect Gas | |

15. NUMBER OF PAGES
221

16. PRICE CODE
A10

17. SECURITY CLASSIFICATION OF REPORT Unclassified	18. SECURITY CLASSIFICATION OF THIS PAGE Unclassified	19. SECURITY CLASSIFICATION OF ABSTRACT	20. LIMITATION OF ABSTRACT

NSN 7540-01-280-5500